

# NOTE TO USERS

This reproduction is the best copy available.

**UMI**<sup>®</sup>



**New Insights on the Chemical Speciation of Nickel and Copper  
in a Naturally Metal-Rich Soil from the  
Thetford Mines Area, Quebec**

**by**

**Catherine Anne Murimboh**

A thesis submitted to the Faculty of Science  
in partial fulfillment of the requirements for the degree of  
Master of Science

Department of Chemistry  
Carleton University  
Ottawa, Ontario  
September 2005

Copyright © 2005

Catherine Anne Murimboh



Library and  
Archives Canada

Bibliothèque et  
Archives Canada

Published Heritage  
Branch

Direction du  
Patrimoine de l'édition

395 Wellington Street  
Ottawa ON K1A 0N4  
Canada

395, rue Wellington  
Ottawa ON K1A 0N4  
Canada

*Your file* *Votre référence*

*ISBN: 0-494-10142-3*

*Our file* *Notre référence*

*ISBN: 0-494-10142-3*

#### NOTICE:

The author has granted a non-exclusive license allowing Library and Archives Canada to reproduce, publish, archive, preserve, conserve, communicate to the public by telecommunication or on the Internet, loan, distribute and sell theses worldwide, for commercial or non-commercial purposes, in microform, paper, electronic and/or any other formats.

The author retains copyright ownership and moral rights in this thesis. Neither the thesis nor substantial extracts from it may be printed or otherwise reproduced without the author's permission.

#### AVIS:

L'auteur a accordé une licence non exclusive permettant à la Bibliothèque et Archives Canada de reproduire, publier, archiver, sauvegarder, conserver, transmettre au public par télécommunication ou par l'Internet, prêter, distribuer et vendre des thèses partout dans le monde, à des fins commerciales ou autres, sur support microforme, papier, électronique et/ou autres formats.

L'auteur conserve la propriété du droit d'auteur et des droits moraux qui protègent cette thèse. Ni la thèse ni des extraits substantiels de celle-ci ne doivent être imprimés ou autrement reproduits sans son autorisation.

---

In compliance with the Canadian Privacy Act some supporting forms may have been removed from this thesis.

Conformément à la loi canadienne sur la protection de la vie privée, quelques formulaires secondaires ont été enlevés de cette thèse.

While these forms may be included in the document page count, their removal does not represent any loss of content from the thesis.

Bien que ces formulaires aient inclus dans la pagination, il n'y aura aucun contenu manquant.

  
**Canada**

*In memory of Grandma Burroughs*

## **Abstract**

The objective of this research was to investigate trace metal speciation in a naturally metal-rich soil from the Thetford Mines area (Quebec, Canada) by 1) identifying the principal mineral host(s) of Ni, and 2) characterizing relative vertical changes in the kinetic reactivity of Ni and Cu in the soil profile. SEM-EDS was used to characterize the mineralogy of individual silt- and clay-sized (< 0.063 mm) soil particles. ToF-SIMS analysis of these grains found several Mg-bearing phyllosilicates (i.e. biotite and chlorite) to contain Ni. Kinetic fractionation studies were used to characterize the change in the kinetics of Ni and Cu extraction from the soil as a function of depth. The results indicated that Ni became less labile towards the surface, while Cu displayed the opposite trend. These trends likely reflect the differential effects of soil weathering processes with depth, which act to varying extents on the two elements because of differences in their chemical forms. This research has important implications for interpretation of natural background levels of trace metals in soils and the associated environmental risk.

## **Acknowledgements**

I wish to acknowledge all those who have helped me in the course of this research. I would especially like to thank my supervisor, Professor C.L. Chakrabarti (a.k.a. “Chak”) who encouraged me to use a multidisciplinary approach for this research, bridging the gap between the disparate disciplines of Chemistry and Earth Sciences. His enthusiasm and determination, both in life and in his never-ending pursuit of knowledge are an inspiration to me.

I would like to express my gratitude to Dr. Rod Klassen from the Geological Survey of Canada (GSC) for introducing me to this research project, and for his invaluable help and support. I am also indebted to several other people at the GSC for lending me their advice and expertise, especially Ross Knight, Pat Hunt and Dr. Conrad Grégoire. Special thanks also go to Dr. Rana Sodhi and Dr. Peter Broderson for their help with the ToF-SIMS work at the University of Toronto, as well as to Dan MacDonald for providing training and assistance on the SEM-EDS system at Acadia University.

I would also like to thank my husband, Dr. John Murimboh for his continued guidance and encouragement, as well as all the members of Chak’s research group, past and present, for enriching my experience as a graduate student at Carleton University: Ismail Al-Fasfous, Partha Chakraborty, Jian Fu (Andrew) Deng, Jeff Guthrie, Nouri Hassan, Jamaluddin, Jie (Jack) Meng, Rupasri Mandal, Rebekha Rooney, Mohamed Salam, Soheila Shahmiri, Lin Si, Joya (Rong) Wang, Min Yang, Tahir Yapici, Janel Yu and Jiujuan (JJ) Zhao. Last but not least, I wish to express my deepest appreciation to my family for their continued love and support.

Financial support for a Canada Graduate Scholarship for the M.Sc. program from the Natural Sciences and Engineering Research Council of Canada is also gratefully acknowledged.

## **Table of Contents**

<b>Abstract</b>	<b>i</b>
<b>Acknowledgements</b>	<b>ii</b>
<b>Table of Contents</b>	<b>iii</b>
<b>List of Figures</b>	<b>v</b>
<b>List of Tables</b>	<b>ix</b>
<b>Chapter 1 Introduction</b>	<b>1</b>
1.1 Statement of the Problem.....	2
1.2 Objectives.....	3
1.3 Outline of the Thesis.....	3
1.4 References.....	4
<b>Chapter 2 Scientific Background</b>	<b>5</b>
2.1 Current State of Knowledge.....	6
2.1.1 Glacial Soil Formation.....	6
2.1.2 Mineral Hosts for Trace Metals.....	7
2.1.3 Trace Metal Speciation in Soils.....	9
2.2 Knowledge Gaps.....	11
2.3 Study Area.....	12
2.4 Previous Research.....	13
2.5 Hypothesis.....	22
2.6 Experimental Design.....	22
2.7 References.....	23
<b>Chapter 3 Determination of the Mineral Host for Nickel</b>	<b>27</b>
3.1 Introduction.....	28
3.2 Theoretical Background.....	30
3.2.1 Fundamentals of SEM-EDS.....	30
3.2.2 Fundamentals of ToF-SIMS.....	30
3.2.3 ToF-SIMS Modes of Operation.....	34
3.3 Experimental.....	37
3.3.1 Sample Preparation.....	37
3.3.2 SEM-EDS Data Acquisition.....	37
3.3.3 SEM-EDS Image Analysis.....	39
3.3.4 ToF-SIMS Data Acquisition.....	41
3.4 Results and Discussion.....	41
3.4.1 Sample Puck 63B.....	41
3.4.2 Sample Puck 63C.....	59
3.4.3 Sample Puck 63E.....	67
3.4.4 Isotope Ratios.....	75
3.4.5 Additional Merits of ToF-SIMS.....	79
3.5 Conclusions.....	81
3.6 References.....	85

<b>Chapter 4</b>	<b>Kinetic Fractionation of Nickel and Copper</b>	<b>88</b>
4.1	Introduction.....	89
4.1.1	Weathering and Soil Formation Processes .....	90
4.1.2	Ethylenediaminetetraacetic Acid (EDTA).....	92
4.2	Kinetic Fractionation Theory.....	97
4.3	Experimental.....	98
4.3.1	Reagents and Materials.....	98
4.3.2	Soil Samples.....	99
4.3.3	Apparatus .....	99
4.3.4	Optimization Experiments.....	101
4.3.5	Kinetic Experiments .....	101
4.3.6	Data Analysis.....	102
4.4	Results and Discussion .....	104
4.4.1	Optimization of Experimental Parameters .....	104
4.4.2	Kinetic Fractionation Results .....	108
4.4.3	Validation of Data Fitting.....	117
4.4.4	EDTA-Extractable Metal Species .....	121
4.4.5	Physical Significance of $C_L$ and $C_{SL}$ .....	122
4.4.6	Kinetic Trends.....	123
4.5	Conclusions.....	139
4.6	References .....	140
<b>Chapter 5</b>	<b>Conclusions</b>	<b>145</b>
<b>Appendix A</b>		<b>149</b>

## List of Figures

Figure 2.1	Basic structure of phyllosilicate minerals.....	10
Figure 2.2	Map of the Thetford Mines area, Quebec.....	17
Figure 2.3	Depth profiles for pH and concentrations of Mg, Ni and Cu in profiles 63 and 64.....	18
Figure 2.4	Trace metal-Mg correlation diagrams for profiles 63 and 64.....	21
Figure 3.1	Schematic diagram of a ToF-SIMS instrument.....	32
Figure 3.2	Conceptual diagram of the SIMS process.....	32
Figure 3.3	Conceptual example of secondary ion spectra using the three operational modes.....	36
Figure 3.4	Sample epoxy puck used for SEM-EDS mapping and ToF-SIMS analysis.....	38
Figure 3.5	Secondary electron images of sample puck 63B.....	44
Figure 3.6	EDS element maps for sample puck 63B.....	45
Figure 3.7	Mineral map for sample puck 63B.....	46
Figure 3.8	Secondary electron and BSE images used to locate individual mineral grains in sample area 63B.....	47
Figure 3.9	EDS spectrum for mineral grain 1 (chlorite) in sample area 63B.....	48
Figure 3.10	Variation in relative positive secondary ion yield as a function of atomic number.....	49
Figure 3.11	Mass spectrum for sample area 63B (Spectral mode, 0 – 100 amu).....	54
Figure 3.12	Individual mass spectra of major elements in sample area 63B (Spectral mode).....	55
Figure 3.13	Individual mass spectra for $^{58}\text{Ni} + ^{58}\text{Fe}$ and $^{60}\text{Ni}$ in sample area 63B (Spectral mode).....	56
Figure 3.14	Individual mass spectra of major elements in sample area 63B (Compromise mode).....	57
Figure 3.15	Individual mass spectrum for $^{58}\text{Ni}$ in sample area 63B (Compromise mode).....	58
Figure 3.16	Secondary ion images for sample area 63B (Spectral mode).....	60
Figure 3.17	Secondary ion images for sample area 63B (Compromise mode).....	61
Figure 3.18	Mineral map for sample puck 63C.....	63
Figure 3.19	Secondary electron image used to locate individual mineral grains in sample area 63C1.....	64

Figure 3.20	EDS spectra for mineral grains 1 (biotite), 3 (Fe sulphide) and 6 (chlorite) in sample area 63C1 .....	65
Figure 3.21	Secondary electron image used to locate individual mineral grains in sample area 63C2.....	66
Figure 3.22	Secondary ion images for sample area 63C1 (Spectral mode).....	68
Figure 3.23	Secondary ion images for sample area 63C1 (Compromise mode).....	69
Figure 3.24	Secondary ion images for sample area 63C2 (Spectral mode).....	70
Figure 3.25	Secondary ion images for sample area 63C2 (Compromise mode).....	71
Figure 3.26	Mineral map for sample puck 63E.....	72
Figure 3.27	BSE image used to locate individual mineral grains in sample area 63E2 .....	73
Figure 3.28	EDS spectra for mineral grains 1 (olivine) and 4 (chlorite) in sample area 63E2. ....	74
Figure 3.29	Secondary ion images for sample area 63E2 (Spectral mode) .....	76
Figure 3.30	Secondary ion images for sample area 63E2 (Compromise mode).....	77
Figure 3.31	ToF-SIMS secondary electron images of sample area 63E1 before and after oxygen sputtering .....	80
Figure 3.32	SEM secondary electron and BSE images of sample area 63E1 .....	80
Figure 3.33	EDS spectrum for mineral grain 1 (apatite) in sample area 63E1 .....	82
Figure 3.34	Secondary ion images for sample area 63E1 (Spectral mode, negative ions).....	83
Figure 4.1	Generalized scheme for mineral weathering and formation pathways.....	93
Figure 4.2	Structure of neutral EDTA molecule .....	95
Figure 4.3	Speciation diagram for EDTA as a function of pH.....	95
Figure 4.4	Structure of EDTA complex with a metal ion .....	96
Figure 4.5	Experimental set-up for the kinetic experiments .....	103
Figure 4.6	Optimization of pH for Ni and Cu extractions.....	106
Figure 4.7	Optimization of EDTA concentration for Ni and Cu extractions .....	107
Figure 4.8	Replicate Ni and Cu kinetic curves for sample 63B .....	109
Figure 4.9	Replicate Ni and Cu kinetic curves for sample 63L .....	110
Figure 4.10	Ni kinetic curves for samples from profile 63 .....	111
Figure 4.11	Cu kinetic curves for samples from profile 63.....	112
Figure 4.12	Ni kinetic curves for samples from profile 64 .....	113
Figure 4.13	Cu kinetic curves for samples from profile 64.....	114

Figure 4.14	Expanded view of the beginning of the Ni kinetic curve for sample 63F, illustrating the poor non-linear regression fit to the data points representing the fast component .....	118
Figure 4.15	Natural logarithmic transform of exponential rise data for Cu in samples from profile 64 .....	120
Figure 4.16	%C <sub>L</sub> and %C <sub>SL</sub> vs. depth for Ni in profile 63 .....	125
Figure 4.17	k <sub>SL</sub> vs. depth for Ni in profile 63 .....	126
Figure 4.18	%C <sub>L</sub> and %C <sub>SL</sub> vs. depth for Ni in profile 64 .....	127
Figure 4.19	k <sub>SL</sub> vs. depth for Ni in profile 64.....	128
Figure 4.20	%C <sub>L</sub> and %C <sub>SL</sub> vs. depth for Cu in profile 63 .....	129
Figure 4.21	k <sub>SL</sub> vs. depth for Cu in profile 63 .....	130
Figure 4.22	%C <sub>L</sub> and %C <sub>SL</sub> vs. depth for Cu in profile 64 .....	131
Figure 4.23	k <sub>SL</sub> vs. depth for Cu in profile 64.....	132
Figure 4.24	Ni kinetic curves illustrating contrast in %C <sub>L</sub> between samples 63B & 63E and between 64C & 64E.....	133
Figure 4.25	Conceptual diagram of metal ions occupying octahedral lattice sites in a chlorite crystal.....	138
Figure A.1	Ni kinetic curve for sample 63B .....	150
Figure A.2	Ni kinetic curve for sample 63E .....	150
Figure A.3	Ni kinetic curve for sample 63F.....	151
Figure A.4	Ni kinetic curve for sample 63G.....	151
Figure A.5	Ni kinetic curve for sample 63L. ....	152
Figure A.6	Ni kinetic curve for sample 63O.....	152
Figure A.7	Ni kinetic curve for sample 64C.....	153
Figure A.8	Ni kinetic curve for sample 64E .....	153
Figure A.9	Ni kinetic curve for sample 64G.....	154
Figure A.10	Ni kinetic curve for sample 64I .....	154
Figure A.11	Ni kinetic curve for sample 64K.....	155
Figure A.12	Ni kinetic curve for sample 64L .....	155
Figure A.13	Cu kinetic curve for sample 63B .....	156
Figure A.14	Cu kinetic curve for sample 63E.....	156
Figure A.15	Cu kinetic curve for sample 63F.....	157
Figure A.16	Cu kinetic curve for sample 63G .....	157

Figure A.17	Cu kinetic curve for sample 63L.....	158
Figure A.18	Cu kinetic curve for sample 63O .....	158
Figure A.19	Cu kinetic curve for sample 64C .....	159
Figure A.20	Cu kinetic curve for sample 64E.....	159
Figure A.21	Cu kinetic curve for sample 64G .....	160
Figure A.22	Cu kinetic curve for sample 64I.....	160
Figure A.23	Cu kinetic curve for sample 64K. ....	161
Figure A.24	Cu kinetic curve for sample 64L.....	161

## **List of Tables**

Table 2.1	X-ray diffraction results for clay-sized soil samples .....	19
Table 2.2	Carbon content for silt- and clay-sized soil samples .....	20
Table 3.1	Operating conditions of the two instruments used for acquisition of SEM-EDS images.....	38
Table 3.2	Added and subtracted elements for mapping the mineralogy of individual soil particles in the sample pucks .....	40
Table 3.3	Instrumental conditions for ToF-SIMS analyses .....	42
Table 3.4	Positive secondary ion yield for selected metals compared to that of their corresponding oxides.....	51
Table 3.5	Isotope ratios and proportion of $^{58}\text{Ni}$ out of $^{58}\text{Tot}$ for all analysis areas...	78
Table 4.1	Formation constants for M-EDTA complexes.....	96
Table 4.2	Instrumental conditions for determination of Ni by GFAAS .....	100
Table 4.3	Instrumental conditions for determination of Cu by GFAAS.....	100
Table 4.4	Kinetically distinguishable components for Ni in profile 63.....	115
Table 4.5	Kinetically distinguishable components for Cu in profile 63 .....	115
Table 4.6	Kinetically distinguishable components for Ni in profile 64.....	116
Table 4.7	Kinetically distinguishable components for Cu in profile 64.....	116

## **Chapter 1    Introduction**

---

### **1.1 Statement of the Problem**

Natural background concentrations of elements in the soil environment are highly variable and play a key role in the maintenance of life by providing a supply of essential nutrients required for biological processes. Many trace metals (e.g. Ni, Cu, Zn, Co) are essential micronutrients to organisms at low concentrations, but can be toxic at relatively high concentrations. Elevated levels of trace metals in soils are a growing environmental concern, as they represent a global threat to human and ecosystem health. Although trace metal contamination of soils from anthropogenic sources (e.g. industrial and metal smelter effluents) is a prominent and persistent environmental dilemma, many soils are naturally enriched in trace metals. Large areas (> 1000s of km<sup>2</sup>) of some Canadian terrains have natural background levels that exceed regulatory environmental thresholds [1-3]. However, the transport, fate, and bioavailability of trace metals in soils are determined not only by their total concentrations, but also by their chemical speciation. In the context of the soil environment, chemical speciation is commonly defined as the specific species, forms or phases of an element, which can further be defined functionally (e.g. “plant-available” species) or operationally by the procedures or reagents used to isolate the element [4]. In this thesis, chemical speciation refers to the characterization of trace metals in terms of their geochemical phases and kinetic reactivities.

Soils inherit the physical and chemical properties of the parent materials; hence, the natural trace metal signal is predominantly of geologic control. Metals originate in the crystal lattices of the rock-forming minerals that make up the soil parent material. What metals are present and how they are released during soil weathering processes depend on the physical and chemical properties of the original mineral host. Identification of the principal mineralogical controls on natural background levels of trace metals in soils and evaluation of their reactivity in the soil environment are crucial for developing environmental tests in support of risk management and regulation.

This research investigates the chemical speciation of Ni and Cu in a naturally metal-rich soil from the Thetford Mines area, located in the Eastern Townships of Quebec. The soil samples used in this research were collected as part of a wider study within the Geological Survey of Canada's Metals in the Environment (MITE) research program. Ni and Cu were chosen for comparative purposes because Cu is present in relatively low concentrations typical of average natural background levels (~ 20 ppm) [5], whereas Ni is highly enriched in the soil, reaching concentrations as high as 1800 ppm [6]. The limit for safe levels of total Ni concentrations in soils, as set by the Canadian Environmental Quality Guidelines, is 50 ppm [7]; however, little is known about the geochemical forms and reactivity of Ni and other trace metals in this soil, which control the delicate balance between their roles as nutrients and toxicants.

## **1.2 Objectives**

For the naturally metal-rich soil from the Thetford Mines area, the objectives of this research were:

- 1) To identify the principal mineral host(s) of Ni.
- 2) To characterize relative changes in the kinetic reactivity of Ni and Cu as a function of depth within the soil profile.

## **1.3 Outline of the Thesis**

The thesis is divided into five chapters. The statement of the problem, the main objectives and an outline of the thesis are presented in Chapter 1. Chapter 2 describes the current state of knowledge and its main limitations, provides some background information on the study area, proposes a hypothesis based on results from previous studies on these soil samples, and outlines the experimental approaches taken. Chapter 3 deals with the investigation of the mineral host for Ni on an individual particle basis using a combination of surface analytical techniques. Chapter 4 describes kinetic fractionation studies of Ni and Cu in the bulk soil based on the kinetics of metal

extraction as a function of depth through the profile. A summary of the major findings and final conclusions drawn from this study as well as their overall significance are presented in Chapter 5.

#### **1.4 References**

---

1. R.G. Garrett, Natural Distribution and Abundance of Elements, in *Essentials of Medical Geology*, Olle Selinus (Ed.), Elsevier Academic Press, London, UK, 2005, Chapter 2.
2. J.R. Bélanger, *Can. J. Remote Sens.*, 1991, **17**, 112.
3. J. Fitchko, *Pollut. Eng.*, 1989, **21**, 90.
4. A.M. Ure, in *Heavy Metals in Soils*, B.J. Alloway (Ed.), Blackie and Son, Glasgow, UK, 1990, Chapter 4.
5. J. Emsley, *Nature's Building Blocks: An A-Z Guide to the Elements*, Oxford University Press, New York, USA, 2003, p. 124.
6. J.R. Bélanger, *Adv. Space Res.*, 1983, **3**, 187.
7. Canadian Environmental Quality Guidelines, Environment Canada, 2003.

## **Chapter 2      Scientific Background**

---

## **2.1 Current State of Knowledge**

### *2.1.1 Glacial Soil Formation*

Soils are complex natural systems having properties derived from the integrated effects of physical, chemical, and biological processes [1,2]. Over 90 % of Canada has been glaciated; hence, soils in many parts of the country are of glacial origin [3]. During the last ice age (~ 10,000 – 23,000 years ago), the Laurentide ice sheet covered most of Canada. The glaciers, often several kilometres high, acted like giant bulldozers, mechanically ripping up the underlying bedrock and transporting the eroded material along the path of ice flow. The glaciers began to retreat about 8,000 – 12,000 years ago, leaving in their wake an unsorted mixture of rocks and debris, known as glacial till. These deposits of till could be up to hundreds of metres deep, and comprise the geologic precursor, or parent material, to many Canadian soils [2,3].

Soil is formed as a result of complex interactions between a variety of factors, including climate (e.g. temperature, precipitation), biota (e.g. vegetation, micro-organisms), topography, parent materials, and time [2]. Differential weathering (both physical and chemical) of the parent materials with depth leads to the formation of vertical zonations through the profile, known as soil horizons. The A horizon is generally characterized by a dark colour due to accumulation of organic matter, and is sometimes underlain by a lighter coloured leached (or eluviated) layer, designated Ae. The B horizon often contains an accumulation of clays, Fe-oxides, and leached elements from overlying layers, and the underlying C horizon consists of the relatively unweathered parent materials [1,2,4].

Many characteristics of soils formed on glaciated terrains are distinct from soils formed by chemical, aeolian or fluvial processes. During glacial grinding and abrasion of the bedrock, mineral partitioning among size fractions tends to concentrate the softer minerals (e.g. phyllosilicates, hematite, and serpentine) in the clay-sized fraction

(< 0.002 mm) [3,5-7]. Hence, the minerals in the fine fraction of glacial soils consist primarily of physically comminuted detritus, rather than the extensively weathered materials that characterize the fine fraction of many soils in unglaciated terrains. In addition, glacial soils have developed under temperate climatic conditions, and are young on a geologic timescale, having had only a few thousand years to equilibrate with their local environment [3]. Hence, the principal effects of weathering and soil formation processes generally only extend to a depth of about 50 cm [8]. In addition, as a result of the limited intensity and duration of postglacial weathering processes, the minerals in these soils are primarily those derived from the till parent materials, and are not extensively leached of their constituent elements. In contrast, older ( $\geq 100,000$  years), 'residual' soils are relatively depleted of their chemical elements due to extensive mineral weathering and leaching and are characterized by an abundance of secondary precipitates (e.g. Al-, Fe- and Mn-oxides) and authigenic clay minerals [1].

#### 2.1.2 Mineral Hosts for Trace Metals

The chemical diversity of soils arises from the diverse mineralogy of the parent materials. Soil minerals bearing trace elements serve as reservoirs for these elements, and release them into the soil solution via weathering processes [1,9,10]. While trace metals can occur as major components of some minerals, including sulphides (e.g. pentlandite,  $(\text{Ni,Fe})_9\text{S}_8$ ), oxides (e.g. chromite,  $\text{FeCr}_2\text{O}_4$ ), and carbonates (e.g. malachite,  $\text{Cu}_2(\text{CO}_3)(\text{OH})_2$ ), they are more often found as trace constituents in a wide variety of other minerals [1,2,4,9]. This occurs through a process known as isomorphic substitution, in which a major constituent element in the mineral structure is replaced by a trace element of comparable radius and oxidation state. For example,  $\text{Mg}^{2+}$  and  $\text{Fe}^{2+}$  in ferromagnesian minerals (e.g. olivine, pyroxene, and biotite) have ionic radii of 0.74 Å and 0.83 Å, respectively, and can be replaced by other divalent ions, such as  $\text{Ni}^{2+}$  (0.69 Å),  $\text{Cu}^{2+}$  (0.72 Å),  $\text{Co}^{2+}$  (0.72 Å) and  $\text{Zn}^{2+}$  (0.74 Å). Other trace elements, such as

$Ba^{2+}$ ,  $Sr^{2+}$  and  $Ga^{3+}$  are known to occur in some aluminosilicate minerals (e.g. feldspars and muscovite) as replacements for  $K^+$ ,  $Ca^{2+}$  and  $Al^{3+}$  [9,11].

#### *Importance of Phyllosilicates*

Many studies have alluded to the important role of phyllosilicates minerals as hosts for trace metals in soils. With their leaf-like crystal structures, these soft, easily cleaved minerals tend to concentrate in the clay-sized fraction ( $< 0.002$  mm) of glacial soils [3,5-7]. The highest concentrations of some trace metals (e.g. Cu, Pb and Zn) are also commonly found to occur in the finer soil material [3,12,13], which is commonly attributed to sequestration of dissolved metals from the soil solution by the charged surfaces of clay minerals and secondary precipitates [13-15], as well as to the occurrence of these metals in the crystal lattices of clay-sized phyllosilicates [5,16].

Phyllosilicates are an important group of minerals in the soil as both unweathered rock-forming minerals and their weathering products, and constitute one of the largest and most highly diversified groups of minerals. They include silicate (e.g. talc, serpentine) and aluminosilicate minerals, commonly known as micas (e.g. muscovite, biotite, chlorite, phlogopite), as well as secondary (authigenic) clay minerals (e.g. montmorillonite, vermiculite) [2,4]. The fundamental structural components of these minerals are tetrahedral and octahedral units, as illustrated in Figure 2.1. Interlocking arrays of  $SiO_4$  tetrahedra form tetrahedral (T) sheets, and linked octahedra, containing a central  $Al^{3+}$ ,  $Mg^{2+}$ , or  $Fe^{2+}$  ion, give rise to octahedral (O) sheets. Each phyllosilicate mineral consists of a characteristic combination of stacked T and O sheets, termed layers. In some clay minerals, the layers are separated by interlayer spaces, containing water and adsorbed cations (e.g. micas) or an additional Mg-dominated octahedral sheet, known as a brucite layer (e.g. chlorite). While atoms within the sheets are held together by strong covalent bonds, the layers are only weakly held together by electrostatic attraction, which gives rise to their easily cleaved, sheet-like nature [2,4].

In the tetrahedral sheets of phyllosilicates,  $\text{Al}^{3+}$  may isomorphically substitute for  $\text{Si}^{4+}$ , resulting in a net negative charge on the layers. Additionally, pH-dependent surface charges originate from  $\text{OH}^-$  and  $\text{O}^{2-}$  groups on broken surfaces and crystal edges. The charged surfaces of these minerals make them highly reactive materials in soils, giving them the ability to adsorb cations in the soil solution. However, substitution can also take place in the octahedral sheets, where trace amounts of metals such as  $\text{Co}^{2+}$ ,  $\text{Zn}^{2+}$ ,  $\text{Ni}^{2+}$ , and  $\text{Cu}^{2+}$  substitute for  $\text{Mg}^{2+}$  or  $\text{Fe}^{2+}$ , making these trace metals minor structural components of the minerals [17,18].

### 2.1.3 Trace Metal Speciation in Soils

Physical breakdown and chemical decomposition of the minerals hosting trace metals during weathering and soil formation releases the metals into the soil solution, where they can be leached by drainage water, taken up by plant roots, or retained in the soil by being sorbed to charged soil particles (e.g. clay minerals, organic matter, secondary Fe and Mn precipitates) or incorporated into secondary soil minerals (e.g. carbonates, oxides and hydroxides) [19,20]. The occurrence of trace metals in a diversity of physicochemical forms and associations in soils renders trace metal behaviour difficult to assess.

The dominant tool used to study trace metal partitioning among the various geochemical phases (and thereby to estimate their mobility and bioavailability to biota) is extractive chemical analysis, which differentially decomposes the compounds and minerals hosting trace elements. From these data, the concentration, form and distribution of the elements are inferred. Single extractions are used to provide a relative empirical assessment of the amount of metal associated with one or more specific soil phases [20]. For example, single-step acid digestions using the relatively weak acid hydroxylamine hydrochloride ( $\text{NH}_2\text{OH}\cdot\text{HCl}$ ), and the relatively strong acid aqua regia ( $\text{HNO}_3:\text{HCl} = 1:3$ ) are routinely used to separate soil components based on differences in their solubilities

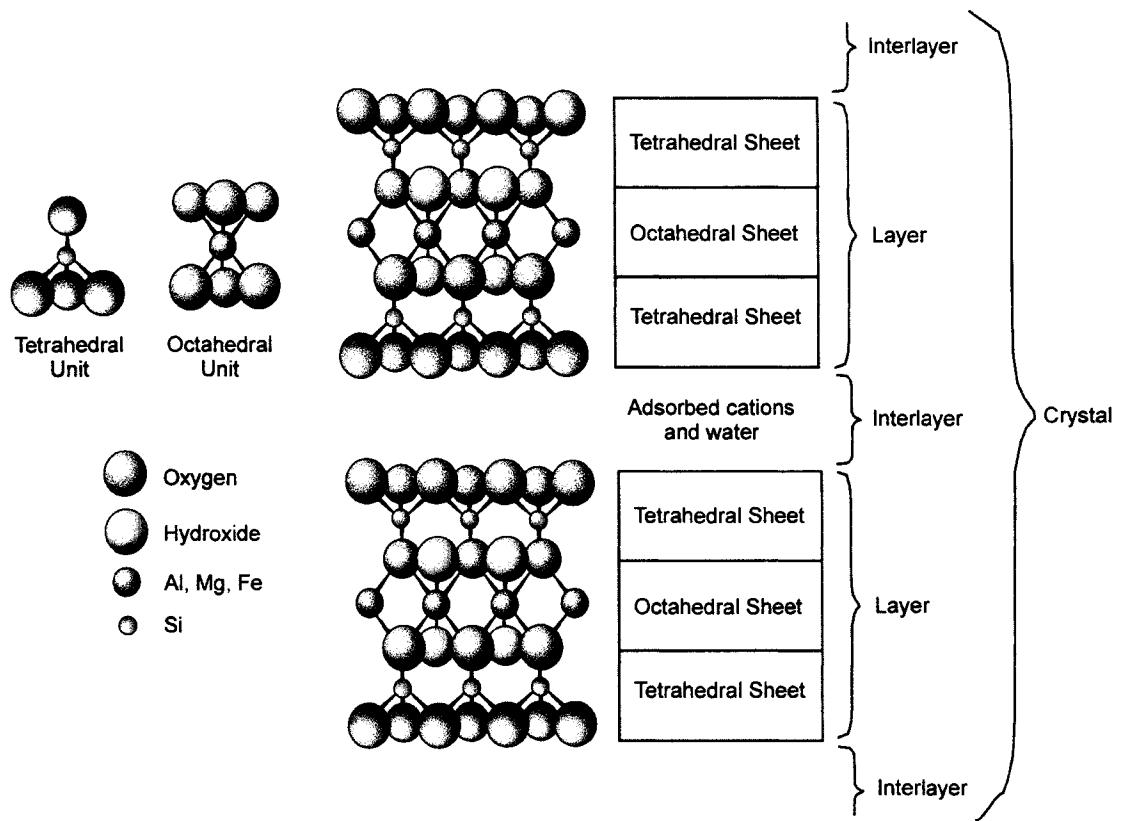


Figure 2.1 The basic molecular and structural components of phyllosilicate minerals (adapted from Brady et al. [2]).

in the two acids. More elaborate multi-step extractions are designed to partition trace metals into various chemical forms in an attempt to evaluate their potential for remobilization over time due to changes in soil chemistry (e.g. pH, redox potential, ionic strength, etc.). This method is based on the use of different reagents to successively solubilize trace elements from soil components by gradually increasing the dissolution strength down the extract series. Most sequential extraction schemes are based on the procedure developed by Tessier et al. [21]. This scheme establishes several operationally defined soil fractions into which trace metals can be partitioned: exchangeable (i.e. electrostatically bound), carbonates, Fe and Mn oxides, organic matter, and residual (i.e. held in the crystal lattices of silicate minerals). Common reagents used to dissolve each of these soil phases include electrolytes (e.g.  $MgCl_2$ ,  $CaCl_2$ ,  $NH_4OAc$ ), weak acids (e.g.  $HOAc$ ,  $EDTA$ ), reducing agents (e.g.  $NH_2OH \cdot HCl$ ,  $(NH_4)_2C_2O_4$ ), oxidizing agents (e.g.  $H_2O_2$ ,  $NaClO$ ), and strong acids (e.g. aqua regia,  $HF$ ,  $HClO_4$ ), respectively [20,22-24].

## **2.2 Knowledge Gaps**

A key knowledge gap in the current approaches for studying trace metal speciation in soils is the lack of a basis for estimating which minerals are the original hosts for the metals and what their relative importance is as controls on the natural geochemical background. Both single and sequential extraction protocols are routinely used to determine the speciation of trace metals in soils; however, these speciation schemes have been widely criticized because they are plagued by a number of inherent problems, such as lack of selectivity of extractive reagents, incomplete dissolution, readsorption and reprecipitation of previously dissolved elements, and lack of uniformity among different fractionation schemes [19,25-28]. Separated geochemical fractions are commonly classified according to the operational procedure used to isolate them, and distinctions between extractable and non-extractable forms are arbitrary and not accurate

indicators of chemical species. Consequently, the results are defined by laboratory protocol, making their interpretation difficult. In addition, the blind use of bulk chemical methods overlooks the complexity of soil systems, which are both chemically and physically heterogeneous.

Another major weakness in the conventional methodologies is the lack of consideration for the kinetic aspects of trace metal speciation in soils. Chemical extraction is an equilibrium-based method, where trace metals are quantified in the extract after equilibrium is assumed to have been attained. However, natural soils are dynamic biogeochemical systems which are often removed from equilibrium. Hence, time-dependent reactions are important in determining the transport, fate, and bioavailability of trace metals in the soil environment [29,30].

### **2.3 Study Area**

Thetford Mines is located in the Eastern Townships of Quebec and is home to one of the world's largest asbestos deposits. Asbestos was discovered in the region in 1876, and the town became a global leader in asbestos production [31]; however, recent health concerns associated with asbestos have led to a decline in mining operations. Asbestos is a generic term for a variety of fibrous minerals. Serpentine ( $\text{Mg}_3[\text{Si}_2\text{O}_5](\text{OH})_4$ ) is the most widely used form of asbestos and is the predominant form found in Thetford Mines [3].

The area lies in the northwest part of the Appalachian structural province. The bedrock is composed of a succession of metasediments and volcanic rocks intruded by an ophiolitic suite of igneous ultrabasic (i.e.  $\leq 45$  wt %  $\text{SiO}_2$ ) rocks. These rocks are highly enriched in Ni, Cr, Co, Fe and Mg, and occur within a serpentinized band forming an "asbestos belt" that extends over 80 km [32]. The rocks contain an abundance of Ni-rich mafic (i.e. Mg- and Fe-rich) minerals, such as olivine, pyroxene, and their hydrothermal alteration products, serpentine and chlorite [3,32-34]. Ni is also present in much less

abundant phases, such as awaruite (NiFe) and hazelwoodite ((NiFe)<sub>3</sub>S<sub>2</sub>) [35].

During the last glaciation, continental glaciers flowed southeast and eroded the soft serpentized bedrock. Nickel-rich debris was incorporated into glacial till and deposited as a dispersal train that extends up to 70 km away from the source [32]. Nickel concentrations in the till decrease with increasing distance down-ice from the ultrabasic outcrop, as shown in Figure 2.2 [3]. These Ni concentrations are reflected in the soil that developed from the till. The elevated Ni concentrations in the soil within the glacial dispersal train has been reported to be the primary factor affecting the distribution and health of local vegetation [3,32,36]. Nickel is an essential micronutrient for most plant species but is usually only present in trace quantities [37,38]. In the Thetford Mines area, maximum accumulation of Ni in plant tissues has been reported to be considerably higher than 'normal' levels for most vegetation [3]. Certain species, such as sugar maple, do not grow within the glacial dispersal train, and many deciduous trees show signs of vegetation stress, including dwarfism, deformation, chlorosis of the leaves, and premature senescence [32].

#### **2.4 Previous Research**

The soil profiles selected for this research project have been previously studied as part of the Geological Survey of Canada's Metals in The Environment (MITE) research program. A key component of the MITE study involved an interpretive approach to link elements to their mineral hosts using empirical element associations based on data from acid digestion analyses of the silt- and clay-sized soil fraction. Some of the results and interpretations drawn from this previous research are presented below. A more detailed description of this study is provided by Klassen [8].

The two soil profile samples used in this research were collected in October 1998 from two sites approximately 10 km south of Thetford Mines, QC. The two profile sites – labelled 63 and 64 – were located approximately 5 km apart within the glacial dispersal

train, as shown in Figure 2.2. Ni concentrations in the soil in this area are on the order of several 100s of ppm, while Cu concentrations average around 10s of ppm. The soil is classified as Brunisolic [39]. The soil parent material is Lennoxville Till [3,40] derived from the ultrabasic outcrop, as well as greywacke along the path of ice flow. From soil pit walls, samples were collected in a contiguous series of 5 cm vertical increments to depths of 60-70 cm, below which samples represent 5 cm vertical intervals and are spaced 10 cm apart. The samples were labelled from A to O from top to bottom, as shown in Figure 2.3. Prior to geochemical analysis, the samples were air-dried (< 30 °C) and sieved to obtain the silt- and clay-sized (< 0.063 mm) fraction and centrifuged to obtain the clay-sized (< 0.002 mm) fraction.

X-ray diffraction (XRD) analysis was used to characterize the mineralogy of the clay-sized fraction at selected depths. The results, shown in Table 2.1, indicate that quartz, feldspars, illite and chlorite are the principal minerals. Interestingly, the Ni-rich minerals (e.g. serpentine and olivine) from the ultrabasic bedrock, which were expected to be present in the soil, were found to be at or below the analytical detection limits of XRD (i.e. 3-5 wt%). Carbon content of the silt- and clay-sized soil fraction was determined using a LECO CR412 CO<sub>2</sub> gas spectrometer following thermal decomposition at 750°C (organic C) and 1350 °C (organic and inorganic C). The results, given in Table 2.2, indicate that organic carbon content is low (~ 1 wt %) in samples within 12.5 cm of the surface for profile 63 and 22.5 cm of the surface for profile 64, and drops to 0.1 wt % in the underlying samples. Inorganic carbon only occurs at or below detection limits of 0.1 wt %. Analytical data are not available for some depths because of insufficient sample quantities. The pH of the soil was determined on the < 2 mm (unground) size fraction using an Omega PHH-7x pH pen (Sheldrick, 1984) in a CaCl<sub>2</sub> buffer solution. Soil pH increases with depth in both profiles, as illustrated in Figure 2.3.

Major element concentrations (i.e. those elements typically found in most rock-forming minerals) in the silt- and clay-sized soil fraction were determined using acid

digestion analyses. Soil subsamples were digested using aqua regia (AR), followed by determination of the extracted elemental concentrations by Inductively Coupled Plasma – Atomic Emission Spectroscopy (ICP-AES). Another set of subsamples was digested using hot (60°C) 0.5 mol/L hydroxylamine hydrochloride (HA), and the element concentrations in the extract were determined using Inductively Coupled Plasma – Mass Spectroscopy (ICP-MS). All chemical analyses were conducted by CHEMEX Ltd (Vancouver, BC). For both weak (HA) and strong (AR) acid digestions, Ni, Cu and Mg concentrations increase downwards in both profiles, as illustrated in Figure 2.3. The difference in values obtained from the two reagents reflects differences in extraction efficiencies between the strong and weak acid digestions. In general, compositional differences in soil profiles of glaciated terrains can be attributed to mineral alteration due to weathering processes, or can be related to primary geological factors (e.g. variations in till provenance and glacial processes). In the two profiles from this study, no sedimentological structures or stratigraphic differences were found to indicate any change in parent material composition, and the geochemical trends are too strong to reflect primary variations, such as imperfect mixing of till parent materials. Hence, the progressive increase in element concentration with increasing depth was interpreted to reflect the effects of weathering and soil formation (e.g. leaching from the upper solum).

In both profiles, Cu and Ni concentrations determined after both acid digestions are strongly correlated with those for Mg, as shown in Figures 2.4 a) and b). These linear correlations of metal with Mg were interpreted to suggest that the metals are held in a common Mg-bearing host, in direct proportion to Mg. Aqua regia is reported to digest organic matter, secondary Fe- and Mn-oxides and hydroxides, sulphides, carbonates, clay minerals and Mg-bearing phyllosilicates [7,41,42]. The weaker hydroxylamine hydrochloride is reported to digest only organic matter and secondary Fe and Mn compounds [21,43]; however, the linear correlations suggest that it also partially digests Mg-bearing minerals and compounds. In this soil profile, Mg after aqua regia digestion

could reflect dolomite ( $\text{MgCa}(\text{CO}_3)_2$ ), sorbed species on secondary organic and inorganic compounds, and Mg-bearing phyllosilicate minerals. Dolomite is an unlikely candidate, as it only occurs in the silt- and clay-sized fractions of Lennoxville Till at concentrations < 1 wt % [40] and has likely been leached from the solum. The downward increase in Mg concentrations suggest that sorbed forms of Mg are likely minor components, as they could be expected to produce a concentration trend that increases upwards, rather than downwards. Furthermore, such strong linear correlations are generally not expected for metals held on the charged surfaces of soil particles, especially for samples in the upper solum, because of the random nature of sorption processes. Hence, the Mg extracted by aqua regia was probably derived from Mg-bearing phyllosilicates.

The strong linear correlations of Cu and Ni with Mg suggests that these metals are held as minor structural components within the octahedral sites of a Mg-bearing phyllosilicate, such as chlorite, serpentine, biotite or phlogopite. The results from the XRD analyses of the clay-sized soil fraction indicate that chlorite is by far the most abundant (17 – 35 wt %) Mg-bearing phyllosilicate mineral, suggesting that it may be a significant geochemical control. Interestingly, the samples that do not contain measurable amounts of chlorite do contain vermiculite, which is a common alteration product of chlorite [17]. Chlorite is also known to be abundant in the ultramafic bedrock from which the till parent materials were derived – most of the Ni-rich mafic minerals (e.g. olivine and pyroxene) in the ophiolite complex have undergone extensive hydrothermal alteration to chlorite [33]. Hence, the majority of the chlorite in the soil within the glacial dispersal train probably originated directly from the bedrock. Although Ni is well recognized as being highly enriched in the bedrock minerals and their alteration products, Cu is not known to be associated with these minerals. However, the fact that it has the same linear relations to Mg as Ni suggests that it is held in the same Mg-bearing phyllosilicate mineral host.

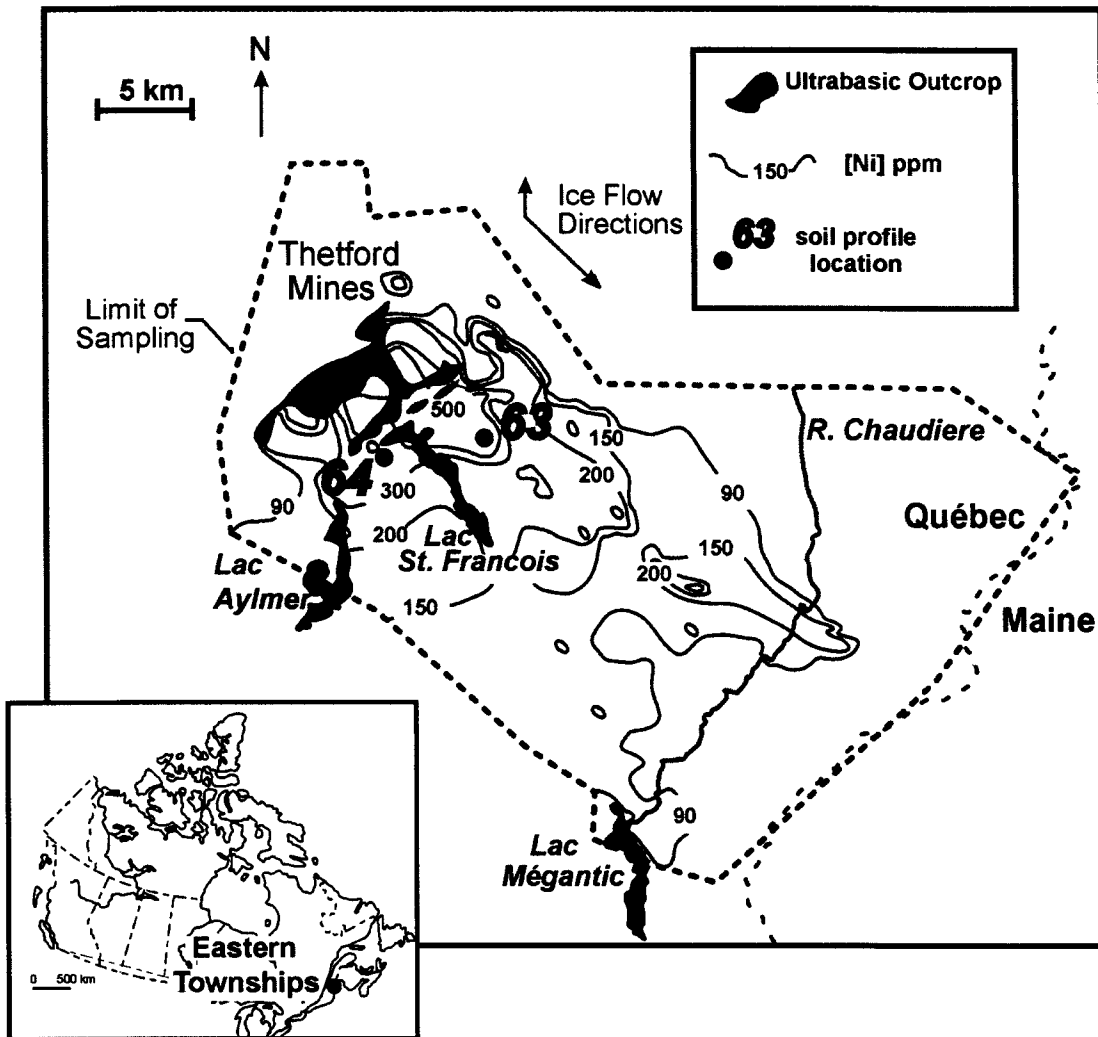


Figure 2.2 Map of the Thetford Mines area, QC, showing sampling sites (63 and 64) in relation to the ultrabasic outcrop and the Ni-rich glacial dispersal train. Contours indicate Ni concentrations in silt- and clay-sized fractions of till, based on analyses of ~ 800 samples evenly spaced within the area outlined by the dotted lines (adapted from Rencz et al. [3]).

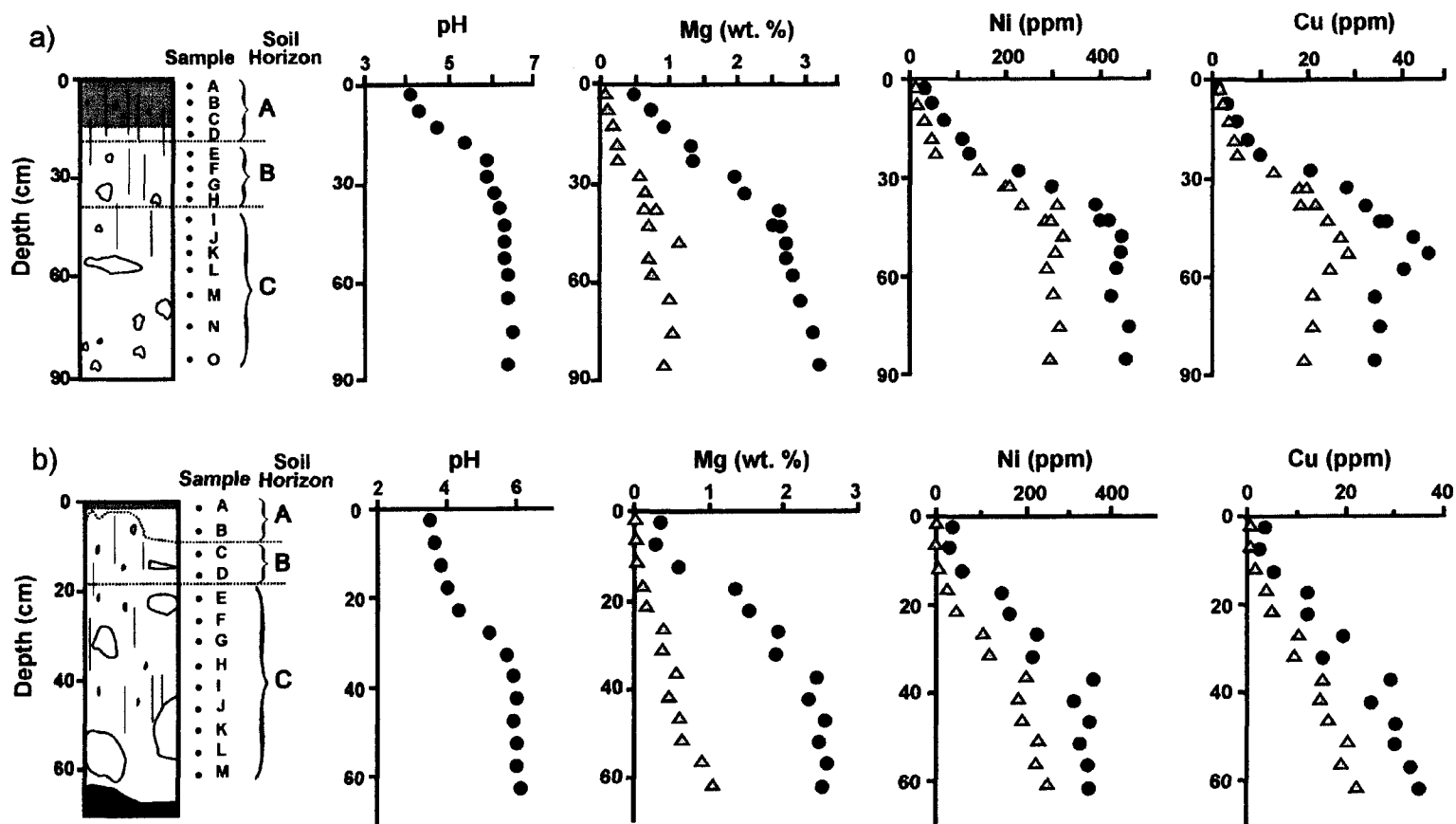


Figure 2.3 Depth profiles for pH and concentrations of Mg, Ni and Cu in a) profile 63 and b) profile 64. ▲ hydroxylamine hydrochloride, ● aqua regia. In profile sketches: △ rock clasts, ■ bedrock (shale), | plant rootlets (adapted from Klassen [8]).

Table 2.1 X-ray diffraction results for clay-sized (< 0.002 mm) soil samples. All values are in wt %. Tr = trace, ND = Not Detected (i.e. below analysis detection limits of 5 wt %).

Sample	Quartz	Plagioclase Feldspar	K Feldspar	Biotite	Illite	Chlorite	Vermiculite	Sulphides	Serpentine	Smectite
63B	28	17	Tr	ND	35	20	ND	Tr	Tr	Tr
63C	19	8	9	ND	39	26	ND	ND	Tr	Tr
63E	11	7	8	ND	43	32	ND	ND	Tr	Tr
63G	17	7	3	ND	38	35	ND	ND	Tr	Tr
63O	13	14	12	ND	45	17	ND	ND	ND	ND
64C	41	10	13	ND	12	24	ND	ND	ND	ND
64J	27	12	12	ND	28	ND	21	ND	ND	ND
64L	23	19	ND	ND	32	ND	25	ND	ND	ND

Table 2.2 Carbon content for silt- and clay-sized (< 0.063 mm) soil samples. ND = Not Detected (i.e. below analytical detection limits of 0.1 wt %).

<b>Sample</b>	<b>Organic C (<math>\pm</math> 0.1 wt %)</b>	<b>Inorganic C (<math>\pm</math> 0.1 wt %)</b>
<b>63A</b>	0.8	ND
<b>63B</b>	0.4	ND
<b>63C</b>	0.2	ND
<b>63D</b>	0.1	ND
<b>63E</b>	0.1	ND
<b>63F</b>	0.1	ND
<b>63G</b>	0.1	ND
<b>63L</b>	0.1	ND
<b>63O</b>	0.1	ND
<b>64C</b>	1.5	ND
<b>64E</b>	0.6	ND
<b>64G</b>	0.1	ND
<b>64I</b>	0.1	ND
<b>64K</b>	0.1	ND
<b>64J</b>	0.1	ND
<b>64L</b>	0.1	0.1
<b>64M</b>	0.1	0.1

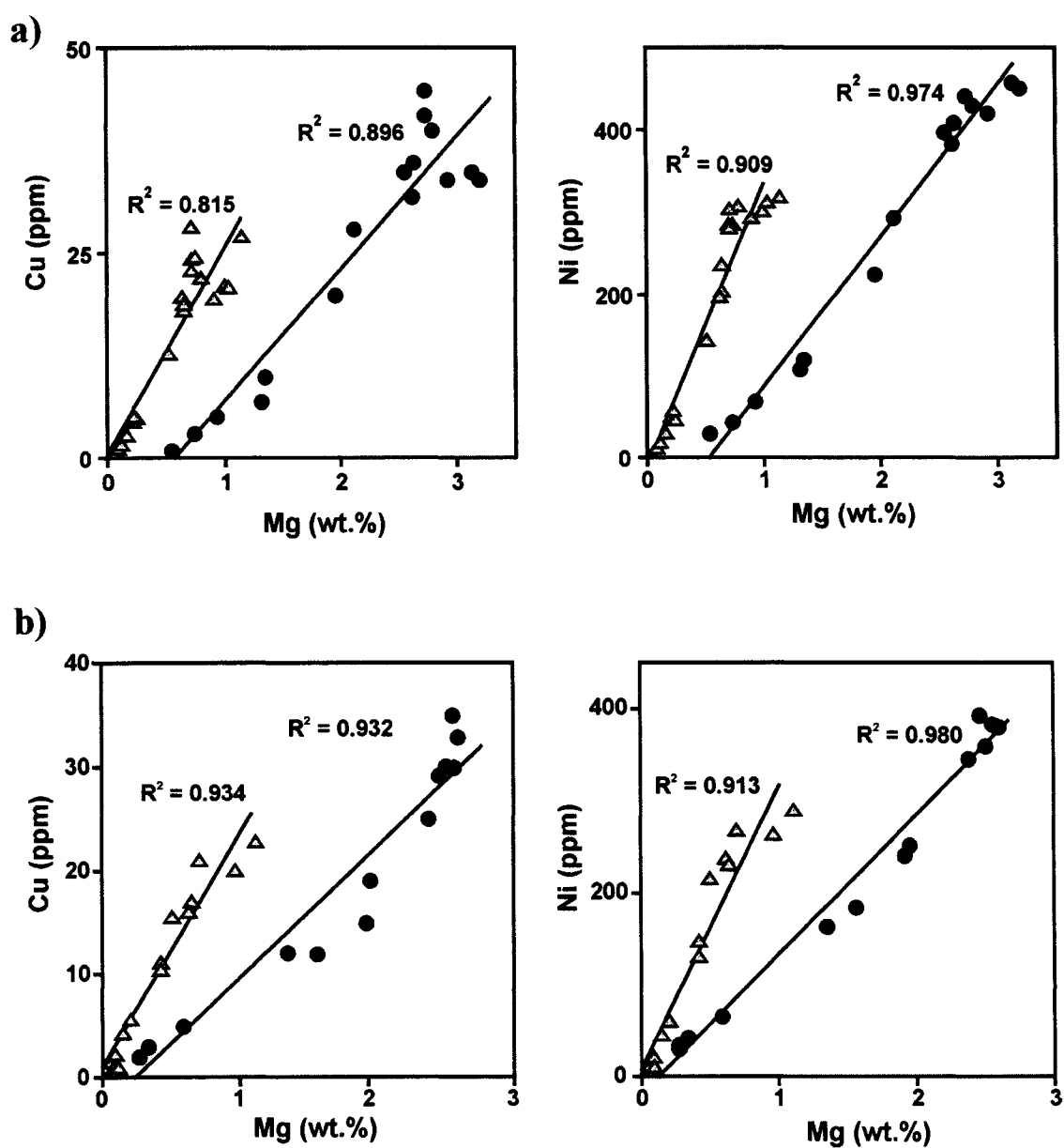


Figure 2.4 Trace metal-Mg correlation diagrams for a) profile 63, b) profile 64. Soil samples < 0.063 mm, ▲, hydroxylamine hydrochloride, ●, aqua regia.

## **2.5 Hypothesis**

Based on the empirical evidence from the data presented above, the hypothesis is that Mg-bearing phyllosilicates are the principal mineral hosts for Ni and Cu in the naturally enriched soil from the Thetford Mines area. In addition, if these trace metals are held in the crystal lattice of one or more phyllosilicate minerals, the relative kinetic reactivity of these metals is expected to change down the profile as a result of the effects of differential weathering of the host mineral with depth.

The fundamental premise for the hypothesis is that metals originate in mineral hosts in the youthful soils characteristic of glaciated terrains. In addition, because the metal ions have not been extensively leached from the minerals in glacial soils, as they often are in highly weathered residual soils, it is possible to observe changes in their kinetic reactivity arising from transformation processes within the first metre of the profile.

## **2.6 Experimental Design**

The key strategy of this research was to integrate chemical and geological characterization of Ni and Cu in the soil profiles in an effort to contribute to the ultimate goal of linking trace metal species on a microscopic scale (i.e. individual soil particles) with their overall kinetic behaviour on a macroscopic scale (i.e. bulk soil). The hypothesis was tested using two experimental approaches, as described below. The analytical results from both approaches will be interpreted in the context of the existing body of knowledge outlined in this chapter.

1) Direct determination of the mineralogy and chemistry of individual soil particles was performed using Time of Flight – Secondary Ion Mass Spectrometry (ToF-SIMS) in combination with Scanning Electron Microscopy – Energy Dispersive x-ray Spectroscopy (SEM-EDS). This work focused on critically testing the role of Mg-bearing phyllosilicate minerals in hosting Ni (the detection limits of ToF-SIMS

precluded the investigation of Cu because of its lower abundance in the sample).

2) The reactivity of Ni and Cu in the bulk soil was investigated as a function of depth in the profile using kinetic fractionation studies. Ethylenediaminetetraacetic acid (EDTA) was used as the extracting reagent and Graphite Furnace Atomic Absorption Spectrometry was employed to monitor the extraction kinetics. The inferred mineral host for the metal from the ToF-SIMS study was used as a mineralogical context for interpreting vertical changes in Ni and Cu reactivity through the soil profile, since the rate and mechanisms for release of these metals depend on the properties of the host mineral. The kinetic fractionation studies elucidate the relative rates of release of bound metal species to the soil solution, which provide insight into the effects of pedological weathering and soil formation processes on trace metal reactivity with depth.

## 2.7 References

---

1. G. Sposito, *The Chemistry of Soils*, Oxford University Press, New York, USA, 1989, Chapter 1.
2. N.C. Brady, R.R. Weil, *The Nature and Properties of Soils*, 13<sup>th</sup> Ed., Prentice Hall, New Jersey, USA, 2002, Chapters 1 and 8.
3. A.N. Rencz, W.W. Shilts, Nickel in Soils and Vegetation of Glaciated Terrains, in *Nickel in the Environment*, J.O. Nriagu (Ed.), Wiley, New York, USA, 1980, pp 151-188.
4. G. Faure, *Principles and Applications of Geochemistry*, 2<sup>nd</sup> Ed., Prentice Hall, New Jersey, USA, 1998, Chapters 13 and 19.
5. W.W. Shilts, Geochemical Partitioning in Till, in *Drift Exploration*, P.T. Bobrowsky, S.J. Sibbick, J.M. Newell, P.F. Matysek (Eds.), B.C. Ministry of Energy, Mines and Petroleum Resources, British Columbia, Canada, 1995, pp.149-166.
6. M. L. Raisanen, M. Tenhola, J. Makinen, *Bull. Geol. Soc. Finland*, 1992, **64**, 35.

- 
7. T. Tarvainen, *J. Geochem. Explor.*, 1995, **54**, 187.
  8. R.A. Klassen, *Soil Profiles in Naturally Metal-Rich Terrains of Eastern Canada: Physical and Geochemical Data*, Open File 1745, CD, Geological Survey of Canada, 2003.
  9. R.G. Garrett, Natural Distribution and Abundance of Elements, in *Essentials of Medical Geology*, Olle Selinus (Ed.), Elsevier Academic Press, London, UK, 2005, Chapter 2.
  10. S.M. Ross, *Sources and Forms of Potentially Toxic Metals in Soil-Plant Systems*, John Wiley and Sons, Chichester, UK, 1994, Chapter 1.
  11. R.L. Mitchell, Trace Elements in Soils, in *Chemistry of the Soil*, F.E. Bear (Ed.), Reinhold Publishing, New York, USA, 1964, Chapter 8.
  12. R.A. Klassen, *Geochem.: Explor. Environ., Anal.*, 2001, **1**, 163.
  13. B. Chen, C.A. Shand, R. Beckett, *J. Environ. Monit.*, 2001, **3**, 7.
  14. W.F. Pickering, *Ore Geol. Rev.*, 1986, **1**, 83.
  15. G.A. Brown, H.A. Elliott, *Water, Air, Soil Pollut.*, 1992, **62**, 157.
  16. D.J. Huisman, F.J.H. Vermeulen, J. Baker, A. Veldkamp, S.B. Kroonenberg, G.Th. Klaver, *J. Geochem. Explor.*, 1997, **59**, 163.
  17. W.A. Deer, R.A. Howie, J. Zussman, *An Introduction to the Rock-Forming Minerals*, 2<sup>nd</sup> Ed., Longman Scientific and Technical, Essex, UK, 1992, pp. 306, 334, 335, 381.
  18. A.C.D. Newman, *Chemistry of Clays and Clay Minerals*, Longman Scientific and Technical, Mineralogical Society, Essex, UK, 1987, pp. 81-92.
  19. L.M. Shuman, *Soil Sci.*, 1985, **140**, 11.
  20. V.H. Kennedy, A.L. Sanche, D.H. Oughton, A.P. Rowland, *Analyst*, 1997, **122**, 89R.
  21. A. Tessier, P.G.C. Campbell, M. Bisson, *Anal. Chem.*, 1979, **51**, 844.
  22. A.M. Ure, *Sci. Total Environ.*, 1996, **178**, 3.
  23. L.M. Shuman, *Soil Sci.*, 1985, **140**, 11.

- 
24. A.M. Ure, *Int. J. Environ. Anal. Chem.*, 1993, **51**, 135.
  25. A.M. Ure, *Mikrochim. Acta*, 1991, **2**, 49.
  26. C. Gleyzes, S. Tellier, M. Astruc, *Trends Anal. Chem.*, 2002, **21**, 451.
  27. A. Sahuquillo, A. Rigol, G. Rauret, *J. Environ. Monit.*, 2002, **4**, 1003.
  28. A.V. Filgueiras, I. Lavilla, C. Bendicho, *J. Environ. Monit.*, 2002, **4**, 823.
  29. A. Bermond, I. Yousfi, J.P. Ghestem, *Analyst*, 1998, **123**, 785.
  30. D.L. Sparks, Kinetics of Sorption/Release Reactions on Natural Particles, in *Structure and Surface Reactions of Soil Particles*, Vol. 4, P.M. Huang, N. Senesi, J. Buffle (Eds.), John Wiley and Sons, Chichester, UK, 1998, Chapter 11.
  31. A. Nayebzadeh, H. Vali, *Arch. Environ. Health*, 2001, **56**, 65.
  32. J.R. Bélanger, *Can. J. Remote Sens.*, 1991, **17**, 112.
  33. R. Laurent, R. Hébert, *Chem. Geol.*, 1989, **77**, 287.
  34. R. Hébert, R. Laurent, *Chem. Geol.*, 1989, **77**, 265.
  35. J.A. Chamberlain, *Can. Mineral.*, 1966, **8**, 519.
  36. J.R. Bélanger, *Prospecting in Glaciated Terrains: An Approach Based on Geobotany, Biogeochemistry, and Remote Sensing*: Bulletin 387, Geological Survey of Canada, 1988.
  37. P.H. Brown, R.M. Welch, E.E. Cary, *Plant Physiol.*, 1987, **85**, 801.
  38. F.R. Siegel, *Environmental Geochemistry of Potentially Toxic Metals*, Springer-Verlag, Berlin, Germany, 2002, p. 12.
  39. Canadian Agricultural Services Coordinating Committee, Soil Classification Working Group, *The Canadian System of Soil Classification*, 3<sup>rd</sup> Ed., Agriculture and Agri-Food Canada Publication 1646, NRC Research Press, Ottawa, Canada, 1998, Chapter 4.
  40. W.W. Shilts, *Detailed Sedimentological Study of Till Sheets in a Stratigraphic Section, Samson River, Quebec*: Bulletin 285, Geological Survey of Canada, 1978.

- 
41. M.L. Räsänen, G. Kashulina, I. Bogatyrev, *J. Geochem. Explor.*, 1997, **59**, 175.
  42. S. Snäll, T. Liljefors, *J. Geochem. Explor.*, 2000, **71**, 1.
  43. G.E.M. Hall, G. Gauthier, J.C. Pelchat, P. Pelchat, J.E. Vaive, *Can. J. Anal. Sci. Spectros.*, 1996, **11**, 787.

## **Chapter 3    Determination of the Mineral Host for Nickel**

---

### **3.1 Introduction**

Metals in soils originate in the parent materials, occurring both as major components and as trace impurities in the crystal lattices of rock-forming minerals. Identification of the source mineral host of trace metals in soils holds important implications for interpreting the geologic controls on natural background levels and the associated environmental risk.

Individual particle analysis is at the forefront of environmental analytical chemistry, as it can provide detailed information about the origin, formation, transport and reactivity of particles associated with trace metals in the environment, making it a valuable complement to conventional bulk analytical techniques [1]. Time of Flight – Secondary Ion Mass Spectrometry (ToF-SIMS) is ideal for analyzing trace elements in individual particles, as it has one of the lowest detection limits of the many microbeam techniques currently available [2], and can provide simultaneous, multielement analysis with excellent mass resolution, high sensitivity, and high spatial resolution [3-6]. This technique has revolutionized mass spectral imaging by facilitating rapid collection and storage of images containing a full mass spectrum at every pixel. However, ToF-SIMS and conventional SIMS have been used primarily for materials science and corrosion studies, and applications to individual environmental particles are rare [1]. Studies that have used ToF-SIMS and SIMS to analyse trace elements associated with individual particles have focussed primarily on surface analysis of well-characterized particles from relatively simple systems, such as isolated mineral grains [3,7-9], sediments [10], synthetic Fe oxides [11], aerosols [12], and interplanetary dust [6]. Soils represent a unique challenge for imaging analytical chemistry, as they are characterized by a diverse mineralogy, complex mineral compositions, and a wide range of grain sizes. The situation is further complicated when using ToF-SIMS to study soils, as the wealth of information obtained by this technique can make it difficult to interpret the mass spectra

and analyze the images [2,4,13].

In order to optimally characterize such a complex sample, ToF-SIMS should be carried out in combination with complementary spectroscopic techniques, such as Auger Microscopy [14], Atomic Force Microscopy [15,16], Transmission Electron Microscopy [10,11], Electron Microprobe Analysis [14], and Scanning Electron Microscopy – Energy Dispersive x-ray Spectroscopy (SEM-EDS) [10,11,13,17,18]. The overwhelming amount of data that can come from multi-technique imaging must be reduced into concise chemical information in order to produce images that are more amenable to interpretation. Computer-based image analysis plays a crucial role in the integration of images obtained from multiple sources by facilitating accurate correlation of spatial and chemical information in order to characterize and map compositional features of the sample surface. This application of image analysis has become an increasingly important field in recent years, and has been extensively used to characterize the mineralogy of sediments, rocks and soils [13,18,19].

The experimental approach used to determine the mineral host for Ni in the soil samples from the Thetford Mines area, was to infer and map the mineralogy of individual silt- and clay-sized (< 0.063 mm) soil particles embedded in polished epoxy pucks using Scanning Electron Microscopy (SEM) combined with Energy Dispersive x-ray Spectroscopy (EDS). Although SEM-EDS is ideal for estimating the mineralogy of a relatively large number of mineral grains (e.g. 100s), EDS detection limits are on the order of parts per thousand [20] – too high to detect trace elements. Hence, because of its lower detection limits (ppm-range), ToF-SIMS was used to analyze the identified mineral grains of interest for Ni. Copper was also an element of interest, but preliminary experiments found it to be below the detection limits of ToF-SIMS. Mapping of mineral grains by SEM-EDS allows for a direct comparison to be made of the mineralogy and ToF-SIMS element distribution images.

## **3.2 Theoretical Background**

### **3.2.1 Fundamentals of SEM-EDS**

In SEM-EDS, the interaction of the primary electron beam with the target atoms in the sample surface produces a variety of secondary signals. Inelastic scattering of the electron beam results in the ejection of secondary electrons from the conduction band (metals) or from the outer-shell valence band (semiconductors and insulators), as well as the emission of characteristic x-rays. X-rays are produced when a beam electron ejects an inner-shell electron, and the resulting excited atom relaxes to ground state when an outer-shell electron falls down to fill the vacancy. The energy lost during the transition is emitted as a photon having a discrete energy characteristic of the element. Elastic interactions of the beam electrons with the sample can cause the incident electrons to be scattered backwards. These backscattered electrons are emitted from regions deeper in the sample than secondary electrons, and the relative signal intensity strongly depends on the average atomic number of the sample [20,21].

### **3.2.2 Fundamentals of ToF-SIMS**

ToF-SIMS has become one of the most important and versatile surface analytical techniques because of its ability to identify and locate surface chemistry with great precision and accuracy. Its high surface sensitivity and low detection limits make it suitable for trace element and isotopic studies, and its high mass range (~ 10 - 100 kDa), excellent spatial and mass resolution, as well as depth profiling capabilities make ToF-SIMS a valuable tool for obtaining chemical structure information [4-6].

A schematic diagram of a typical ToF-SIMS instrument is shown in Figure 3.1. The main components consist of a primary ion source, a mass spectrometer, and a detector. The Ga Liquid Metal Ion Gun (LMIG) is the standard primary ion gun used for routine analysis due to its ability to perform rapid, sub-micron surface imaging. A constant flow of  $\text{Ga}^+$  ions are emitted from a very small region at the tip of the gun,

producing a narrow primary ion beam about 200 nm in diameter. This primary ion current is pulsed by blanking the continuous ion beam, producing single Ga<sup>+</sup> ion packages that can be varied in duration from a few μs down to several ns [4,6,22]. The SIMS process is initiated by bombarding the surface of a solid sample with this pulsed beam of energetic ions (1-50 keV). The atomic collisions transfer the primary ion's energy to the target atoms and set up a "collision cascade", as illustrated in Figure 3.2. Some collisions return to the surface, resulting in the ejection of secondary particles from the surface region, including electrons, neutral atoms and molecular fragments, as well as atomic and molecular ions – a process known as 'sputtering' [4-6,22]. The primary ion gun is pulsed in alternation with an electron flood gun, as illustrated in Figure 3.1, which provides charge compensation for insulating samples, preventing excessive build up of positive charge on the sample surface due to ionization and primary ion implantation during the sputtering process [4-6]. When the primary ion dose is kept low (i.e. below the 'static limit' of 10<sup>13</sup> ions cm<sup>-2</sup>), the sampling depth of ToF-SIMS is only 1-2 monolayers, as only those particles in the outermost surface region of the sample have enough energy to overcome the surface binding energy to be ejected from the substrate. The structure and composition of the ejected particles is directly related to the molecular structure of the surface they were emitted from [5,6].

While the vast majority (~ 95 – 99 %) of these sputtered surface particles are neutral, a small percentage (~ 1 – 5 %) are ions. The ejected secondary ions are extracted into a field-free flight tube by a high-voltage electrical field, which accelerates them to between 3 and 8 keV, giving all ions the same kinetic energy. When kinetic energy, E<sub>k</sub>, is constant, velocity, v, varies inversely with mass, m,

$$v = \sqrt{\frac{2E_k}{m}} \quad (3.1)$$

Hence, the ions can be separated by their mass-to-charge ratios (m/z) based on the time it

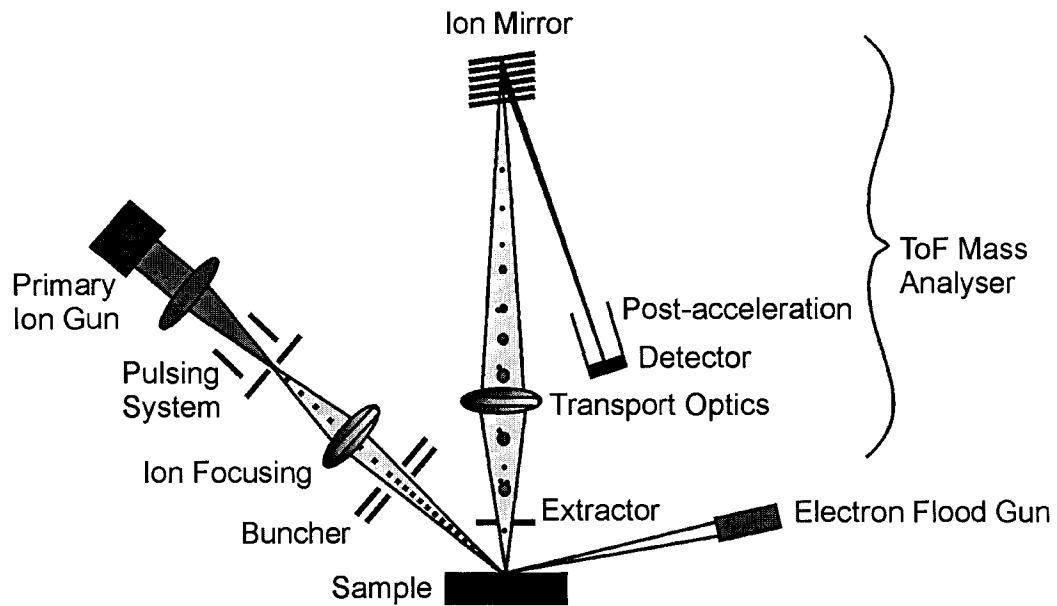


Figure 3.1 Schematic diagram of a ToF-SIMS instrument (adapted from Stephan [6]).

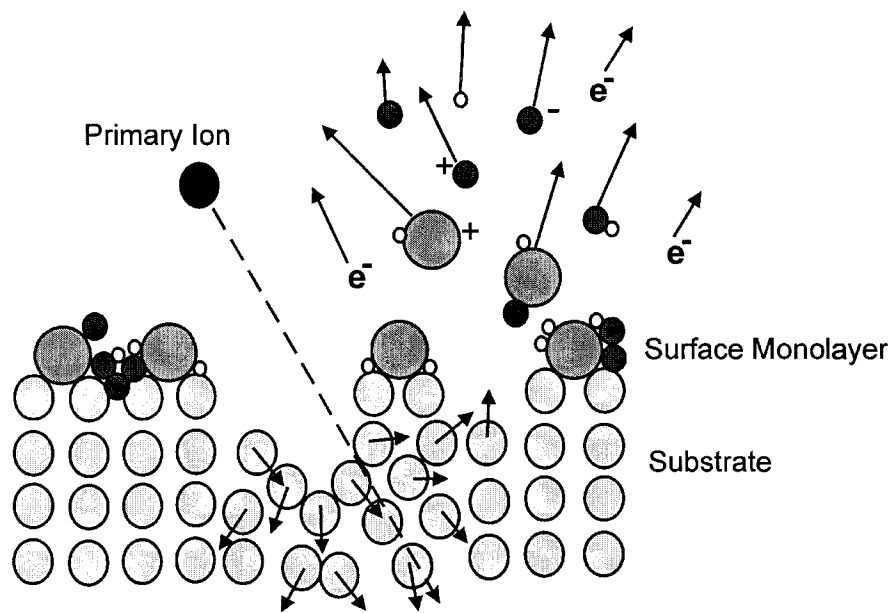


Figure 3.2 Conceptual diagram of the SIMS process, showing ejection of sputtered secondary particles following primary ion bombardment (adapted from Vickerman [5]).

takes them to travel from the sample to the detector. For singly-charged ions, a flight time spectrum is converted to an ion mass spectrum according to the following equation

$$\frac{m}{z} = \frac{2V}{s^2} t^2 \quad (3.2)$$

where  $V$  is the potential of the accelerating electric field,  $t$  is the flight time, and  $s$  is the flight path, defined by the length of the drift tube [5,6]. The Time of Flight (ToF) mass analyzer was introduced in the 1980s and has become the major evolving capability for SIMS instrumentation because of its versatility and sensitivity [4,6]. In conventional SIMS, a double-focusing, magnetic sector, or quadrupole mass spectrometer is used; however, the sensitivity of analysis is limited due to low transmission efficiency as a result of the scanning nature of the detection logic, which discards most of the information. ToF mass analyzers have mass resolution and mass range capabilities comparable to conventional mass spectrometers, but are much more sensitive because they use parallel detection logic, where all secondary ions having one polarity are measured quasi-simultaneously [5,6].

Ions of the same mass can have slightly different starting energies, resulting in slightly different flight times, which can degrade the spectrum. This effect is minimized by focusing the energy of the ions using an ion mirror, as shown in Figure 3.1, which consists of a series of rings, to which a gradually increasing retarding electric field is applied. Ions having higher energies penetrate the field deeper before they are reflected, and are delayed compared to lower energy ions. When tuned correctly, all ions of the same mass will arrive at the detector at the same time, despite slight differences in starting energies [5,6]. Following the ion mirror, the ions are accelerated to 8 – 10 keV before reaching the detector, which consists of microchannel plates for ion-to-electron conversion, a scintillator for electron-to-photon conversion and a photomultiplier tube [6]. Most instruments also come equipped with a secondary electron detector which detects the ion-induced emission of secondary electrons during the sputtering process,

providing images to complement the secondary ion images obtained [6].

‘Static’ SIMS maintains a low primary ion dose ( $< 10^{13}$  ions  $\text{cm}^{-2}$ ) so that within the timescale of the experiment, much less than 1 % of particles in the upper monolayer receive an ion impact. On a random impact basis, no spot on the surface should receive more than one primary ion strike; hence, the surface is essentially undamaged. In contrast, ‘dynamic’ SIMS involves a second primary ion gun to provide high primary ion flux densities of over  $1 \mu\text{A cm}^{-2}$  ( $> 10^{13}$  ions  $\text{cm}^{-2}$ ). This produces rapid erosion rates which can be used for cleaning the sample surface or for dual-beam depth profiling [4,5,22]. The choice of ion as an additional sputter source depends on the type of information desired –  $\text{Cs}^+$  is often used to enhance the yield of electronegative ions (e.g. halides), while  $\text{O}_2^+$  enhances that of electropositive ions (e.g. metals) [23-25].

### 3.2.3 ToF-SIMS Modes of Operation

ToF-SIMS has three modes of operation, which are summarized in Figure 3.3. It is important to understand the interaction between mass resolution, spatial resolution and signal intensity in order to correctly design an analysis using the optimal mode of operation [4]. Both mass resolution and spatial resolution are limited by the secondary ion yield per pixel. Mass resolution depends primarily on the duration of the primary ion pulse. A shorter pulse length increases the mass resolution, but leads to a reduction in signal intensity as a result of the lower primary ion dose. Spatial resolution is a function of the diameter of the primary ion beam. A smaller beam diameter results in higher spatial resolution, but also reduces the number of secondary ions that can be generated in an area of a single image pixel [6].

#### *High Mass Resolution (‘Spectral’) Mode*

For a given ion mass and beam energy, the pulse duration corresponds directly with the spatial extent of the pulse, therefore the pulse can be shortened in time by compressing it in space [22]. In the high mass resolution, or ‘spectral’ mode, the raw

primary ion pulse of between 20 and 100 ns is axially compressed to about 600 ps using an electrodynamic bunching system (or “buncher”), which enables achievement of very high mass resolution. The first example spectrum shown in Figure 3.3 shows that  $^{28}\text{Si}$  is well resolved from  $\text{C}_2\text{H}_4$ , and two additional peaks can be distinguished for  $\text{AlH}$  and  $\text{CH}_2\text{N}$ . Because the primary ion beam is compressed rather than chopped, there is no reduction in the total number of primary ions, and therefore no reduction in signal intensity. However, the bunching system introduces an energy spread of 1 keV to the beam, which results in serious chromatic aberrations in the target lens, reducing the spatial resolution to a nominal 2-5  $\mu\text{m}$  [4-6].

#### *High Spatial Resolution ('Imaging') Mode*

Operation of the beam in an un-bunched mode provides high, submicron spatial resolution ( $\sim 200$  nm). This can be improved ( $\sim 100$  nm) by using apertures to further narrow the beam ('collimated' mode). However, this comes at a sacrifice to mass resolution because the pulses must be relatively long ( $\sim 20 - 100$  ns) in order to obtain an acceptable signal intensity [4].

#### *Compromise Mode*

In order to obtain good mass resolution and spatial resolution, the compromise mode can be used, in which the primary ion beam is chopped, delivering a series of short pulses, about 1.5 ns in duration and spaced about 25 ns apart in each shot cycle [6]. The relatively short pulses provide good mass resolution, and because the pulses are unbunched, spatial resolution is also good ( $\sim 250$  nm). The pulse is repeated 5-10 times in each cycle, resulting in a spectrum consisting of a series of overlapping peaks, as shown in Figure 3.3, for which the peak areas in each series are summed up by the analysis software. The net signal intensity of the replicate pulses increases the signal-to-noise ratio, partially compensating for the loss in primary ion dose per pulse [4-6]. This mode is patented by ION-TOF, and is generally not available on all instruments [4].

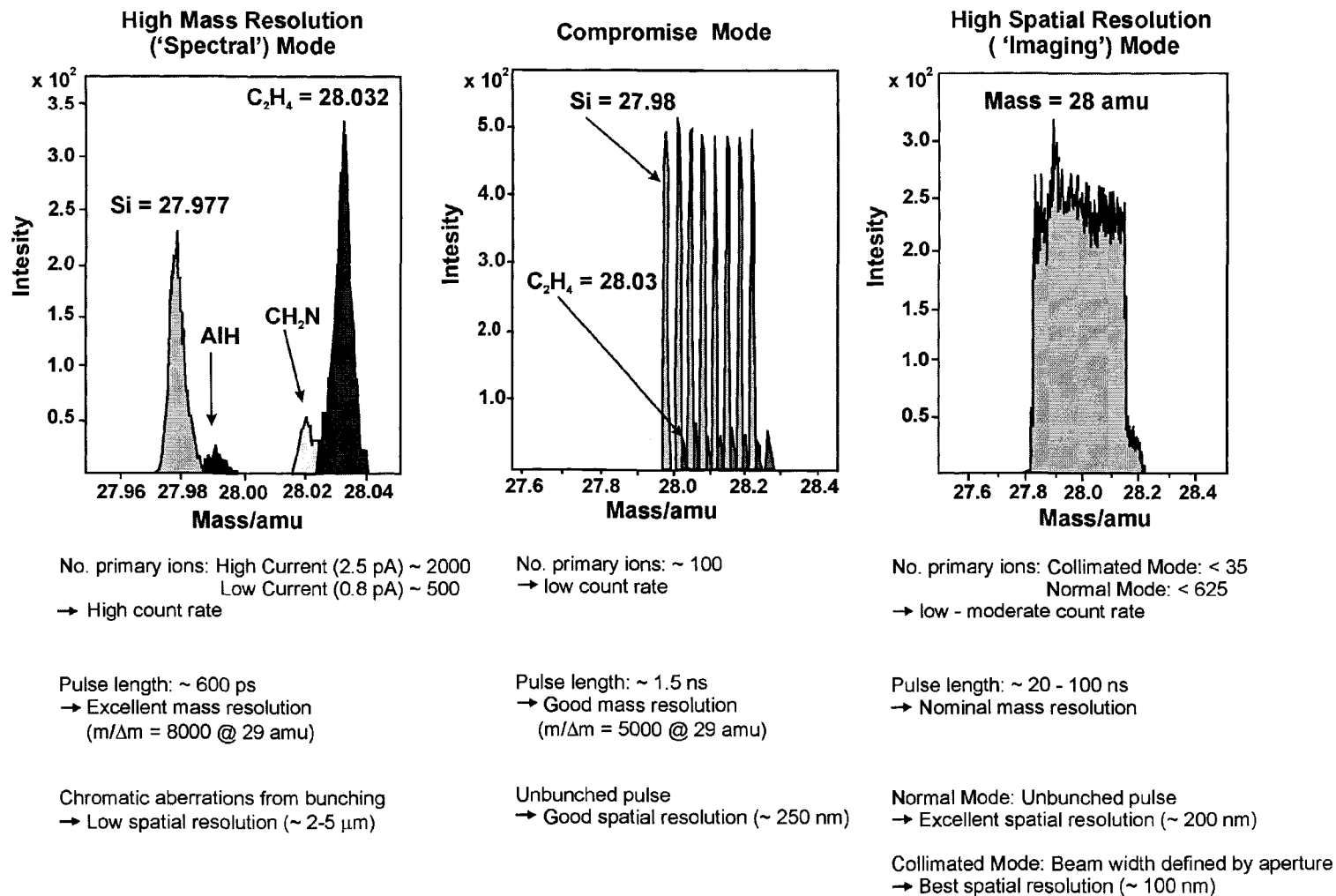


Figure 3.3 Conceptual example of positive ion spectra near mass 28 produced with a Ga<sup>+</sup> primary ion beam using the three operational modes (adapted from Sodhi [4]).

### **3.3 Experimental**

#### **3.3.1 Sample Preparation**

The silt- and clay-sized fraction of three soil samples (63B, 63C, 63E) was mixed in 10 wt % with a low viscosity, carbon-based epoxy (Araldite®, Ciba Geigy) to form a puck (2.5 cm diameter × 1 cm thick). One surface of the puck was then polished with diamond paste and coated with an ultra-thin carbon condensate layer using an Edwards E306A carbon coater. A ‘V’ was drawn on the surface of the puck with a marker, as shown in Figure 3.4, to serve as a reference point for EDS image locations.

#### **3.3.2 SEM-EDS Data Acquisition**

SEM and EDS digital images were generated using two different instruments. The first was a Cambridge S-360 SEM interfaced with an Oxford-Link eXLII EDS with mapping capabilities, located at the Geological Survey of Canada (Ottawa, ON). The second instrument was a JEOL JSM – 5900LV SEM equipped with a Princeton Gamma-Tech IMIX-PC EDS located at Acadia University (Wolfville, NS). The operating conditions for both systems are listed in Table 3.1. Two SEM images were taken at the tip of the ‘V’ – one at low magnification ( $\sim \times 45$ ) to locate the analysis area in relation to the ‘V’ marker, and one at higher magnification ( $\sim \times 100$ ) to locate the individual minerals grains for EDS element mapping. The higher magnification was chosen so that between 50 and 300 silt-sized particles (0.002 - 0.063 mm) were in the field of view. EDS data was collected over a period of about 14 h. The elements chosen to represent the major components of most rock-forming minerals likely to be present in this soil were Si, Al, Fe, Mg, K, Ca, and Na (Ti and S were included in some EDS element maps). A digital map of each element in the analysis area was created using a greyscale intensity of 0 - 255 to represent relative elemental abundance.

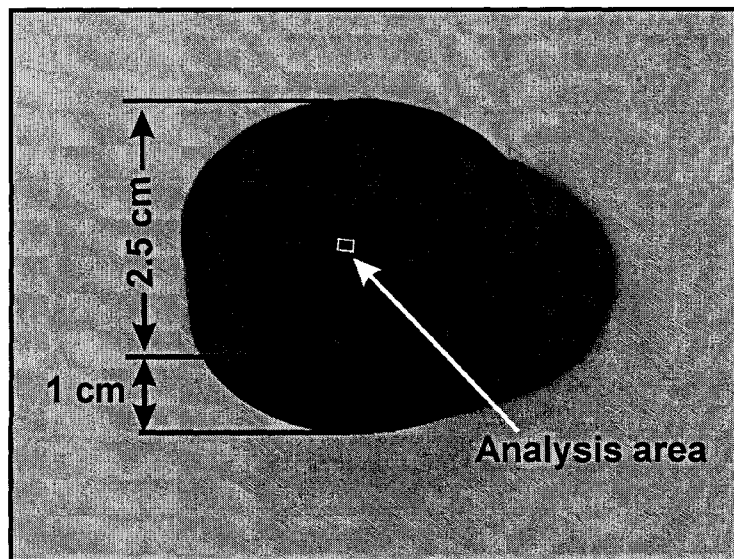


Figure 3.4 Sample epoxy puck used for SEM-EDS mapping and ToF-SIMS analysis.

Table 3.1 Operating conditions of the two instruments used for acquisition of SEM-EDS images.

	Cambridge SEM with Oxford Link EDS	JEOL SEM with PGT EDS
Accelerating Voltage (kV)	20	20
Spot size	n/a	32
Working distance (mm)	25	16
Dwell time per pixel (ms)	150	164
Image resolution (pixels)	512 × 512	512 × 408
Dead time (%)	30	32

### 3.3.3 SEM-EDS Image Analysis

EDS digital images were processed and analyzed using Adobe Photoshop 8.0 and Fovea Pro 2.0 (Reindeer Graphics) following the procedure developed by Knight et al. [26]. The raw grayscale EDS element maps were converted into binary images in order to separate features from background by selecting an appropriate threshold greyscale value. Particles smaller than 5 pixels were removed from the image to reduce background noise. Mineral maps were then created using Boolean algebra and mathematical operations to sequentially add and subtract the element maps. The added and subtracted elements used to construct individual mineral maps are listed in Table 3.2. Each mineral map consisted of only those mineral grains that contained all of the added elements, but not the subtracted elements. Not all elements were included in the mapping equation for each mineral in order to allow for variability in their chemical compositions, as most minerals can contain minor amounts of elements that are not listed in their chemical formulae. Remaining unclassified grains, which reflect small grain sizes, edge effects, choice of threshold values, or minerals containing elements that were not mapped, were identified by subtracting all of the mineral maps from a composite of all of the element maps. The individual mineral maps were then combined to generate the final map of the area.

Although the SEM-EDS maps cannot provide an unambiguous identification of mineral phases, as some minerals have very similar elemental compositions, they are useful for reconnaissance purposes to locate potential mineral grains of interest. Smaller areas on the final map ( $\sim 100 \mu\text{m}^2$ ) containing the desired mineral grains were selected for analysis by ToF-SIMS to determine whether or not the grains contained Ni. The sample pucks were later recoated with carbon, and the mineral grains were examined individually by EDS x-ray spot analysis ( $\sim 100$  s collection time) to obtain a more accurate mineral assignment.

Table 3.2 Added and subtracted elements for mapping the mineralogy of individual soil particles in the sample pucks. Elements in brackets may not have to be added or subtracted to characterize the mineral (adapted from Knight et al. [26]). \*minerals not identified in all mineral maps because of unavailable data for Ti and/or S.

Mineral	Added Elements	Subtracted Elements
Quartz: $\text{SiO}_2$	Si	Al, K, Mg, Na, Ca, Fe, Ti
Plagioclase Feldspar:	$\left\{ \begin{array}{l} \text{Albite: Na[AlSi}_3\text{O}_8] \\ \text{Anorthite: Ca[Al}_2\text{Si}_2\text{O}_8] \end{array} \right.$	$\left\{ \begin{array}{l} \text{K, Fe, Ti} \\ \text{K, Fe, Ti} \end{array} \right.$
K Feldspar: $(\text{K,Na})[\text{AlSi}_3\text{O}_8]$	Si, Al, K	Mg, Ti
Orthopyroxene/ Olivine:	$\left\{ \begin{array}{l} \text{Orthopyroxene: (Mg,Fe)}_2\text{Si}_2\text{O}_6 \\ \text{Olivine: (Fe,Mg)}_2\text{SiO}_4 \end{array} \right.$	$\left\{ \begin{array}{l} \text{Mg, Fe} \\ \text{Ca, Al} \end{array} \right.$
Clinopyroxene/ Amphibole:	$\left\{ \begin{array}{l} \text{Clinopyroxene: (Ca,Mg,Fe,Al)}_2(\text{Si,Al)}_2\text{O}_6 \\ \text{Amph: (Na,K)}_{0-1}\text{Ca}_2(\text{Mg,Fe,Al})_5(\text{Si,Al})_8\text{O}_{22}(\text{OH})_2 \end{array} \right.$	$\left\{ \begin{array}{l} \text{Ca, Mg,(Fe)} \\ \text{(Fe, K)} \\ \text{Mg, Al, (Ca, Na, Fe)} \\ \text{(Si, Fe, K)} \end{array} \right.$
Mica:	$\left\{ \begin{array}{l} \text{Muscovite: K}_2\text{Al}_4[\text{Si}_6\text{Al}_2\text{O}_{20}](\text{OH,F})_4 \\ \text{Biotite: K}_2(\text{Mg,Fe})_3\text{AlSi}_3\text{O}_{10}(\text{OH,O,F}_2)_2 \end{array} \right.$	$\left\{ \begin{array}{l} \text{Si, Al, K} \\ \text{Si, Al, K, Mg} \end{array} \right.$
Chlorite: $(\text{Mg,Fe,Mn,Al})_{12}[(\text{Si,Al})_8\text{O}_{20}](\text{OH})_{16}$	Mg, Al, Fe	Ca, (K)
Epidote: $\text{Ca}_2\text{Fe}^{3+}\text{Al}_2\text{O}(\text{Si}_2\text{O}_7)(\text{SiO}_4)(\text{OH})$	Al, Ca, Fe	K, Na
Ferrihydrite: $\text{Fe}(\text{OH})_3$ / Geothite: $\alpha\text{-FeOOH}$ / Hematite: $\alpha\text{-Fe}_2\text{O}_3$ / Magnetite: $\text{Fe}_3\text{O}_4$	Fe	Si, Al, K, Mg, Na, Ca, Ti
Kyanite / Andalusite: $\text{Al}_2\text{SiO}_5$	Al, Si	Na, Ca, K, Fe, Mg, Ti
*Sphene: $\text{CaTi}[\text{SiO}_4](\text{O,OH,F})$	Ca, Ti	Fe
*Rutile: $\text{TiO}_2$	Ti	Al, Mg, Fe, Si, Ca
*Ilmenite: $\text{FeTiO}_3$	Ti, Fe	Al, Mg, Si
*Sulfides:	S	Na, Ca, K, Fe, Mg, Ti

### 3.3.4 ToF-SIMS Data Acquisition

The ToF-SIMS analyses were carried out using an ION-TOF ToF-SIMS IV static secondary ion mass spectrometer (ION-TOF GmbH, Münster, Germany) located at Surface Interface Ontario (University of Toronto). The instrument is equipped with two primary ion sources – a Ga LMIG gun for routine analysis and an electron impact gun used as an additional sputter source for oxygen and argon ions. Prior to analysis, the carbon coating on the surface of the puck was removed by sputtering an area of about  $200 \times 200 \mu\text{m}^2$  over the desired analysis areas with oxygen ions for 30 minutes. The analysis areas ( $\sim 100 \times 100 \mu\text{m}^2$ ) were then scanned between 500 and 1000 times using both the Spectral and Compromise modes. The operating conditions for the oxygen sputter gun and the Ga LMIG in both modes are outlined in Table 3.3. The ion dose when using the Ga LMIG never exceeded the static limit of  $10^{13}$  ions  $\text{cm}^{-2}$ . Positive ion spectra were obtained for all sample areas, whereas negative ion spectra were obtained only for sample area 63E1. The data collected were analyzed using the *IonSpec* and *IonImage* software programs (IonSpec Co.).

## 3.4 Results and Discussion

### 3.4.1 Sample Puck 63B

#### *SEM-EDS Results*

SEM images for the chosen analysis area on sample puck 63B are shown in Figures 3.5 a) and b) at low ( $\times 45$ ) and high ( $\times 100$ ) magnifications, respectively. The EDS element maps for the same area are shown in Figure 3.6, where the greyscale intensity is proportional to elemental abundance. Image analysis of these EDS maps was used to create the mineral map shown in Figure 3.7. The area inside the box drawn on the mineral map was selected for analysis by ToF-SIMS, as it contained a relatively large grain classified as chlorite – a Mg-bearing phyllosilicate. Secondary electron and

Table 3.3 Instrumental conditions for ToF-SIMS analyses.

	Oxygen sputter gun	Ga analysis gun	
		Compromise mode	Spectral mode
Area scanned ( $\mu\text{m}^2$ )	$\sim 200 \times 200$	$\sim 100 \times 100$	$\sim 100 \times 100$
Resolution (pixels)	n/a	$256 \times 256$	$128 \times 128$
No. scans	(30 min.)	500 - 1000	500 - 1000
Pulse width (ns)	n/a	1.3 ns	600 ps
Pulse frequency (MHz)	n/a	40	n/a
Cycle time ( $\mu\text{s}$ )	n/a	100	100
Beam current (pA)	47,000	2.5	2.5
Beam potential (keV)	3	25	25

backscatter electron (BSE) images taken for the same area after ToF-SIMS analysis are shown in Figures 3.8 a) and b), respectively. The secondary electron image reveals a raster of holes embedded in the epoxy matrix, approximately 1  $\mu\text{m}$  in diameter and regularly spaced about 2.5  $\mu\text{m}$  apart. This is probably a result of oxygen ion beam damage incurred during the sputter pre-cleaning step used to remove the carbon coating prior to ToF-SIMS analysis. The BSE image provides an estimate of the mean atomic number at each pixel, which acts as supporting evidence for the mineral classifications in the mineral map.

Grain 1 in sample area 63B was classified as chlorite in the mineral map (Figure 3.7). In order to verify its identity, this grain was individually examined by EDS x-ray spot analysis, and the resulting EDS spectrum is shown in Figure 3.9. The spectrum verifies that the grain contains appreciable amounts of Mg, Al and Si, and moderate amounts of Fe – a composition indicative of clinocllore, the Mg-rich end member of the chlorite solid solution series [27]. The x-ray spot analysis was also used to identify several smaller particles in the area that could not be identified in the mineral map because of their small size, including titanite (grain 10), muscovite (grain 6), and K feldspar (grains 7, 9).

#### *ToF-SIMS Results: Factors Affecting Secondary Ion Yields*

The relative peak intensities obtained from a ToF-SIMS spectrum reflect both the composition of the sample surface (i.e. relative elemental abundances), as well as the nature of the elements themselves, as the ion yields are strongly influenced by the ionization energy and electron affinity of the elements for generation of positive and negative ions, respectively [5,6,24]. Hence, alkali and alkaline earth metals tend to have the highest positive ion yields, while halides tend to have the highest negative ion yields. Secondary ion yields can vary by several orders of magnitude across the periodic table, as illustrated in Figure 3.10 [24].

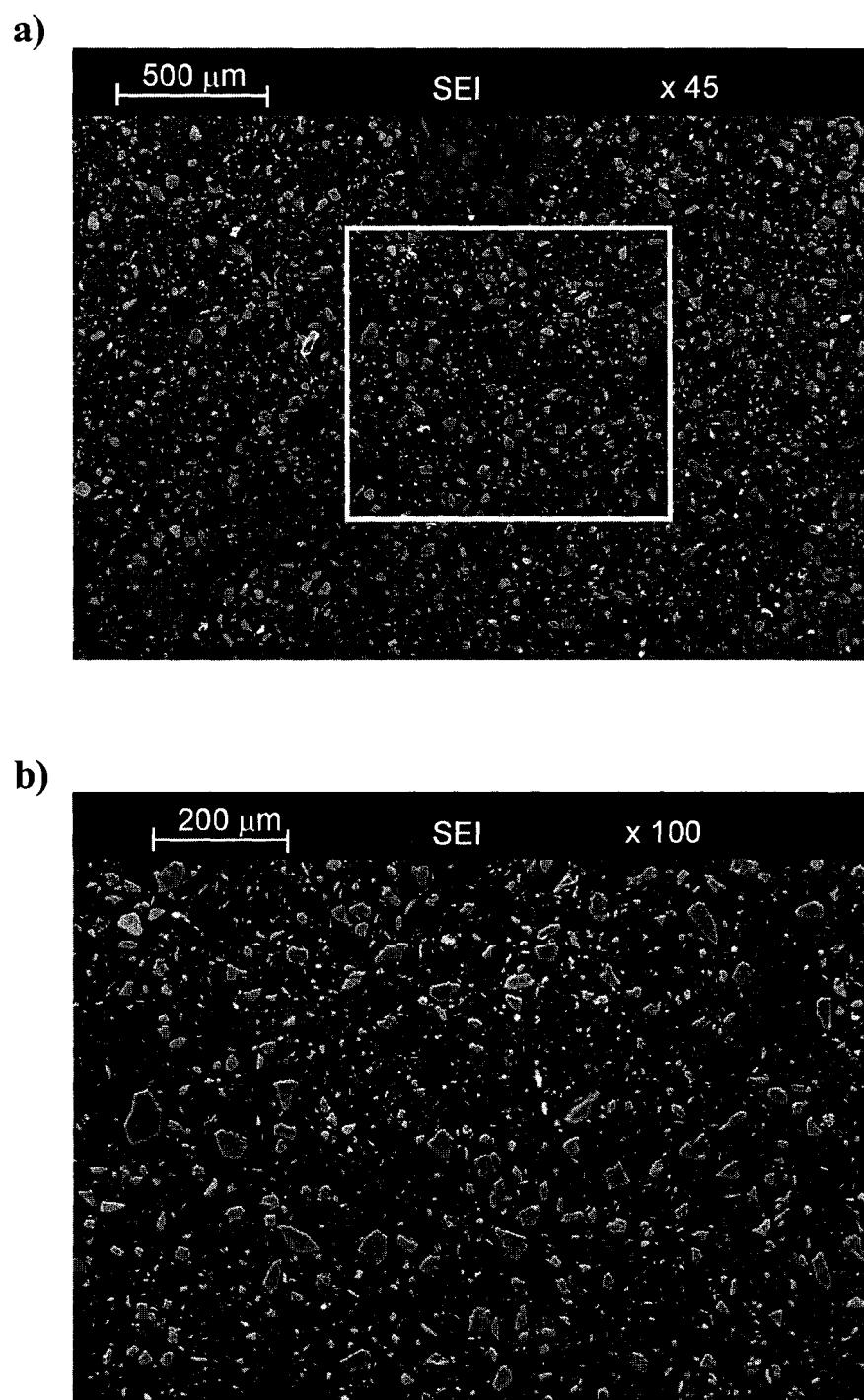


Figure 3.5 Secondary electron images of sample puck 63B: a) area at the tip of the 'V' at low magnification ( $\times 45$ ), where the white box indicates the area used for EDS element mapping, (b) area used for EDS element mapping at higher magnification ( $\times 100$ ). Cambridge SEM.

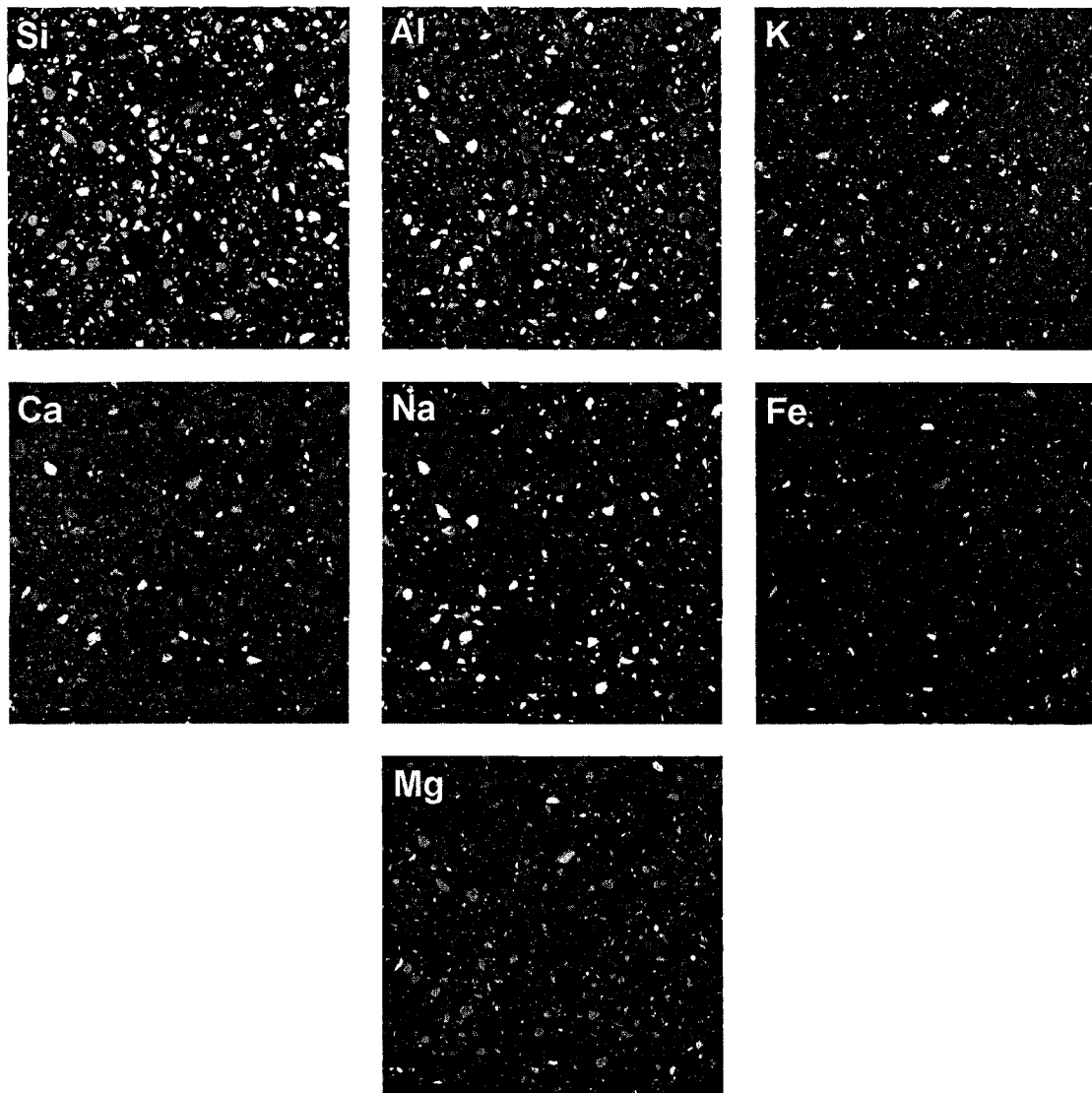


Figure 3.6 EDS element maps for sample puck 63B ( $1250 \times 1250 \mu\text{m}^2$ ). Cambridge SEM with Oxford Link EDS.

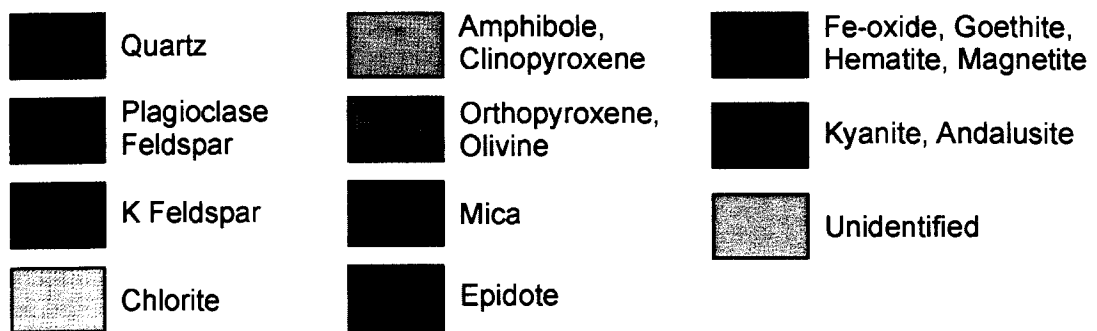
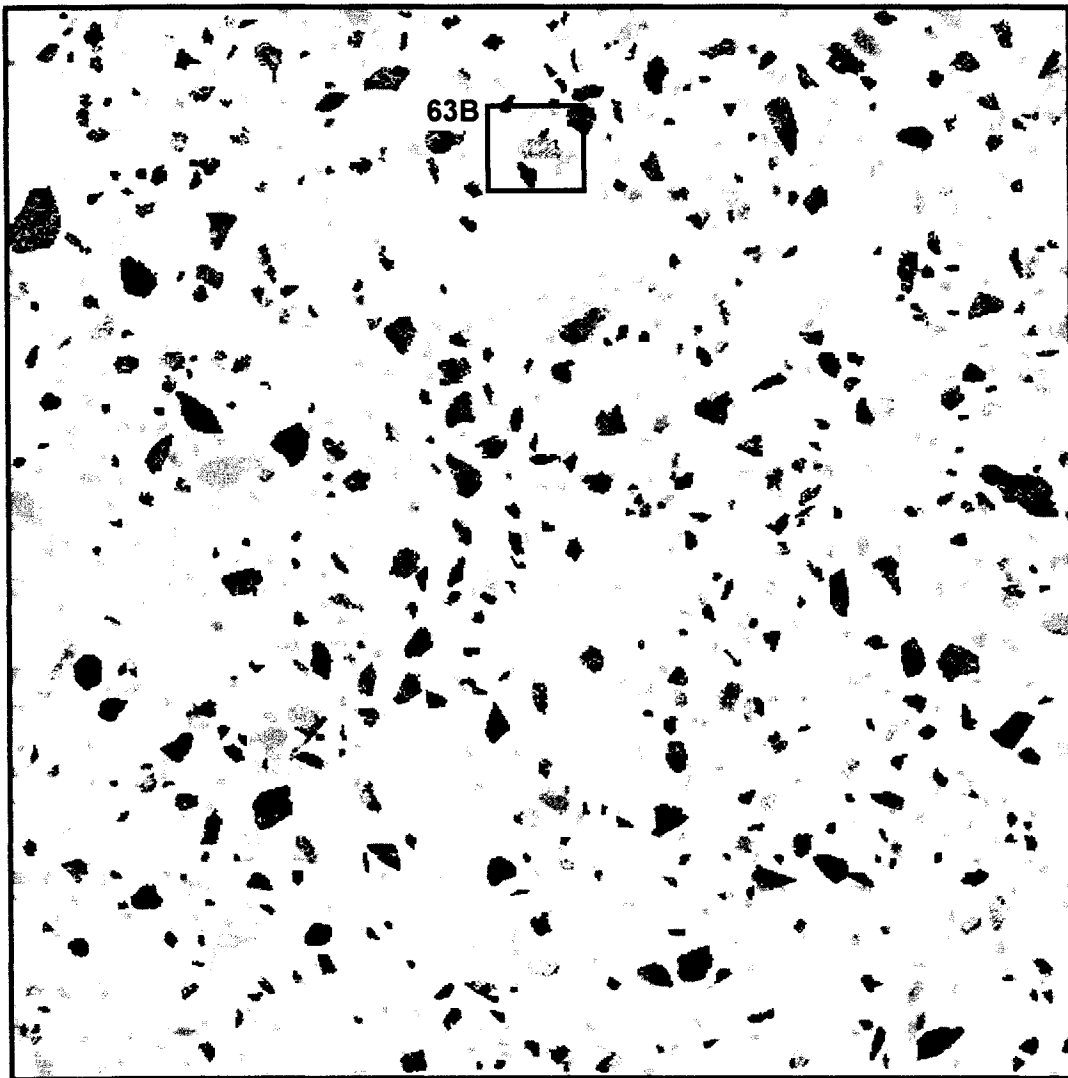
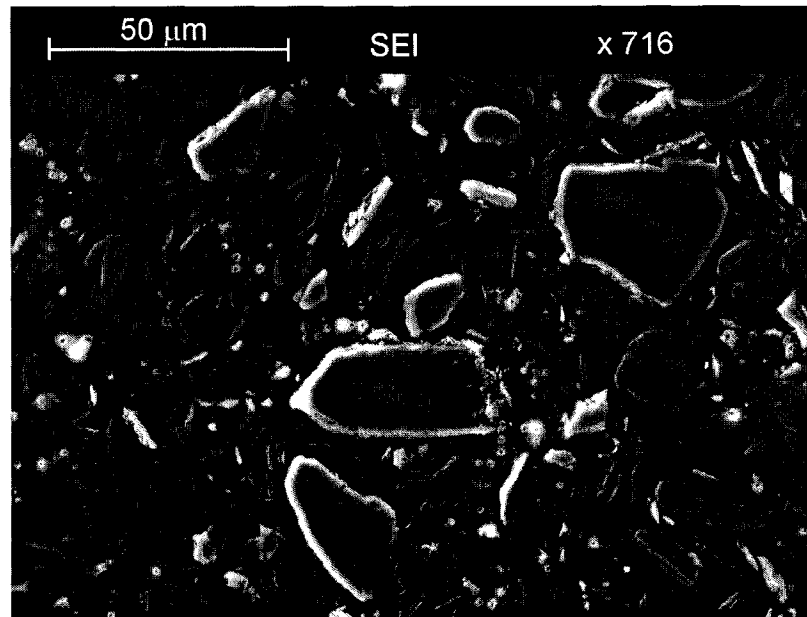


Figure 3.7 Mineral map for sample puck 63B ( $1250 \times 1250 \mu\text{m}^2$ ). The black box indicates the sample area chosen for analysis by ToF-SIMS.

a)



b)

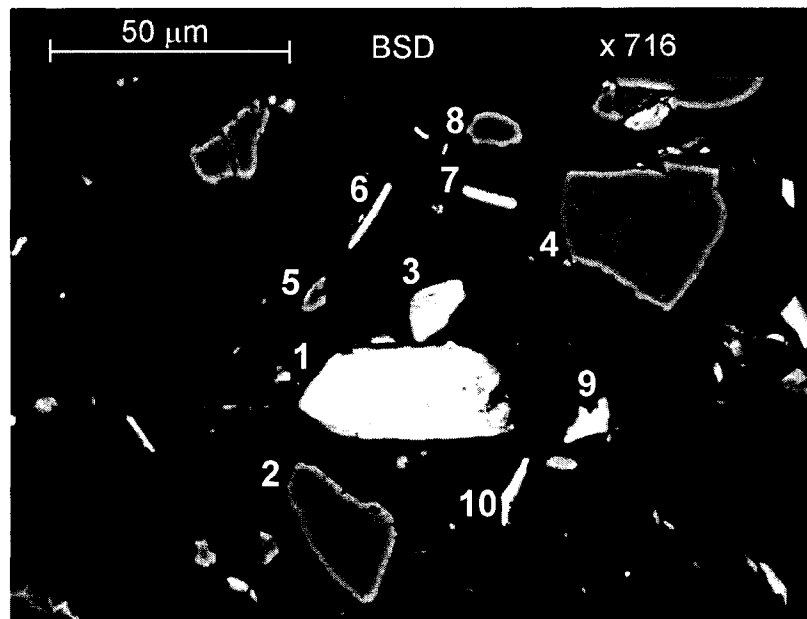


Figure 3.8 SEM images used to locate individual mineral grains in sample area 63B: a) secondary electron image ( $\times 716$ ), b) BSE image ( $\times 716$ ). Mineral grains: 1 - chlorite, 2 - plagioclase, 3 - K feldspar, 4 - quartz, 5 - quartz, 6 - muscovite, 7 - K feldspar, 8 - quartz, 9 - K feldspar, 10 - titanite. Cambridge SEM.

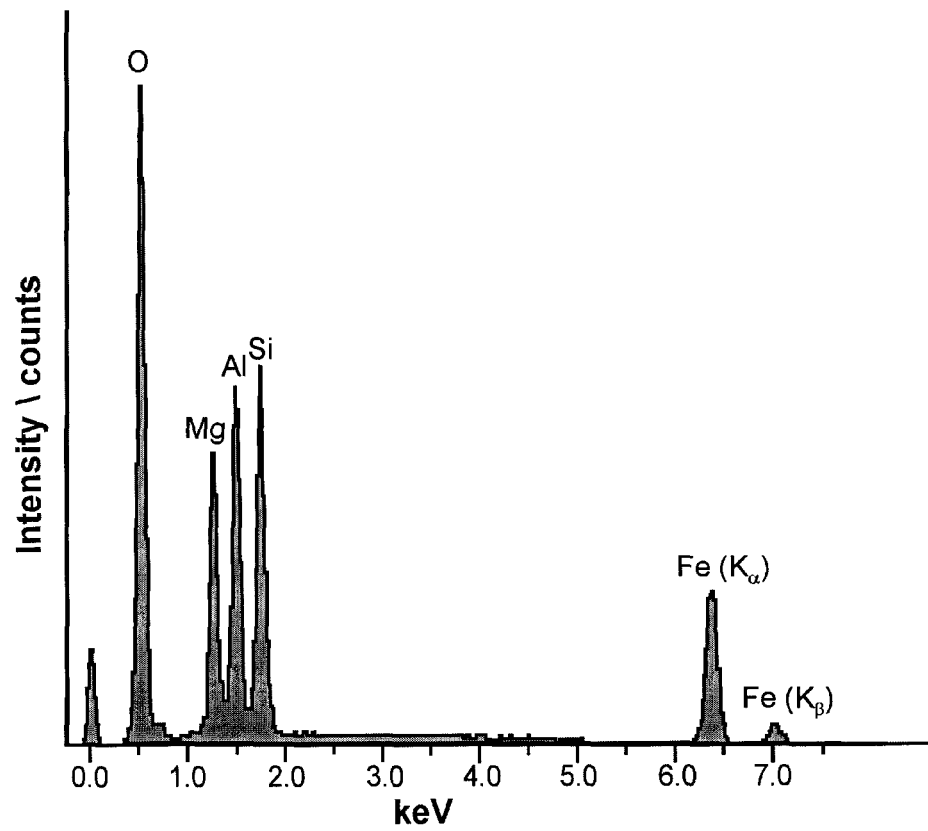


Figure 3.9 EDS spectrum for grain 1 (chlorite) from sample area 63B. Cambridge SEM with Oxford Link EDS.

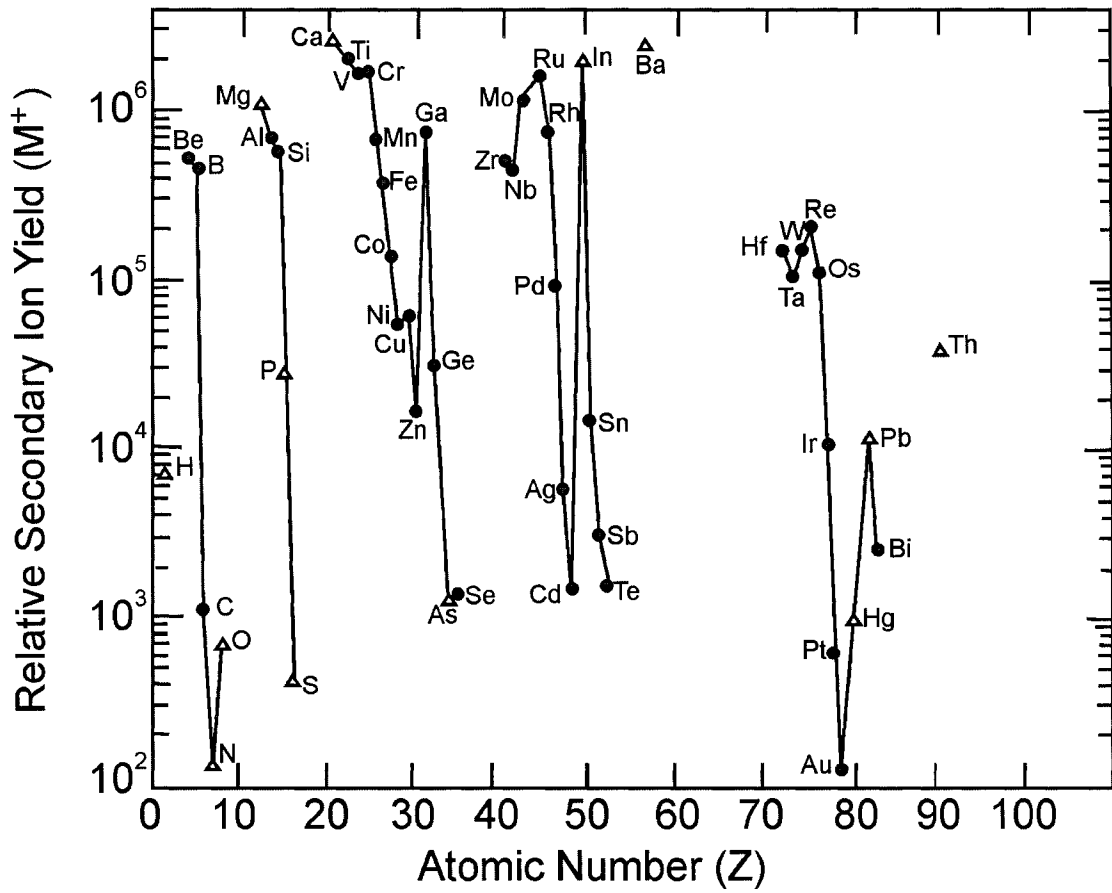


Figure 3.10 Variation in relative positive secondary ion yield ( $M^+$ ) as a function of atomic number. ● pure element, ▲ compound [24].

Secondary ion yields also depend on the surface topography of the sample and the material beneath the surface (i.e. matrix), which can obscure features associated with the surface chemistry [28]. Topographic effects can influence signal intensities, where features that are at optimum focus relative to the secondary ion extraction lens appear overly bright in the secondary ion images [18]. Hence, the flat, polished surfaces of the pucks used in this study are ideally suited for properly interpreting relative signal intensities in the images. Because the matrix participates in the electronic processes involved during sputtering, the ion yield is strongly influenced by the chemical environment of the element [6]. For example, the ion yield for a metal differs markedly from that of the metal oxide [5,6], as shown in Table 3.4. Although this matrix effect makes it difficult to determine useful element ratios for quantification purposes [6], it works to the benefit of trace element analysis in geological materials, as elements are usually present in oxide forms in most minerals, which enhances their secondary ion yields. In addition, it has been demonstrated that bombardment of the sample surface with electronegative gases, such as oxygen ( $O_2^+$ ), can increase positive sputtered ion emission by orders of magnitude [3,23,25]. For this reason, oxygen was chosen as the sputter ion to remove the carbon coating off the surfaces of the pucks prior to analysis.

#### *ToF-SIMS Results: Mass Spectra*

Following removal of the carbon coating by oxygen ion sputtering, sample area 63B was scanned 1000 times using the Spectral mode and 750 times using the Compromise mode. The complete mass spectrum from 0 to 100 amu obtained from the Spectral mode analysis, shown in Figure 3.11, contains numerous peaks, especially in the higher mass range. These probably reflect the fragmentation of organic compounds in the epoxy matrix during primary ion bombardment. The highest ion yields were observed for the alkali metals Na and K ( $\sim 10^6$  counts), which is most likely a result of both their relatively low ionization potentials, as well as their high abundances in minerals such as

Table 3.4 Elemental positive secondary ion yield from a number of metals compared to the corresponding oxides [5].

<b>Metal</b>	<b>Clean metal M<sup>+</sup> yield</b>	<b>Metal Oxide M<sup>+</sup> yield</b>
Mg	0.01	0.9
Al	0.007	0.7
Si	0.0084	0.58
Ti	0.0013	0.4
Fe	0.0015	0.35
Ni	0.0006	0.045
Cu	0.0003	0.007

plagioclase feldspar and K feldspar, respectively. Despite the fact that Li is known to occur only as a trace-to-minor component in two of the minerals in this sample area – i. e. chlorite (grain 1) and muscovite (grain 6) [27] – a relatively high signal intensity was observed for Li ( $\sim 10^5$  counts), likely as a result of its low ionization energy.

The wealth of information in such a complex spectrum can be problematic; however, the *a priori* knowledge about the composition of the minerals analyzed aids in simplifying the spectral interpretation. Because it is neither necessary nor efficient to identify all mass species, only the peaks corresponding to Ni and the eight major elements chosen to represent the composition of most minerals (i.e. Si, Al, K, Ca, Na, Ti, Mg and Fe) were used to map the elemental distribution at the sample surface. Individual peaks for the elements of interest from sample area 63B are shown in Figures 3.12 to 3.13 and Figures 3.14 to 3.15 for the Spectral and Compromise modes, respectively.

In the mass spectra obtained using the Spectral mode, the signal intensity for all eight major elements (Figure 3.12) was relatively high ( $\sim 10^5 - 10^6$  counts) and the peaks were well resolved from any potential interfering species. The signal for  $^{58}\text{Ni}$ , shown in Figure 3.13 a), had a much lower intensity ( $\sim 10^3$  counts) than the major elements because of its lower abundance in the sample, as well as the inherently lower secondary ion yield of Ni compared to that of the major elements, as shown in Table 3.4. Despite the low signal intensity of  $^{58}\text{Ni}$ , the high mass resolution capabilities of the Spectral mode allowed it to be resolved from the numerous neighbouring peaks. These peaks are probably organic fragments and polyatomic compounds (e.g. hydrides and oxides) produced during the sputtering process, including species such as  $\text{Si}_2\text{H}_2$  at 57.97 amu,  $\text{H}_3\text{SiAl}$  at 57.98 amu,  $\text{C}_2\text{H}_7\text{Al}$  at 58.03 amu, and  $\text{C}_4\text{H}_{10}$  at 58.08 amu. Unfortunately, there is an isobaric interference for  $^{58}\text{Ni}$  (57.9353 amu) by  $^{58}\text{Fe}$  (57.9333 amu), for which the mass difference (0.0020 amu) is far beyond the resolution of the instrument, even in the Spectral mode. Although the relative isotopic abundance of  $^{58}\text{Fe}$  is only 0.28 %, it is still a major interfering species, as most of the Mg-bearing mineral grains of interest are also

Fe-rich. For ferromagnesian minerals, the observed signal at mass 58 is a composite of both  $^{58}\text{Ni}$  and  $^{58}\text{Fe}$ , and is therefore not a reliable indicator of the presence of Ni in these mineral grains. A solution to this problem is to use the second-most abundant isotope of Ni at mass 60, the spectrum of which is shown in Figure 3.13 b). There are no major isobaric interferences associated with this isotope, and although the natural isotopic abundance of  $^{60}\text{Ni}$  is only 26.22 %, it was still detectable when using the Spectral mode, due to the relatively high primary ion dose associated with this operational mode.

The individual mass spectra obtained from the Compromise mode analysis, given in Figures 3.14 and 3.15, show a series of five repeated peaks, all of which correspond to one mass species. Because these peaks are spread out along the x-axis, the analysis software only recognizes the mass scale as being applicable to the first peak in the series, but calculates the corresponding signal intensity as the sum of the five peak areas. Similar to the Spectral mode, the individual peaks for the major elements were also relatively large and well-resolved. Although organic fragments and polyatomic species were minor spectral components and did not interfere with the signals for major elements (Figure 3.14); they did represent significant interfering species for  $^{58}\text{Ni}$  in the Compromise mode spectrum (Figure 3.15). Although the series of peaks for mass 58 overlapped with those of the adjacent series, they fell within the valleys of the neighboring series, allowing them to be resolved well enough to be reliably integrated. The loss in the number of primary ions per pulse in this mode was somewhat compensated for by the pulse repetition; however, the overall signal intensity for each element was still significantly lower than in the Spectral mode analysis. Consequently,  $^{60}\text{Ni}$  was not detectable in the Compromise mode spectrum.

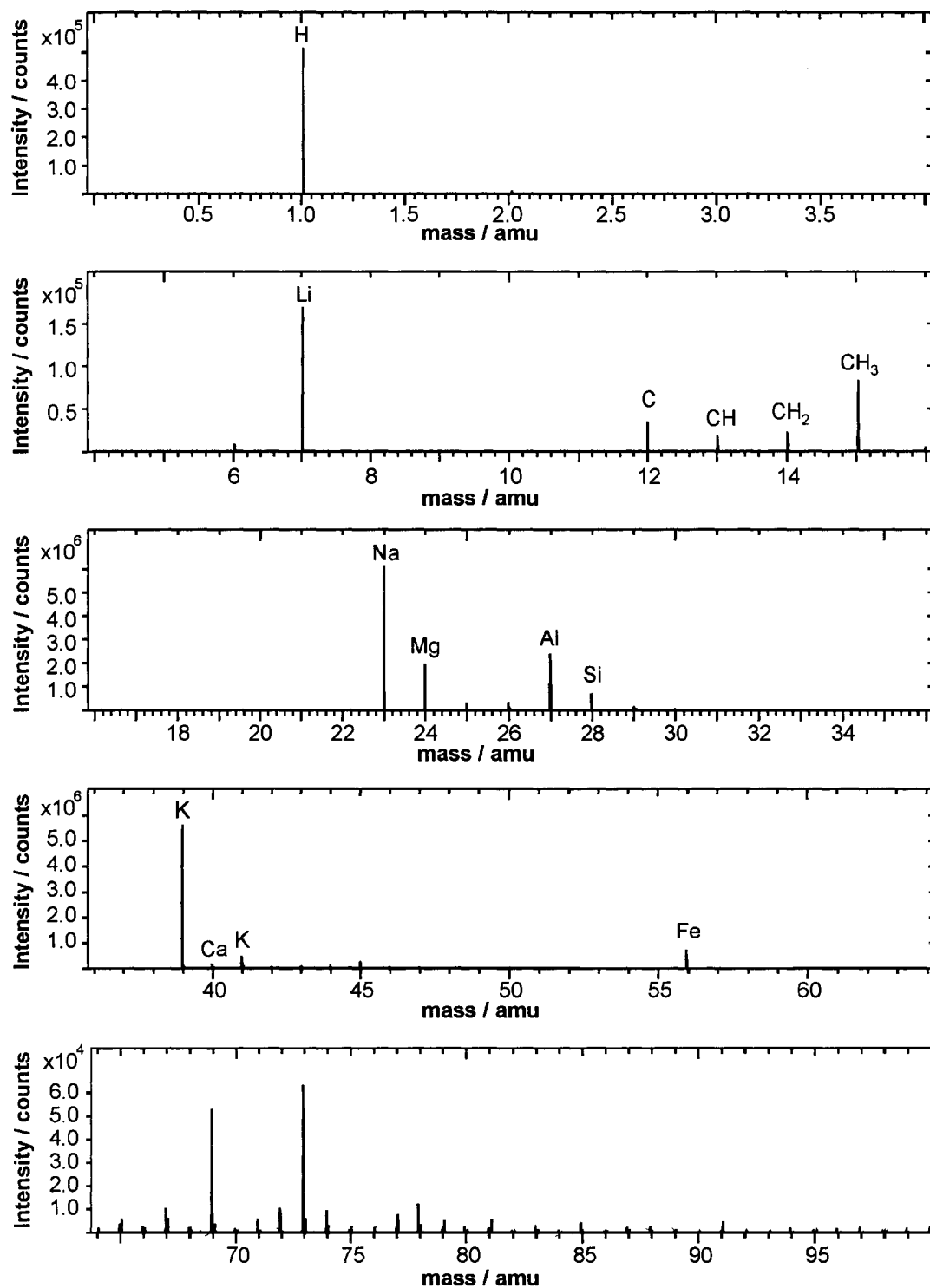


Figure 3.11 Complete mass spectrum for sample area 63B from 0 – 100 amu. Spectral mode, positive ions, 1000 scans.

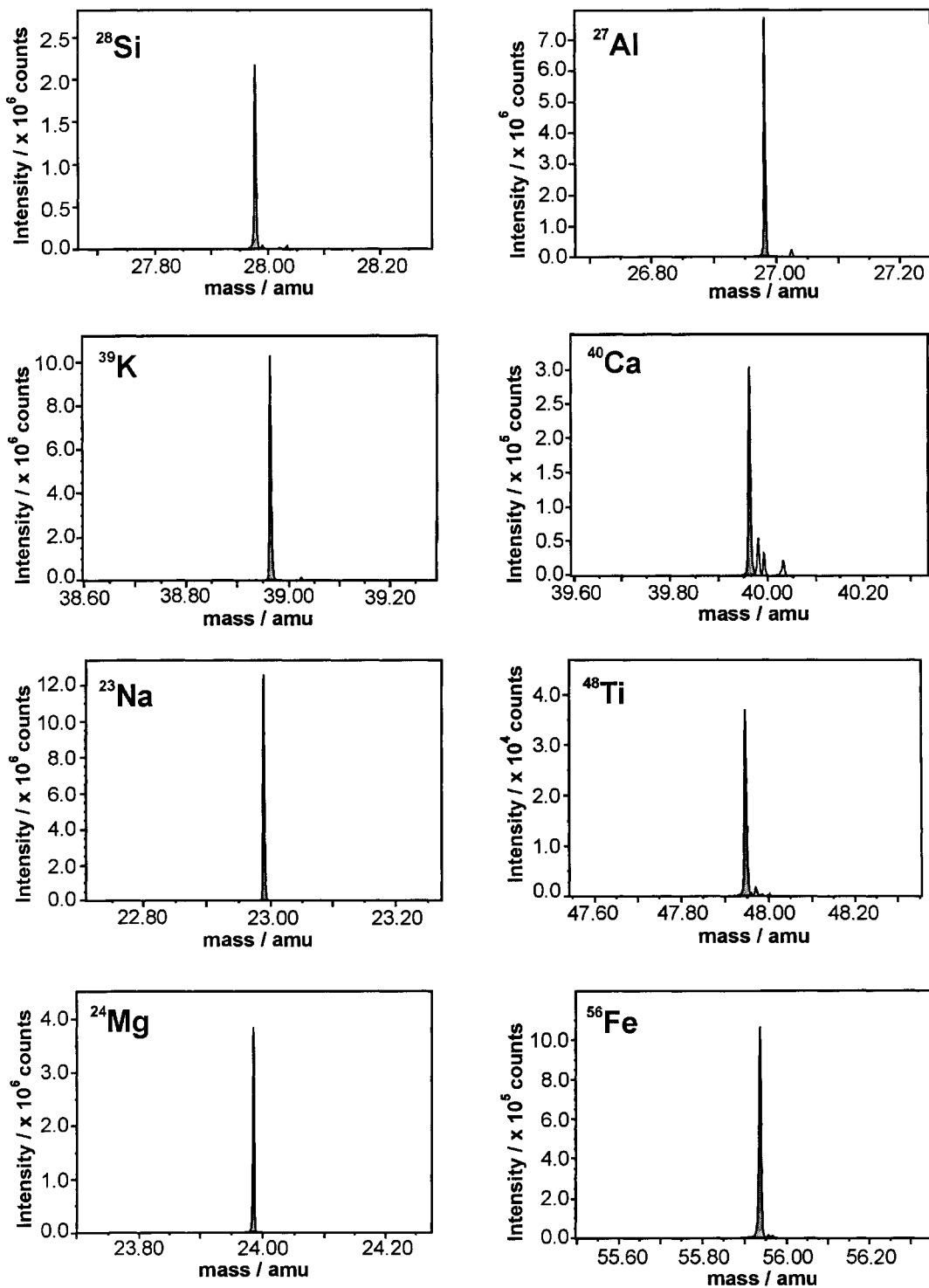


Figure 3.12 Individual mass spectra of major elements for sample area 63B. Integrated peak areas are shown in grey. Spectral mode, positive ions, 1000 scans.

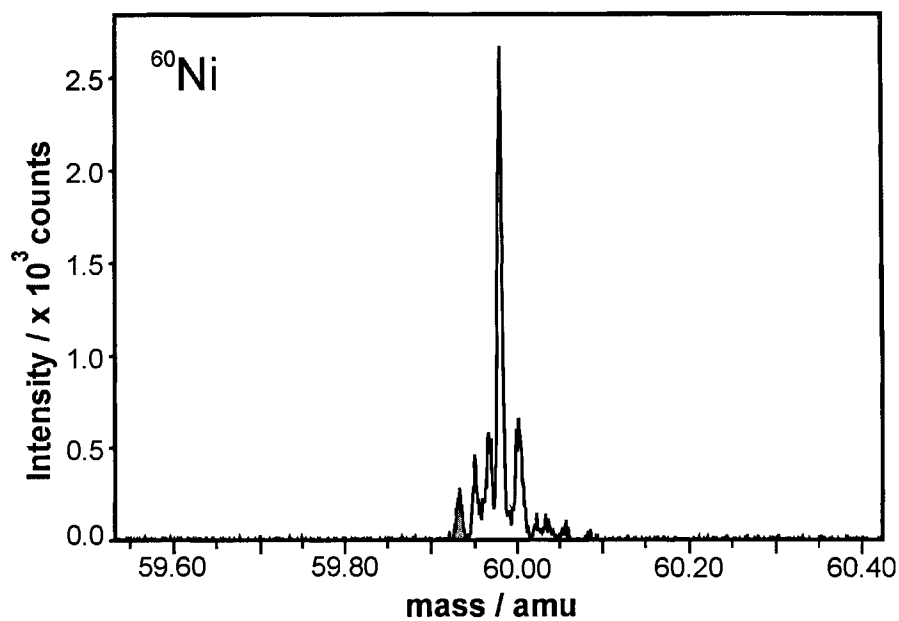
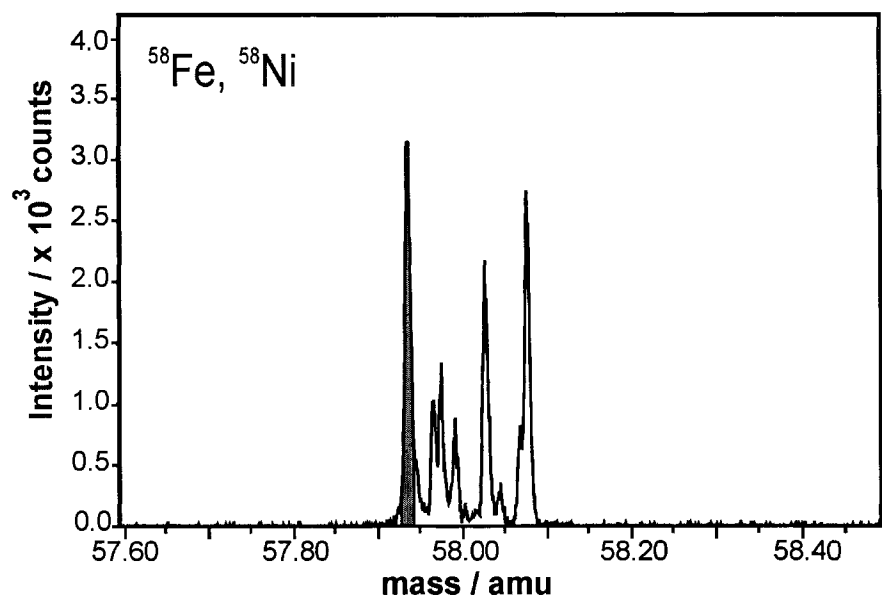


Figure 3.13 Individual mass spectra for sample area 63B: a)  $^{58}\text{Ni}$  and  $^{58}\text{Fe}$ , b)  $^{60}\text{Ni}$ . Integrated peak areas are shown in grey. Spectral mode, positive ions, 1000 scans.

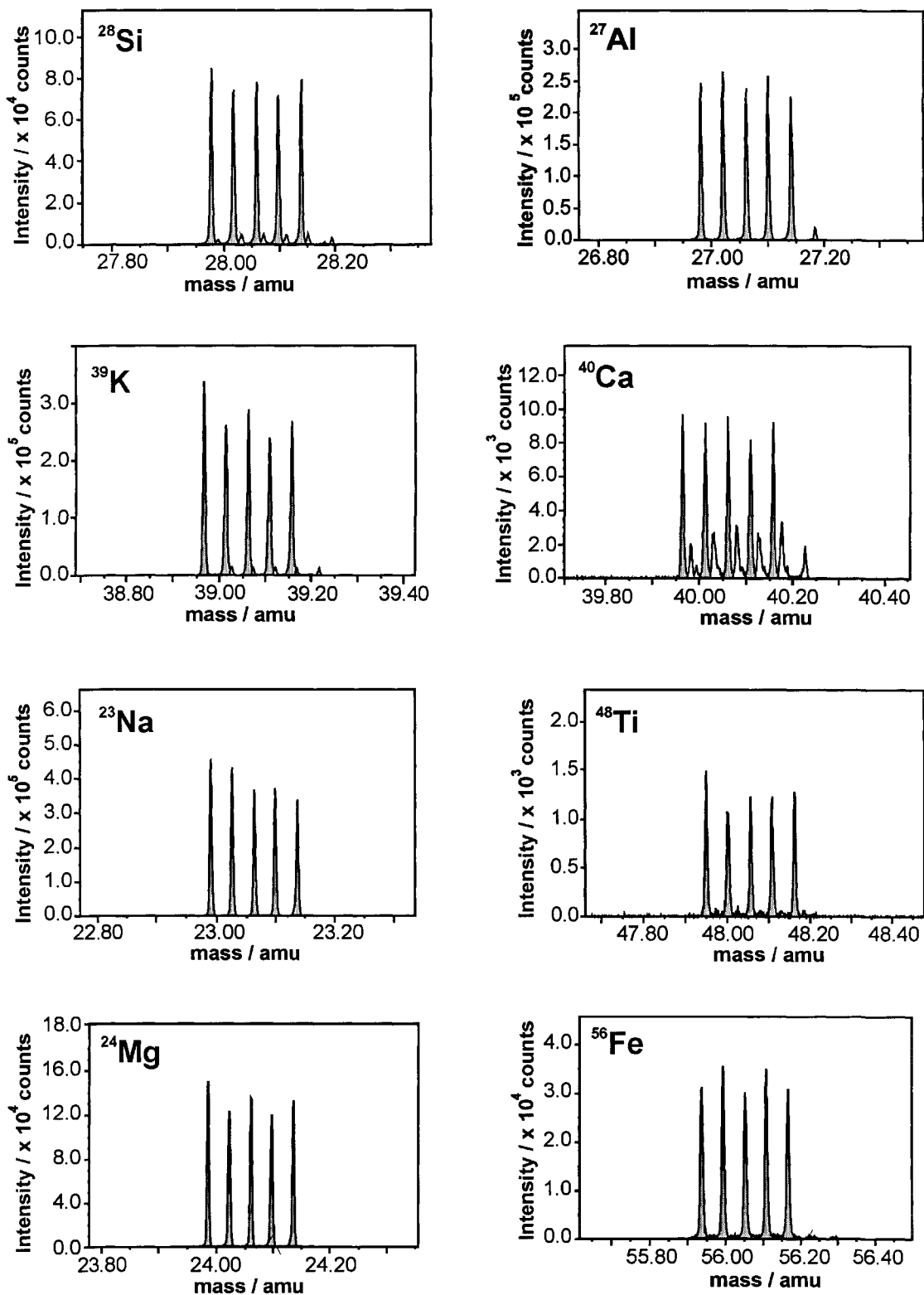


Figure 3.14 Individual mass spectra of major elements for sample area 63B. Integrated peak areas are shown in grey. Compromise mode, positive ions, 750 scans.

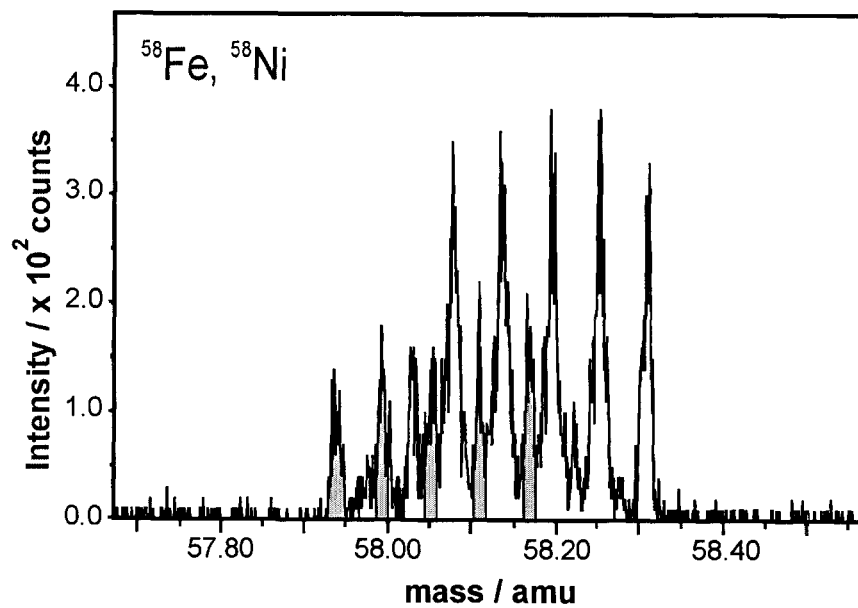


Figure 3.15 Mass spectrum for <sup>58</sup>Ni for sample area 63B. Integrated peak areas are shown in grey. Compromise mode, positive ions, 750 scans.

### *ToF-SIMS Results: Secondary Ion Images*

The secondary ion images for sample area 63B obtained using the Spectral mode are shown in Figure 3.16. As a result of polishing the sample pucks, the mineral grains analyzed by ToF-SIMS are predominantly cross-sections through the grains. Hence, the secondary ion images reflect the elemental distribution within each grain, rather than the surface chemistry. The aim of this work was to establish a spatial correlation between Ni and Mg-bearing phyllosilicate grains. Although the signal intensities were relatively high in the Spectral mode images, the spatial resolution was poor as a result of the wide diameter of the primary ion beam that is characteristic of this mode. Hence, in order to more accurately estimate the grain boundaries, these images were compared and correlated with the images obtained using the Compromise mode, shown in Figure 3.17. Although the Compromise mode provided clearer images than those of the spectral mode, the lower brightness levels in the images made it more difficult to distinguish between features and background for some elements. Because  $^{60}\text{Ni}$  was found to be below the detection limits of this mode, the signal at mass 58 for all particles that contained appreciable amounts of Fe had to be interpreted in conjunction with the Spectral mode images of  $^{60}\text{Ni}$  to confirm the presence of Ni. In the Spectral mode secondary ion images, a spatial correlation was observed between the chlorite grain (grain 1) and the signal for  $^{60}\text{Ni}$ . Although the signal-to-noise ratio for  $^{60}\text{Ni}$  was quite low, the majority of the ion counts were concentrated in the area where the chlorite grain was located.

#### *3.4.2 Sample Puck 63C*

##### *SEM-EDS Results*

The mineral map for sample puck 63C is given in Figure 3.18, and the secondary electron images of sample areas 63C1 and 63C2 are given in Figures 3.19 and 3.21, respectively. The JEOL SEM used to obtain these images was not equipped with a

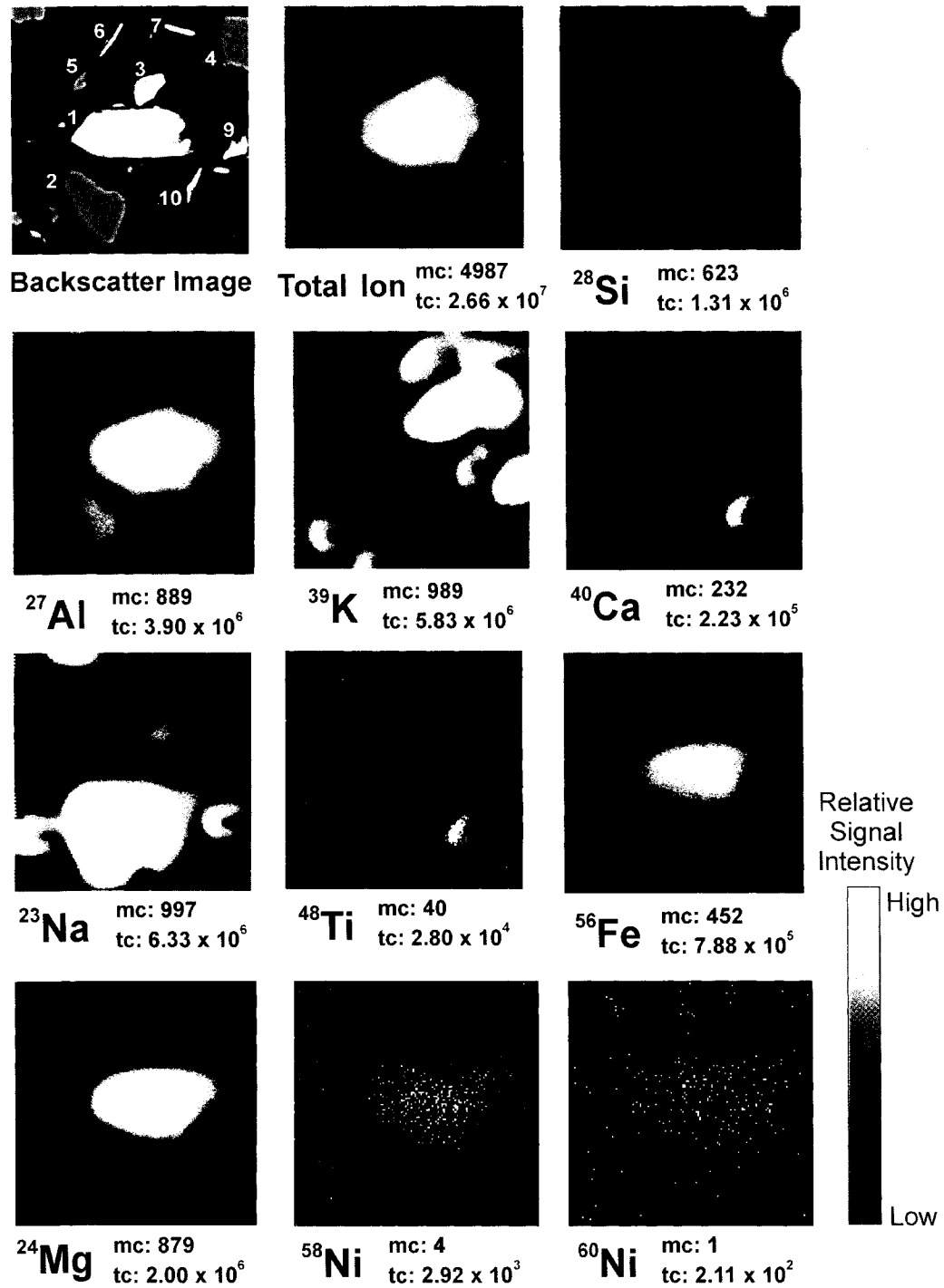


Figure 3.16 Secondary ion images for sample area 63B ( $100 \times 100 \mu\text{m}^2$ ). Spectral mode, positive ions, 1000 scans,  $128 \times 128$  pixels. mc = max. number of counts, tc = total number of counts. Mineral grains in BSE image ( $\times 716$ ): 1 - chlorite, 2 - plagioclase, 3 - K feldspar, 4 - quartz, 5 - quartz, 6 - muscovite, 7 - K feldspar, 8 - quartz, 9 - K feldspar, 10 - titanite.

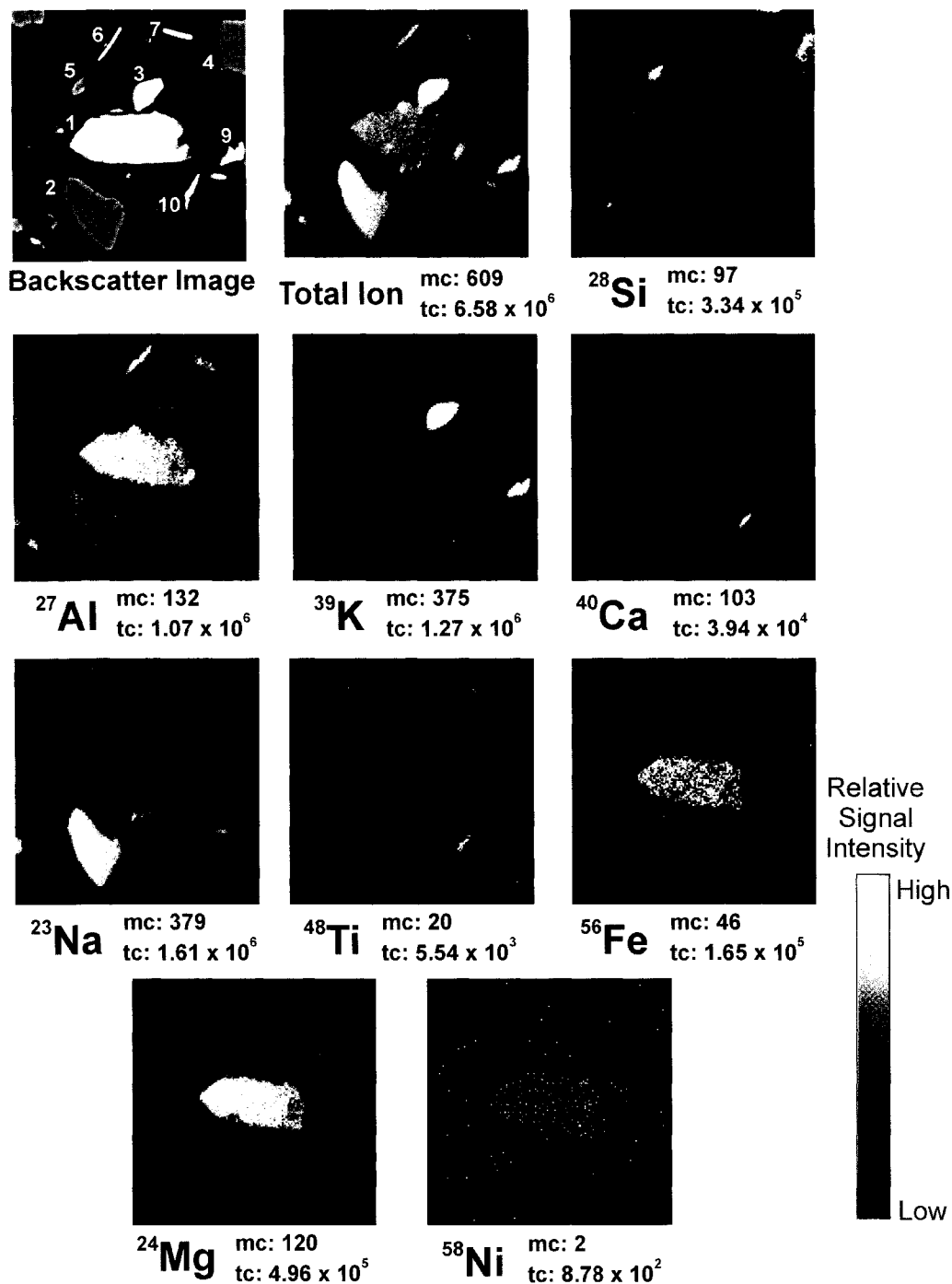


Figure 3.17 Secondary ion images for sample area 63B ( $100 \times 100 \mu\text{m}^2$ ). Compromise mode, positive ions, 750 scans,  $256 \times 256$  pixels. mc = max. number of counts, tc = total number of counts. Mineral grains in BSE image ( $\times 716$ ): 1 - chlorite, 2 - plagioclase, 3 - K feldspar, 4 - quartz, 5 - quartz, 6 - muscovite, 7 - K feldspar, 8 - quartz, 9 - K feldspar, 10 - titanite.

backscatter electron detector; hence, in order to clearly identify individual particles, the prominent mineral grains in the secondary electron images for areas 63C1 and 63C2 were outlined and labelled in yellow in Figures 3.19 b) and 3.21 b), respectively. The raster of holes in the epoxy due to oxygen sputtering is quite prominent in these images.

Grain 1 in area 63C1 was characterized as a chlorite in the mineral map (Figure 3.18); however, its EDS spectrum, shown in Figure 3.20 a), had less prominent Mg and Al peaks than the spectrum for the chlorite grain in area 63B, and contained a significant peak for K – a composition more consistent with that of a biotite [27]. The EDS spectra of chlorite grains 2 and 4 in area 63C1 were very similar to that for the chlorite in area 63B. The spectrum for chlorite grain 6, shown in Figure 3.20 b), resembled that of chlorite grains 2 and 4, but also contained a small peak for K, suggesting that this chlorite grain may have once been a biotite. Hydrothermal alteration of biotite, involving the loss of interlayer  $K^+$  ions and fixation of  $Fe^{2+}$  and  $Mg^{2+}$ , gradually transforms the mineral into chlorite. Chlorite, in turn, can alter to vermiculite via replacement of the brucite sheet by hydrated cations and a partially filled  $H_2O-Mg^{2+}-H_2O$  double sheet [27]. Hence, an alternative interpretation of the observed K in the chlorite spectrum is that it may reflect the presence of hydrated  $K^+$  ions in the interlayer spaces during alteration to vermiculite. Furthermore, soil minerals are not always present as discrete phases – interstratified clay minerals (e.g. mixed-layer vermiculite-chlorite and chlorite-biotite) commonly occur in the soil environment, having compositions intermediate between those of their constituent minerals [27,29]. The weathered till parent material for this soil is reported to be abundant in mixed-layer clays and products of chlorite alteration [30]. The EDS spectrum for sulphide grains 3 and 5, presented in Figure 3.20 c), showed prominent peaks for Fe and S, which is probably indicative of pyrite ( $FeS_2$ ) or pyrrhotite ( $Fe_{1-x}S$ ,  $x = 0 - 0.2$ ) [27]. In sample area 63C2 (Figure 3.21), the EDS spectra of chlorite grains 1, 2 and 3 revealed similar compositions to chlorite grains 2 and 4 from area 63C1.

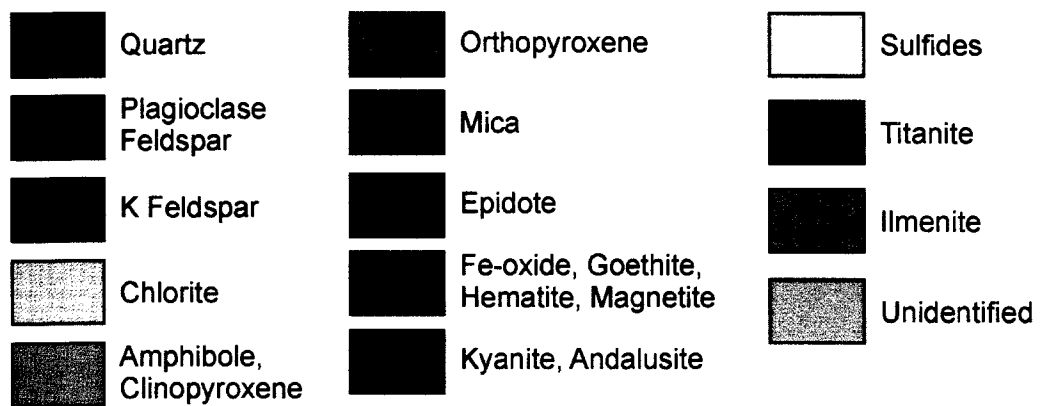
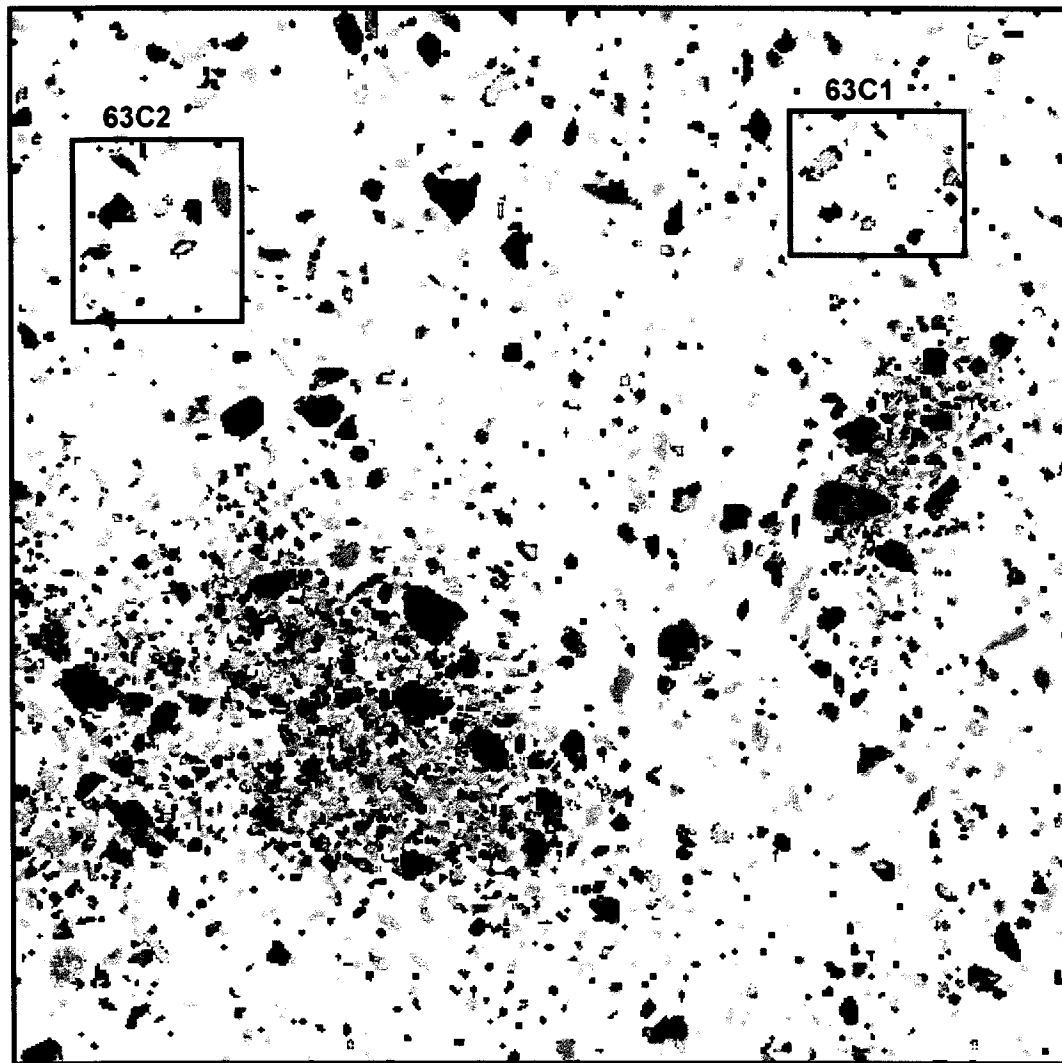


Figure 3.18 Mineral map for sample puck 63C ( $1100 \times 1100 \mu\text{m}^2$ ). The black boxes indicate the sample areas chosen for analysis by ToF-SIMS.

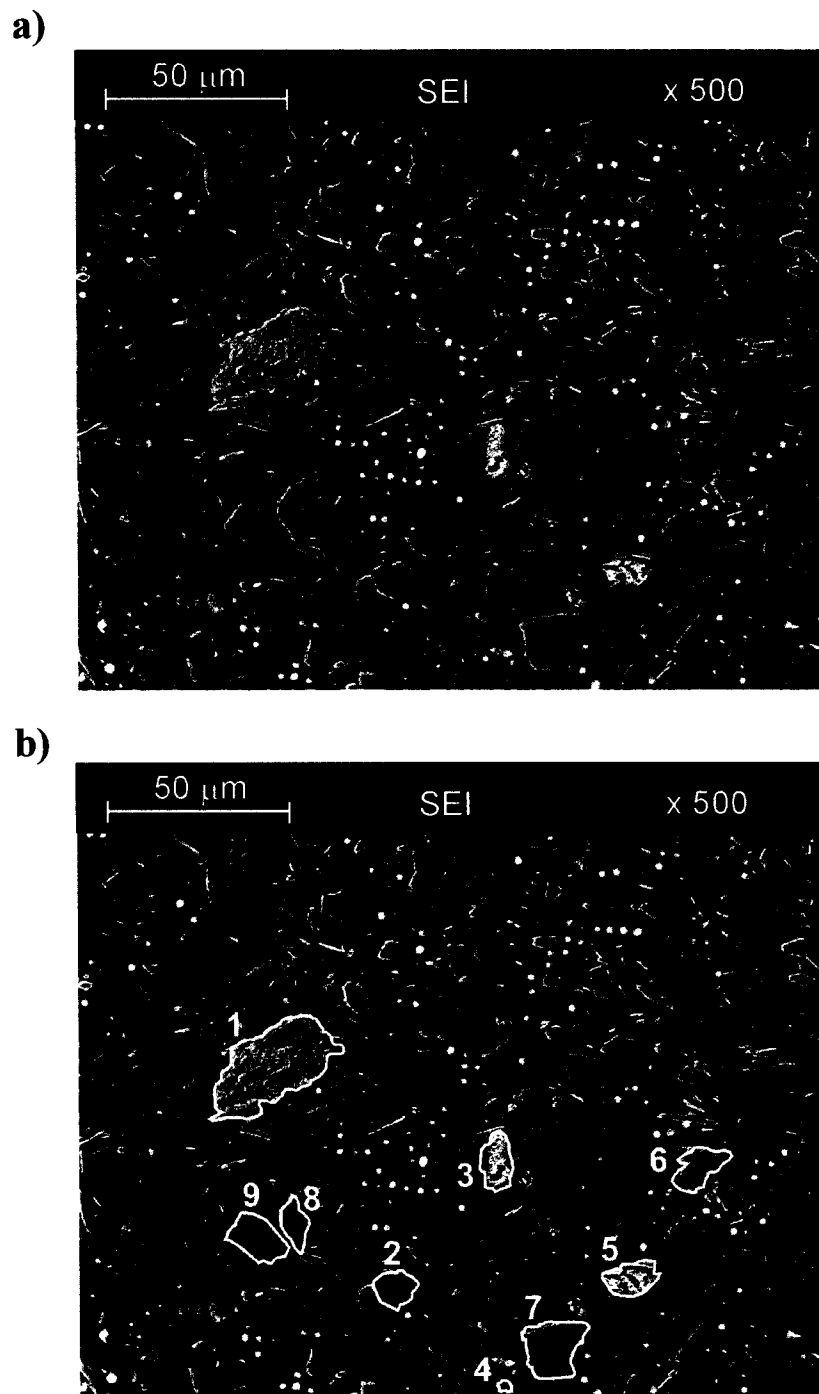


Figure 3.19 SEM image used to locate individual mineral grains in sample area 63C1 ( $\times 500$ ): a) original secondary electron image, b) secondary electron image overlain with outlines of prominent mineral grains: 1 - biotite, 2 - chlorite, 3 - Fe sulphide, 4 - chlorite, 5 - Fe sulphide, 6 - chlorite, 7 - quartz, 8 - quartz, 9 - quartz. JEOL SEM.

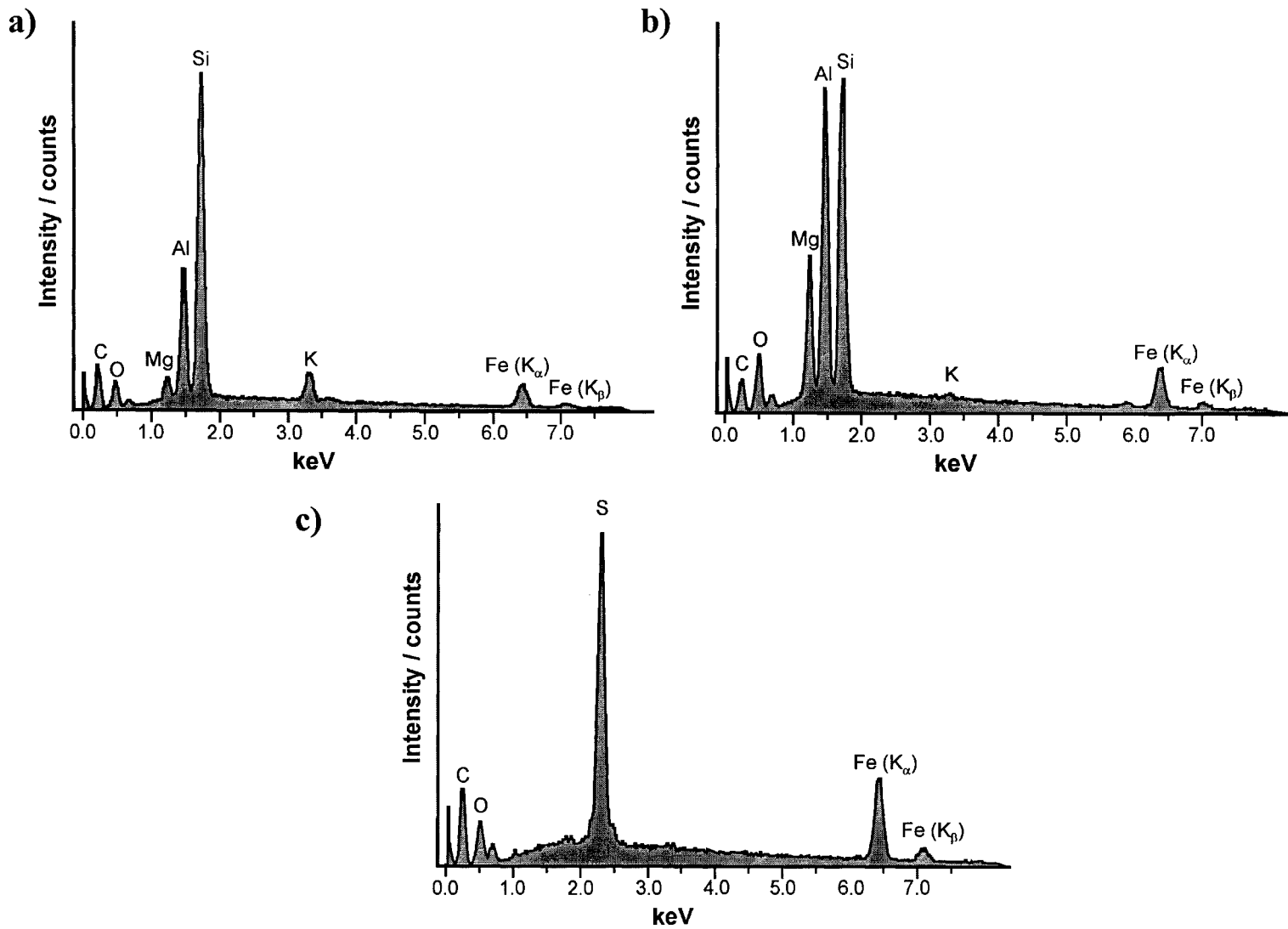


Figure 3.20 EDS spectra for mineral grains in sample area 63C1: a) grain 1 (biotite), b) grain 6 (chlorite), c) grain 3 (Fe-sulphide). JEOL SEM with PGT EDS.

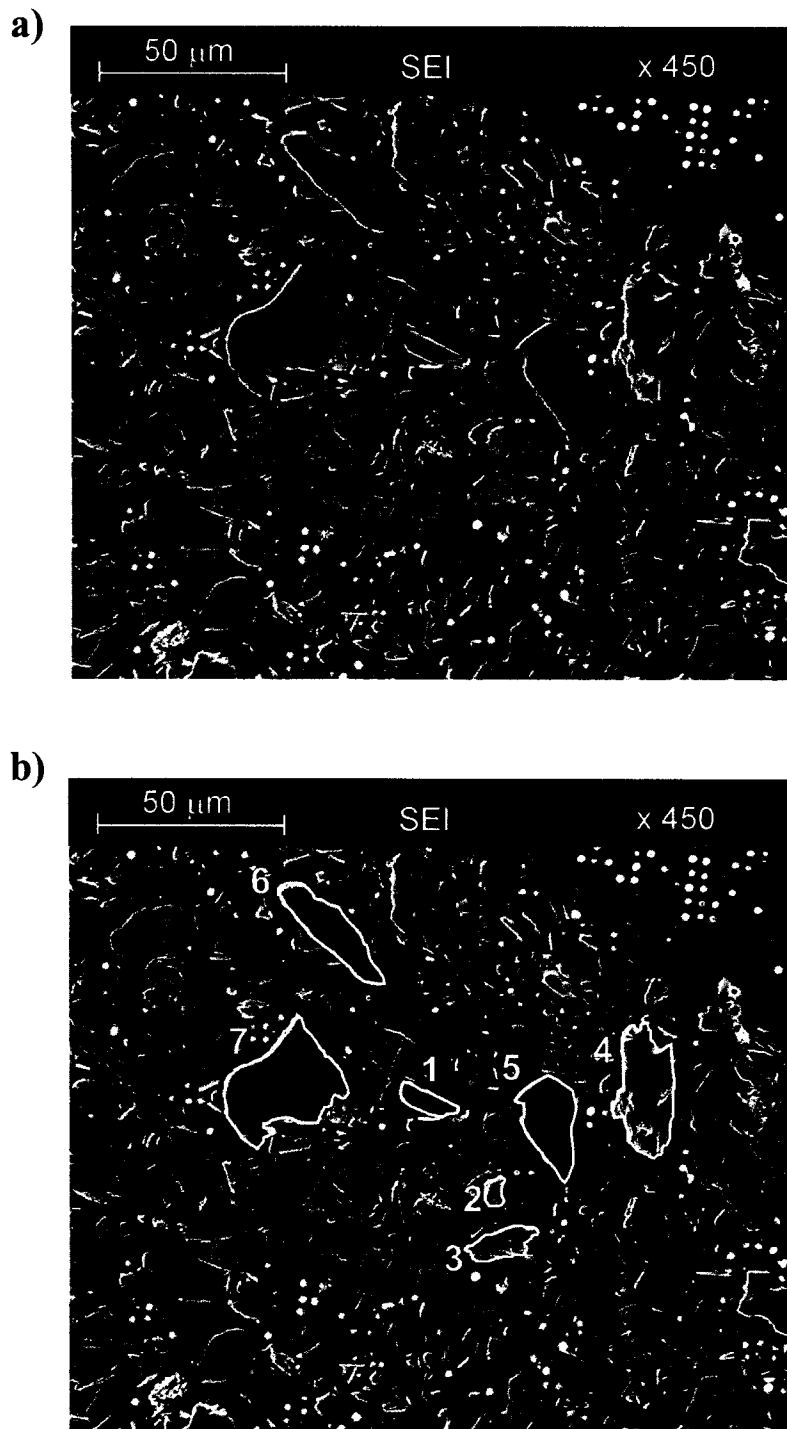


Figure 3.21 SEM image used to locate individual mineral grains in sample area 63C2 ( $\times 450$ ): a) original secondary electron image, b) secondary electron image overlain with outlines of prominent mineral grains: 1 - chlorite, 2 - chlorite, 3 - chlorite, 4 - epidote, 5 - quartz, 6 - quartz, 7 - quartz. JEOL SEM.

### *ToF-SIMS Results: Secondary Ion Images*

Figures 3.22 and 3.23 show the secondary ion maps for sample area 63C1 obtained using the Spectral and Compromise modes, respectively. In order to simplify interpretation of the element maps for Ni, the outlines of the Mg-bearing grains (i.e. biotite and chlorite) and sulphide grains from the secondary electron image were overlain in yellow on the images for  $^{58}\text{Ni}$  and  $^{60}\text{Ni}$ . It is important to keep in mind that the pixels corresponding to counts for  $^{60}\text{Ni}$  do not necessarily fall exactly within the grain boundaries of the minerals they originate from because of the poor spatial resolution of the Spectral mode. Despite this fact, a strong spatial correlation was observed between  $^{60}\text{Ni}$  and the biotite grain (grain 1). Weaker correlations were evident for chlorite grains 2, 4, and 6. One of the sulphide grains (grain 3) was also observed to contain some  $^{60}\text{Ni}$ . Similar correlations with  $^{60}\text{Ni}$  were observed for chlorite grain 1 in sample area 63C2, for which the secondary ion images are presented in Figures 3.24 and 3.25 for the Spectral and Compromise modes, respectively.

#### *3.4.3 Sample Puck 63E*

##### *SEM-EDS Results*

The mineral map for sample puck 63E is shown in Figure 3.26 and the BSE image of sample area 63E2 is given in Figure 3.27. Grain 1 was broadly classified as olivine/orthopyroxene in the mineral map because these two minerals have very similar compositions which make them difficult to differentiate based on EDS element maps alone. However, the relative signal intensities in the EDS spectrum for this grain, shown in Figure 3.28 a), enabled a more definitive identification of grain 1 as a Mg-rich olivine (forsterite) [27]. The composition of chlorite grains 3, 5, 6 and 8 was very similar to that of grain 1 from sample area 63B (i.e. no K). The EDS spectrum for chlorite grain 4, shown in Figure 3.28 b), contained a small signal for K, similar to that observed in the spectrum for chlorite grain 6 in sample area 63C1.

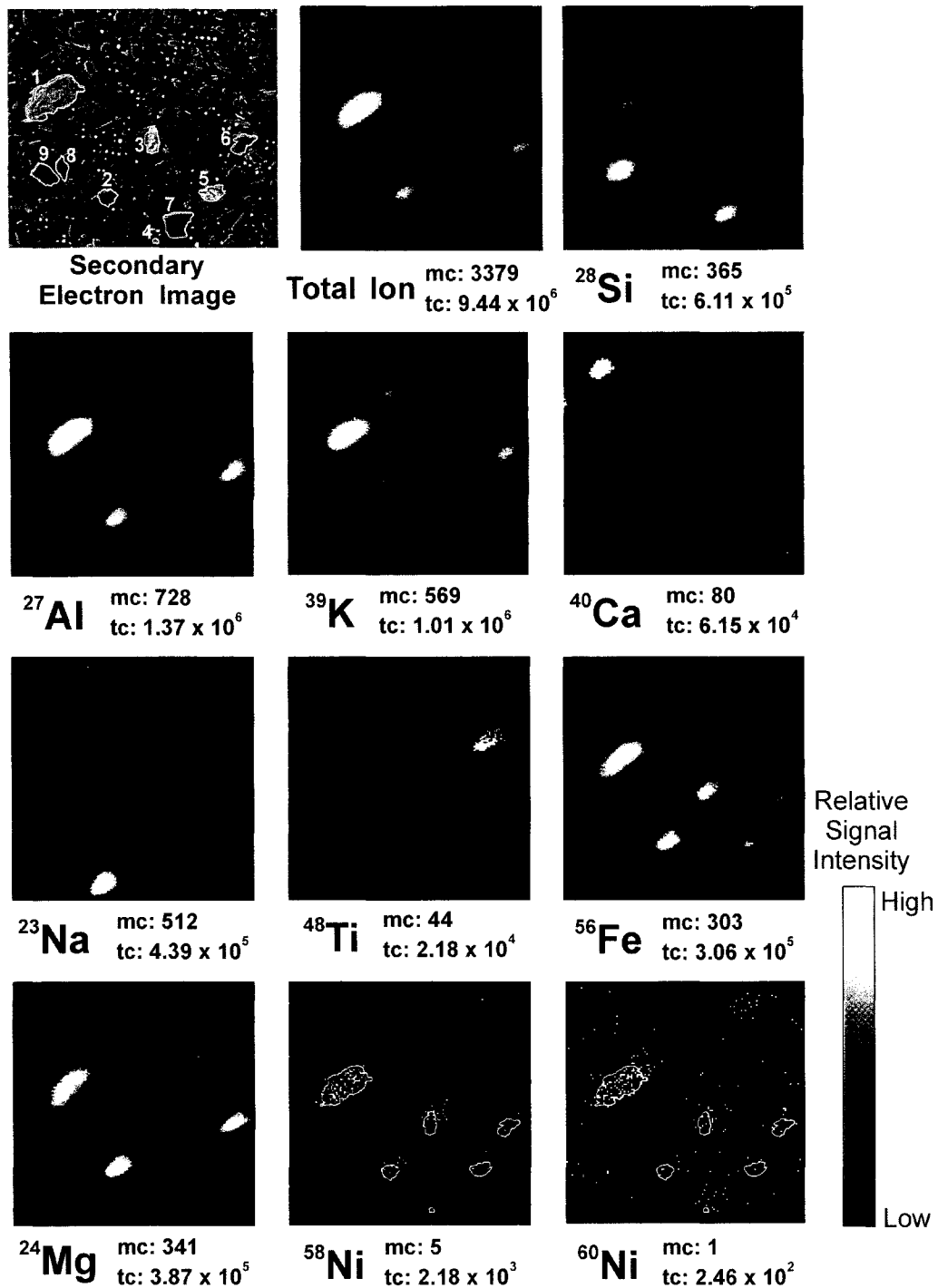


Figure 3.22 Secondary ion images for sample area 63C1 ( $175 \times 175 \mu\text{m}^2$ ). Spectral mode, positive ions, 1000 scans,  $128 \times 128$  pixels. mc = max. number of counts, tc = total number of counts. Mineral grains in secondary electron image ( $\times 500$ ): 1 - biotite, 2 - chlorite, 3 - Fe sulphide, 4 - chlorite, 5 - Fe sulphide, 6 - chlorite, 7 - quartz, 8 - quartz, 9 - quartz. Outlines of Mg-bearing minerals (biotite, chlorite) and sulphides from the secondary electron image are overlain in yellow on the images for  $^{58}\text{Ni}$  and  $^{60}\text{Ni}$ .

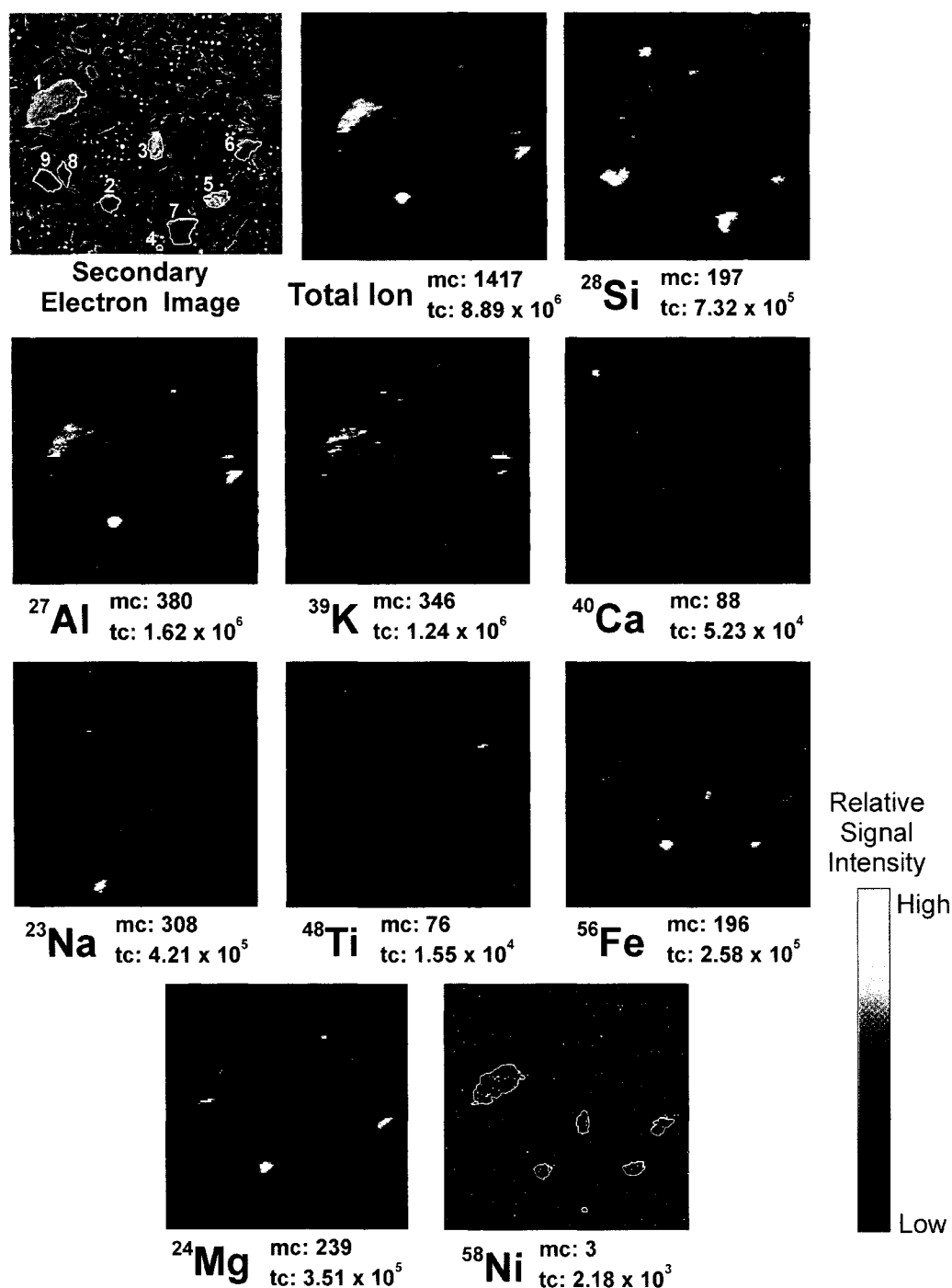


Figure 3.23 Secondary ion images for sample area 63C1 ( $175 \times 175 \mu\text{m}^2$ ). Compromise mode, positive ions, 1000 scans,  $256 \times 256$  pixels. mc = max. number of counts, tc = total number of counts. Mineral grains in secondary electron image ( $\times 500$ ): 1 - biotite, 2 - chlorite, 3 - Fe sulphide, 4 - chlorite, 5 - Fe sulphide, 6 - chlorite, 7 - quartz, 8 - quartz, 9 - quartz. Outlines of Mg-bearing minerals (biotite, chlorite) and sulphides from the secondary electron image are overlain in yellow on the image for  $^{58}\text{Ni}$ .

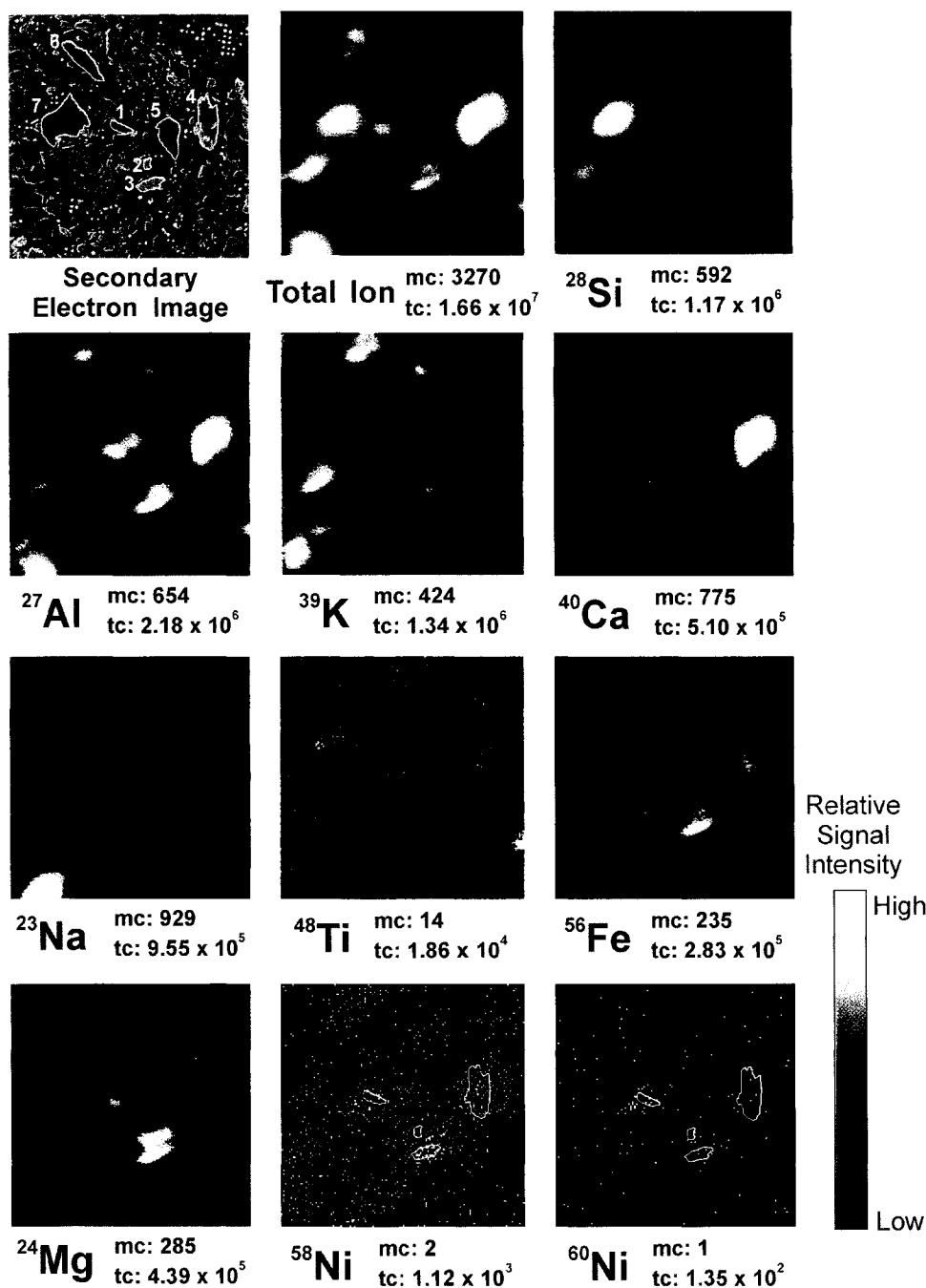


Figure 3.24 Secondary ion images for sample area 63C2 ( $175 \times 175 \mu\text{m}^2$ ). Spectral mode, positive ions, 1000 scans,  $128 \times 128$  pixels. mc = max. number of counts, tc = total number of counts. Mineral grains in secondary electron image ( $\times 450$ ): 1 - chlorite, 2 - chlorite, 3 - chlorite, 4 - epidote, 5 - quartz, 6 - quartz, 7 - quartz. Outlines of Mg-bearing minerals (chlorite) and epidote from the secondary electron image are overlain in yellow on images for  $^{58}\text{Ni}$  and  $^{60}\text{Ni}$ .

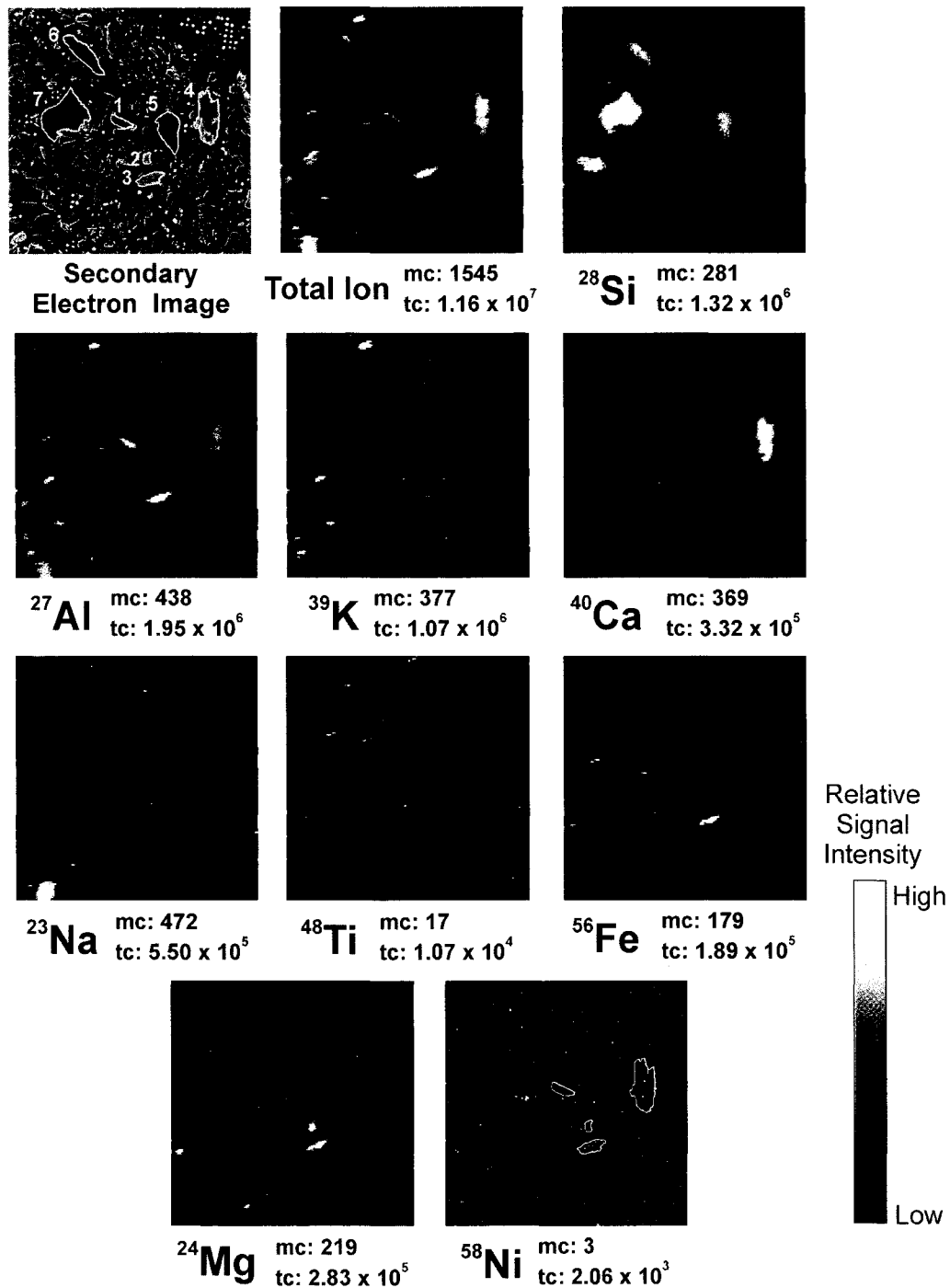


Figure 3.25 Secondary ion images for sample area 63C2 ( $175 \times 175 \mu\text{m}^2$ ). Compromise mode, positive ions, 1000 scans,  $256 \times 256$  pixels. mc = max. number of counts, tc = total number of counts. Mineral grains in secondary electron image ( $\times 450$ ): 1 - chlorite, 2 - chlorite, 3 - chlorite, 4 - epidote, 5 - quartz, 6 - quartz, 7 - quartz. Outlines of Mg-bearing minerals (chlorite) and epidote from the secondary electron image are overlain in yellow on image for  $^{58}\text{Ni}$ .

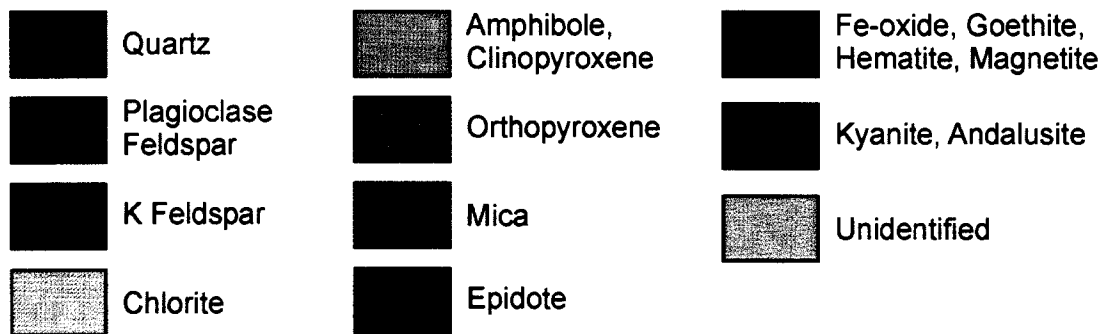
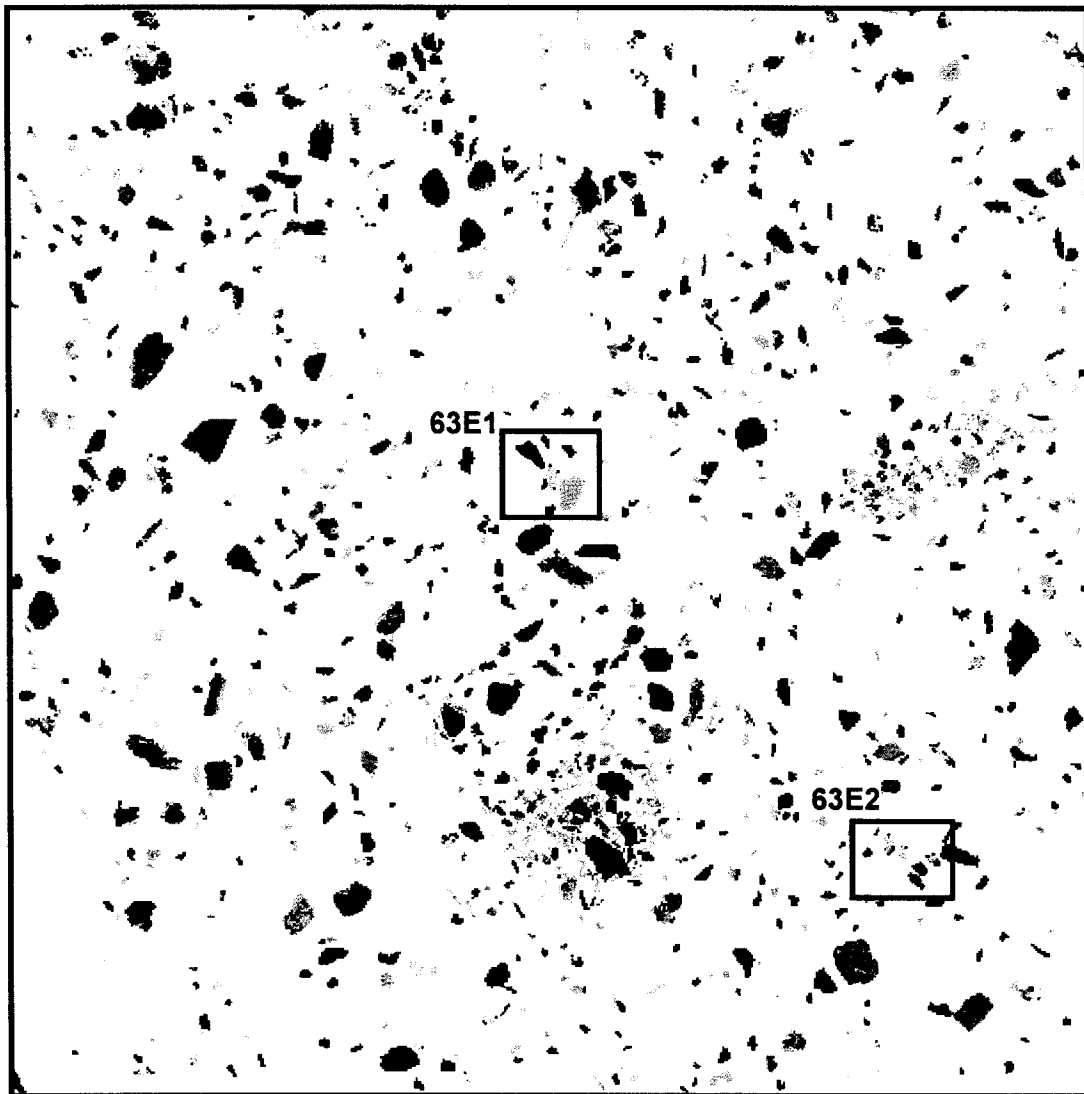


Figure 3.26 Mineral map for sample puck 63E ( $1200 \times 1200 \mu\text{m}^2$ ). The black boxes indicate the sample areas chosen for analysis by ToF-SIMS.

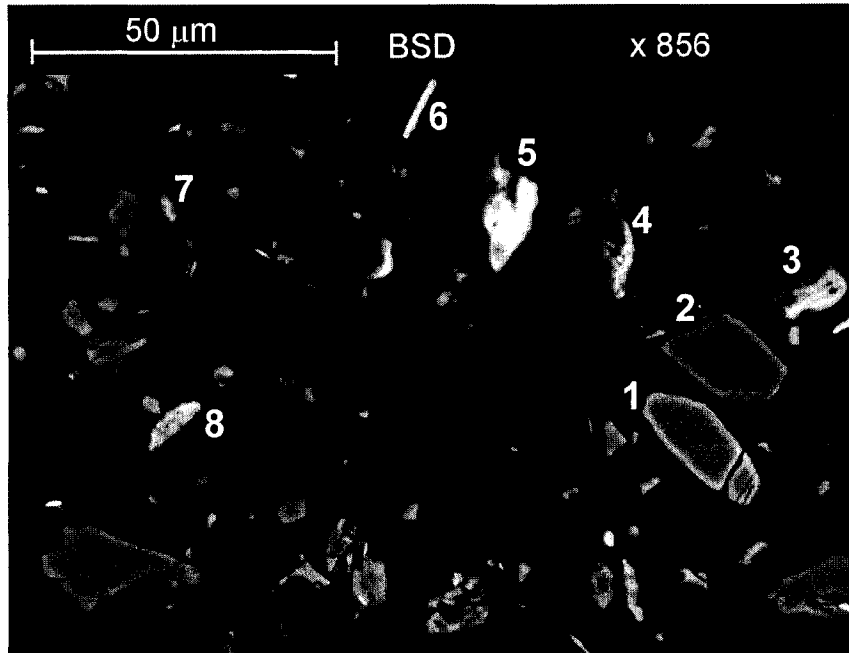


Figure 3.27 BSE image used to locate individual mineral grains in sample area 63E2 ( $\times 856$ ). Mineral grains: 1 - olivine, 2 - quartz, 3 - chlorite, 4 - chlorite, 5 - chlorite, 6 - chlorite, 7 - biotite, 8 - chlorite. Cambridge SEM.

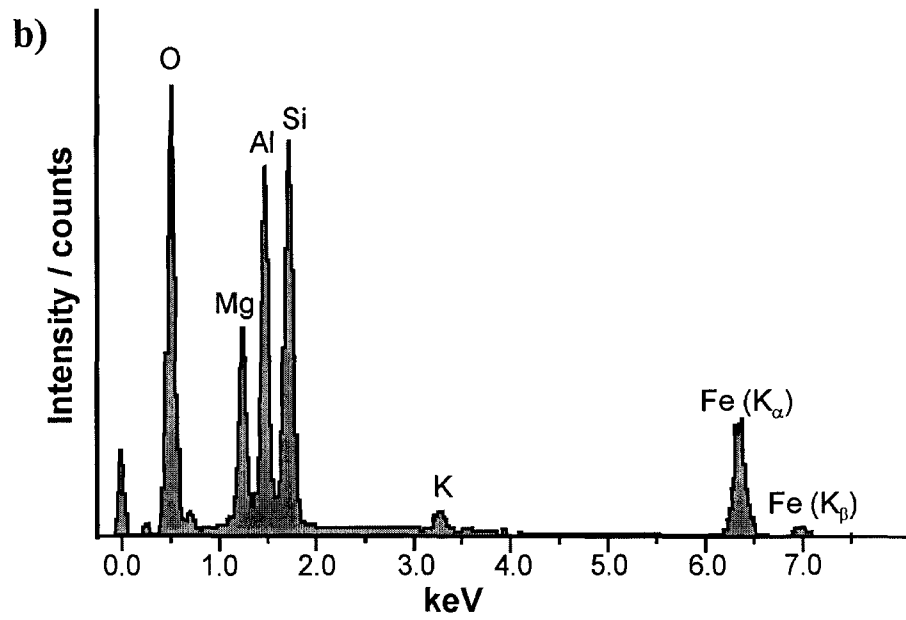
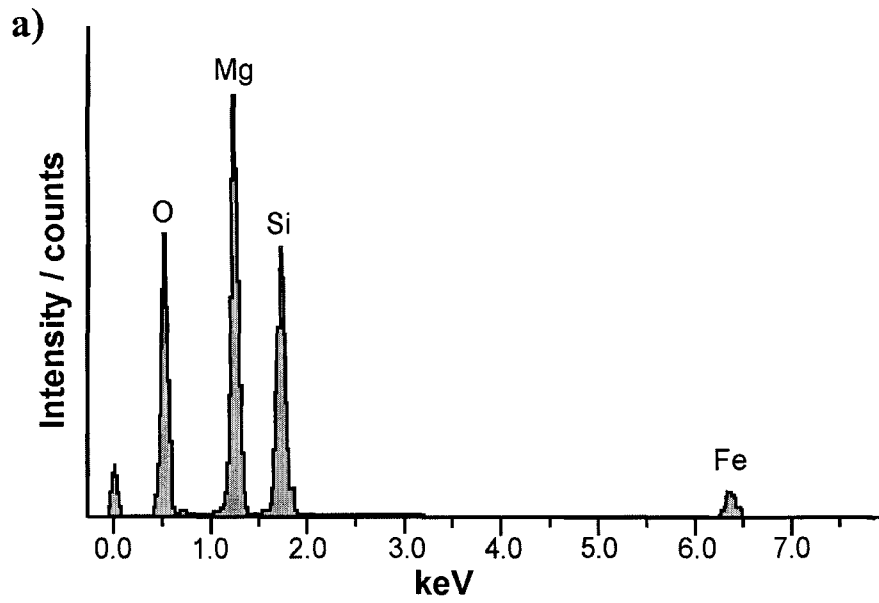


Figure 3.28 EDS spectra for mineral grains in sample area 63E2: a) grain 1 (olivine), b) grain 4 (chlorite). Cambridge SEM with Oxford Link EDS.

### *ToF-SIMS results: Secondary Ion Images*

The secondary ion images corresponding to the Spectral and Compromise mode analyses of area 63E2 are given in Figures 3.29 and 3.30, respectively. This area was only scanned 73 times using the Spectral mode, and 570 times using the Compromise mode due to time constraints, and consequently, the signal-to-noise ratio was relatively low. Despite the low signal intensity of  $^{60}\text{Ni}$  in the Spectral mode secondary ion image (Figure 3.29), a spatial correlation was observed between  $^{60}\text{Ni}$  and four of the chlorites (grains 3, 4, 5 and 8), as well as the olivine grain (grain 1). Interestingly, this olivine grain contained very little Fe; hence, in the area corresponding to the location of grain 1, the signal at mass 58 in the secondary ion images from both the Spectral and Compromise modes can be attributed almost entirely to  $^{58}\text{Ni}$ .

#### *3.4.4 Isotope Ratios*

An alternative way to verify that the mineral grains contain Ni is to examine the isotope ratios of Fe and Ni. The ratio of the natural abundance of  $^{58}\text{Fe}$  to that of  $^{56}\text{Fe}$  is 0.31 %. This was compared with the ratio of the secondary ion signal intensity obtained at mass 58,  $^{58}\text{Tot}$ , to that for  $^{56}\text{Fe}$ , as shown in Table 3.5 for all of the areas analyzed using the Spectral mode. All of the  $^{58}\text{Tot}/^{56}\text{Fe}$  ratios were higher than 0.31 %, indicating that there was at least some contribution from  $^{58}\text{Ni}$  to the overall signal. The proportion of the signal at mass 58 due to  $^{58}\text{Ni}$  was calculated from the signal intensities obtained for  $^{60}\text{Ni}$ ,  $^{58}\text{Tot}$ , and the ratio of the natural isotopic abundances for Ni ( $^{60}\text{Ni}/^{58}\text{Ni} = 0.385$ ), as shown in the equation below.

$$\%^{58}\text{Ni} = \frac{^{60}\text{Ni}}{0.385 \times ^{58}\text{Tot}} \times 100\% \quad (3.3)$$

The results, shown in Table 3.5, indicate that  $^{58}\text{Ni}$  comprised between 19 % and 54 % of the total signal at mass 58. The sample area having the highest contribution of Ni to the total signal at mass 58 was area 63E2, which contained the Fe-poor olivine grain.

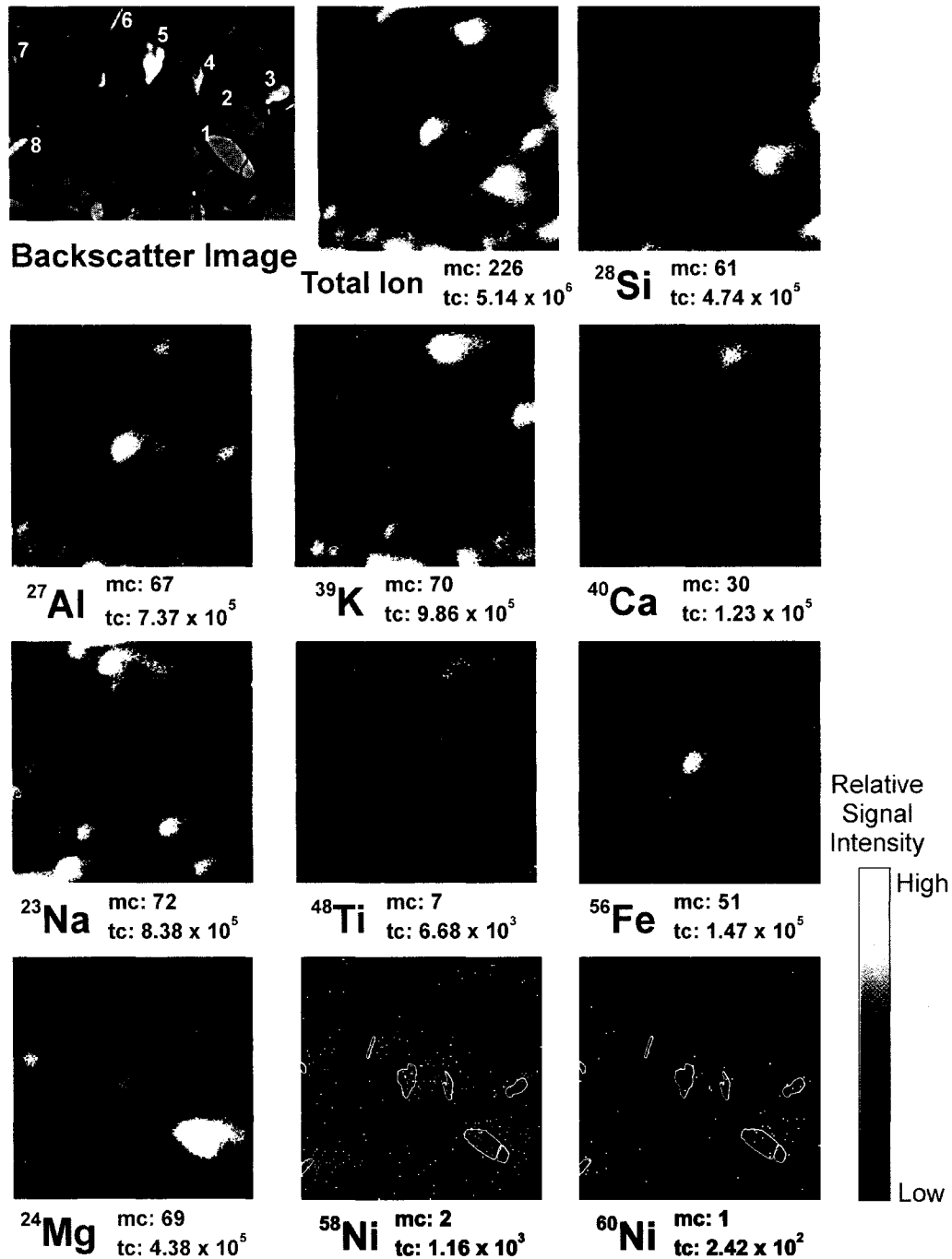


Figure 3.29 Secondary ion images for sample area 63E2 ( $123 \times 123 \mu\text{m}^2$ ). Spectral mode, positive ions, 73 scans,  $128 \times 128$  pixels. mc = max. number of counts, tc = total number of counts. Mineral grains in BSE image ( $\times 856$ ): 1 - olivine, 2 - quartz, 3 - chlorite, 4 - chlorite, 5 - chlorite, 6 - chlorite, 7 - biotite, 8 - chlorite. Outlines of Mg-bearing minerals (biotite, chlorite and olivine) from the BSE image are overlain in yellow on images for  $^{58}\text{Ni}$  and  $^{60}\text{Ni}$ .

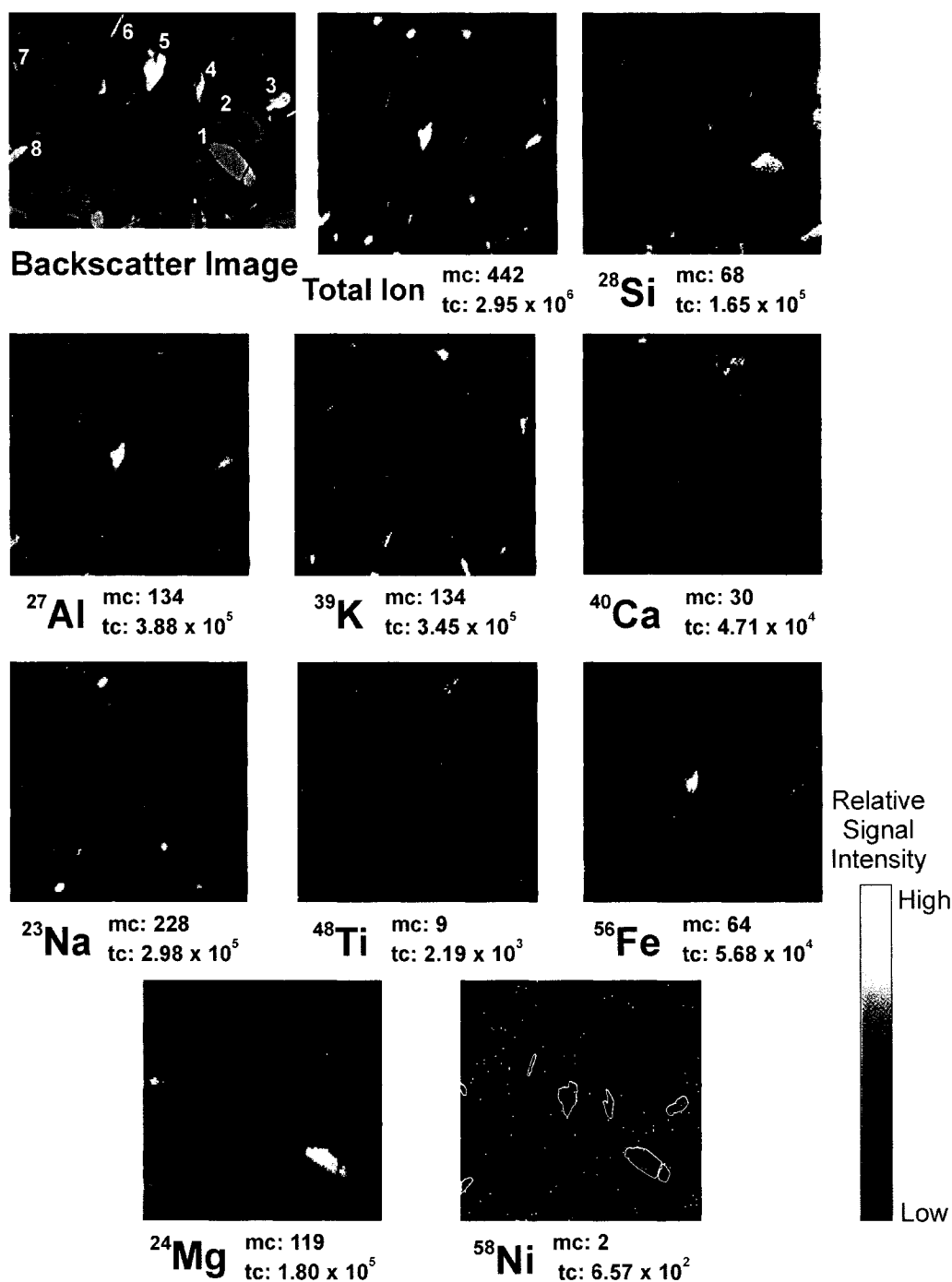


Figure 3.30 Secondary ion images for sample area 63E2 ( $123 \times 123 \mu\text{m}^2$ ). Compromise mode, positive ions, 570 scans,  $256 \times 256$  pixels. mc = max. number of counts, tc = total number of counts. Mineral grains in BSE image ( $\times 856$ ): 1 - olivine, 2 - quartz, 3 - chlorite, 4 - chlorite, 5 - chlorite, 6 - chlorite, 7 - biotite, 8 - chlorite. Outlines of Mg-bearing minerals (biotite, chlorite, olivine) from the BSE image are overlain in yellow on the image for  $^{58}\text{Ni}$ .

Table 3.5 Isotope ratios and proportion of  $^{58}\text{Ni}$  out of  $^{58}\text{Tot}$  for all analysis areas (Spectral mode).  $^{58}\text{Fe}/^{56}\text{Fe} = 0.31\%$

Sample area	$^{58}\text{Tot}/^{56}\text{Fe}$ (%)	$^{58}\text{Ni}$ (%)
63B	0.37	19
63C1	0.71	29
63C2	0.40	31
63E2	0.79	54

### 3.4.5 Additional Merits of ToF-SIMS

#### *Surface Sensitivity*

The surface sensitivity of ToF-SIMS, as compared to SEM, is demonstrated in Figures 3.31 a) and 3.32 a), which show secondary electron images of sample area 63E1 (still coated with carbon) obtained using the ToF-SIMS and SEM instruments, respectively. The ultrathin carbon condensate layer is seen coating the mineral grains in the ToF-SIMS image (Figure 3.31 a)), but is not visible in the SEM image (Figure 3.32 a)). This is primarily a result of the difference in secondary electron escape depths between the two techniques. The incident SEM electron beam interacts directly with the target atoms, typically imparting 3 – 5 eV to the ejected secondary electrons, which allows them to escape the sample surface from depths as great as tens of nanometers (electrons produced from deeper in the sample are absorbed) [20,21]. In contrast, the primary ion beam in ToF-SIMS indirectly induces secondary electron emission by transferring its energy to the surface atoms in a collision cascade, where successions of recoiling atoms progressively lose energy as they propagate towards the surface. Hence, the secondary electrons produced by ionization of higher order recoil atoms have relatively low energies, and can only escape from depths of a few monolayers (i.e.  $\sim 0.2 - 0.5$  nm) [5,6]. The secondary electron image of the same area taken by the ToF-SIMS secondary electron detector following 30 minutes of oxygen ion sputtering, shown in Figure 3.31 b), illustrates the effectiveness of the sputter pre-cleaning step for removing the carbon coating. The BSE image of area 63E1 (still coated with carbon) in Figure 3.32 b) demonstrates an even lower sensitivity to the surface topography, as few backscattered electrons are produced from the specimen surface because of their high energies and wide escape angles [20,21]. Typical escape depths for backscatter electrons are on the order of a few  $\mu\text{m}$  – similar to that for x-rays in EDS [20].

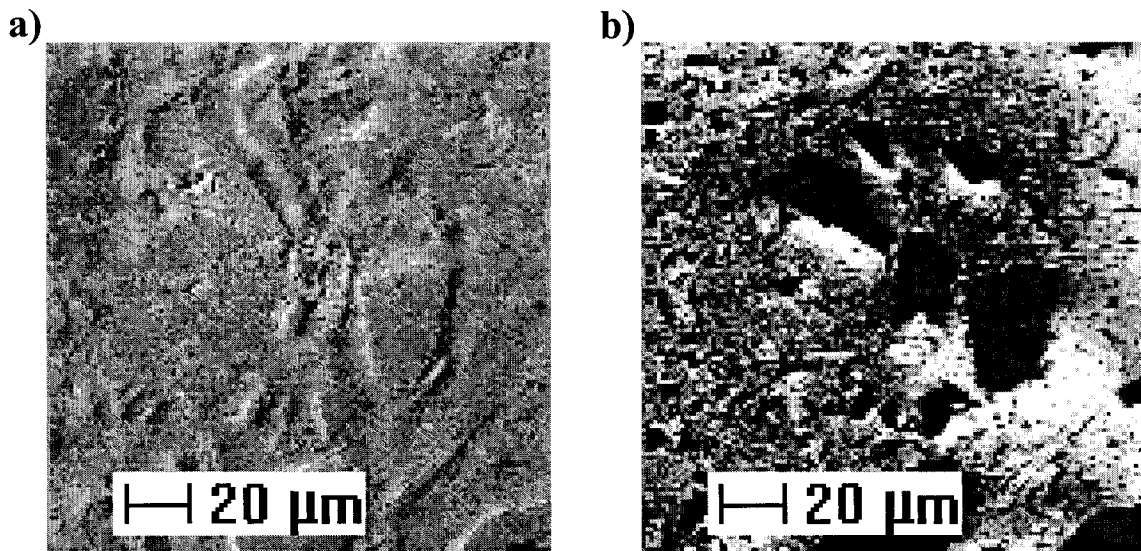


Figure 3.31 Secondary electron images of sample area 63E1 obtained using the ToF-SIMS secondary electron detector: a) carbon-coated prior to oxygen sputtering, b) carbon coating removed after 30 min. of oxygen sputtering.

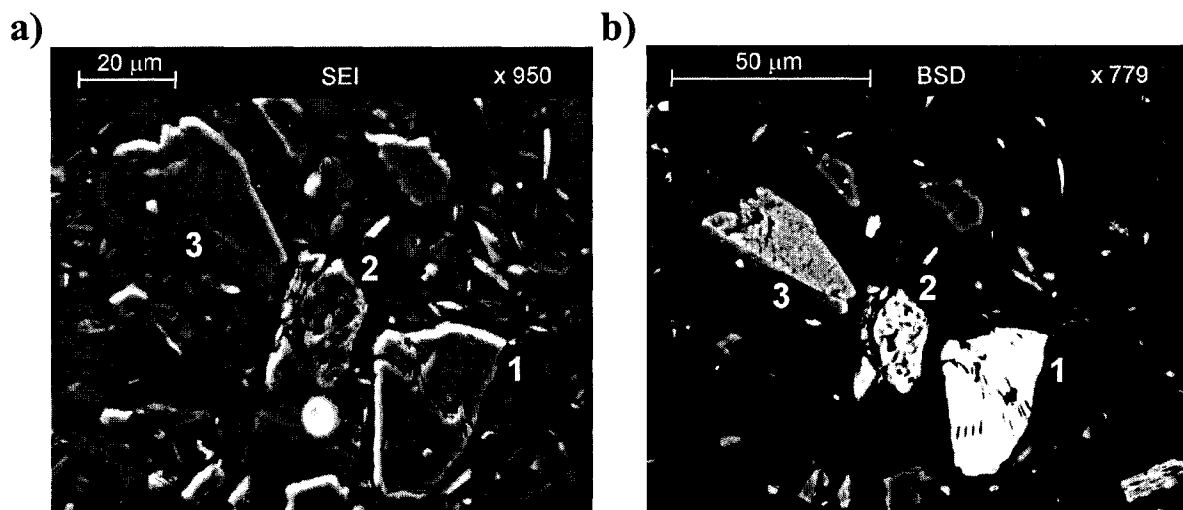


Figure 3.32 SEM images of sample area 63E1 (carbon-coated): a) secondary electron image ( $\times 950$ ), b) backscatter electron image ( $\times 779$ ). Mineral grains: 1 - apatite, 2 - chlorite, 3 - mica. Cambridge SEM.

### *Low Detection Limits and Detection of Anions*

Grain 1 in sample area 63E1 was classified as 'unidentified' in the mineral map (Figure 3.26), because out of the seven elements mapped by EDS, this grain only produced a signal for Ca. However, subsequent investigation by x-ray spot analysis identified grain 1 as the mineral apatite,  $\text{Ca}_5(\text{PO}_4)_3(\text{OH},\text{F},\text{Cl})$ . The anions  $\text{F}^-$ ,  $\text{Cl}^-$  and  $\text{OH}^-$  are usually all present in every specimen of apatite, as they can freely substitute for one another in the crystal lattice, although one usually predominates. In the EDS spectrum for grain 1, shown in Figure 3.33, only Ca, P and O were detected. However, because of the lower detection limits of ToF-SIMS, the negative secondary ion images for area 63E1, presented in Figure 3.34, exhibited significant signal intensities ( $10^5 - 10^6$  counts) for all three anion species ( $\text{F}^-$ ,  $\text{Cl}^-$ ,  $\text{OH}^-$ ). Although phosphorous was observed in the positive ion spectrum, it had a much greater signal intensity in the negative ion spectrum as a result of its relatively high electron affinity. In addition to  $\text{OH}^-$ , other polyatomic anions detected included  $\text{PO}_2^-$ ,  $\text{PO}_3^-$  and  $\text{SiO}_2^-$ . This example demonstrates the ability of ToF-SIMS to detect negative ions, including molecular species, at elemental concentrations below the detection limits of EDS.

### **3.5 Conclusions**

The spatial correlations observed between  $^{60}\text{Ni}$  and the location of several Mg-bearing phyllosilicate grains (i.e. chlorite and biotite) in the secondary ion images indicate that these minerals do contain Ni. However, ToF-SIMS can not be used to quantify elemental abundances in the minerals because of insufficient knowledge of sputter volumes, absolute ion yields and detection efficiencies [6]. In addition, because of the relatively high cost of ToF-SIMS instrument time, too few grains were analyzed to be able to demonstrate a statistical relationship. Hence, a mass balance calculation to determine the relative importance of these Mg-bearing minerals for hosting Ni in the soil

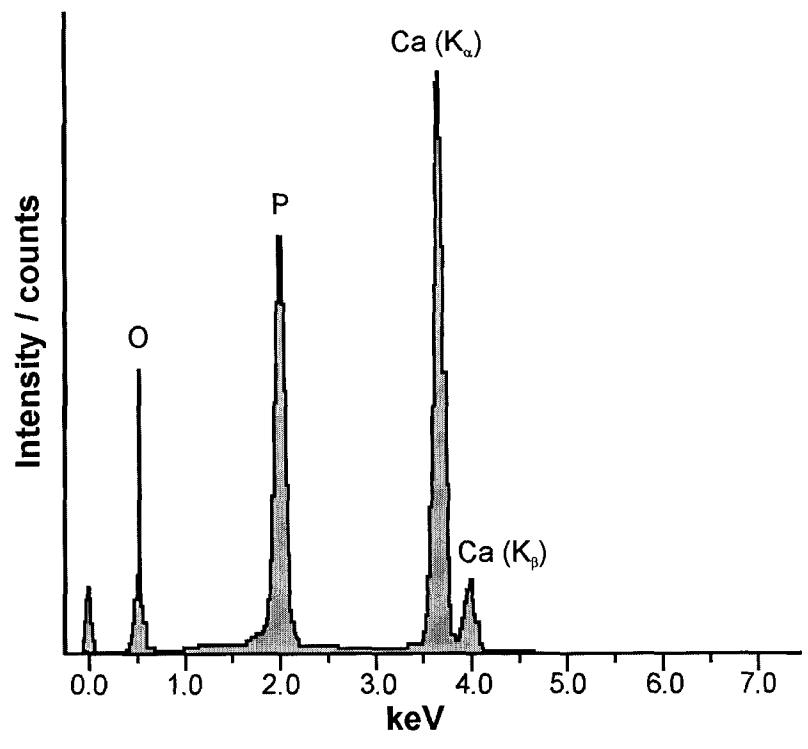


Figure 3.33 EDS spectrum for grain 1 (apatite) from sample area 63E1. Cambridge SEM with Oxford Link EDS.

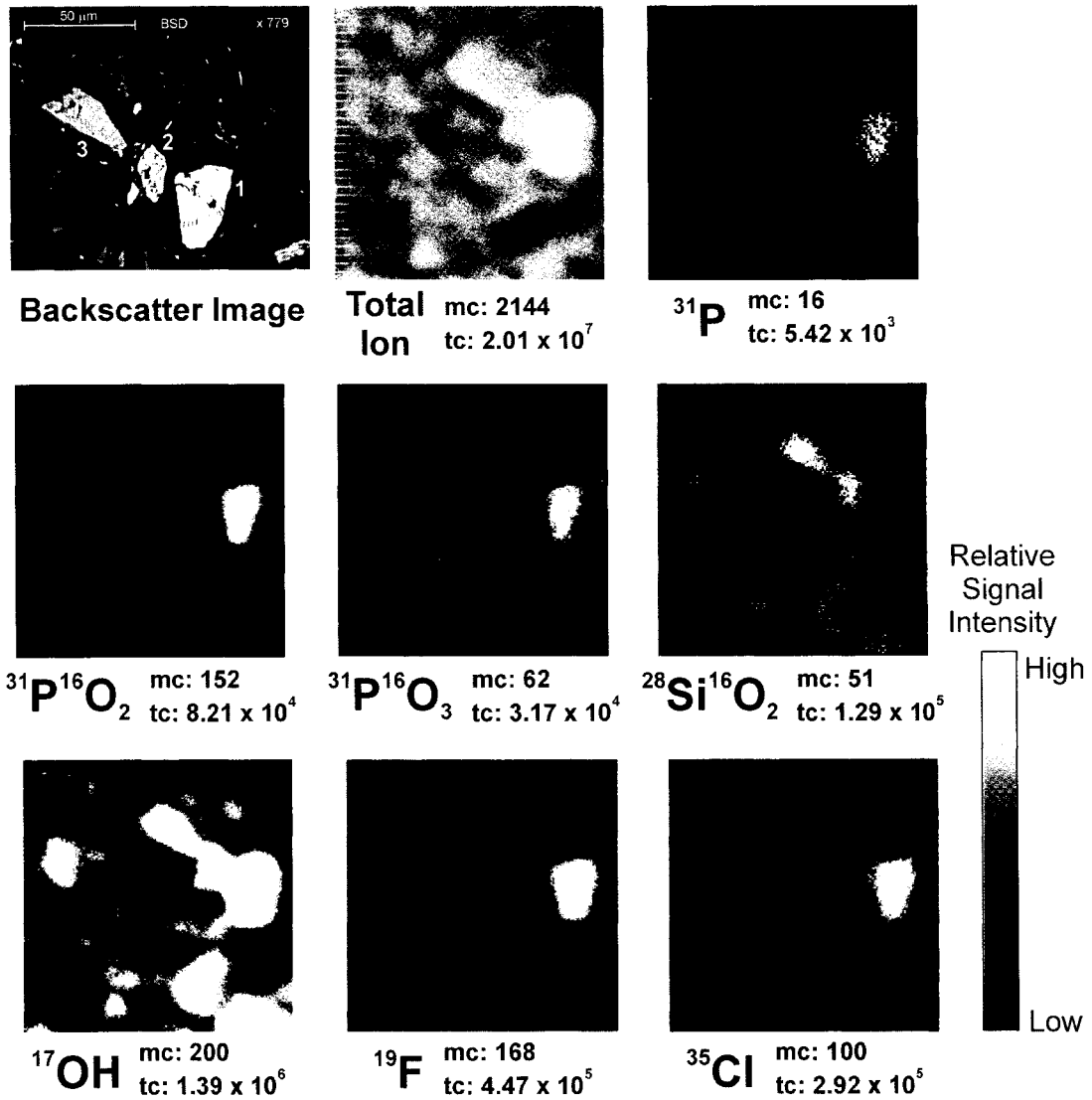


Figure 3.34 Secondary ion images for sample area 63E1 ( $178 \times 178 \mu\text{m}^2$ ). Spectral mode, negative ions, 500 scans,  $128 \times 128$  pixels. mc = max. number of counts, tc = total number of counts. Mineral grains in BSE image ( $\times 779$ ): 1 - apatite, 2 - chlorite, 3 - mica.

from the Thetford Mines area is not feasible. Although the ToF-SIMS results do not provide conclusive evidence as to the predominant mineral host for Ni in this soil, they do lend support to the hypothesis that Mg-bearing phyllosilicates, including chlorite and biotite, probably represent a significant control on Ni concentrations. The EDS spectra of these mineral grains indicated a significant degree of chemical variation. These observations are not surprising, as the soil environment is a dynamic system in which minerals are constantly being weathered and altered as part of soil formation processes. The linear correlations observed between Ni and Mg concentrations as determined by the acid digestion analyses (Figure 2.4), could reflect release of Ni and Mg from related phyllosilicate minerals in various stages of alteration or intermixing, as they would still have very similar chemical compositions.

The presence of Ni in the olivine and sulfide grains is not surprising, as olivine is known to be enriched in Ni in the ultrabasic bedrock from which the soil parent materials were derived [34] and Ni is commonly found in sulphide ores [4]. However, in the context of the existing body of empirical evidence it is doubtful that these minerals represent the predominant mineral hosts for Ni in the soil. Olivine is unlikely to be responsible for the linear correlations observed between Ni and Mg in the acid digestion experiments, as it is not reported to be digested by aqua regia. In addition, XRD analyses of the clay-sized fraction of the soil from the two profiles found olivine and sulfide minerals to be either absent or only present in trace amounts.

This work has demonstrated the utility of ToF-SIMS in combination with SEM-EDS for trace metal analysis in individual soil mineral grains. This combination of techniques constitutes a powerful tool, which can provide information that can not be obtained from conventional bulk analytical techniques. The results presented also demonstrate the advantages and disadvantages of the Spectral and Compromise modes of operation, as well as the benefits of using them in conjunction with one another to aid in interpretation of results. Although trace analysis of transition metals can be difficult

because of their relatively high ionization potentials, which hinders production of positive secondary ions, ToF-SIMS has significant potential for trace analysis of highly electropositive elements (e.g. alkali metals) and electronegative elements (e.g. halides). Even when present in trace concentrations, these elements can produce relatively high secondary ion yields, as was demonstrated by the pronounced Li signal observed in the positive ion spectrum for sample area 63B, as well as the high signal intensities for Cl<sup>-</sup> and F<sup>-</sup> in the negative secondary ion images for the apatite grain from sample area 63E1.

The combination of the SEM-EDS maps and the ToF-SIMS images also facilitates further analysis of the samples by providing prior information as to the location and identity of the mineral grains that contain Ni. Because these techniques are essentially non-destructive, the mineral grains of interest can be re-analyzed using other complementary techniques, such as cathodoluminescence or microbeam Extended X-ray Absorption Fine Structure (EXAFS) and X-ray Absorption Near-Edge Structure (XANES), which can provide additional information about the bonding environment of the Ni within the host mineral.

### 3.6 References

---

1. W. Jambers, L. De Bock, R. Van Grieken, *Analyst*, 1995, **120**, 681.
2. M. Grasserbauer, G. Friedbacher, H. Hutter, G. Stingeder, *Fresenius J. Anal. Chem.*, 1993, **346**, 594.
3. W. Shotyk, J.B. Metson, *Rev. Geophys.*, 1994, **32**, 197.
4. R.N.S. Sodhi, *Analyst*, 2004, **129**, 483.
5. J.C. Vickerman, ToF-SIMS – An Overview, in *ToF-SIMS: Surface Analysis by Mass Spectrometry*, J.C. Vickerman, D. Briggs (Eds.), IM Publications and Surface Spectra Limited, Chichester, UK, 2001, Chapter 1.
6. T. Stephan, *Planet. Space Sci.*, 2001, **49**, 859.

- 
7. M.F. Roden, N. Shimizu, *Chem. Geol.*, 2000, **165**, 283.
  8. S. Klemme, C. Dalpe, *Am. Mineral.*, 2003, **88**, 639.
  9. N.M. Lindsay, J.P.F. Sellschop, *Nucl. Instrum. Methods*, 1988, **B35**, 358.
  10. J.A. Coston, C.C. Fuller, J.A. Davis, *Geochim. Cosmochim. Acta*, 1995, **59**, 3535.
  11. S.L.S. Stipp, M. Hansen, R. Kristensen, M.F. Hochella, L. Bennedsen, K. Dideriksen, T. Balic-Zunic, D. Leonard, H.J. Mathieu, *Chem. Geol.*, 2002, **190**, 321.
  12. J. Goschnick, M. Fichtner, M. Lipp, J. Schuricht, H.J. Ache, *Appl. Surf. Sci.*, 1993, **70/71**, 63.
  13. B.J. Tyler, ToF-SIMS Image Analysis, in *ToF-SIMS: Surface Analysis by Mass Spectrometry*, J.C. Vickerman, D. Briggs (Eds.), IM Publications and Surface Spectra Limited, Chichester, UK, 2001, Chapter 17.
  14. S.D. Boehmig, B.M. Reichl, H. Stoeri, H. Hutter, *Fresenius J. Anal. Chem.*, 1994, **349**, 197.
  15. B. Pignataro, S. Panebianco, C. Consalvo, A. Licciardello, *Surf. Interface Anal.*, 1999, **27**, 396.
  16. M.L. Wagter, A.H. Clarke, K.F. Taylor, P.A.W. van der Heide, N.S. McIntyre, *Surf. Interface Anal.*, 1997, **25**, 788.
  17. A.H. Clarke, N.S. McIntyre, *Surf. Interface Anal.*, 1997, **25**, 948.
  18. G.S. Groenewold, J.C. Ingram, T. M. Ling, A.K. Gianotto, *Anal. Chem.*, 1998, **70**, 534.
  19. D.H. Krinsley, K. Pye, S. Boggs, N.K. Tovey, in *Backscattered Scanning Electron Microscopy and Image Analysis of Sediments and Sedimentary Rocks*, Cambridge University Press, Cambridge, UK, 1998, Chapter 9.
  20. S.L. Flegler, J.W. Heckman, K.L. Klomparens, *Scanning and Transmission Electron Microscopy: An Introduction*, Oxford University Press, New York, USA, 1993, Chapter 8.

- 
21. J.I. Goldstein, D.E. Newbury, P. Echlin, D.C. Joy, A.D. Romig, C.E. Lyman, C. Fiori, E. Lifshin, *Scanning Electron Microscopy and X-Ray Microanalysis*, Plenum Press, New York, USA, 1992, Chapter 3.
  22. R. Hill, Primary Ion Beam Systems, in *ToF-SIMS: Surface Analysis by Mass Spectrometry*, J.C. Vickerman, D. Briggs (Eds.), IM Publications and Surface Spectra Limited, Chichester, UK, 2001, Chapter 4.
  23. M.L. Yu, Nucl. Instrum. Methods Phys. Res., Sect. B, 1986, 15, 151.
  24. H.A. Storms, K.F. Brown, J.D. Stein, *Anal. Chem.*, 1977, **49**, 2023.
  25. C.A. Andersen, *Int. J. Mass Spectrom. Ion Processes*, 1970, **3**, 413.
  26. R.D. Knight, R.A. Klassen, P. Hunt, *Environ. Geol.*, 2002, **42**, 32.
  27. W.A. Deer, R.A. Howie, J. Zussman, *An Introduction to the Rock-Forming Minerals*, 2<sup>nd</sup> Ed., Longman Scientific and Technical, Essex, UK, 1992, pp 335, 289, 381.
  28. K.G. Stowe, S.L. Chryssoulis, J.Y. Kim, *Miner. Eng.*, 1995, **8**, 421.
  29. N.C. Brady, R.R. Weil, *The Nature and Properties of Soils*, 13<sup>th</sup> Ed., Prentice Hall, New Jersey, USA, 2002, Chapter 8.
  30. W.W. Shilts, *Detailed Sedimentological Study of Till Sheets in a Stratigraphic Section, Samson River, Quebec*: Bulletin 285, Geological Survey of Canada, 1978.

## **Chapter 4      Kinetic Fractionation of Nickel and Copper**

#### **4.1 Introduction**

Single and sequential extraction schemes have been proposed for determining trace metal speciation in soils [1-5]; however, these approaches are based on measurements made under equilibrium conditions, which are of limited application, as most subsurface systems are dynamic and far removed from equilibrium. Kinetic studies may more correctly reflect the distribution and behaviour of trace metals in the soil environment, as they provide information about the lability of trace metal species [6-11]. If the time required to extract the metal into the soil solution is slower than the time required for plant uptake, the extraction step is likely the rate-determining step for its bioavailability [12]. Hence, the kinetic aspects of trace metal speciation in soils can play a crucial role in determining the metal's beneficial or adverse environmental impacts.

Various experimental approaches that have been used for investigating kinetic processes in soils include batch techniques [7-9,11-14], flow techniques [15-17], as well as *in situ* sampling techniques such as Diffusive Gradients in Thin Films (DGT) [18,19]. Some of the first studies on kinetic reactions in soils involved determination of the dynamics of potassium release from biotite and vermiculite [20,21]. Over the years, similar studies on the kinetic speciation of trace metals have been performed on model soil compounds, such as biotite [20,21], goethite [8], and hydrous ferric oxides [13], as well as on contaminated sediments [6] and soils [7,11,14]. Trace metals in contaminated and metal-amended soils exist primarily in readily available chemical forms (e.g. sorbed/exchangeable). However, the kinetic speciation of trace metals in naturally enriched, unpolluted soils is an area of soil chemistry not yet explored in great detail.

The goal of this work was to investigate the kinetics of Ni and Cu extraction from the naturally metal-rich soil of the Thetford Mines area as a function of depth. Field observations of the soil profiles found a lack of evidence for primary variations in parent material composition and mixing, which allows downward changes in relative trace metal

concentrations and labilities to be most readily attributed to the differential effects of soil formation and weathering processes with depth [22]. In glacial soils, these processes are largely confined to the uppermost 50 cm; hence, within a meter of the surface, the maximum range of soil transformations can be observed [23].

#### 4.1.1 *Weathering and Soil Formation Processes*

Weathering and soil forming processes play a key role in controlling the distribution and behaviour of trace elements in the soil environment. These processes occur simultaneously to mobilize, transform, redistribute, accumulate and remove elements within the profile.

##### *Weathering Processes*

Soil weathering involves the physical and chemical breakdown of minerals that are unstable under surface conditions [24,25]. The predominant chemical weathering mechanism for silicates and aluminosilicates is hydrolysis. This process involves the replacement of structural cations with  $H^+$  from the soil solution, which gradually dissolves the crystal lattice [26]. Chelating agents produced by soil biological processes (e.g. root exudates, such as tartaric and citric acid) can also extract structural cations from minerals into the soil solution [27]. Redox reactions are the predominant weathering processes for Fe-, Mn- and S-containing minerals in which a change in size and oxidation state of these elements disrupts the lattice arrangement and electrical neutrality of the mineral, resulting in destabilization of the crystal structure [24,28].

Chemical weathering is controlled by *capacity factors* and *intensity factors* [24]. *Capacity factors* involve the characteristics of the weathering mineral grain itself. For example, the degree of alteration of a soil mineral strongly depends on its reactive surface area and its inherent stability. Smaller grain sizes have relatively high surface areas, and are therefore more susceptible to chemical weathering. A mineral's inherent resistance to weathering depends primarily on the strength of the bonds in its crystal lattice. In general,

Si-O bonds tend to be stronger than Al-O bonds, which in turn are stronger than metal-O bonds [29,30]. Hence, parent material mineralogy is a fundamental factor underlying the development of a soil, as the susceptibility of the various minerals to weathering processes ultimately determines the identity, form and rate of release of elements into the soil solution [31]. *Intensity factors* consist of the parameters that determine the magnitude of weathering reactions, some of the most obvious of which are the characteristics of the soil solution, such as temperature, pH and redox potential [29]. Moisture flux is one of the most important intensity factors, as it controls the extent of leaching, which in turn plays a key role in determining the course of mineral alteration and/or dissolution [29,32]. The nature and abundance of natural organic matter, including simple biomolecules and complex humic substances play a significant role in mineral weathering. Organic acids (e.g. acetic, tartaric, citric, and amino acids) can attack and dissolve minerals, as well as form soluble complexes with released metal ions [27,33]. Metal ions can also be held in insoluble organic complexes that are non-leachable and relatively unavailable to plants [25,27]. Biological activity influences chemical weathering by facilitating ion uptake cycles and production of complexing organic residues. In addition, both micro-organisms and higher plants exchange  $H^+$  and other cations with charge sites on the surfaces of soil minerals [24].

#### *Soil Formation Processes*

The four fundamental soil forming, or pedogenic, processes which drive soil-profile development are *transformations*, *translocations*, *additions* and *losses* [28]. *Transformations* involve the chemical and physical alteration or destruction of soil minerals, as well as synthesis of secondary phases by recombination of decomposition products (e.g. Al, Fe and Mn oxides and hydroxides) [28]. As elements are removed from their host minerals during weathering, the residual minerals are progressively altered to new, more stable mineral phases. Several alteration pathways for clay minerals that commonly take place in soils are outlined in Figure 4.1 [29]. Leaching and replacement

of interlayer cations can lead to the formation of various mixed-layer clay minerals (e.g. illite-vermiculite or chlorite-vermiculite) [28]. Other important transformations involve the decomposition of organic matter and the synthesis of organic acids and humus. *Translocations* occur when soil materials, such as dispersed clay particles, ions and dissolved organic compounds are moved laterally or vertically through the soil profile by water (e.g. downward percolation and upward capillary action), as well as by mixing and disturbance by soil organisms (i.e. pedoturbation) [26,28,34]. *Additions* refer to the input of any material to the developing soil profile from outside sources, such as organic matter from plant leaves and roots, as well as airborne dust particles [27,28]. Anthropogenic additions, such as fertilizers, pesticides and waste products are also common in industrialized areas. *Losses* most often involve removal of water and dissolved substances from the soil profile by leaching to groundwater, by surface runoff, or by uptake by plant roots and other soil organisms. Erosion leads to loss of surface materials, and organic matter can be lost by microbial decomposition [28,29,32,34].

#### 4.1.2 Ethylenediaminetetraacetic Acid (EDTA)

EDTA is a well-known complexing reagent that is used extensively for industrial and agricultural applications [35]. It is also very commonly used in soil science research to directly remove and recuperate trace metals from contaminated and metal-amended soils, often as part of a multi-step sequential extraction procedure [11,35-40]. EDTA is reported to be able to extract metals from a variety of soil components, including carbonates, oxides, sulphides, and organic phases [41,42]. Because it is a non-specific complexing agent, extracted trace metals cannot be localized *a priori* within a particular soil component, as the concentration of metal extracted is not necessarily related to classical soil species [6-9,12,14].

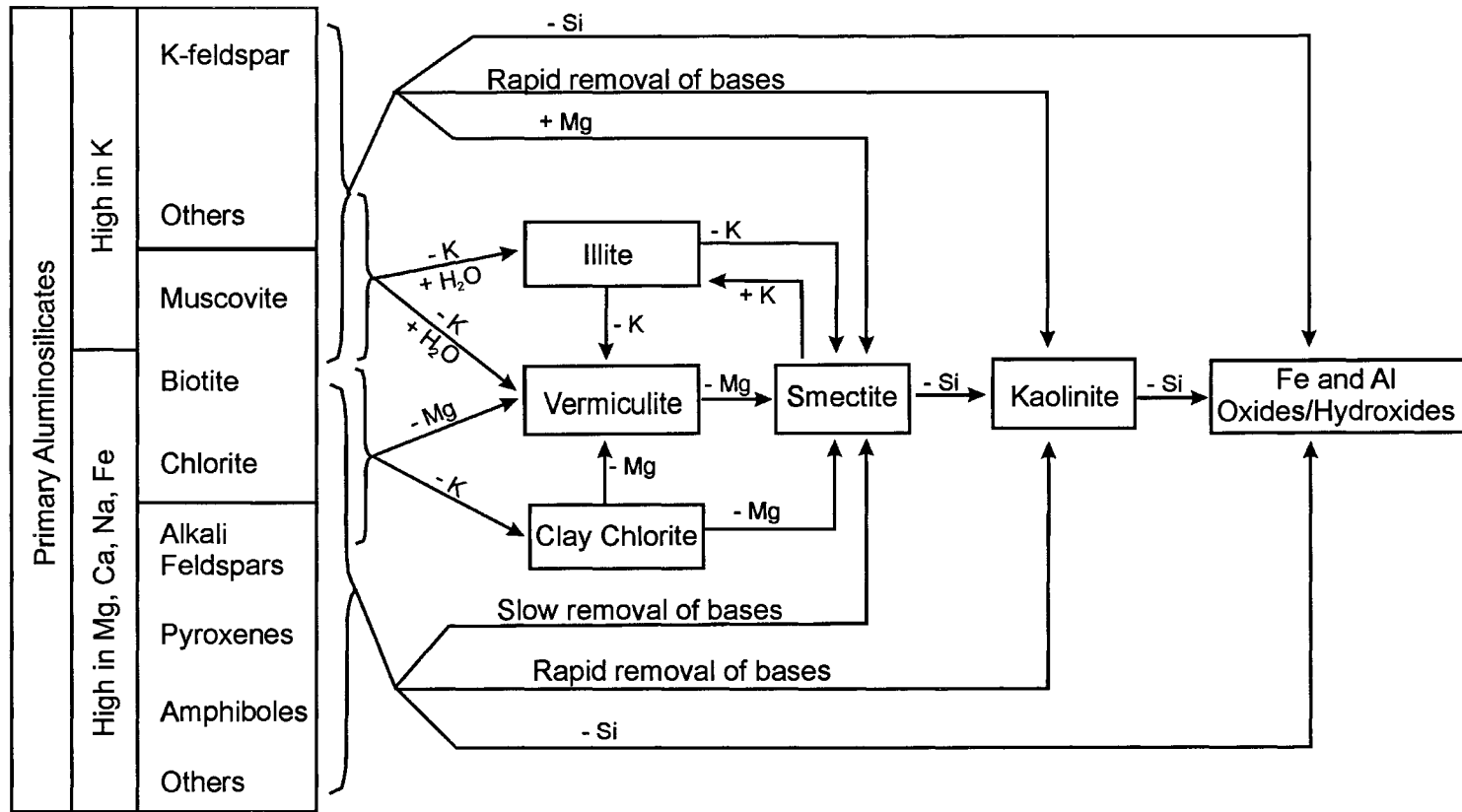


Figure 4.1 A generalized scheme for mineral weathering and formation pathways (adapted from Karathanasis [29]).

EDTA is a hexaprotic acid, having the formula  $H_6Y^{2+}$ . The structure of EDTA is shown in Figure 4.2 for the neutral tetraprotic species ( $H_4Y$ ). The deprotonation of EDTA with increasing pH gives rise to six  $pK_a$  values ( $pK_{a,1} = 0.0$ ,  $pK_{a,2} = 1.5$ ,  $pK_{a,3} = 2.0$ ,  $pK_{a,4} = 2.66$ ,  $pK_{a,5} = 6.16$ ,  $pK_{a,6} = 10.24$ ), the first four of which correspond to the carboxyl protons, and the last two to the ammonium protons. The speciation diagram for EDTA as a function of pH is shown in Figure 4.3. When completely deprotonated to  $Y^{4-}$ , EDTA acts as a hexadentate chelating agent for metal ions, binding through four oxygen and two nitrogen atoms, as shown in Figure 4.4 [43]. The conditional formation constants for the complexation of  $Ni^{2+}$  and  $Cu^{2+}$  by  $Y^{4-}$  are given in Table 4.1, and can be calculated using the equations below.



$$K_f' = \alpha_{Y^{4-}} K_f = \frac{[MY^{2-}]}{[M^{2+}][EDTA]} \quad (4.2)$$

where  $[EDTA]$  is the total concentration of all EDTA species not bound to the metal ion, and  $\alpha_{Y^{4-}}$  is the fraction of EDTA in the form  $Y^{4-}$  [43].

$$\alpha_{Y^{4-}} = \frac{[Y^{4-}]}{[EDTA]} \quad (4.3)$$

EDTA was chosen as the extracting reagent, as it is a well-characterized, strong chelating agent that allows for good control of experimental variables. Most metal-EDTA chelate complexes are formed rapidly and are extremely stable [44]. As a weak hexaprotic acid, EDTA acts as a natural buffer at six different pH values. Furthermore, at pH values greater than 6, the predominant EDTA species (i.e.  $H_2Y^{2-}$ ,  $HY^{3-}$  and  $Y^{4-}$ ) form neutral and negatively charged metal complexes with divalent ions, helping to keep extracted metals in solution by minimizing adsorption of the metal-EDTA complexes to negatively charged exchange sites on the soil particles. As a result of the similar formation constants of EDTA with  $Cu^{2+}$  and  $Ni^{2+}$ , as shown in Table 4.1, any differences

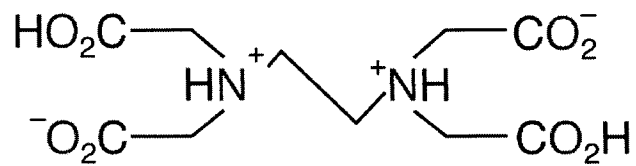


Figure 4.2 Structure of neutral EDTA molecule ( $\text{H}_4\text{Y}$ ) [43].

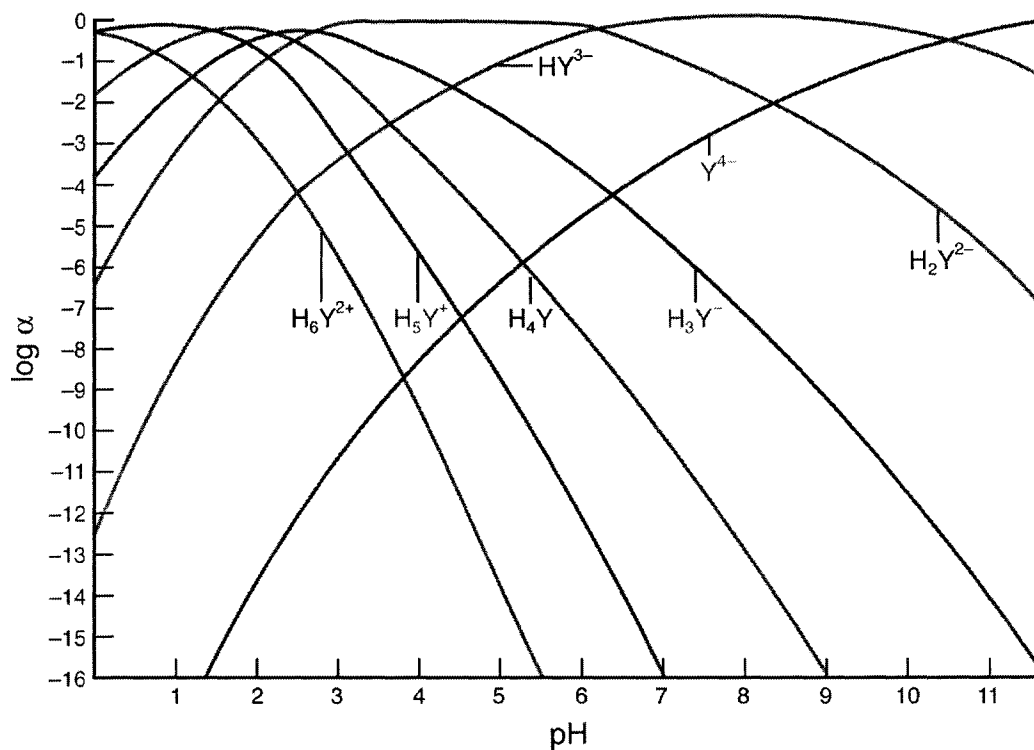


Figure 4.3 Speciation diagram for EDTA as a function of pH [43].

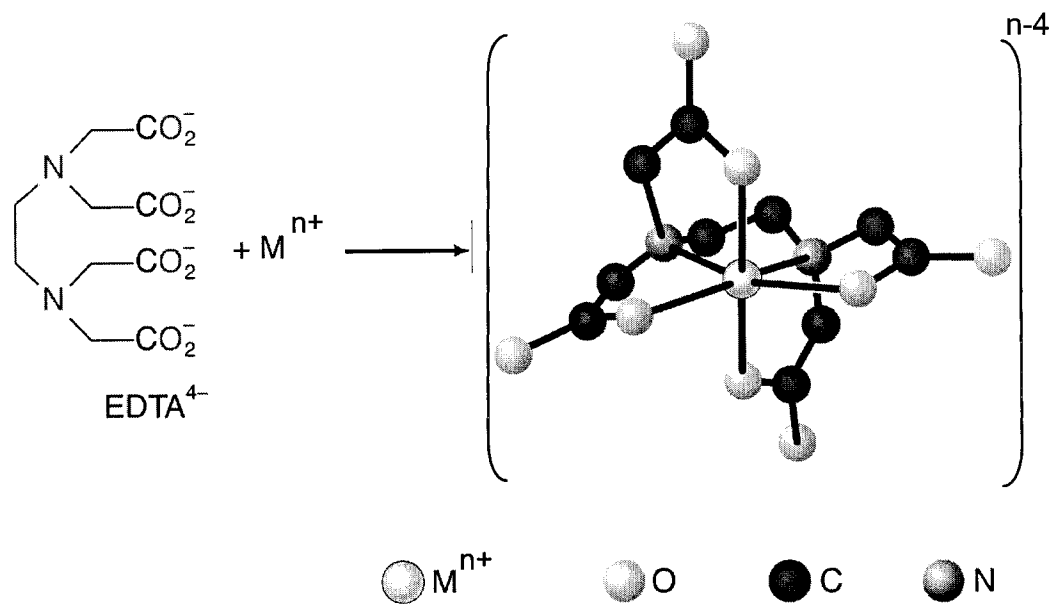


Figure 4.4 Structure of EDTA ( $Y^{4-}$ ) complex with a metal ion,  $M^{n+}$  [43].

Table 4.1 Formation constants for M-EDTA complexes (20°C,  $I = 0.1$  mol/L).  
 $\alpha_{Y^{4-}} = 2.3 \times 10^{-5}$  at pH 6, [EDTA] = 0.10 mol/L [45].

	$Ni^{2+}$	$Cu^{2+}$
$\log K_f$	18.62	18.80
$\log K_f'$	$4.28 \times 10^{-4}$	$4.32 \times 10^{-4}$

in the observed behaviour of the two metals is more likely to reflect differences in affinity of the metals for the soil phase with which they are associated, rather than differences in affinity for the EDTA molecule [35]. An additional advantage of using EDTA is that it has been reported to predict the plant-available trace metal fraction [42,46,47].

#### 4.2 Kinetic Fractionation Theory

The methodological approach employed in this study is more appropriately termed ‘kinetic fractionation’ as opposed to ‘kinetic speciation,’ in accordance with the recent IUPAC recommendation to distinguish ‘speciation’, which involves determination of individual compounds, from ‘fractionation’, which involves determination of species that are operationally defined by a specific experimental protocol [48].

The extraction of a metal ion, M, from the  $i^{\text{th}}$  soil binding site, Soil<sub>*i*</sub>, using EDTA is represented by the following reaction (charges are omitted for simplicity) [11]:



where M-Soil<sub>*i*</sub> and M-EDTA represent a metal ion bound to Soil<sub>*i*</sub>, and EDTA, respectively, and  $k_i$  is the rate constant of the reaction. If EDTA is added in large excess over the metal, the change in concentration of M-Soil<sub>*i*</sub>, designated  $C_i$ , with time is given by the following pseudo first-order rate law.

$$-\frac{dC_i}{dt} = k_i C_i \quad (4.5)$$

The integrated rate law for this reaction, given in equation 4.6, shows that the concentration of metal extracted by EDTA at time  $t$ ,  $C(t)$ , rises exponentially over time to a limiting value. Unfortunately, there is no way to *a priori* know the number of discrete soil binding sites or to study them individually [13]. Hence, equation 4.6 is written as a summation of exponentials,

$$C(t) = \sum_i C_i^0 (1 - e^{-k_i t}) \quad (4.6)$$

where  $C_i^0$  represents the total concentration of metal initially bound to the  $i^{\text{th}}$  soil binding site.

The system described by equation 4.6 can be approximated by a two-component first-order reaction model [8,11],

$$C(t) = C_L(1 - e^{-k_L t}) + C_{SL}(1 - e^{-k_{SL} t}) \quad (4.7)$$

where  $C_L$  and  $C_{SL}$  are the concentrations of EDTA-extractable metal initially bound to labile (rapidly extracted) and slowly-labile (slowly extracted) soil binding sites, respectively, and  $k_L$  and  $k_{SL}$  are the corresponding rate constants. The use of two kinetic components (labile and slowly-labile) to describe similar systems is well reported in the literature [7-9,11,12,49].

### **4.3 Experimental**

#### **4.3.1 Reagents and Materials**

Ultrapure water of resistivity 18.2 M $\Omega$ cm was obtained direct from a Milli-Q-Plus water purification system (Millipore, USA), fitted with an organic purification column to remove organic matter. Standard solutions of 10  $\mu$ g/mL each of Ni(II) and Cu(II) were prepared by dilution of 1000  $\mu$ g/mL stock solutions (ICP grade, SCP Science) with ultrapure water, acidified to contain 1% (v/v) ultrapure nitric acid (Seastar). Various concentrations of ethylenediaminetetraacetic acid (EDTA) solutions were prepared prior to each experiment, by mixing an appropriate quantity of solid EDTA (free acid, 99.9 %, Aldrich) with ultrapure water, and adding approximately 4.5 mL of ultrapure ammonium hydroxide (Seastar) while stirring and heating until dissolved. The solution was then diluted to the appropriate volume with ultrapure water, and the pH adjusted using small volumes of ultrapure nitric acid and/or ultrapure ammonium hydroxide. Although much less soluble in water, the free acid form of EDTA was chosen over the disodium salt, in order to avoid problems with salt build-up during analysis by Graphite Furnace Atomic

Absorption Spectroscopy. Matrix matched calibration standards were prepared by diluting an appropriate amount of the 10 µg/mL Ni(II) and Cu(II) stock solutions with a portion of the same EDTA solution used for the kinetic experiments.

#### 4.3.2 *Soil Samples*

Air-dried silt- and clay-sized soil samples from six depths in profiles 63 and 64 were used for the kinetic experiments. The six samples selected from each profile were chosen to provide the greatest range in sampling depth as possible within the constraints of sample availability and quantity.

#### 4.3.3 *Apparatus*

All Ni and Cu concentrations were determined using a Perkin-Elmer 4100ZL Zeeman graphite furnace atomic absorption spectrometer (GFAAS) equipped with an AS-40 autosampler, an HGA-600 graphite furnace, and Zeeman background correction. The transversely heated graphite tubes (Perkin-Elmer) were pyrolytically-coated, and were equipped with integrated L'vov platforms. Tables 4.2 and 4.3 describe the instrumental parameters used in the graphite furnace atomic absorption spectrometric determination of Ni and Cu. For the determination of the metal concentrations, 20 µL of the solution were injected into the graphite furnace, where it was dried, ashed and atomized. The signal was measured in the peak area mode. Each completed determination was followed by a 2-s clean-up cycle of the graphite tube at 2400 °C. During the drying, ashing and clean-up cycles, the internal argon gas was passed through the furnace at 300 mL/min, but the gas flow was interrupted during the atomization step. A new graphite tube was used for each experiment in order to avoid excessive degradation of the tube and associated smoke production during the read step.

Table 4.2 Instrumental conditions for determination of Ni with the Perkin-Elmer 4100ZL GFAAS,  $\lambda = 232.0$  nm, slit width = 0.2 nm.

Step	Temperature (°C)	Time Ramp (s)	Time Hold (s)
Drying	110	1	20
	130	5	30
Ashing	1100	10	20
Atomization	2300	0	5
Clean-up	2400	1	2

Table 4.3 Instrumental conditions for determination of Cu with the Perkin-Elmer 4100ZL GFAAS,  $\lambda = 324.8$  nm, slit width = 0.7 nm.

Step	Temperature (°C)	Time Ramp (s)	Time Hold (s)
Drying	110	1	20
	130	5	30
Ashing	1100	10	20
Atomization	1900	0	5
Clean-up	2400	1	2

#### 4.3.4 Optimization Experiments

For the pH optimization experiments, 50.0 mL aliquots of 0.05 mol/L EDTA solution were prepared at five different pH values (pH 4.0, 5.0, 6.0, 7.0, 8.0). For EDTA concentration optimization experiments, 50.0 mL aliquots of EDTA solution were prepared at six different EDTA concentrations (0.001, 0.010, 0.025, 0.050, 0.075, 0.100 mol/L), and each sample was adjusted to pH 6.0 using ultrapure nitric acid and/or ultrapure ammonium hydroxide. 0.5000 g of soil (sample 63E, < 0.063 mm) were added to each of the EDTA solutions (mass/volume = 0.01) and the samples were shaken using a wrist-action shaker (Burrell, model no. 75) for 24 h at room temperature. The optimization experiments were performed on sample 63E, as this sample was available in the largest quantity. The sample suspensions were then allowed to settle for ½ h and 2.5 mL of each sample were filtered through 0.2 µm Supor (Polyethersulfone) syringe filters immediately prior to analysis. The remaining samples were decanted into separate containers and the final pH of each determined.

#### 4.3.5 Kinetic Experiments

The experimental set up for the kinetic extraction experiments is illustrated in Figure 4.5. Three grams of soil were added to 300 mL of 0.05 mol/L EDTA solution (pH 6.00 ± 0.02) in a 500 mL Teflon bottle, and the mixture was continually stirred with a Teflon-coated magnetic stirring bar throughout the experiment. The ratio of the mass of soil to the volume of EDTA solution (mass/volume) was set at 0.01, as this ratio provided sufficiently high metal concentrations in the extract to be accurately quantified, while requiring a minimum amount of soil, which was only available in limited quantities. A special effort was made to maintain a homogeneous suspension in order to avoid changing the mass/volume ratio during sampling. Larger mass/volume ratios would be undesirable, as they could cause problems with filtration. At set time intervals, 2 mL of the suspension were filtered through a 0.2 µm Supor syringe filter. Sample aliquots were

collected over a 32 h period. The initial time for the kinetic measurement (i.e.  $t = 0$ ) was taken as the time just before the soil was added to the EDTA solution. The filtrate samples were then analyzed by GFAAS to monitor the concentration of Ni in the extract solution as a function of time. A reagent blank and procedural blank were also collected and analyzed for each experiment. Each sample was analyzed four times to ensure that the absorbance readings were reproducible, and the kinetic experiments were performed in duplicate for most samples to ensure repeatability of results. To account for the instrument drift (e.g. because of degradation of the graphite tube), the sensitivity of the instrument was monitored throughout each experiment by analyzing a standard solution followed by a reagent blank after every 5<sup>th</sup> sample. If the sensitivity changed more than 10 % during an experiment, a correction factor was used to correct for the drift.

#### 4.3.6 Data Analysis

The total concentration of Ni and Cu in each sample was determined by external calibration. Because of the characteristic non-linearity of the Ni analytical calibration curve at high concentrations in AAS [50], a quadratic function was used to fit the data in the Ni calibration curves. The data from the kinetic curves were smoothed using power, logarithm or ligand binding functions. The data smoothing was required to obtain optimal visual and statistical fits of the kinetic function to the experimental data, and did not introduce any bias into the fitted data, as the smoothing functions used have no physical significance. The smoothed data were then fitted to the two-component first-order reaction model (equation 4.7) by non-linear regression analysis using the Marquardt-Levenberg algorithm [51]. The calculations were carried out using the computer software package SigmaPlot 9.0 (Systat Software, 2004).

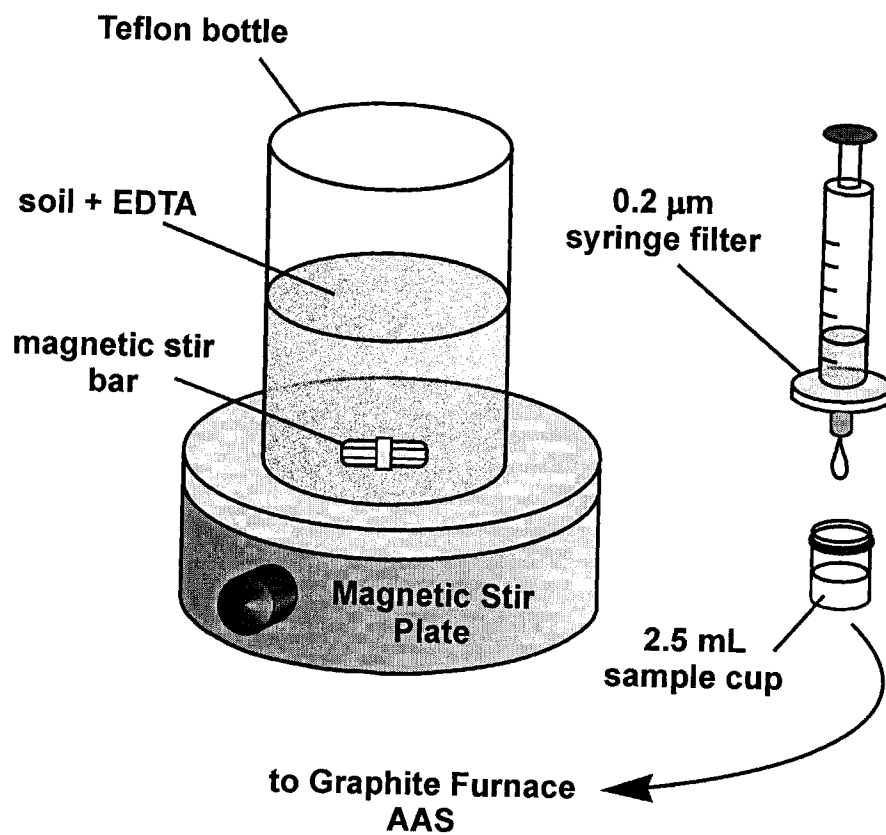


Figure 4.5 Experimental set-up for the kinetic experiments.

## 4.4 Results and Discussion

### 4.4.1 Optimization of Experimental Parameters

In order to identify the optimal experimental conditions, a systematic investigation was performed to determine the influence of pH and EDTA concentration on the efficiency of Ni and Cu extraction from the soil samples. These two parameters have been reported to be the most important factors to consider when performing metal extractions from soils using EDTA [6,7,11,14,35].

#### *Optimization of pH*

The pH dependence of metal extraction by EDTA is due to the competitive extraction by  $H^+$  [6,7,14], as shown in the reaction below.



It is therefore necessary to determine the pH at which this competition is minimized. In addition, major cations (e.g.  $Fe^{2+}$ ,  $Mg^{2+}$ ,  $Ca^{2+}$ ) compete with  $Ni^{2+}$  and  $Cu^{2+}$  for complexation by EDTA. This competition changes with pH due to the pH-dependence of major cation solubility [6,14]. The optimum pH must also minimize two undesirable effects under low and high pH conditions. At very low pH, the complexation efficiency of EDTA is reduced because of protonation of the EDTA molecule, while at very high pH, there is an increasing tendency for the metal ions to hydrolyse water to form sparingly soluble metal hydroxides [44].

The pH range studied was from pH 4 - 8. EDTA precipitated out of solution at pH 3. The change in the concentration of Ni and Cu extracted as a function of pH is shown in Figures 4.6 a) and b), respectively. The results indicate that within a range of approximately pH 6 - 8, no significant change in the concentration of metal extracted was observed, suggesting that the metal was predominantly extracted by EDTA, and not by  $H^+$ . No significant pH changes were observed after 24 h of extraction for any of the pH

values studied. The optimal pH was chosen to be pH 6 because this pH was sufficiently acidic to prevent precipitation of metal hydroxides, and was demonstrated to be sufficiently alkaline to minimize competitive extraction by  $H^+$ . This pH also optimized EDTA buffering capacity, as  $pK_{a,3} = 6.16$  for EDTA, which ensures minimal variations in pH throughout the kinetic extraction experiments.

#### *Optimization of EDTA Concentration*

Solutions containing increasing concentrations of EDTA were spiked with equimolar concentrations of both Ni and Cu and the spiked solutions were analyzed by GFAAS to test for matrix effects. For both metals, EDTA concentration had no effect on the observed peak area, height or shape.

Because EDTA is a non-specific complexing agent, it extracts a wide variety of cations from the soil. Hence, an important parameter to consider is the ratio,  $R$ , between the EDTA concentration and the total concentration of all extracted cations.

$$R = \frac{[EDTA]}{\sum [M_i^{n+}]} \quad (4.9)$$

where  $M_i^{n+}$  is any major cation (e.g.  $Fe^{2+}$ ,  $Mg^{2+}$ ,  $Ca^{2+}$ ,  $K^+$ , etc.). When  $R \ll 1$ , there is a lack of EDTA, and increasing concentrations of EDTA will extract greater concentrations of cations. However, when  $R \gg 1$ , EDTA is in excess and has attained maximum extraction efficiency; hence, any further increases in EDTA concentration will not increase extracted cation concentrations [6,7,14]. Under these conditions, suppression of trace metal extraction as a result of competition by other major cations is minimized [7,14,36]. An excess of EDTA is also a necessary condition in order for the kinetic model to be valid, as it is a prerequisite for making the rate law for reaction 4.4 pseudo first-order. The results for the EDTA concentration optimization experiments, plotted in Figures 4.7 a) and b), indicate that the total amount of Ni and Cu extracted after 24 h increased with increasing concentrations of EDTA, reaching a plateau at approximately 0.05 mol/L, suggesting that this value represents an excess of EDTA. These results are in

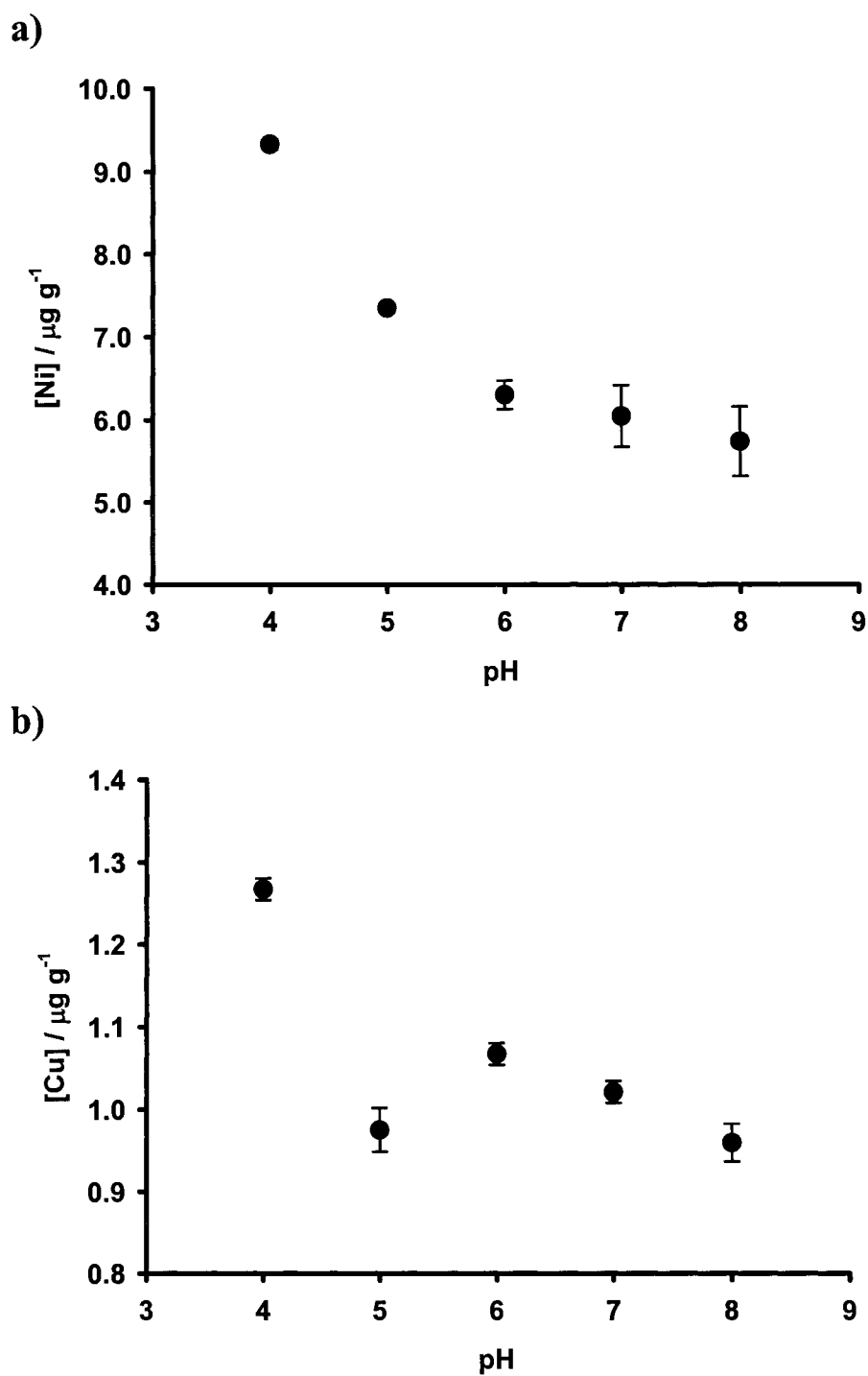


Figure 4.6 Optimization of pH for a) Ni extraction, and b) Cu extraction. Error bars represent one standard deviation of the mean. Sample 63E ( $< 0.063$  mm), mass/volume = 0.01, [EDTA] = 0.05 mol/L,  $23 \pm 2$  °C.

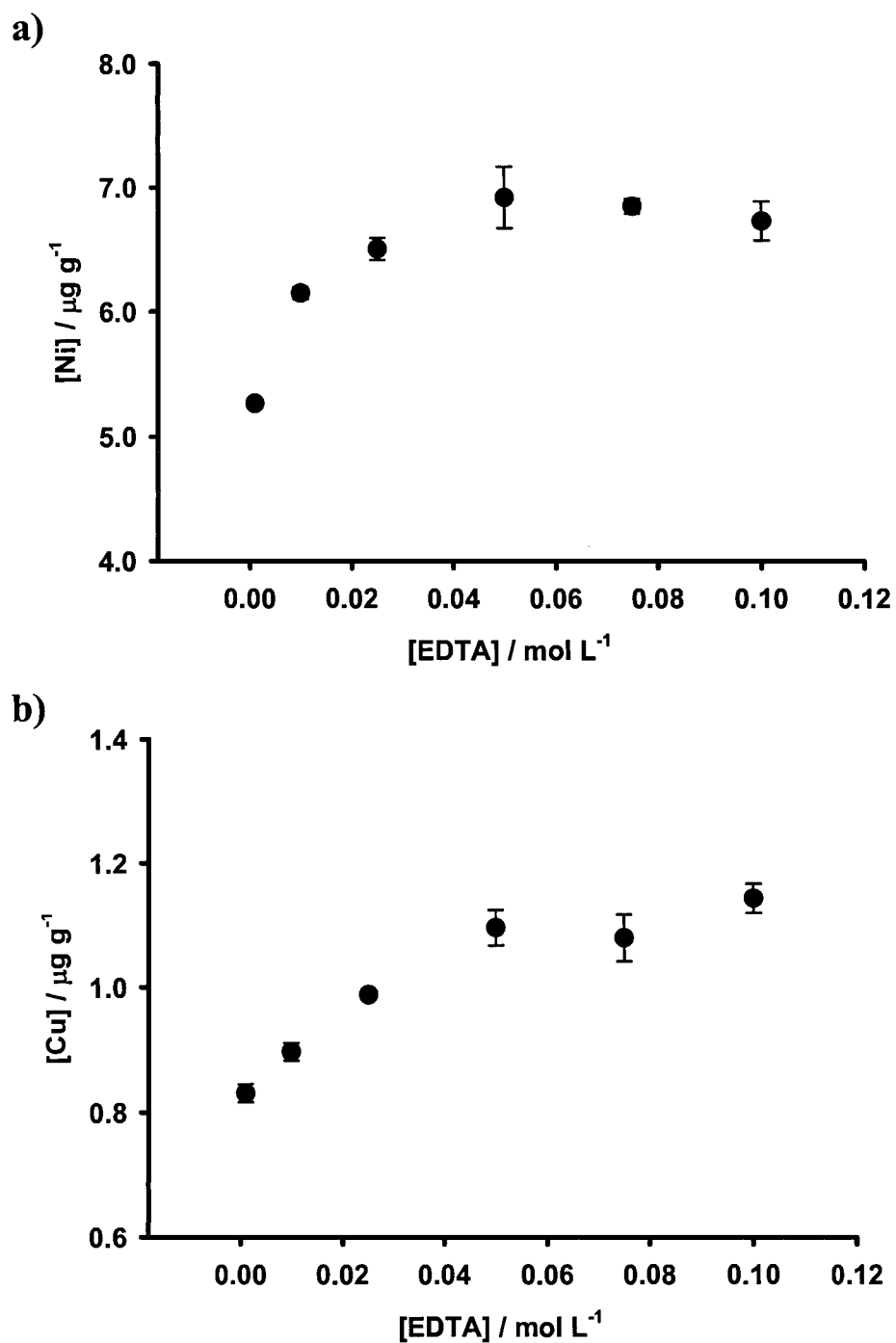


Figure 4.7 Optimization of EDTA concentration for a) Ni extraction, and b) Cu extraction. Error bars represent one standard deviation of the mean. Sample 63E (< 0.063 mm), mass/volume = 0.01, pH  $6.00 \pm 0.02$ ,  $23 \pm 2$  °C.

agreement with results from similar studies [6,7,11,14]. This concentration was also recommended for the harmonization of extraction techniques under the auspices of the Community Bureau of Reference (BCR) [2]. Only a minor drop in the pH after the extraction (~ 0.5 pH units) was observed for the sample having the lowest concentration of EDTA (i.e. 0.001 mol/L), which was probably due to reduction of the buffering capacity of EDTA at lower concentrations.

#### 4.4.2 Kinetic Fractionation Results

The concentrations of Ni and Cu in both the reagent and procedural blanks were below the limits of quantification for both elements. Replicate kinetic experiments for Ni and Cu are shown in Figures 4.8 a) and b), respectively, for sample 63B (from the top of the profile) and in Figures 4.9 a) and b), respectively, for sample 63L (from the bottom of the profile). These graphs demonstrate that despite the inherent complexity and heterogeneity of soils, the results from the kinetic experiments were repeatable within the experimental uncertainty, both at the highest (i.e. 63L) and lowest (i.e. 63B) total metal concentrations. Individual data points were reproducible (< 5 % RSD), as indicated by the error bars, which are smaller than the symbols for most data points.

The extraction curves from the kinetic experiments, given in Figures 4.10 to 4.13, show the change in concentration of extracted metal as a function of time for both profiles. Each curve is displayed individually in Figures A.1 to A.24 in Appendix A. The gap in the series of data points in the middle of each curve corresponds to an approximate 9 – 10 h overnight period, when samples were not collected. The curved lines represent the results from the non-linear regression analysis, and the corresponding numerical results that describe the fitted data are presented in Tables 4.4 - 4.7. In order to normalize the wide range of total metal concentrations in the samples, the concentration of each kinetically-distinguishable component,  $C_L$  and  $C_{SL}$ , was expressed as a fraction of the total EDTA-extractable metal concentration (i.e. as a percentage of  $C_L + C_{SL}$ ).

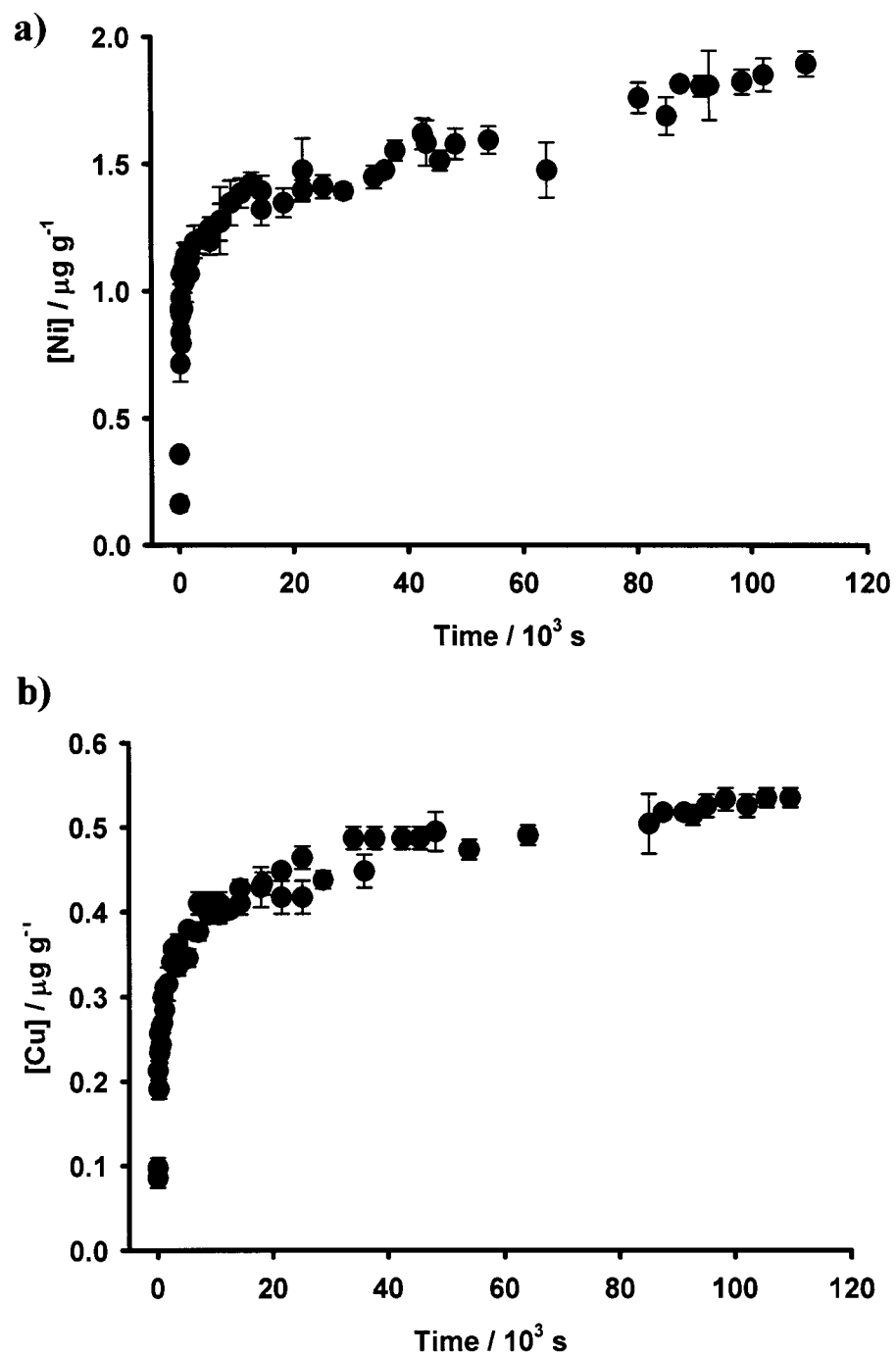


Figure 4.8 Replicate kinetic curves for sample 63B: a) Ni, b) Cu. ● replicate 1, ● replicate 2. Error bars represent one standard deviation of the mean. Sample 63B (< 0.063 mm), mass/volume = 0.01, [EDTA] = 0.05 mol/L, pH 6.00 ± 0.02, 23 ± 2 °C.

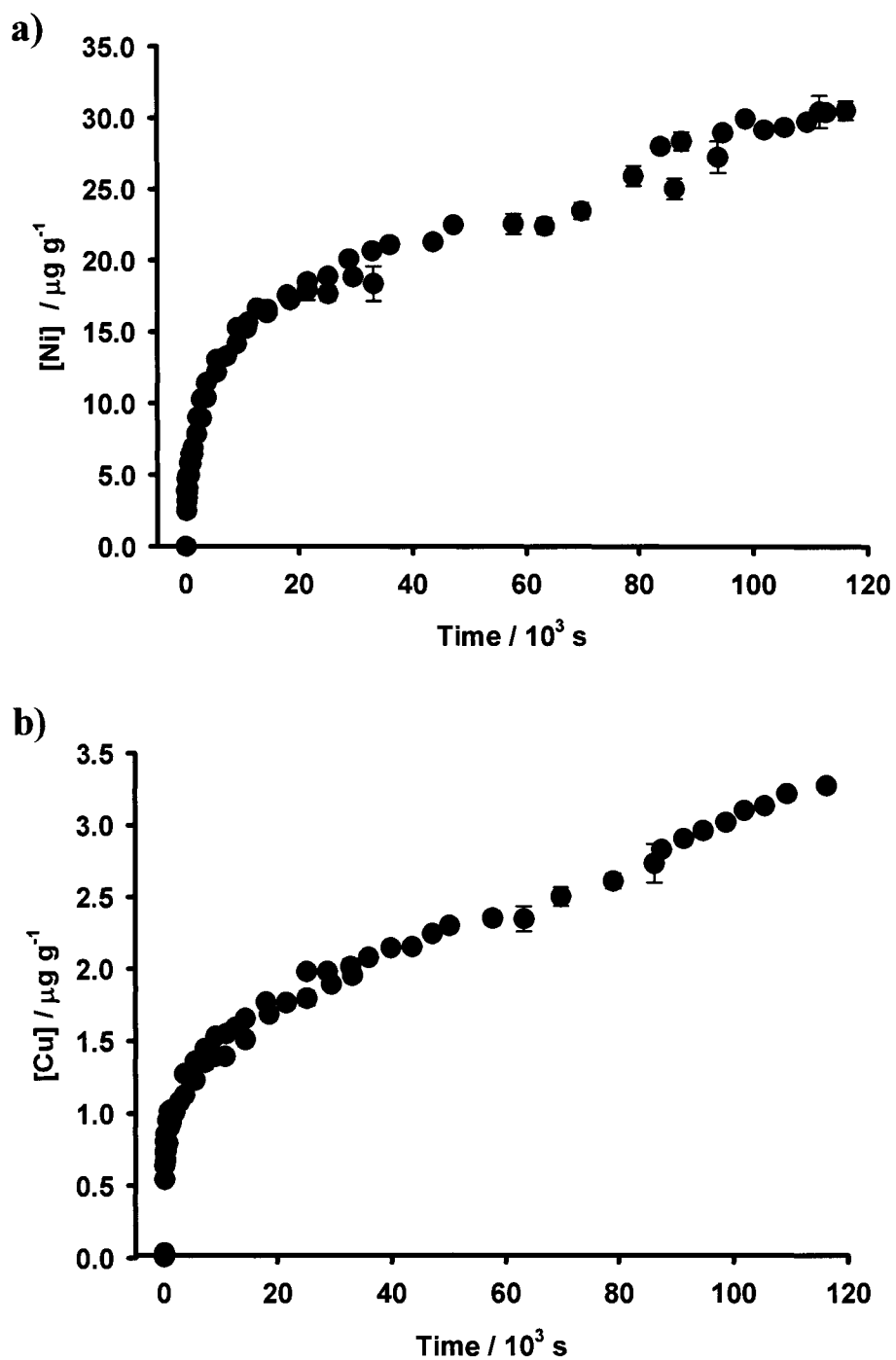


Figure 4.9 Replicate kinetic curves for sample 63L: a) Ni, b) Cu. ● replicate 1, ● replicate 2. Error bars represent one standard deviation of the mean. Sample 63L (< 0.063 mm), mass/volume = 0.01, [EDTA] = 0.05 mol/L, pH 6.00 ± 0.02, 23 ± 2 °C.

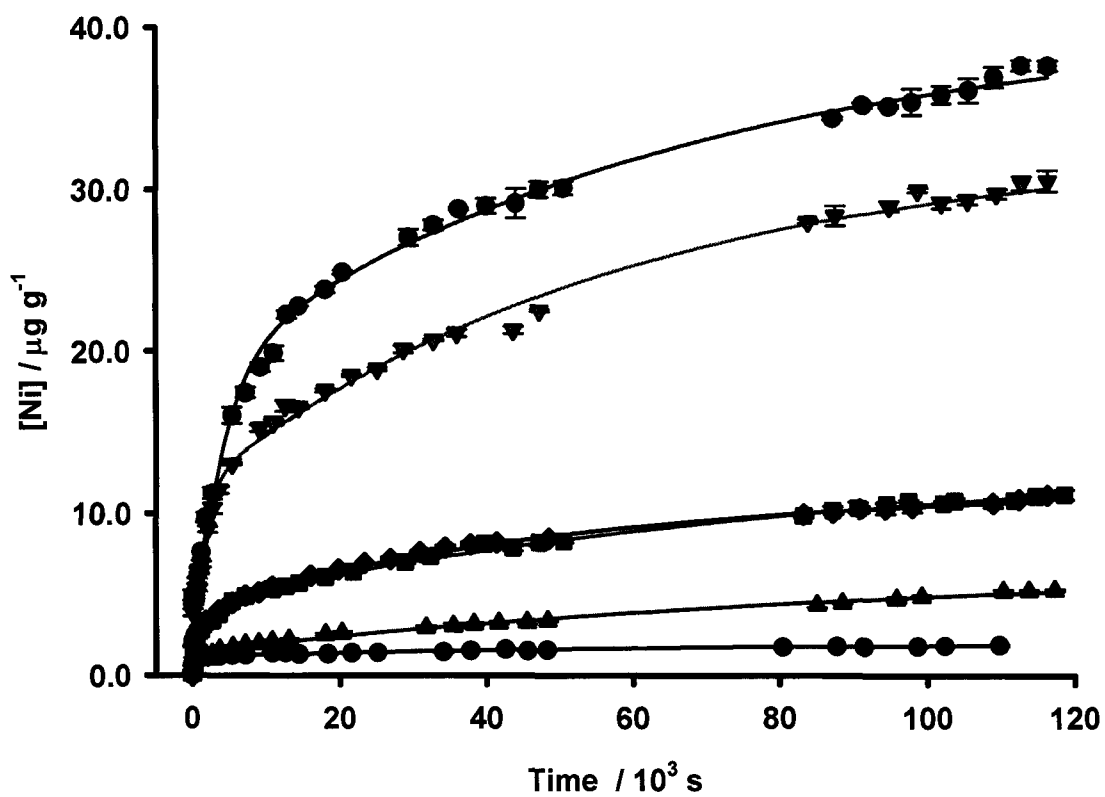


Figure 4.10 Ni kinetic curves for samples from profile 63. Error bars represent one standard deviation of the mean. ● 63B, ▲ 63E, ■ 63F, ◆ 63G, ▼ 63L, ● 63O. Soil samples < 0.063 mm, mass/volume = 0.01, [EDTA] = 0.05 mol/L, pH  $6.00 \pm 0.02$ ,  $23 \pm 2$  °C.

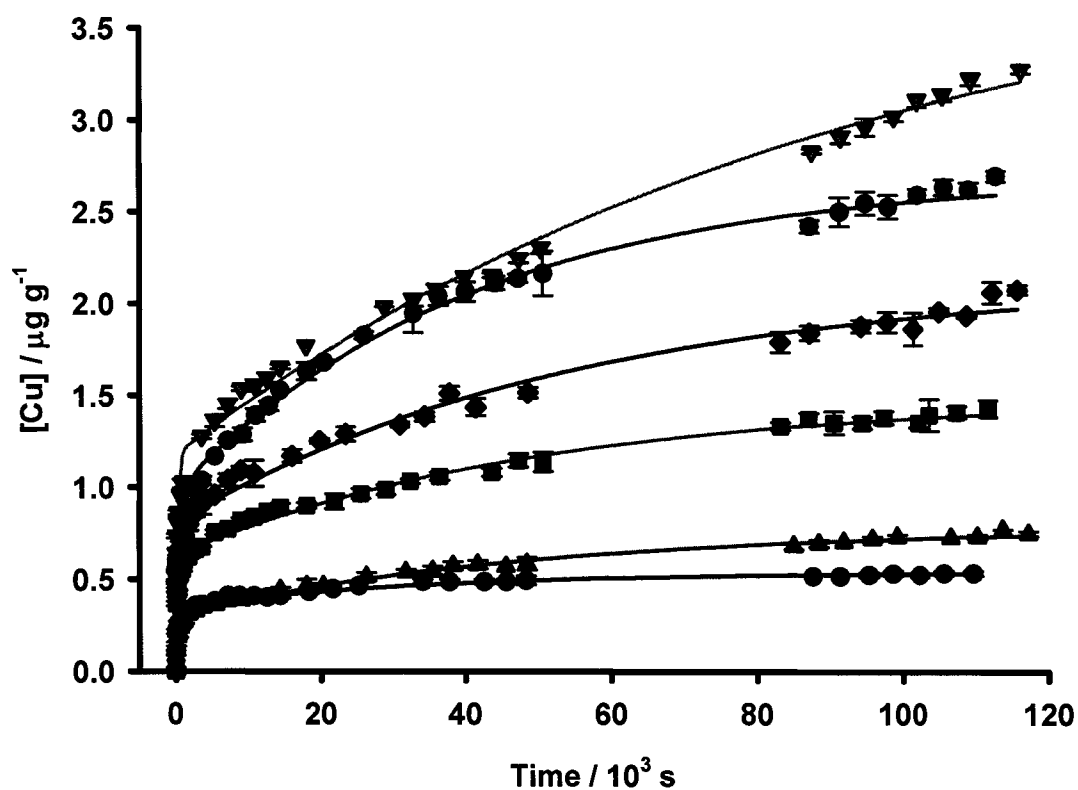


Figure 4.11 Cu kinetic curves for samples from profile 63. Error bars represent one standard deviation of the mean. ● 63B, ▲ 63E, ■ 63F, ◆ 63G, ▼ 63L, ● 63O. Soil samples < 0.063 mm, mass/volume = 0.01, [EDTA] = 0.05 mol/L, pH 6.00 ± 0.02, 23 ± 2 °C.

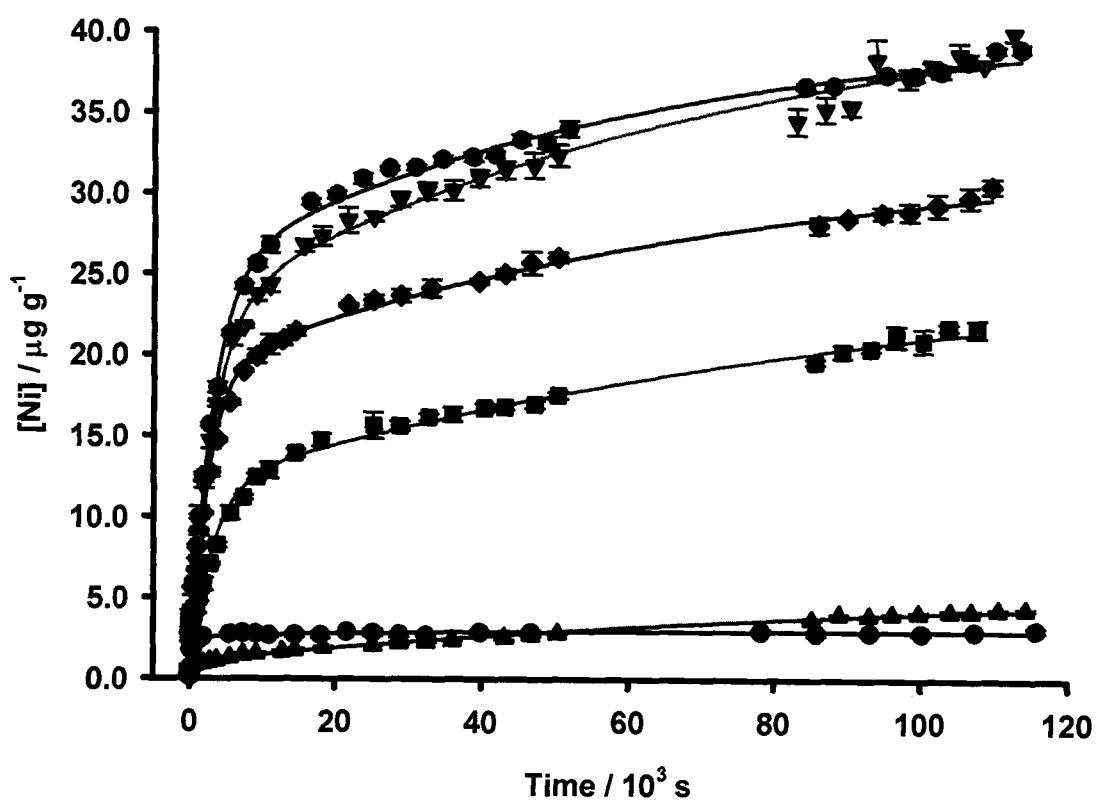


Figure 4.12 Ni kinetic curves for samples from profile 64. Error bars represent one standard deviation of the mean. ● 64C, ▲ 64E, ■ 64G, ◆ 64I, ▼ 64K, ● 64L. Soil samples < 0.063 mm, mass/volume = 0.01, [EDTA] = 0.05 mol/L, pH 6.00 ± 0.02, 23 ± 2 °C.

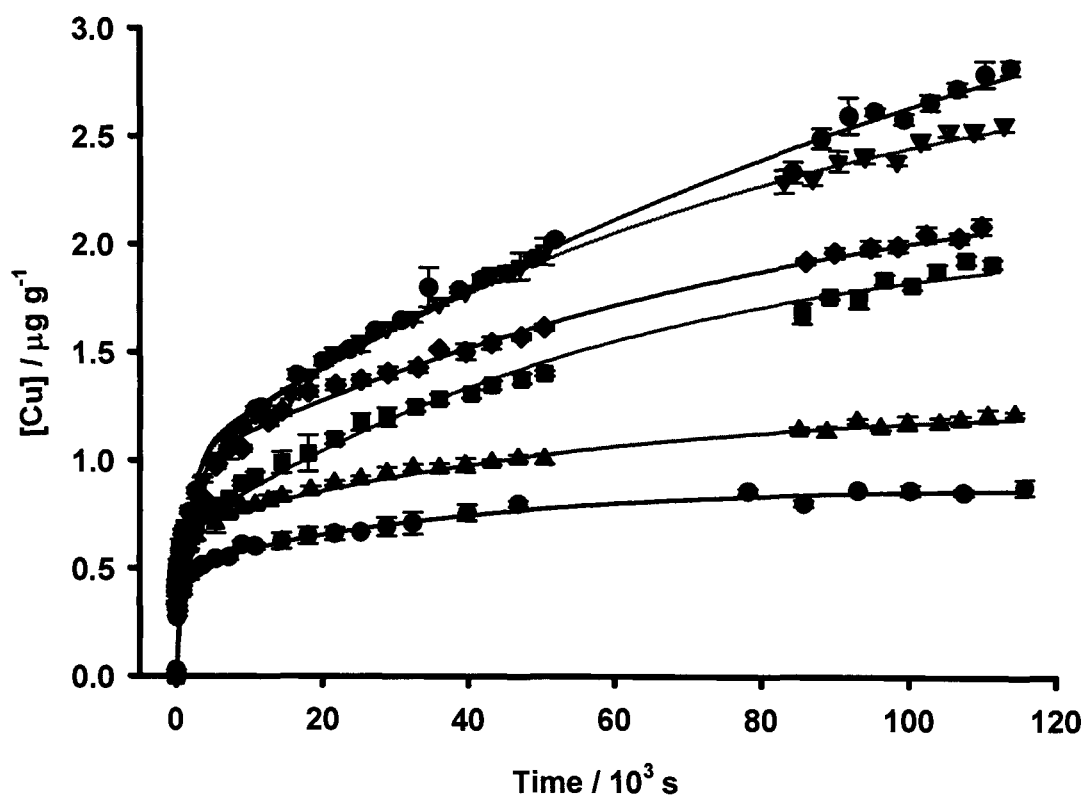


Figure 4.13 Cu kinetic curves for samples from profile 64. Error bars represent one standard deviation of the mean. ● 64C, ▲ 64E, ■ 64G, ◆ 64I, ▼ 64K, ● 64L. Soil samples < 0.063 mm, mass/volume = 0.01, [EDTA] = 0.05 mol/L, pH  $6.00 \pm 0.02$ ,  $23 \pm 2$  °C.

Table 4.4 Kinetically distinguishable components for Ni in samples from profile 63. Soil samples < 0.063 mm, mass/volume = 0.01, [EDTA] = 0.05 mol/L, pH 6.00 ± 0.02, 23 ± 2 °C. \* % of C<sub>L</sub> + C<sub>SL</sub>.

Sample	C <sub>L</sub>		k <sub>L</sub>	C <sub>SL</sub>		k <sub>SL</sub>
	µg/g	% *	× 10 <sup>-4</sup> s <sup>-1</sup>	µg/g	% *	× 10 <sup>-5</sup> s <sup>-1</sup>
<b>B</b>	1.17 ± 0.01	56.4 ± 0.1	58 ± 1	0.91 ± 0.01	43.6 ± 0.2	1.34 ± 0.01
<b>E</b>	1.45 ± 0.04	20.44 ± 0.08	25.2 ± 0.6	5.65 ± 0.02	79.6 ± 0.4	0.94 ± 0.01
<b>F</b>	4.44 ± 0.05	32.4 ± 0.6	5.5 ± 0.3	9.3 ± 0.2	68 ± 1	1.10 ± 0.04
<b>G</b>	4.13 ± 0.05	35.4 ± 0.5	8.5 ± 0.5	7.53 ± 0.06	64.6 ± 0.6	1.84 ± 0.05
<b>L</b>	11.5 ± 0.1	34.7 ± 0.4	6.9 ± 0.3	21.6 ± 0.1	65.3 ± 0.5	1.70 ± 0.04
<b>O</b>	18.7 ± 0.2	45.9 ± 0.6	2.71 ± 0.07	22.1 ± 0.2	54.1 ± 0.7	1.51 ± 0.06

Table 4.5 Kinetically distinguishable components for Cu in samples from profile 63. Soil samples < 0.063 mm, mass/volume = 0.01, [EDTA] = 0.05 mol/L, pH 6.00 ± 0.02, 23 ± 2 °C. \* % of C<sub>L</sub> + C<sub>SL</sub>.

Sample	C <sub>L</sub>		k <sub>L</sub>	C <sub>SL</sub>		k <sub>SL</sub>
	µg/g	% *	× 10 <sup>-4</sup> s <sup>-1</sup>	µg/g	% *	× 10 <sup>-5</sup> s <sup>-1</sup>
<b>B</b>	0.34 ± 0.01	64.6 ± 0.4	29 ± 1	0.19 ± 0.01	35.4 ± 0.3	2.91 ± 0.07
<b>E</b>	0.31 ± 0.01	38.8 ± 0.2	28 ± 1	0.48 ± 0.01	61.2 ± 0.2	1.99 ± 0.02
<b>F</b>	0.63 ± 0.01	42.1 ± 0.1	42 ± 1	0.86 ± 0.01	57.9 ± 0.2	1.98 ± 0.01
<b>G</b>	0.80 ± 0.01	37.5 ± 0.1	42 ± 1	1.34 ± 0.01	62.5 ± 0.2	1.77 ± 0.01
<b>L</b>	1.18 ± 0.01	28.8 ± 0.1	40.0 ± 0.9	2.90 ± 0.01	71.2 ± 0.3	1.04 ± 0.01
<b>O</b>	0.98 ± 0.01	36.2 ± 0.5	15 ± 1	1.73 ± 0.01	63.8 ± 0.5	2.38 ± 0.05

Table 4.6 Kinetically distinguishable components for Ni in samples from profile 64. Soil samples < 0.063 mm, mass/volume = 0.01, [EDTA] = 0.05 mol/L, pH 6.00 ± 0.02, 23 ± 2 °C. \* % of C<sub>L</sub> + C<sub>SL</sub>.

Sample	C <sub>L</sub>		k <sub>L</sub>	C <sub>SL</sub>		k <sub>SL</sub>
	µg/g	%*	× 10 <sup>-4</sup> s <sup>-1</sup>	µg/g	%*	× 10 <sup>-5</sup> s <sup>-1</sup>
C	2.52 ± 0.01	85.0 ± 0.2	44.1 ± 0.9	0.45 ± 0.01	15.0 ± 0.2	4.67 ± 0.09
E	1.04 ± 0.01	17.5 ± 0.3	14 ± 1	4.88 ± 0.07	82 ± 2	0.98 ± 0.03
G	11.90 ± 0.06	44.4 ± 0.5	3.36 ± 0.05	14.9 ± 0.3	56 ± 1	0.95 ± 0.04
I	19.05 ± 0.09	57.3 ± 0.5	4.14 ± 0.06	14.2 ± 0.2	42.7 ± 0.7	1.27 ± 0.05
K	22.7 ± 0.1	53.1 ± 0.5	3.34 ± 0.06	20.0 ± 0.3	46.9 ± 0.7	1.34 ± 0.05
L	25.1 ± 0.1	61.7 ± 0.4	3.36 ± 0.05	15.6 ± 0.1	38.4 ± 0.4	1.62 ± 0.05

Table 4.7 Kinetically distinguishable components for Cu in samples from profile 64. Soil samples < 0.063 mm, mass/volume = 0.01, [EDTA] = 0.05 mol/L, pH 6.00 ± 0.02, 23 ± 2 °C. \* % of C<sub>L</sub> + C<sub>SL</sub>.

Sample	C <sub>L</sub>		k <sub>L</sub>	C <sub>SL</sub>		k <sub>SL</sub>
	µg/g	%*	× 10 <sup>-4</sup> s <sup>-1</sup>	µg/g	%*	× 10 <sup>-5</sup> s <sup>-1</sup>
C	0.50 ± 0.01	56.7 ± 0.4	20.3 ± 0.9	0.38 ± 0.01	43.3 ± 0.4	2.51 ± 0.06
E	0.69 ± 0.01	53.5 ± 0.6	19 ± 1	0.60 ± 0.01	46.5 ± 0.7	1.67 ± 0.07
G	0.65 ± 0.01	30.1 ± 0.1	44 ± 2	1.50 ± 0.01	70.0 ± 0.2	1.54 ± 0.01
I	0.98 ± 0.01	38.2 ± 0.7	5.8 ± 0.2	1.58 ± 0.04	62 ± 2	1.06 ± 0.05
K	0.97 ± 0.01	31.3 ± 0.5	6.7 ± 0.3	2.13 ± 0.03	69 ± 1	1.18 ± 0.04
L	1.01 ± 0.01	23.5 ± 0.6	6.6 ± 0.3	3.3 ± 0.1	77 ± 3	0.68 ± 0.03

The quickly rising section of each curve is due to the rapid extraction of weakly bound (labile) metal from the soil, and the slowly rising section of each curve is due to the slow extraction of more strongly bound (slowly labile) metal from the soil. The extraction curves show that the concentration of extracted metals in most of the samples had not yet reached equilibrium after 32 h. Results from similar studies on polluted soils have shown that it can take weeks to attain equilibrium [6,11,35]. From a visual inspection of the kinetic curves, the relative total metal concentrations extracted by EDTA agree with the relative concentrations determined from the acid digestion analyses (see Figure 2.3), demonstrating the trend of increasing total metal concentration down the profile.

A closer inspection of the beginning of the curve for sample 63F, shown in Figure 4.14, illustrates that the fitted data from the non-linear regression analysis do not provide a good visual estimate of the slope of the experimental data representing the fast component. This is probably due in part to the small number of points in this quickly rising section of the curve. However, the fitted data do appear to accurately estimate the slope of the slow component, as well as the concentrations of both kinetically distinguishable components (i.e. %C<sub>L</sub> and %C<sub>SL</sub>). Similar results were observed for all other samples; hence, the only values for k<sub>SL</sub>, C<sub>L</sub> and C<sub>SL</sub> were considered to be reliable, and were used to describe the kinetic behaviour of Ni and Cu in this soil.

#### 4.4.3 Validation of Data Fitting

A simple, one-component first-order reaction, where the measured signal is for the product, is described by the following exponential rise function [11,13,52-54],

$$C(t) = C^{\infty} (1 - e^{-kt}) \quad (4.10)$$

where  $C(t)$  is the concentration of product measured at time  $t$ ,  $C^{\infty}$  is the concentration of product measured when the reaction is near completion, and  $k$  is the rate constant.

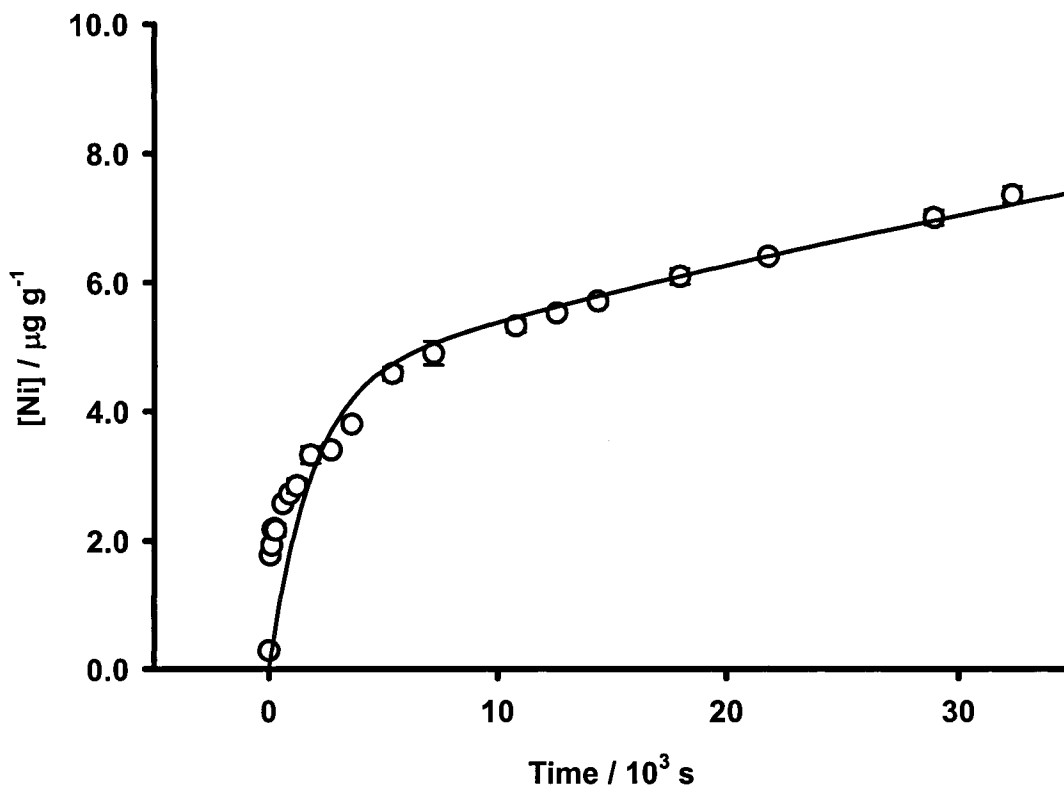


Figure 4.14 Expanded view of the beginning of the Ni kinetic curve for sample 63F, illustrating the poor non-linear regression fit to the data points representing the fast component. Error bars represent one standard deviation of the mean. Sample 63F (< 0.063 mm), mass/volume = 0.01, [EDTA] = 0.05 mol/L, pH 6.00 ± 0.02, 23 ± 2 °C.

The linearized form of equation 4.10 is given below.

$$\ln[C^\infty - C(t)] = \ln C^\infty - kt \quad (4.11)$$

A plot of  $\ln[C^\infty - C(t)]$  vs. time yields a straight line with a slope of  $k$  and an intercept of  $\ln C^\infty$ . However, the problem with using this equation to calculate the rate constant is that the value of  $C^\infty$  from the linear regression fit rarely coincides exactly with the measured one [52]. This problem is compounded further when attempting to model multi-component first-order reactions, as the selection of data points for linear regression analysis of the slope of each component is somewhat arbitrary because of a high degree of parameter cross-correlation [53]. Directly fitting a non-linear model to experimental data by non-linear regression analysis is often a simpler and more convenient approach to find the desired parameters from an exponential equation, such as equation 4.7 [51,52].

Although the conventional approach described above for analyzing first-order kinetic data is not a good model for obtaining accurate parameters from a multi-component system, it is useful for verifying that the kinetic curves from the extraction experiments do not represent simple one-component systems. Equation 4.11 was used to transform the exponential rise curves in Figures 4.10 - 4.13 to linearized decay curves. A typical decay curve is shown in Figure 4.15 for Cu from profile 64. On the y-axis,  $C_{\text{tot}}$  is the total concentration of metal that can be extracted by EDTA within the timescale of the experiment (analogous to  $C^\infty$ ) and is calculated as  $C_L + C_{\text{SL}}$ . Although the initial part of the decay curve is difficult to see because of compression of the data points along the x-axis, this figure shows that at least two distinct slopes are observable, indicating that the data does not represent a simple one-component system. This linear modelling approach was also used to confirm that the results from the non-linear regression analysis were reasonable by verifying that the *relative* values for  $k_{\text{SL}}$ ,  $\%C_L$  and  $\%C_{\text{SL}}$  in each profile agreed with a visual estimation of the *relative* slopes and intercepts of the corresponding linearized decay curves.

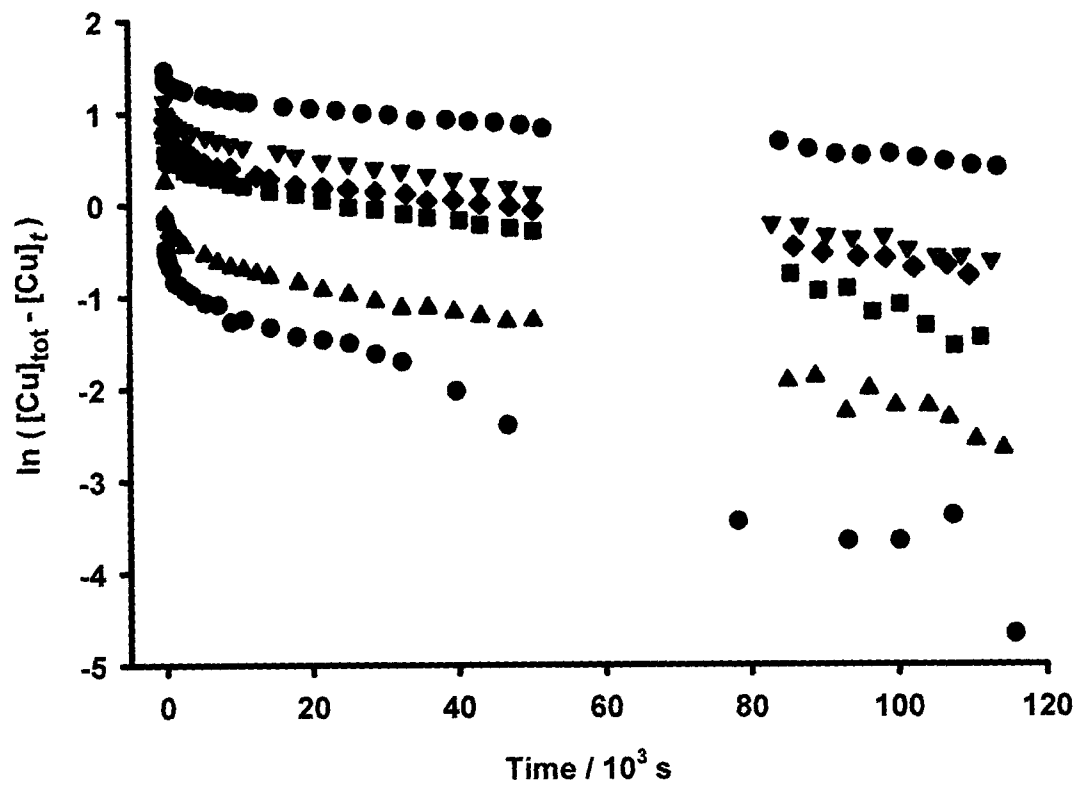


Figure 4.15 Natural logarithmic transform of exponential rise data for Cu in samples from profile 64. ● 64C, ▲ 64E, ■ 64G, ◆ 64I, ▼ 64K, ● 64L. Soil samples < 0.063 mm, mass/volume = 0.01, [EDTA] = 0.05 mol/L, pH 6.00 ± 0.02, 23 ± 2°C.

The experimental data from the kinetic extraction curves were fit to a two-component model because it was the simplest model (i.e. minimum number of components) that gave an adequate statistical and visual fit to the data [54]. Although use of more components in the model often appeared to fit the data better, the additional components were often of negligible concentration and/or had a high degree of uncertainty. The two-component reaction model described here is the model most widely used by soil chemists, where each pseudo first-order reaction is often attributed to different binding sites [10,11,13,49,54-57]. A complication associated with this model is that it often predicts a distinct break between the two reactions, but in most cases, experimental data show a smooth transition [11]. Hence, the approximation of reactions in natural soils by the two-component model should not be considered to imply that there are only two discrete soil binding sites. The model is merely meant to be a simplification of a system having a diversity of sites, where the calculated parameters can be considered to represent average values over a distribution of similar sites with closely spaced rate constants [54].

#### 4.4.4 *EDTA-Extractable Metal Species*

The results from the previously performed acid digestion experiments and the ToF-SIMS work suggest that Mg-bearing phyllosilicates are the predominant mineral hosts for Ni in this soil. However, it is important to keep in mind that the EDTA may extract a different fraction of metal from the soil mineral grains than that which is extractable by the acid digestion procedure, or than that which can be detected by ToF-SIMS. The bulk soil samples used in the kinetic extraction experiments were air-dried, which preserves the solvation sphere of ions [58]. However, the samples for the ToF-SIMS investigations were embedded in an epoxy puck and the process of mixing the soil with the epoxy likely removes the cation hydration spheres.

Although EDTA is routinely used to extract all weakly bound and “exchangeable” metals (e.g. bound to carbonates, Fe- and Mn- oxides, organic matter), it has been reported to complex and remove metals from the crystal lattices of some silicate minerals, including chlorite [59], glauconite [59,60], and serpentine [61], without destroying the crystalline structure. Hence, in addition to being able to extract weakly bound metal from this soil, it is possible that the EDTA used in the kinetic experiments was also able to extract metals from the crystal lattice of the hypothesized mineral host. Therefore, Mg-bearing phyllosilicate trace metal hosts can be justifiably used as a possible mineralogical context for interpreting the kinetic results.

#### 4.4.5 *Physical Significance of $C_L$ and $C_{SL}$*

Biphasic kinetics (i.e. a rapid reaction rate followed by a slower reaction rate) at the particle-solution interface have often been described by two first-order reactions, and is often interpreted to represent two types of sites [49]. In studies on the kinetics of ion sorption to soil particle surfaces, the term ‘sites’ has been reported to have a variety of physical meanings, including [56]:

1. sites of differing degrees of accessibility (e.g. internal vs. external)
2. sites of differing sorbent type (e.g. organic matter vs. mineral surfaces)
3. sites having different sorption mechanisms

These concepts can be adapted and applied to the process of metal ion extraction from soil particles.

#### *Sites of differing degrees of accessibility*

The sheet-like crystal structure of phyllosilicate minerals provides them with external planar and edge sites, as well as internal sites in the interlayer regions. While reactions on the readily accessible planar and edge sites can be quite rapid, internal sites are much less accessible and can be partially to totally collapsed, making extraction reactions slow, tortuous and mass-transfer controlled [49].

### *Sites of differing metal host types*

Soils are complex, heterogeneous mixtures of inorganic and organic components, each having different types of sites with differing reactivities. Hence, another possible interpretation for the two 'sites' may be that the metal is associated with more than one soil phase. Metals bound to organic matter, or to Fe- and Mn-oxides (amorphous or crystalline) likely have very different binding strengths than metals bound inside a mineral structure.

### *Sites having differing bond strengths*

For a given mineral, some cation sites are less stable than others, depending on the strength of the bonds as well as the size and orientation of the metal residence sites. In general, metal ions held in large, distorted binding sites are more weakly bound than those held in a tightly packed, regular lattice arrangement [26]. For example, in dioctahedral micas (e.g. illite, muscovite), the orientation of the hydroxyl groups allows for stronger bonding to interlayer  $K^+$  ions than in trioctahedral micas (e.g. biotite), making the latter more susceptible to dissolution [26]. Another factor affecting the strength of cation sites is the coordination number of the metal within the host mineral structure [58]. Metal ions held in octahedral sites at the edges of the crystal are only partially coordinated by oxygen atoms, and are therefore relatively weakly bound, while metal ions located in the more central regions of the lattice are fully coordinated, and hence more strongly bound.

#### *4.4.6 Kinetic Trends*

In order to identify the presence of any trends in the kinetic results, the values of  $\%C_L$ ,  $\%C_{SL}$  and  $k_{SL}$  from the non-linear regression analyses were plotted as a function of depth in Figures 4.16 to 4.23 (depth is shown as negative values below the surface, with increasing depth going from right to left). Points were only considered to be outliers (i.e. not included in the calculation of the trend line) when the corresponding sample deviated

significantly from the trend (i.e.  $R^2 < 0.7$ ) in both  $\%C_L$  and  $k_{SL}$  in order to ensure that these points more likely represent physically significant outliers rather than random variations in the data.

Figures 4.16 a) and 4.18 a) illustrate that for Ni in both profiles, with the exception of the uppermost samples (i.e. 63B and 64C),  $\%C_L$  decreases almost linearly ( $R^2 = 0.71, 0.79$ ) with decreasing depth. Because  $\%C_{SL} = 100 - \%C_L$ , the results for  $\%C_{SL}$  always display the opposite trend from that of  $\%C_L$ . The anomalously high values of  $\%C_L$  observed for Ni in samples 63B and 64C can be visualized by comparing the kinetic extraction curves for these uppermost samples with those for the samples from the next depth in the profile (i.e. 63E and 64E, respectively), as shown in Figures 4.24 a) and b). In the curves for 63B and 64C, which level out very quickly, the fast component contributes the majority of the total concentration of Ni extracted, while the curves for 63E and 64E are much more sloping, with the fast component contributing only a small proportion of the total amount of extracted Ni. The change in  $k_{SL}$  for Ni in profile 64 as a function of depth ( $R^2 = 0.88$ ), presented in Figure 4.19, shows a similar trend to that observed for  $\%C_L$ . However,  $k_{SL}$  for Ni in profile 63, shown in Figure 4.17, did not demonstrate a trend with depth ( $R^2 = 0.19$ ).

The results for Cu, shown in Figures 4.20 to 4.23, display a reversal in the trends observed for Ni. For both profiles, with the exception of sample 63O,  $\%C_L$  increases almost linearly ( $R^2 = 0.77, 0.80$ ) towards the surface. Similarly,  $k_{SL}$  also increases in both profiles ( $R^2 = 0.99, 0.88$ ) with decreasing depth, again with sample 63O as an outlier.

These systematic trends in trace metal lability observed through the soil profile are interpreted to reflect the influence of the differential effects of weathering and soil formation processes with depth on the residence site and reactivity of Ni and Cu within the host mineral. Weathering intensity usually grades from high to low as one goes down a soil profile [29]. This is primarily a result of the fact that there is generally a more rapid

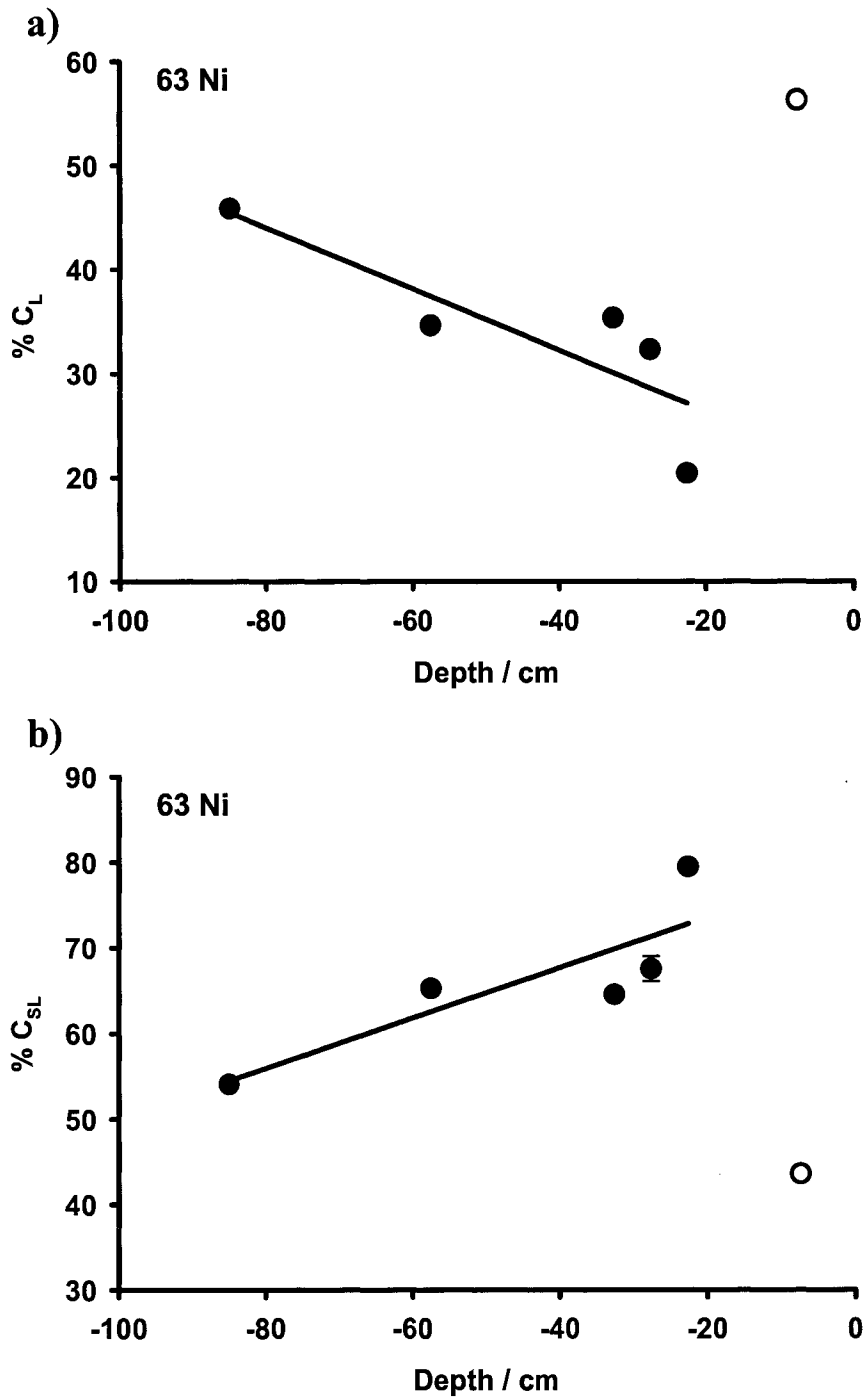


Figure 4.16 Proportion of kinetically distinguishable components as a function of depth for Ni in profile 63: a) labile component, b) slowly labile component. Error bars represent one standard deviation of the mean. ● included in linear regression analysis, ○ omitted from linear regression analysis,  $R^2 = 0.71$ .

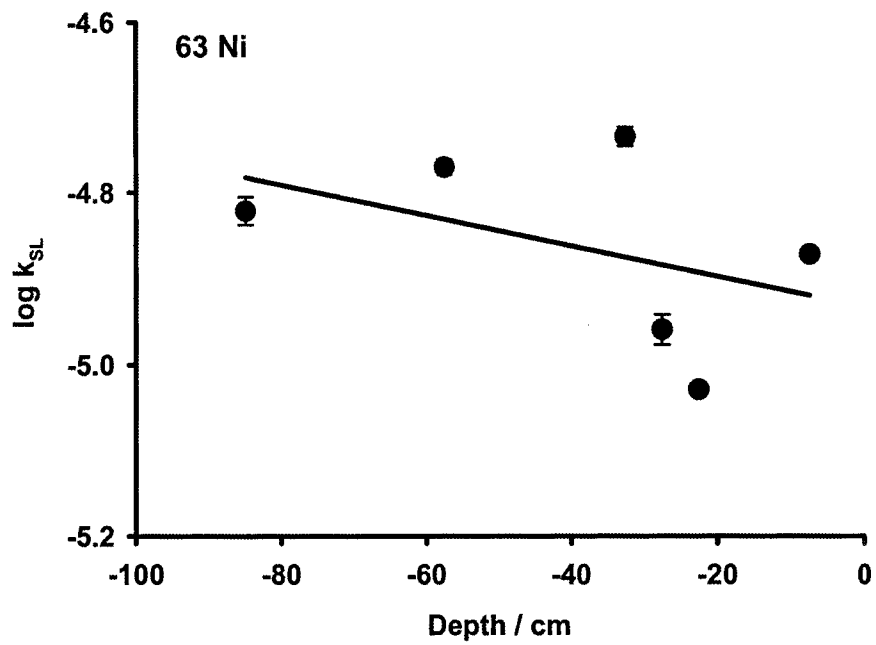


Figure 4.17 Rate constant of slowly labile component as a function of depth for Ni in profile 63. Error bars represent one standard deviation of the mean.  $R^2 = 0.19$ .

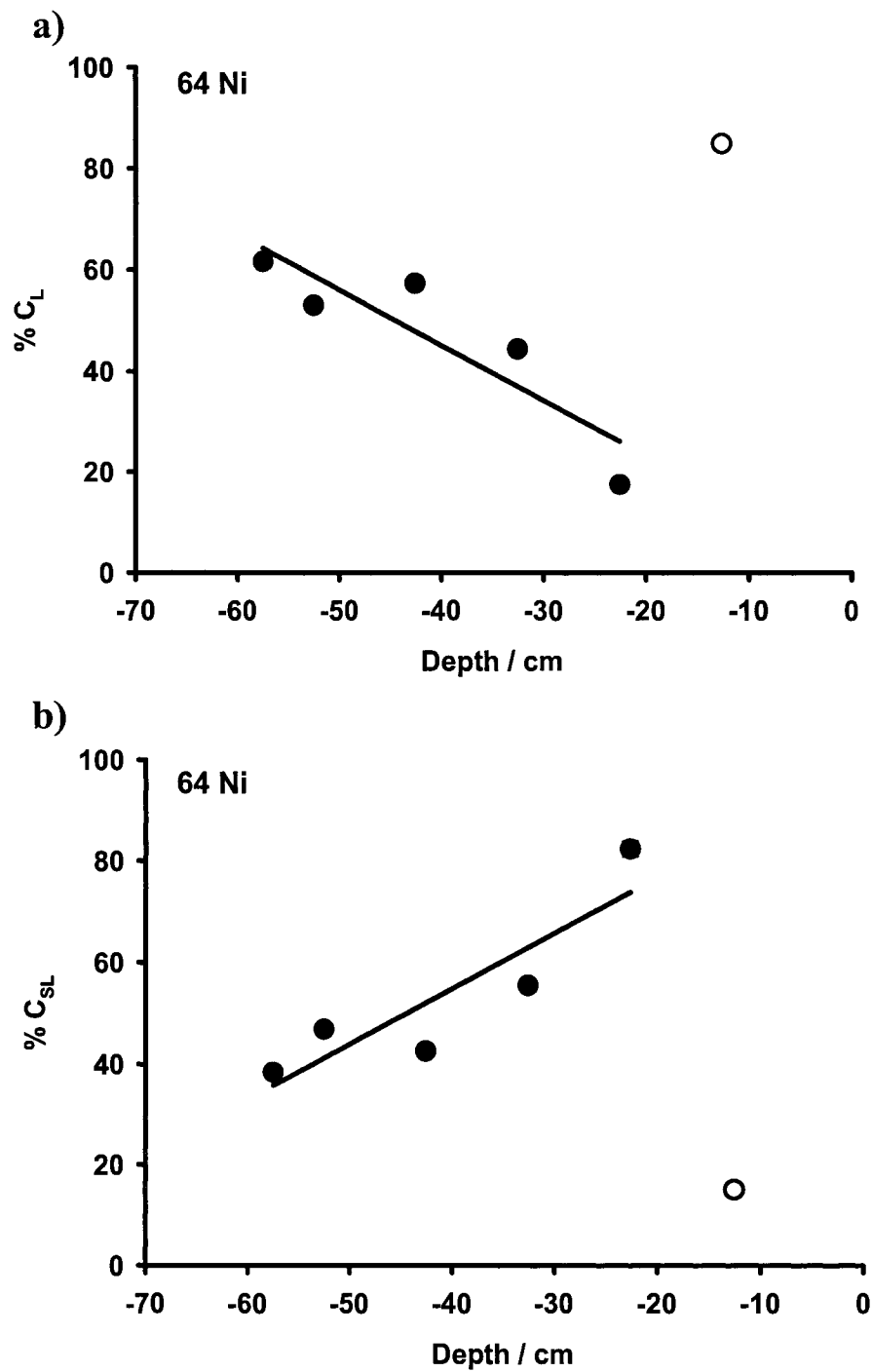


Figure 4.18 Proportion of kinetically distinguishable components as a function of depth for Ni in profile 64: a) labile component, b) slowly labile component. Error bars represent one standard deviation of the mean (smaller than the symbols). • included in linear regression analysis, ○ omitted from linear regression analysis,  $R^2 = 0.79$ .

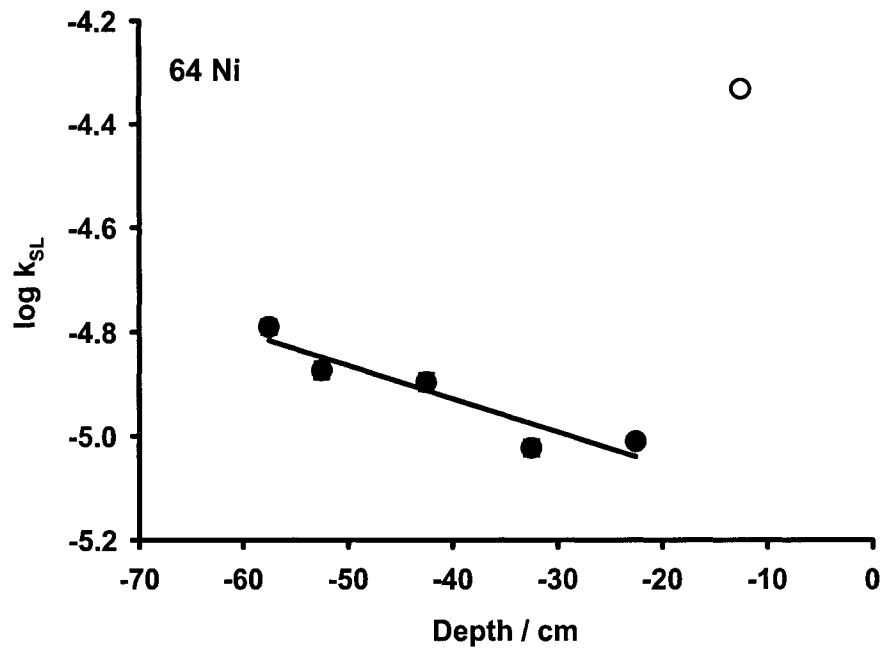


Figure 4.19 Rate constant of slowly labile component as a function of depth for Ni in profile 64. Error bars represent one standard deviation of the mean (smaller than the symbols). ● included in linear regression analysis, ○ omitted from linear regression analysis,  $R^2 = 0.88$ .

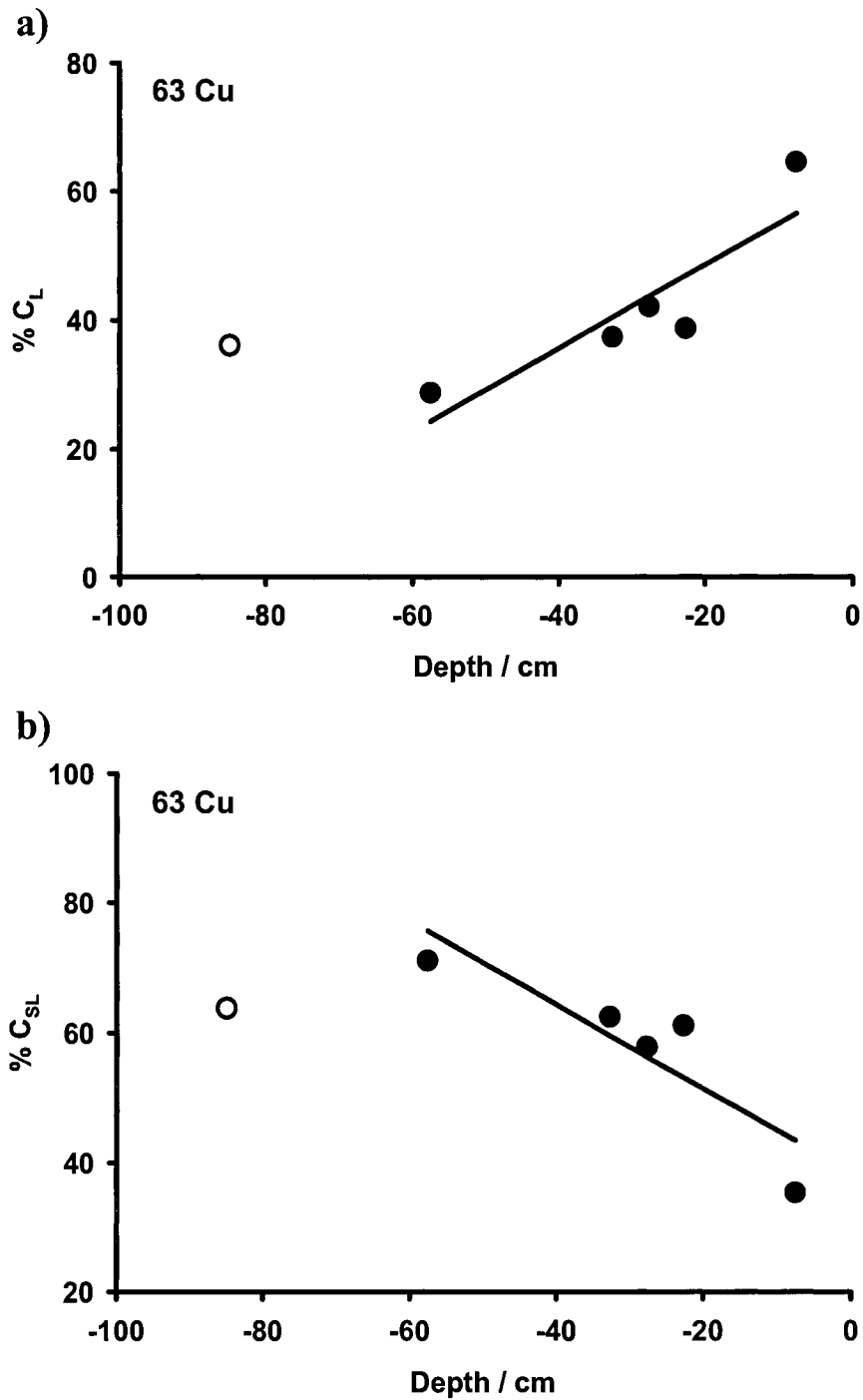


Figure 4.20 Proportion of kinetically distinguishable components as a function of depth for Cu in profile 63: a) labile component, b) slowly labile component. Error bars represent one standard deviation of the mean (smaller than the symbols). ● included in linear regression analysis, ○ omitted from linear regression analysis,  $R^2 = 0.77$ .

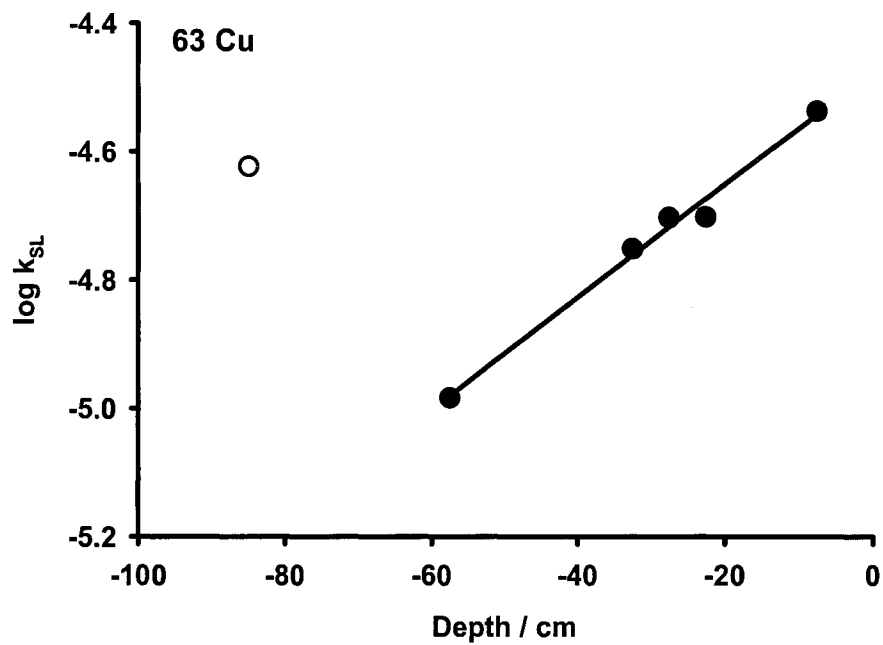


Figure 4.21 Rate constant of slowly labile component as a function of depth for Cu in profile 63. Error bars represent one standard deviation of the mean (smaller than the symbols). ● included in linear regression analysis, ○ omitted from linear regression analysis.  $R^2 = 0.99$ .

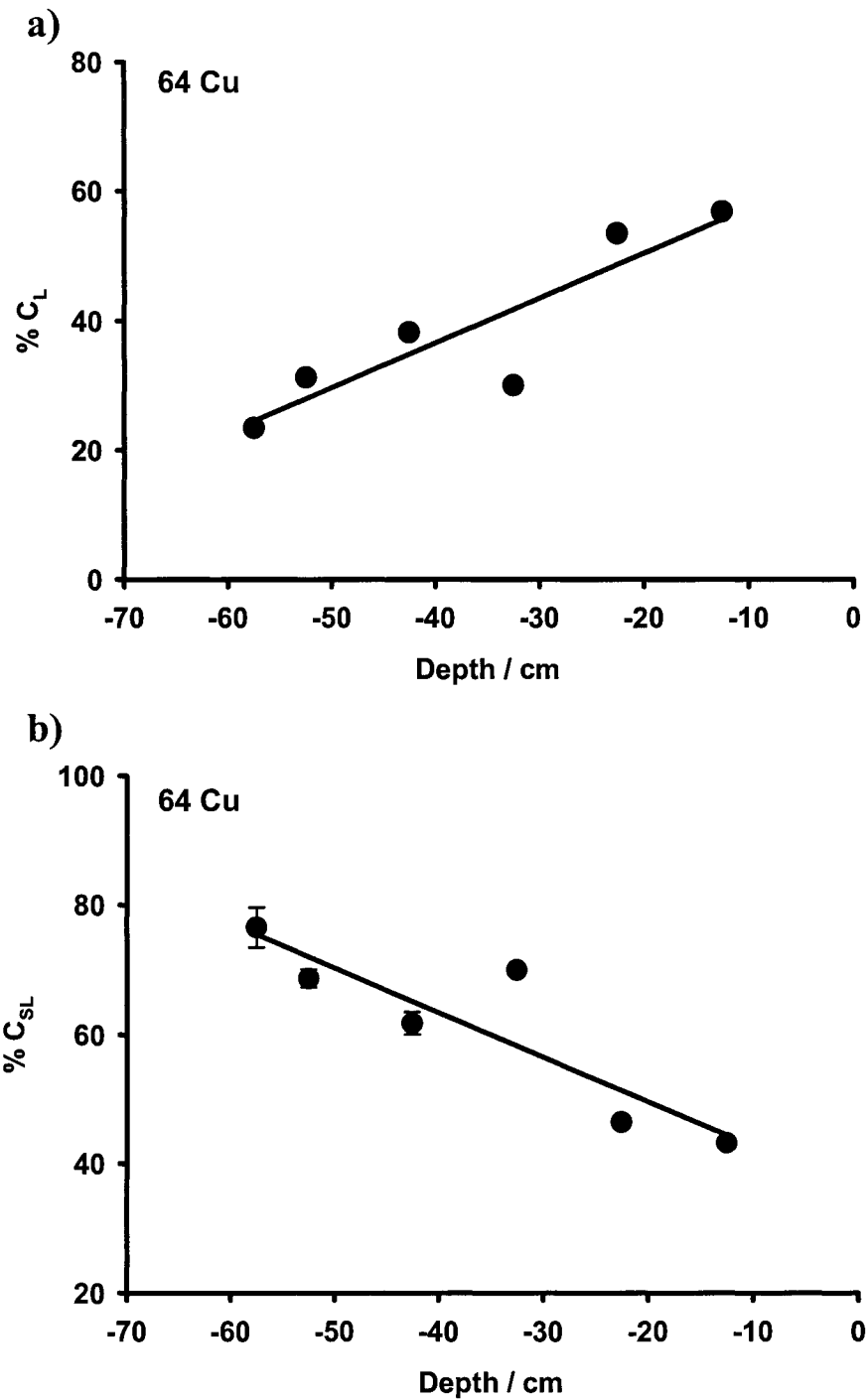


Figure 4.22 Proportion of kinetically distinguishable components as a function of depth for Cu in profile 64: a) labile component, b) slowly labile component. Error bars represent one standard deviation of the mean.  $R^2 = 0.80$ .

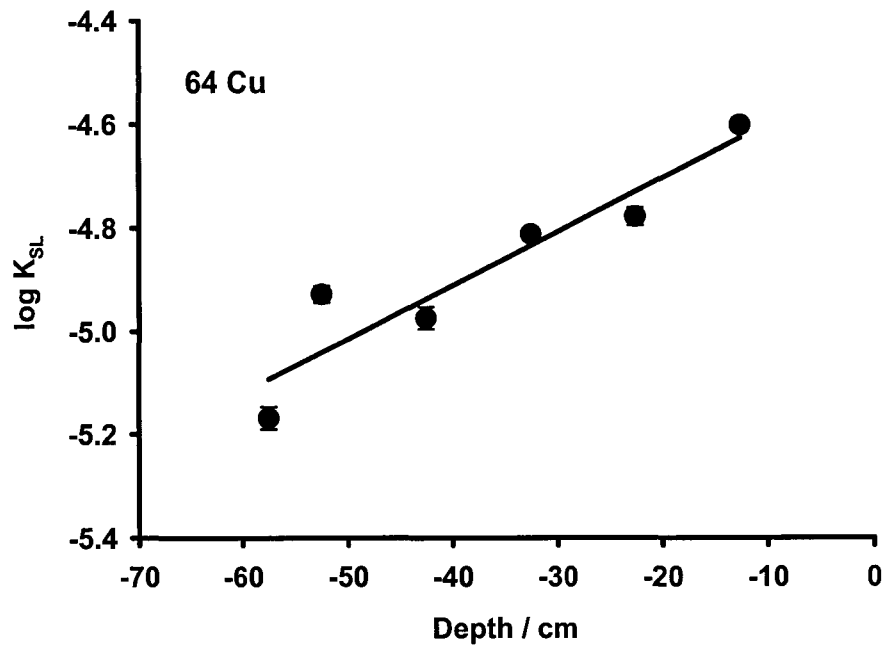


Figure 4.23 Rate constant of slowly labile component as a function of depth for Cu in profile 64. Error bars represent one standard deviation of the mean.  $R^2 = 0.88$ .

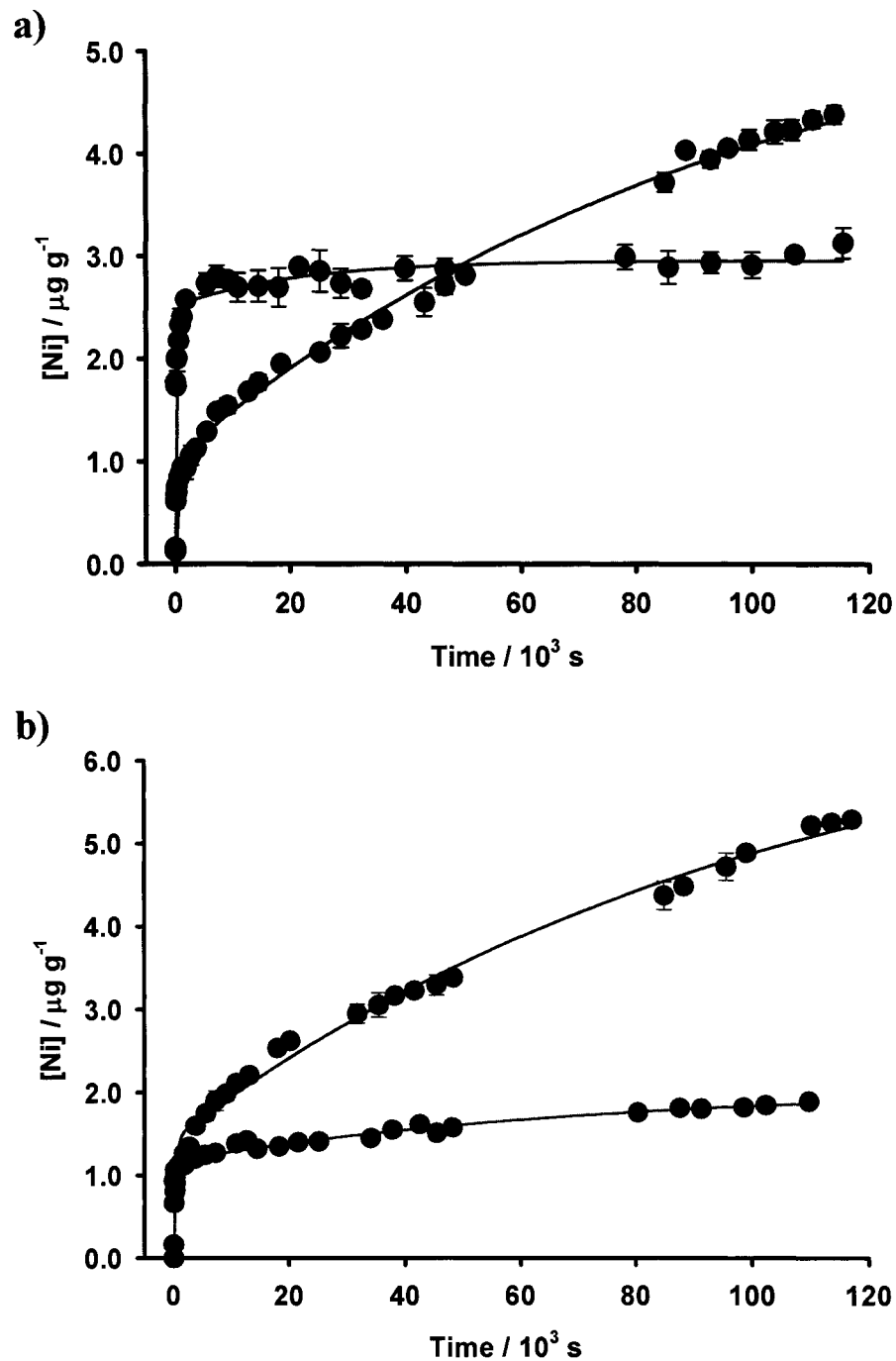


Figure 4.24 Comparison of Ni kinetic curves illustrating relative proportions of the labile component: a) ● 63B and ● 63E, b) ● 64C and ● 64E. Error bars represent one standard deviation of the mean.

flow of water through the upper horizons due the presence of macropores, fractures and root channels, which increase the soil porosity and hydraulic conductivity. Hence, leaching intensity is much greater at the surface than at deeper levels in the profile [24,29,62]. Soil weathering and removal of metal ions is further enhanced towards the surface by the decomposition of organic matter, and increased biological activity, which create acidic conditions and concentrate complexing organic acids in the upper regions of the profile. Plant root uptake is also most intense in the upper soil horizons – the lower limit of plant rootlets observed in profiles 63 and 64 did not extend below a depth of about 50 cm (see Figure 2.3). Increasing depth in the profile corresponds to longer contact times with mineral surfaces, leading to a progressive downward accumulation of elements in the soil pore water. Hence, at the base of the profile, the soil solution is concentrated in metal cations, which compete with  $H^+$  for adsorption sites on the negatively charged surfaces of minerals, thereby inhibiting hydrolysis and dissolution reactions [26,63].

Ni is approximately ten times more concentrated than Cu in this soil; hence, the contrasting kinetic trends observed between these two metals are probably due to the considerable difference in their total concentrations. The high degree of metal loading of Ni in the soil makes it more likely that the EDTA-extractable Ni is predominantly held in relatively weakly bound forms as compared to Cu, and is therefore more susceptible to leaching. Most of the weakly bound Ni was probably derived from the decomposition of serpentine, which is known to be enriched in Ni in the Thetford Mines region and is easily weathered [23]. Although this mineral was once abundant in the till parent materials [22,23,64], x-ray diffraction analyses indicate an absence of serpentine in the clay-sized fraction of till within 3 m of the surface, which has been attributed to its destruction by postglacial weathering [64]. The Ni released during the breakdown of serpentine may have been retained in the soil as exchangeable phases sorbed to the charged surfaces of clay minerals and/or Fe- and Mn-oxides and hydroxides. The labile

kinetic component probably represents these weakly bound species, which are quickly extracted by EDTA or released upon dissolution of EDTA-soluble phases (e.g. amorphous Fe- and Mn-oxides). The slower component may be attributed to Ni held inside the crystal structure of a Mg-bearing phyllosilicate mineral (e.g. chlorite), as a minor replacement for Mg in the octahedral sheets. Ni bound inside the lattice structure can also have varying degrees of reactivity, depending on the bond strength, accessibility and coordination number of the metal ion residence sites. A decrease in Ni lability was observed up the profile, both in terms of the decreasing proportion of the labile component (Figures 4.16 a) and 4.18 a)) and the decreasing rate constant of the slowly-labile component (Figure 4.19). This may be due to surface leaching of both the weakly bound Ni ( $C_L$ ) and the relatively weaker fractions of the more strongly bound Ni in the mineral lattice ( $C_{SL}$ ). The leached Ni could then be transported to the groundwater, leaving the more strongly bound Ni to predominate near the surface. It is unclear why  $k_{SL}$  for Ni in profile 63 did not display a trend (Figure 4.17); however, such behaviour is not surprising given the inherent heterogeneity and complexity of natural soils.

Nickel in the uppermost samples from both profiles (i.e. 63B and 64C) is probably associated with a different soil phase from the rest of the samples, as the data points corresponding to samples 63B and 64C were outliers from the general trends, displaying extremely labile behaviour, both in terms of  $\%C_L$  and  $k_{SL}$ . This may be attributed to Ni bound to organic matter, which is much more abundant in the uppermost samples than in samples from deeper in the profile, as shown in Table 2.2. The two kinetically distinguishable components for Ni-organic complexes may represent Ni bound to sites of differing reactivities, as humic substances are physically and chemically heterogeneous complexants, having a diversity of functional groups with different intrinsic binding strengths (e.g. weak carboxylic and phenolic-type functional groups and stronger N- and S-bearing functional groups). Conformational effects may also play a role, as Ni ions bound to internal sites within the complex three-dimensional framework

of a humic molecule may be less reactive because of the physical inaccessibility of the binding sites to attack by weathering agents, while Ni ions bound to accessible peripheral functional groups are more easily extracted. Leaching did not appear to remove this 'organically-bound' Ni, which reflects the difference between the relative extraction efficiencies of rainwater and EDTA.

Copper in this soil is not known to be associated with the ultramafic source, hence, the mineral host for Cu could be different from that for Ni. However, the linear correlations observed between the trace metals and Mg from the acid digestion experiments (Figure 2.4) suggest that Cu is held as a trace impurity in the same Mg-bearing phyllosilicate mineral host as Ni. The uppermost samples for Cu in both profiles (i.e. 63B and 64C) do not show anomalously high labilities in terms of %C<sub>L</sub> (Figures 4.20 a) and 4.22 a)) or k<sub>SL</sub> (Figures 4.21 and 4.23); hence, Cu is probably not bound to organic matter at the surface as was inferred for Ni, but is more likely to be associated with a mineral that is progressively weathered and altered as a function of depth through the profile. The labile component of Cu could be attributed to relatively weakly bound Cu in the crystal lattice of a Mg-bearing phyllosilicate, held in partially coordinated, accessible residence sites on edges of the crystal lattice. The slowly labile component could represent strongly bound, more fully coordinated and less accessible Cu in the more central regions of the lattice. Weathering reactions, such as hydrolysis, oxidation and physical opening of the sheet-like lattice structure, cause destabilizing adjustments in the crystal structure, leading to an increase in the proportion of weakly bound metal ions by exposing a greater surface area and decreasing the coordination number of metal binding sites at edges. The increase in the values of %C<sub>L</sub> and k<sub>SL</sub> (i.e. increasing lability) with decreasing depth may indicate that the effects of breakdown of the crystal structure due to increased weathering intensity towards the surface predominate over the effects of removal of weakly bound metal ions by leaching. The points corresponding to the deepest sample in profile 63 (i.e. sample 63O) in Figures 4.20 and 4.21 were considered to be

outliers, as the sample appeared to be much more labile than predicted by the general trends in %C<sub>L</sub> and k<sub>SL</sub>. It is unclear why this sample did not follow the trends.

An alternative explanation for the contrasting kinetic behaviour of Ni and Cu may be that the metals occupy distinct residence sites in the same host mineral that have differing resistances to the effects of weathering and leaching processes. Mitchell [65] proposed that dissimilar binding forces at different locations in phyllosilicate minerals could be partially responsible for variations in relative extraction rates of a range of trace metal ions. Whether the host mineral for Ni and Cu in this soil is a 'true' chlorite or biotite, or a related mixed-layer clay mineral, metal ions could be held within the octahedral sheets of the 2:1 (TOT) layers or in an interlayer position, such as in the octahedral brucite sheet of a chlorite. The interlayer metal ion sites are likely to be much more susceptible to weathering and leaching than sites in the 2:1 octahedral sheets, as the latter are directly bound between the two tetrahedral sheets by short, strong oxygen bonds, while the former are only weakly held in place by electrostatic attraction and long-range hydrogen bonds [66]. These proposed models are illustrated in Figure 4.25, which shows a conceptual diagram of metal ions substituting for Mg within both types of octahedral sheets in a chlorite crystal. This diagram also illustrates the difference in coordination number between metal ions held in residence sites on edges and those held in sites in more central regions of the lattice.

A possible cause for the deviation of some samples from the general kinetic trends observed may be the influence of localized processes, such as pockets of redox reactions, and isolated regions of biological activity. Many biochemical compounds (e.g. enzymes and organic acids) are found in localized zones near concentrations of decomposing residues and in the rhizosphere. Complexation of metal ions by these organic compounds often form soluble metal complexes, increasing the availability of the metals to leaching and plant uptake [33]. In addition, Fe-, Mn- and Al-oxides can

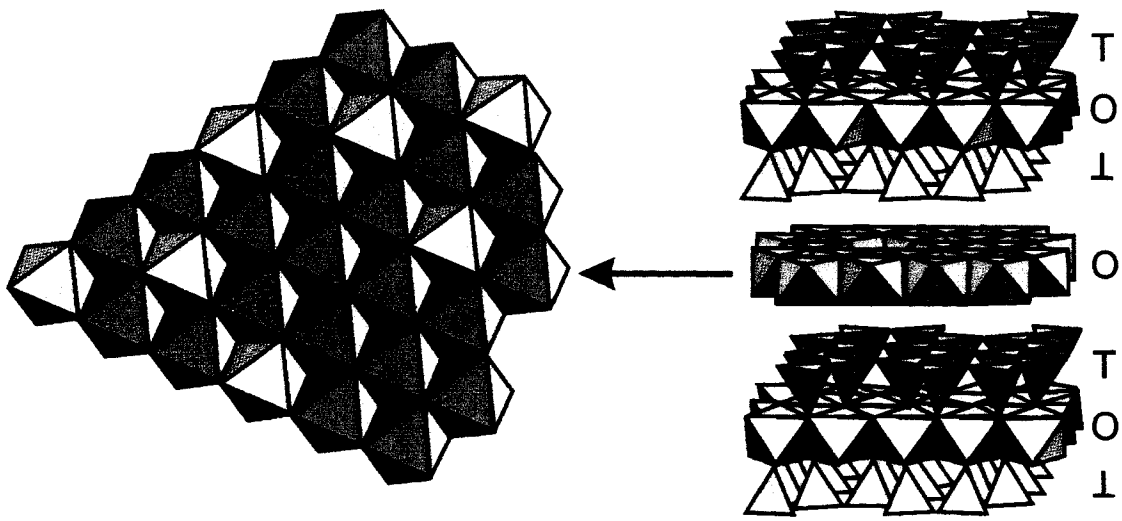


Figure 4.25 Conceptual diagram of metal ions occupying octahedral lattice sites in a chlorite crystal. Yellow octahedra represent sites containing a central Ni or Cu ion, grey octahedra represent sites containing a central Mg ion. T = tetrahedral sheet, O = octahedral sheet (adapted from Scheinost et al. [58]).

precipitate on the surfaces of clay minerals, which can significantly alter their properties by masking external charge sites, interfering with shrinking and swelling, and providing anion-retentive surfaces [28].

It is not possible with the available data to make definitive conclusions about the exact mechanisms or processes affecting the kinetic speciation of Ni and Cu through the soil profile, nor is it feasible to irrefutably isolate the predominant factors responsible for producing the observed kinetic trends. The above interpretations are intended to provide plausible explanations within the context of existing knowledge about these samples; however, the interpretations given are by no means exhaustive.

#### **4.5 Conclusions**

This work has established the validity of applying a kinetic fractionation method to study the kinetics of Ni and Cu extraction in a naturally enriched soil. Although only two soil profiles were studied, the consistency of the kinetic trends observed between them for both Ni and Cu represent a significant advance towards verifying that the results from the kinetic fractionation experiments have chemical significance.

The complexity of natural soils makes it difficult to identify the effects of any single soil-forming factor; however, the clear vertical trends in the kinetic reactivity of Ni and Cu suggest a competition between two dominant processes known to occur near the surface: 1) active soil weathering, which increases the proportion of weakly bound metal and the overall lability, and 2) leaching, which removes this weakly bound metal, decreasing overall lability. The kinetic trends observed for Ni (i.e. decreasing lability towards the surface) suggest that the effects of leaching predominate over the effects of breakdown of the mineral structure, leading to a net loss in weakly bound Ni towards the top of the profile, while the opposite effect was inferred for Cu. These differences are probably a consequence of the ten-fold difference in the concentration of Ni compared to that of Cu, making Ni predominate in more weakly bound, leachable forms.

Although the results from the kinetic fractionation experiments are operationally defined, the observed trends in metal lability as a function of depth through the profiles help to elucidate the *relative* rates of release of bound Ni and Cu species to the soil solution. This can provide insight into the availability of these metals for plant roots extending to different depths or can be used to predict changes in trace metal reactivity that could result from erosion and exposure of underlying, relatively less weathered soil horizons. In addition, the results are relevant to field conditions, as EDTA has been reported to provide an estimate of the plant-available metal fraction. The process of metal extraction from minerals and other soil components by complexation reactions is not far removed from the situation encountered in the real soil environment, especially in the rhizosphere, where plant roots extract metals from soil particles by exuding chelating organic acids. It has been reported that the environmental relevance of establishing operationally defined metal fractions having different labilities is yet to be determined [7]; however, the results from this work suggest otherwise.

#### **4.6 References**

---

1. Ph. Quevauviller, M. Lachica, E. Barahona, A. Gomez, G. Rauret, A. Ure, H. Muntau, *Fresen. J. Anal. Chem.*, 1998, **360**, 505.
2. A.M. Ure, P.h. Quevauviller, H. Muntau, B. Griepink, *Int. J. Environ. Anal. Chem.*, 1993, **51**, 135.
3. L.M. Shuman, *Soil Sci.*, 1985, **140**, 11.
4. A. Tessier, P.G.C. Campbell, M. Bisson, *Anal. Chem.*, 1979, **51**, 844.
5. G.E.M. Hall, G. Gauthier, J.C. Pelchat, P. Pelchat, J.E. Vaive, *Can. J. Anal. Sci. Spectros.*, 1996, **11**, 787.
6. D. Fangueiro, A. Bermond, E. Santos, H. Carapuça, A. Duarte, *Anal. Chim. Acta*, 2002, **459**, 245.

- 
7. A. Bermond, I. Yousfi, J.P. Ghestem, *Analyst*, 1998, **123**, 785.
  8. G. Varrault, Y. Fabre, A. Bermond, *Can. J. Anal. Sci. Spectros.*, 2001, **46**, 101.
  9. A. Bermond, G. Varrault, *Environ. Technol.*, 2004, **25**, 293.
  10. D.L. Sparks, Kinetics of Soil Chemical Processes: Past Progress and Future Needs, in *Kinetics of Soil Chemical Processes*, Academic Press, San Diego, USA, 1989, pp. 61-70.
  11. J. Yu, D. Klarup, *Water, Air, Soil Pollut.*, 1994, **75**, 205.
  12. J.P. Ghestem, A. Bermond, *Environ. Technol.*, 1999, **20**, 1119.
  13. C.H. Langford, D.W. Gutzman, *Anal. Chim. Acta*, 1992, **256**, 183.
  14. J.P. Ghestem, A. Bermond, *Environ. Technol.*, 1998, **19**, 409.
  15. T.H. Carski, D.L. Sparks, *Soil. Sci. Soc. Am. J.*, 1987, **51**, 314.
  16. D. Beauchemin, K. Kyser, D. Chipley, *Anal. Chem.*, 2002, **74**, 3924.
  17. M. Jimoh, W. Frenzel, V. Muller, H. Stephanowitz, E. Hoffmann, *Anal. Chem.*, 2004, **76**, 1197.
  18. W. Davison, G. Fones, M. Harper, P. Teasdale, H. Zhang, Dialysis, DET and DGT: In Situ Diffusional Techniques for Studying Water, Sediments and Soils, in *In Situ Chemical Analysis in Aquatic Systems*, J. Buffle, G. Horvai (Eds.), Wiley, Chichester, UK, 2000, pp 495-569.
  19. H. Zhang, F.J. Zhao, B. Sun., B. Davison, S.P. McGrath, *Env. Sci. Technol.*, 2001 **35**, 2602.
  20. M.M. Mortland, B. Ellis, *Soil Sci. Soc. Am. Pro.*, 1959, **23**, 363.
  21. M. M. Mortland, *Soil Sci. Soc. Am. Pro.*, 1958, **22**,503.
  22. R.A. Klassen, *Soil Profiles in Naturally Metal-Rich Terrains of Eastern Canada: Physical and Geochemical Data*, Open File 1745, CD, Geological Survey of Canada, 2003.

- 
23. A. Rencz, W. Shilts, Nickel in Soils and Vegetation of Glaciated Terrains, in *Nickel in the Environment*, J.O. Nriagu (Ed.), Wiley, New York, USA, 1980, pp 151-188.
  24. M.L. Jackson and G.D. Sherman, Chemical Weathering of Minerals in Soils, in *Advances in Agronomy*, Vol. 5, A.G. Norman (Ed.), Academic Press, New York, USA, 1953, pp. 219-318.
  25. A.M. Cortizas, E.G. Gayoso, J.C. Munoz, X.P. Pombal, P. Buurman, F. Terrible, *Geoderma*, 2003, **117**, 215.
  26. D.B. Nahon, *Introduction to the Petrology of Soils and Chemical Weathering*, Wiley, New York, USA, 1991, Chapters 1 and 3.
  27. G. Sposito, *The Chemistry of Soils*, Oxford University Press, New York, USA, 1989, Chapters 1 and 3.
  28. N.C. Brady, R.R. Weil, *The Nature and Properties of Soils*, 13<sup>th</sup> Ed., Prentice Hall, New Jersey, USA, 2002, Chapters 1 and 8.
  29. A.D. Karathanasis, Weathering and Alteration of Clay Minerals, in *Encyclopedia of Soil Science*, R. Lal (Ed.), Marcel Dekker, New York, USA, 2002, pp. 193-198.
  30. A.F. White, S.L. Brantley, *Rev. Mineral.*, 1995, **31**, 1.
  31. S.M. Ross, *Sources and Forms of Potentially Toxic Metals in Soil-Plant Systems*, Wiley, Chichester, UK, 1994, Chapter 1.
  32. Y. Tardy, *Geochim. Cosmochim. Acta*, 1977, **41**, 87.
  33. F.J. Stevenson, *Humic Chemistry: Genesis, Composition, Reactions*, Wiley, New York, USA, 1982, Chapter 14.
  34. M.L. Jackson, Chemical Composition of Soils, in *Chemistry of the Soil*, F.E. Bear (Ed.), Reinhold Publishing, New York, USA, 1964, Chapter 2.
  35. F. Bordas, A.C.M. Bourg, *Aquat. Geochem.*, 1998, **4**, 201.
  36. R.S. Tejawulan, W.H. Hendershot, *Environ. Pollut.*, 1998, **103**, 135.
  37. G.A. Brown, H.A. Elliott, *Water, Air, Soil Pollut.*, 1992, **62**, 157.

- 
38. B. Chen, C.A. Shand, R. Beckett, *J. Environ. Monit.*, 2001, **3**, 7.
39. A. Sahuquillo, A. Rigol, G. Rauret, *J. Environ. Monit.*, 2002, **4**, 1003.
40. D. McGrath, *Sci. Total Environ.*, 1996, **178**, 37.
41. H. Kennedy, A.L. Sanche, D.H. Oughton, A.P. Rowland, *Analyst*, 1997, **122**, 89R.
42. A.M. Ure, *Mikrochim. Acta*, 1991, **2**, 49.
43. D.C. Harris, *Quantitative Chemical Analysis*, 6<sup>th</sup> Ed., W.H. Freeman, New York, USA, 2003, pp. 261-265.
44. F.J. Welcher, *The Analytical uses of Ethylenediaminetetraacetic Acid*, D. Van Nostrand Company, Toronto, Canada, 1958, Chapter 1.
45. A.E. Martell, R.M. Smith, *Critical Stability Constants*, Vol. 1, Plenum Press, New York, USA, 1974, pp. 204.
46. O. Schramel, B. Michalke, A. Ketrup, *Sci. Total Environ.*, 2000, **263**, 11.
47. .R. Sanders, T.M. Adams, B.T. Christensen, *J. Sci. Food Agric.*, 1986, **37**, 1155.
48. D.M. Templeton, F. Ariese, R. Cornelis, L. Danielsson, H. Muntau, H.P. Van Leeuwen, R. Lobinski, *Pure Appl. Chem.*, 2000, **72**, 1453.
49. D.L. Sparks, Kinetics of Sorption/Release Reactions on Natural Particles, in *Structure and Surface Reactions of Soil Particles*, Vol. 4, P.M. Huang, N. Senesi, J. Buffle (Eds.), Wiley, Chichester, UK, 1998, Chapter 11.
50. B. Welz, M. Sperling, *Atomic Absorption Spectrometry*, 3<sup>rd</sup> Ed., Wiley, Weinheim, Germany, 1999, p. 532.
51. J.F. Rusling, T.F. Kumosinski, *Nonlinear Computer Modeling of Chemical and Biochemical Data*, Academic Press, San Diego, USA, 1996, Chapter 2.
52. L. Meites, Some New Techniques for the Analysis and Interpretation of Chemical Data, in *CRC Critical Reviews in Analytical Chemistry*, Vol. 8, Taylor and Francis, Philadelphia, USA, 1979, pp. 7-15.
53. S.E. Cabaniss, *Environ. Sci. Technol.*, 1990, **24**, 583.

- 
54. D.W. Gutzman, C.H. Langford, *Environ. Sci. Technol.*, 1993, **27**, 1388.
55. P.M. Jardine, D.L. Sparks, *Soil Sci. Soc. Am. J.*, 1984, **48**, 39.
56. M.L. Brusseau, P.S.C. Rao, *Crit. Rev. Env. Contr.*, 1989, **19**, 33.
57. R.N.J. Comans, D.E. Hockley, *Geochim. Cosmochim. Acta*, 1992, **56**, 1157.
58. A.C. Scheinost, R. Kretzschmar, S. Pfister, *Environ. Sci. Technol.*, 2002, **36**, 5021.
59. O.K. Borggaard, *Clay Miner.*, 1982, **17**, 365.
60. E.E. Kohler, H.M. Koster, *Geol. J.*, 1982, **52**, 89.
61. M. Kaupenjohann, W. Wilcke, *Soil Sci. Soc. Am. J.*, 1995, **9**, 1027.
62. B. Ohlander, J. Thunberg, M. Land, L.O. Hoglund, H. Quishang, *Appl. Geochem.*, 2003, **18**, 883.
63. D.A. Stonestrom, A.F. White, K.C. Akstin, *J. Hydrol.*, 1998, **209**, 331.
64. W.W. Shilts, *Detailed Sedimentological Study of Till Sheets in a Stratigraphic Section, Samson River, Quebec*: Bulletin 285, Geological Survey of Canada, 1978.
65. R.L. Mitchell, Trace elements in soils, in *Chemistry of the Soil*, F.E. Bear (Ed.), Reinhold Publishing, New York, USA, 1964, Chapter 8.
66. S.W. Bailey, Chlorites: Structures and Crystal Chemistry, in *Reviews in Mineralogy, Hydrous Phyllosilicates*, Vol. 19, Mineralogical Society of America, Washington, USA, 1988, Chapter 10.

## **Chapter 5      Conclusions**

---

The results from this research support the hypothesis that in the naturally enriched soils of the Thetford Mines area, Ni is hosted by Mg-bearing phyllosilicates and that the kinetic reactivities of Ni and Cu vary in a systematic manner down the profile, probably as a consequence of processes associated with weathering and soil formation. This work represents a significant advance towards achieving the ultimate goal of linking trace metal speciation on an individual particle basis with kinetic properties of the bulk soil. In addition, the concepts discussed contribute to an evolving paradigm shift from macroscopic, equilibrium-based approaches to microscopic, kinetic-based approaches that was initiated by the recognition of the importance of time-dependent reactions at the particle-solution interface in complex, heterogeneous natural soil systems.

Recognition of a mineral group as the principal natural background control on trace metal concentrations in soils provides a fundamental geochemical tool for environmental risk management. The ToF-SIMS studies constitute a novel and independent approach to validate interpretations of the empirical geochemical relations based on Ni-Mg associations from the previously-performed acid digestion analyses. The spatial correlations observed in the secondary ion images provide supporting evidence on an individual particle basis that Mg-bearing phyllosilicates are the principal hosts of Ni in this soil; however, more work is required to confirm this and to establish their significance in the context of the bulk soil. Although the relative importance of these Mg-bearing phyllosilicate minerals for hosting Ni in the soil is difficult to ascertain solely using the methods employed in this study, this work represents a key first-step towards achieving that ultimate goal.

The identification of a broad family of related minerals as the predominant mineral hosts for Ni rather than a single specific mineral results from the fact that phyllosilicate minerals in the soil environment are rarely in a pristine unweathered state, and are frequently subject to intermixing and alteration, which complicates the mineralogical analysis. In addition, ideal analytical tools do not exist, as they are subject

to limitations with respect to factors such as grain size, detection limits and quantification capabilities. As a result, there is no one reliable, direct way to unequivocally identify and quantify the mineralogy. Although investigation of such a complex system can never be a precise science, the obtainable information can still provide valuable insight into the geochemical controls on natural background variations in soils.

The use of ToF-SIMS in conjunction with SEM-EDS extends the utility of ToF-SIMS to analysis of fine-grained, chemically and physically heterogeneous samples. Moreover, this combination of complementary techniques allows for more comprehensive and cost-effective analyses than would be possible using ToF-SIMS alone. Identification of trace amounts of Ni in Fe-rich mineral grains represents a unique challenge because of the isobaric interference of  $^{58}\text{Ni}$  by  $^{58}\text{Fe}$ . This limits the applicability of conventional SIMS as a result of the relatively poor detection limits of quadrupole and magnetic sector mass spectrometers, which hinder their ability to detect the less abundant  $^{60}\text{Ni}$  isotope. The research presented in this thesis constitutes one of the first applications of ToF-SIMS to trace analysis of Ni in individual soil mineral grains. This work also demonstrated the ability of ToF-SIMS to simultaneously detect all secondary ion species generated, including positive and negative atomic and molecular ions – a considerable advantage unique to ToF-SIMS.

The kinetic approach to trace metal speciation employed in this research reveals information about soils that is not attainable from conventional extraction experiments. The kinetic fractionation studies provide a method for differentiating between rapidly and slowly extracted metals from soils, where the labile component can be considered to be a useful surrogate for bioavailability. Although the results are operationally defined, the *relative* labilities provide insight into the effects of transformation processes with depth.

Because the rate of trace element release depends on the properties of the original mineral hosts, Mg-bearing phyllosilicates were used as an interpretive key for proposing possible scenarios to explain the observed vertical changes in trace metal reactivity as

determined from the kinetic fractionation studies. Although it was not possible to make definitive conclusions regarding with which soil phase the EDTA-extractable metal was associated, it was reasoned that the EDTA was probably capable of extracting the metals from the crystal lattices of minerals. The results from the kinetic studies on soil samples from profiles 63 and 64 indicated that Ni and Cu had opposite vertical trends in kinetic reactivity, where Ni became progressively less labile, and Cu became progressively more labile towards the surface. These trends were interpreted to reflect the combined effects of vertical gradients in the intensity of soil weathering and leaching processes, which act to differing extents on the two elements, perhaps because of differences in their chemical forms and/or residence sites. These results merit further study to ascertain the precise cause and significance of the observed trends. Despite the inherent complexity and heterogeneity of natural soils, the kinetic results demonstrated distinct trends in the lability of both Ni and Cu that were consistent between the two profiles, suggesting that these systematic vertical changes in kinetic behaviour may be representative of the effects of soil weathering processes in the general area.

This work is significant to environmental soil science research in that it introduces an innovative, multidisciplinary approach to provide a basis for establishing broad mineralogical controls on the occurrence and distribution of natural background levels of trace metals in soils, and for obtaining insight into how the kinetic reactivity of these metals change with depth through a vertical profile. The results contribute to an improved understanding of trace metal speciation and bioavailability in the terrestrial environment, and holds important implications for evaluation and management of environmental risk associated with large areas of natural trace metal enrichment in soils. In addition, the analytical tools developed from this work can be used to devise new speciation methods for other distinct geological terrains, and may also hold relevance for agricultural applications, including estimation of soil quality and nutrient bioavailability.

## Appendix A

---

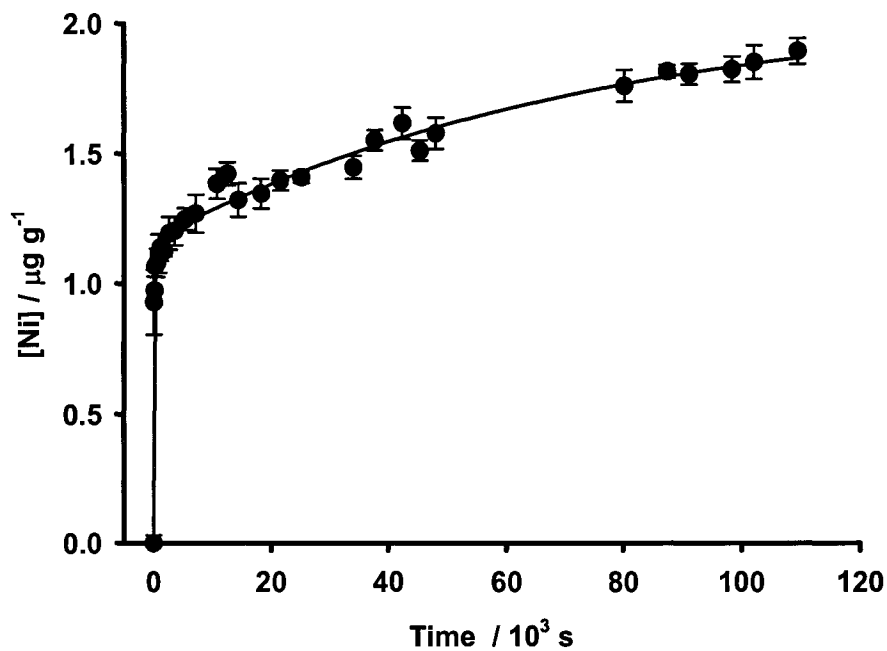


Figure A.1 Ni kinetic curve for sample 63B. Error bars represent one standard deviation of the mean. < 0.063 mm, mass/volume = 0.01, [EDTA] = 0.05 mol/L, pH 6.00 ± 0.02, 23 ± 2 °C.

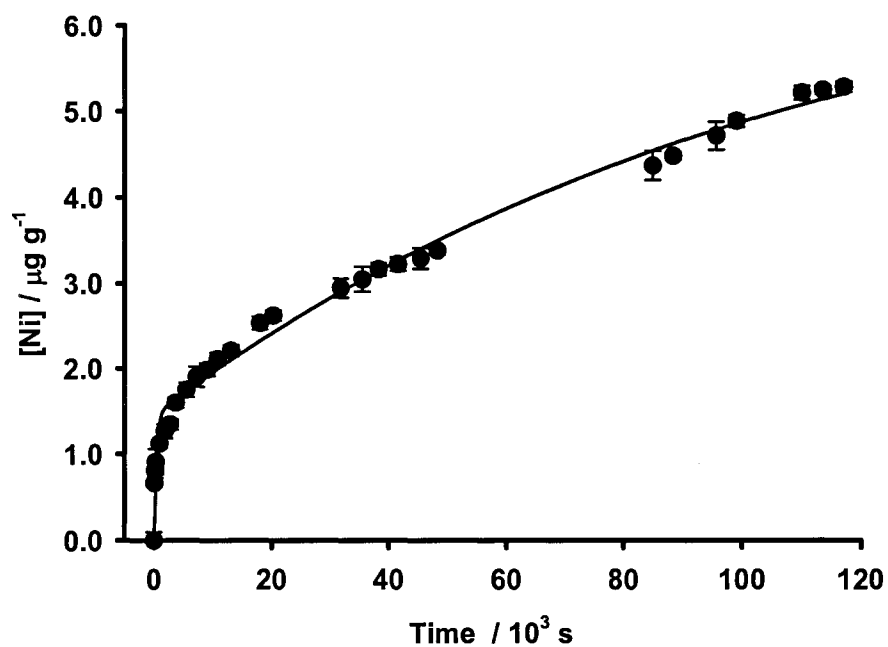


Figure A.2 Ni kinetic curve for sample 63E. Error bars represent one standard deviation of the mean. < 0.063 mm, mass/volume = 0.01, [EDTA] = 0.05 mol/L, pH 6.00 ± 0.02, 23 ± 2 °C.

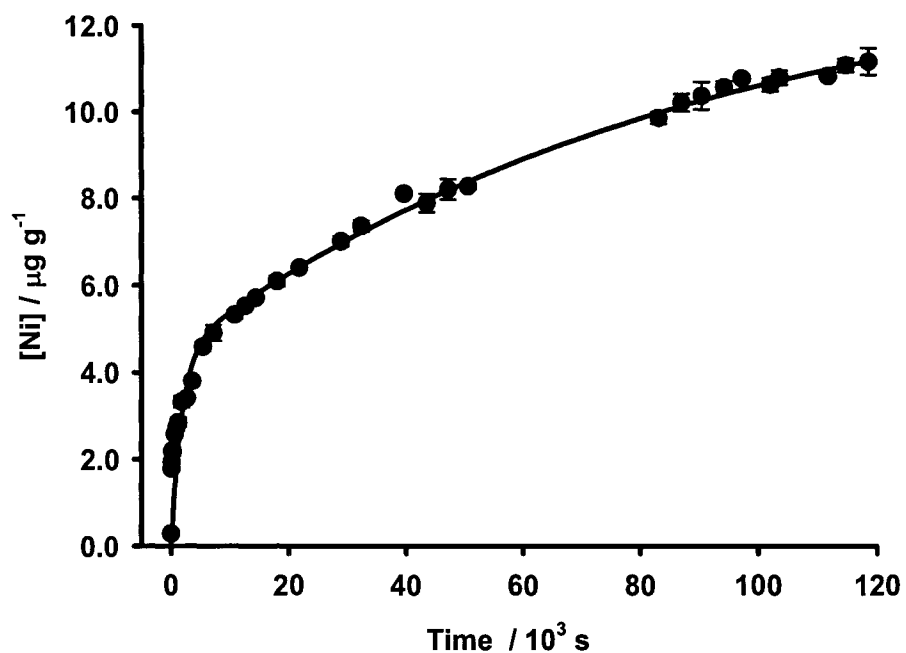


Figure A.3 Ni kinetic curve for sample 63F. Error bars represent one standard deviation of the mean. < 0.063 mm, mass/volume = 0.01, [EDTA] = 0.05 mol/L, pH  $6.00 \pm 0.02$ ,  $23 \pm 2$  °C.

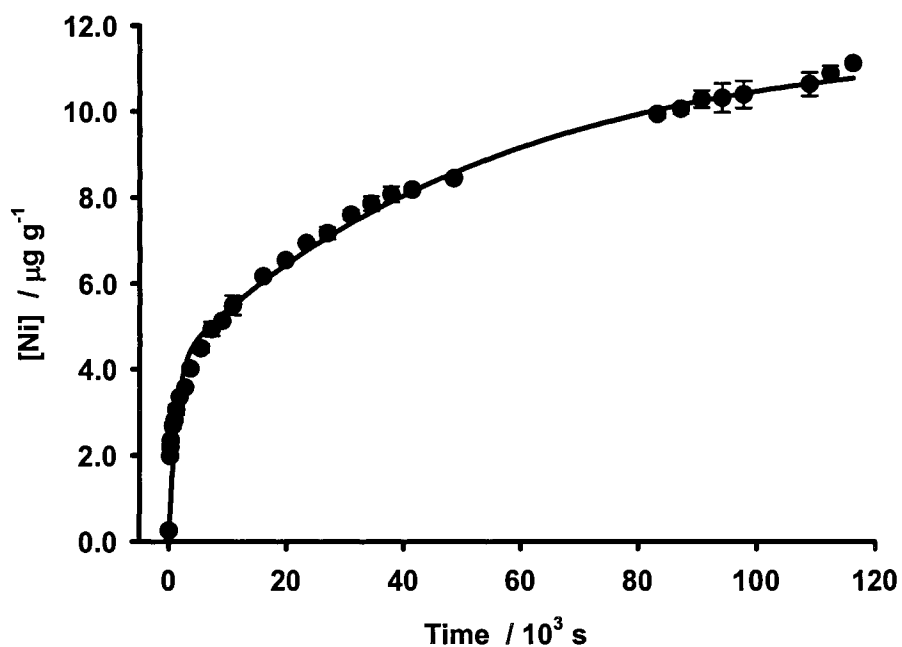


Figure A.4 Ni kinetic curve for sample 63G. Error bars represent one standard deviation of the mean. < 0.063 mm, mass/volume = 0.01, [EDTA] = 0.05 mol/L, pH  $6.00 \pm 0.02$ ,  $23 \pm 2$  °C.

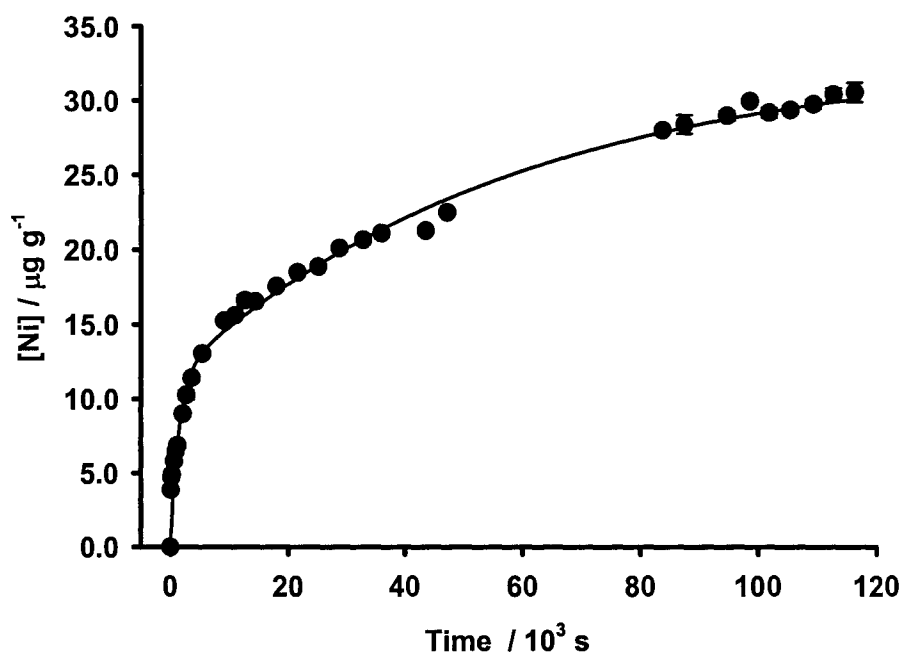


Figure A.5 Ni kinetic curve for sample 63L. Error bars represent one standard deviation of the mean. < 0.063 mm, mass/volume = 0.01, [EDTA] = 0.05 mol/L, pH 6.00 ± 0.02, 23 ± 2 °C.

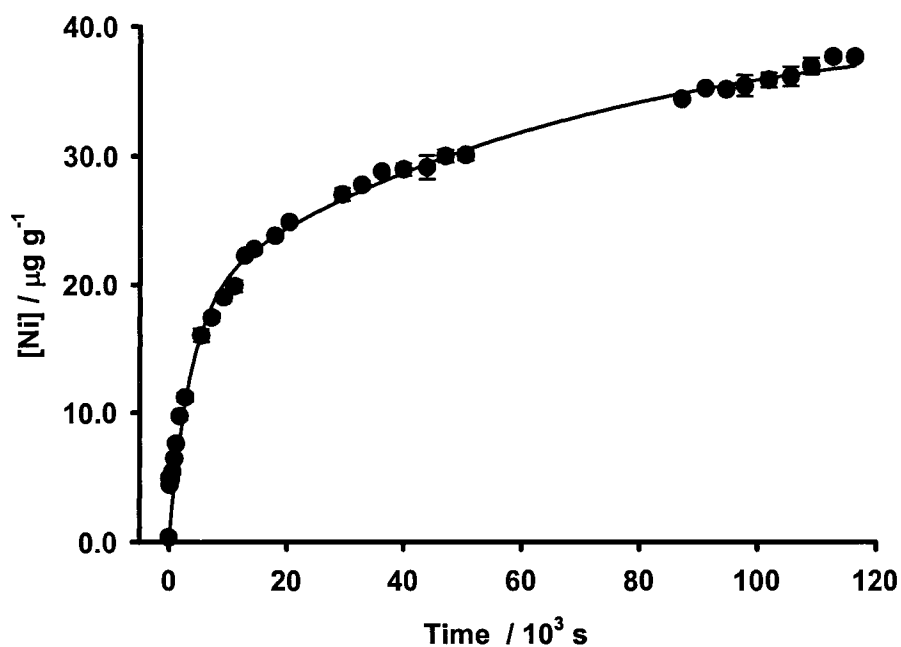


Figure A.6 Ni kinetic curve for sample 63O. Error bars represent one standard deviation of the mean. < 0.063 mm, mass/volume = 0.01, [EDTA] = 0.05 mol/L, pH 6.00 ± 0.02, 23 ± 2 °C.

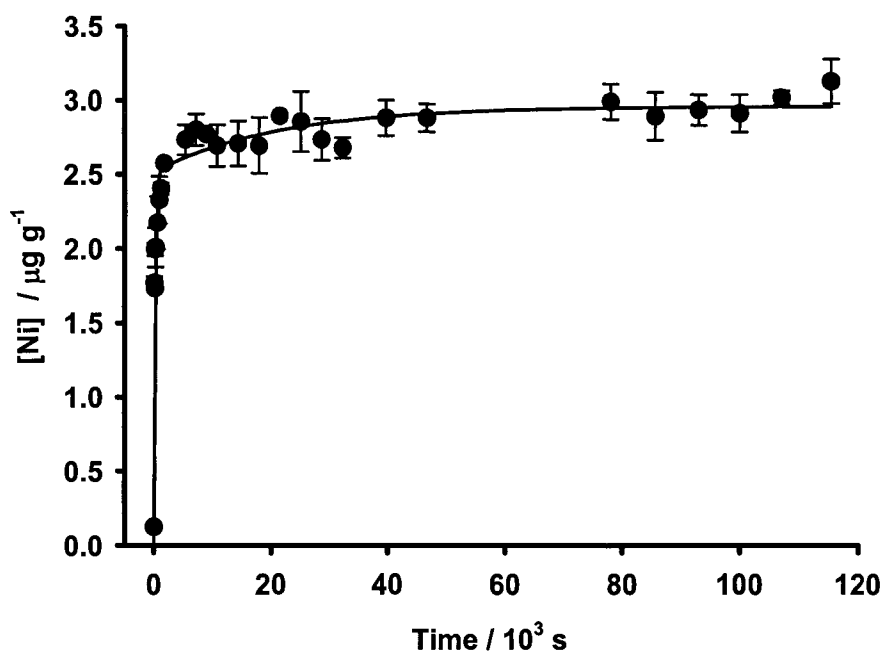


Figure A.7 Ni kinetic curve for sample 64C. Error bars represent one standard deviation of the mean. < 0.063 mm, mass/volume = 0.01, [EDTA] = 0.05 mol/L, pH 6.00 ± 0.02, 23 ± 2 °C.

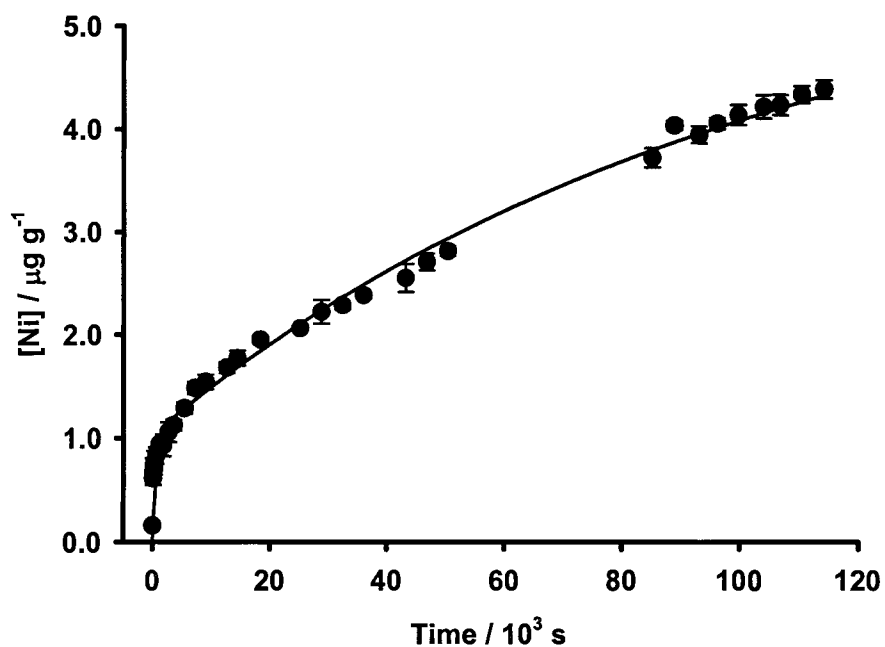


Figure A.8 Ni kinetic curve for sample 64E. Error bars represent one standard deviation of the mean. < 0.063 mm, mass/volume = 0.01, [EDTA] = 0.05 mol/L, pH 6.00 ± 0.02, 23 ± 2 °C.

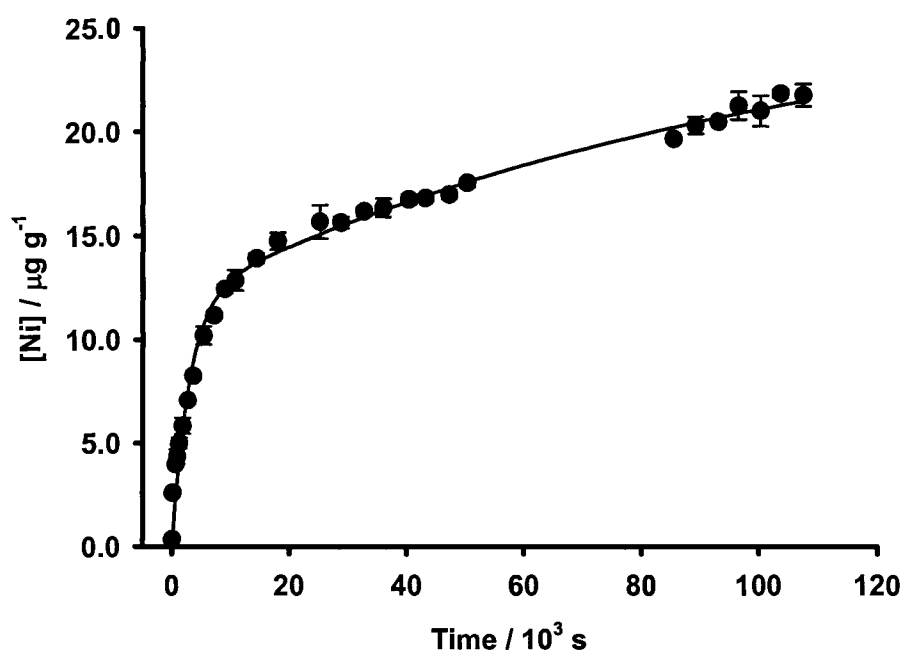


Figure A.9 Ni kinetic curve for sample 64G. Error bars represent one standard deviation of the mean. < 0.063 mm, mass/volume = 0.01, [EDTA] = 0.05 mol/L, pH 6.00 ± 0.02, 23 ± 2 °C.

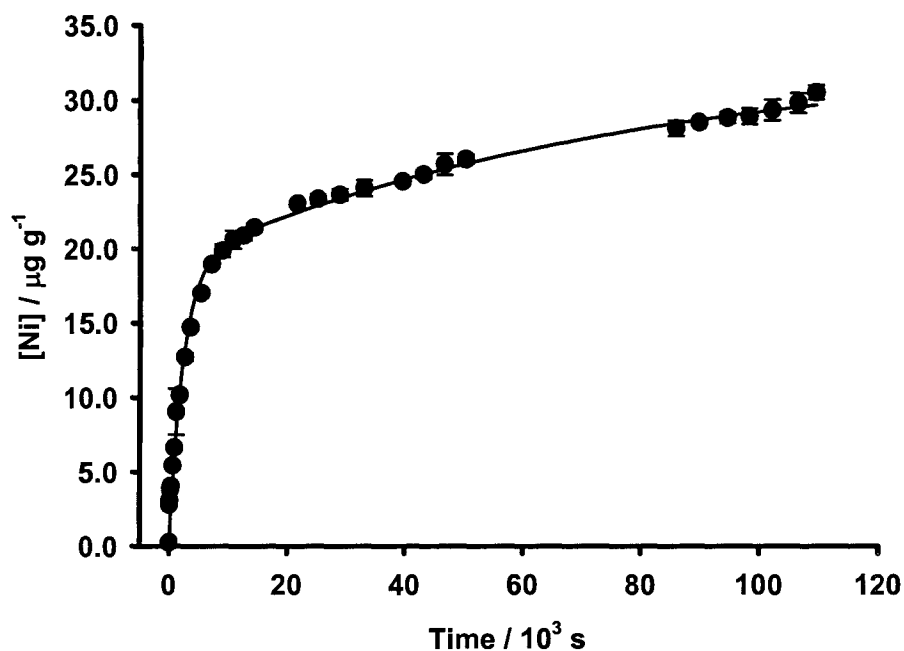


Figure A.10 Ni kinetic curve for sample 64I. Error bars represent one standard deviation of the mean. < 0.063 mm, mass/volume = 0.01, [EDTA] = 0.05 mol/L, pH 6.00 ± 0.02, 23 ± 2 °C.

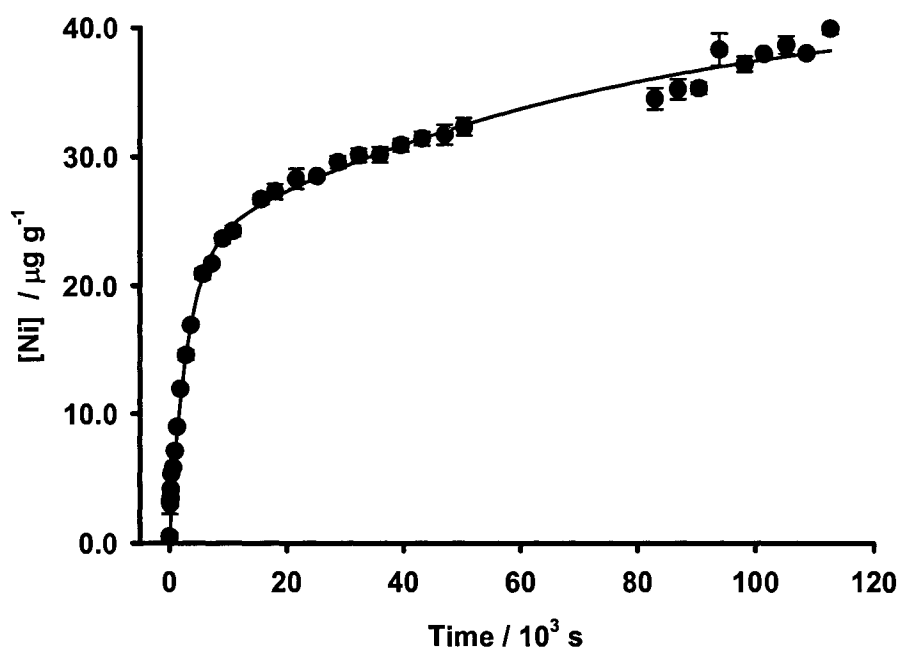


Figure A.11 Ni kinetic curve for sample 64K. Error bars represent one standard deviation of the mean.  $< 0.063$  mm, mass/volume = 0.01, [EDTA] = 0.05 mol/L, pH  $6.00 \pm 0.02$ ,  $23 \pm 2$  °C.

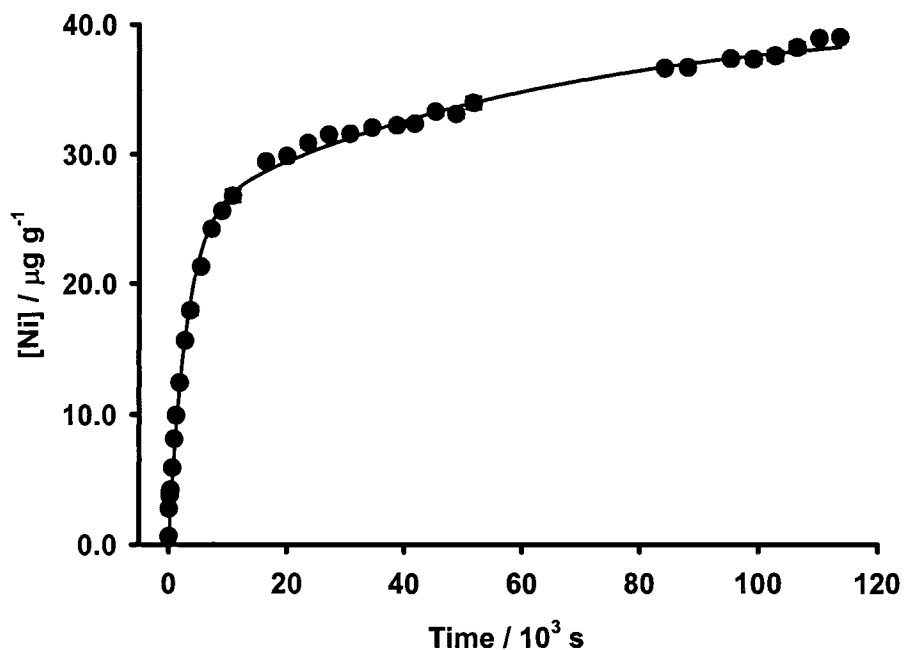


Figure A.12 Ni kinetic curve for sample 64L. Error bars represent one standard deviation of the mean.  $< 0.063$  mm, mass/volume = 0.01, [EDTA] = 0.05 mol/L, pH  $6.00 \pm 0.02$ ,  $23 \pm 2$  °C.

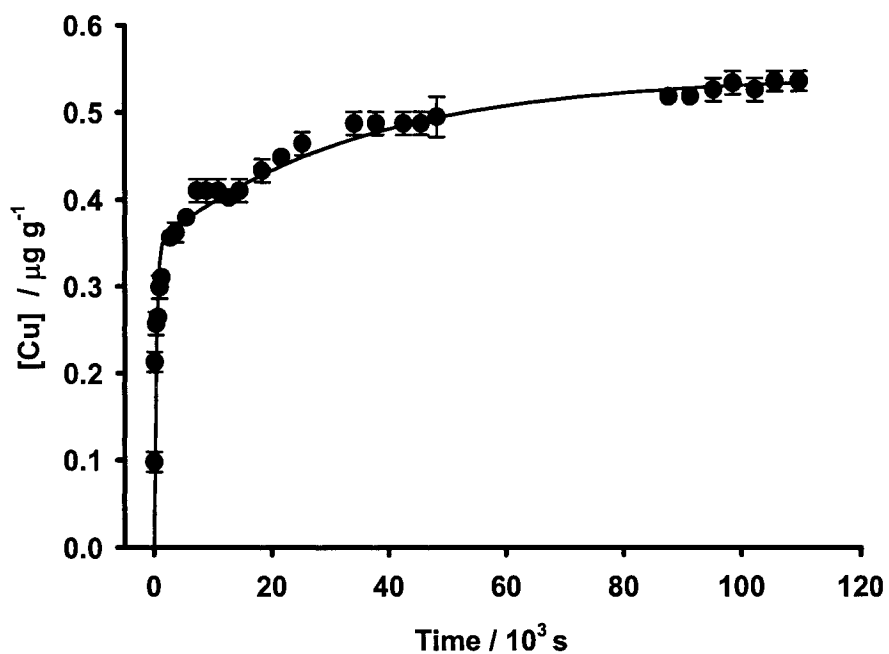


Figure A.13 Cu kinetic curve for sample 63B. Error bars represent one standard deviation of the mean. < 0.063 mm, mass/volume = 0.01, [EDTA] = 0.05 mol/L, pH  $6.00 \pm 0.02$ ,  $23 \pm 2$  °C.

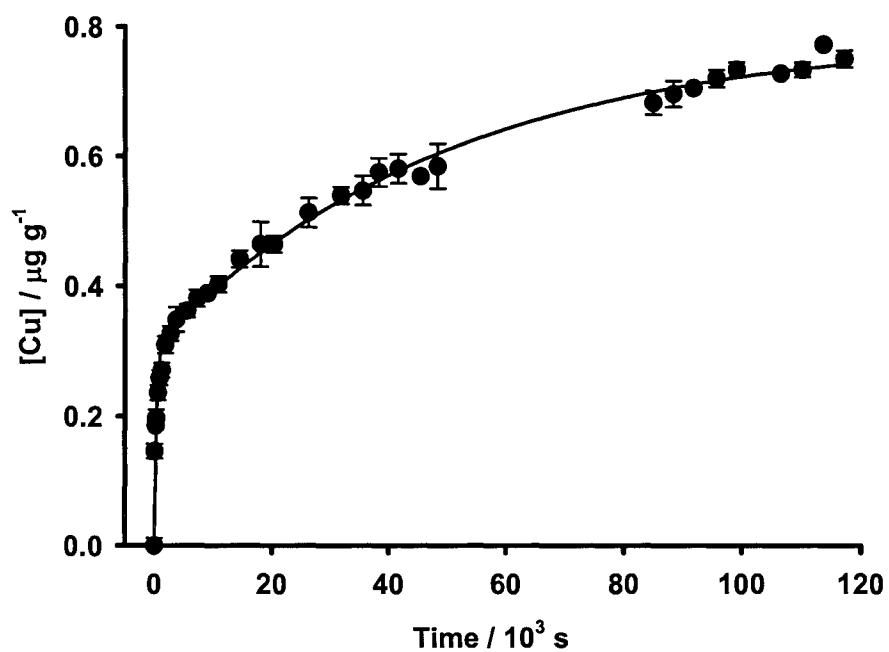


Figure A.14 Cu kinetic curve for sample 63E. Error bars represent one standard deviation of the mean. < 0.063 mm, mass/volume = 0.01, [EDTA] = 0.05 mol/L, pH  $6.00 \pm 0.02$ ,  $23 \pm 2$  °C.

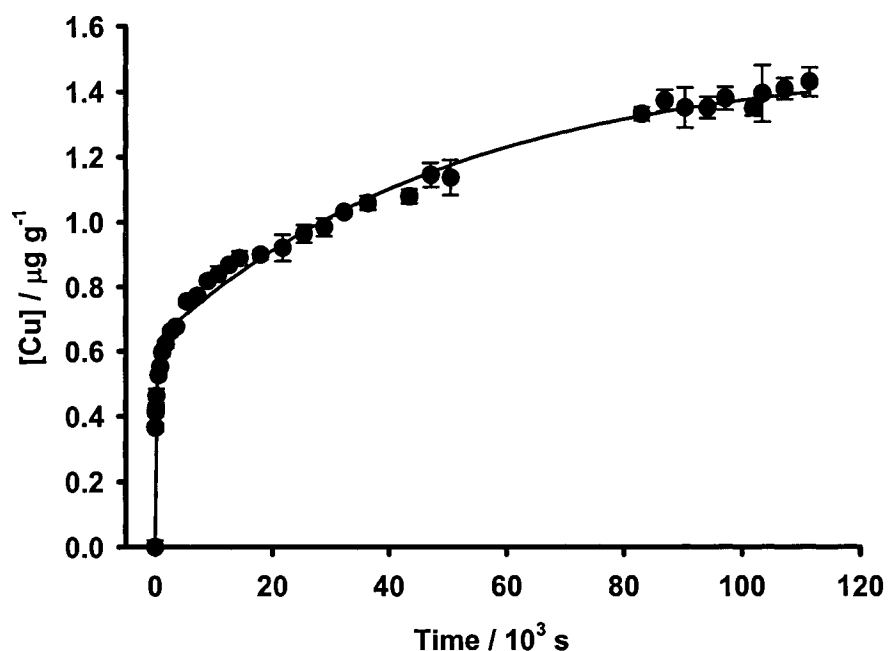


Figure A.15 Cu kinetic curve for sample 63F. Error bars represent one standard deviation of the mean. < 0.063 mm, mass/volume = 0.01, [EDTA] = 0.05 mol/L, pH 6.00 ± 0.02, 23 ± 2 °C.

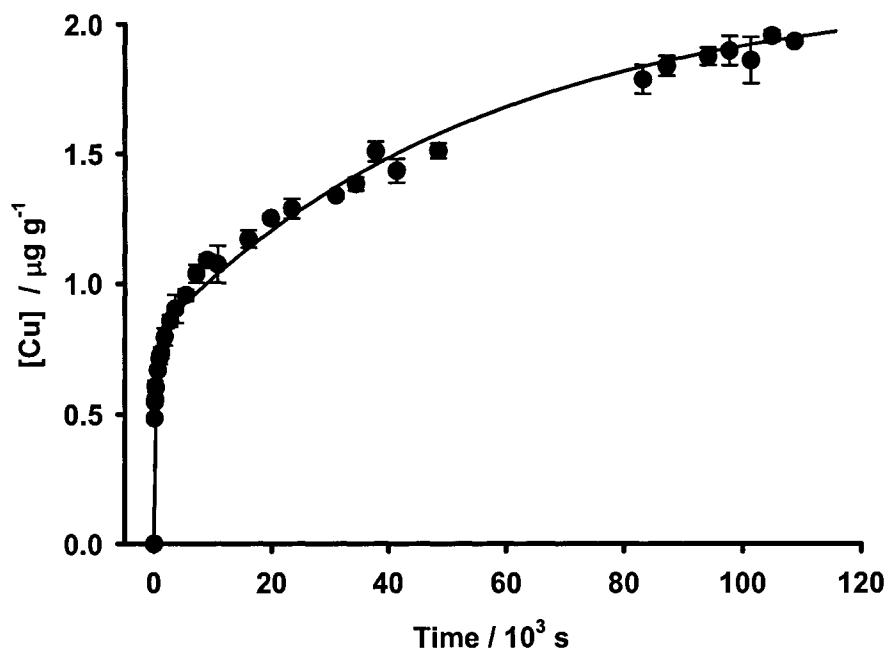


Figure A.16 Cu kinetic curve for sample 63G. Error bars represent one standard deviation of the mean. < 0.063 mm, mass/volume = 0.01, [EDTA] = 0.05 mol/L, pH 6.00 ± 0.02, 23 ± 2 °C.

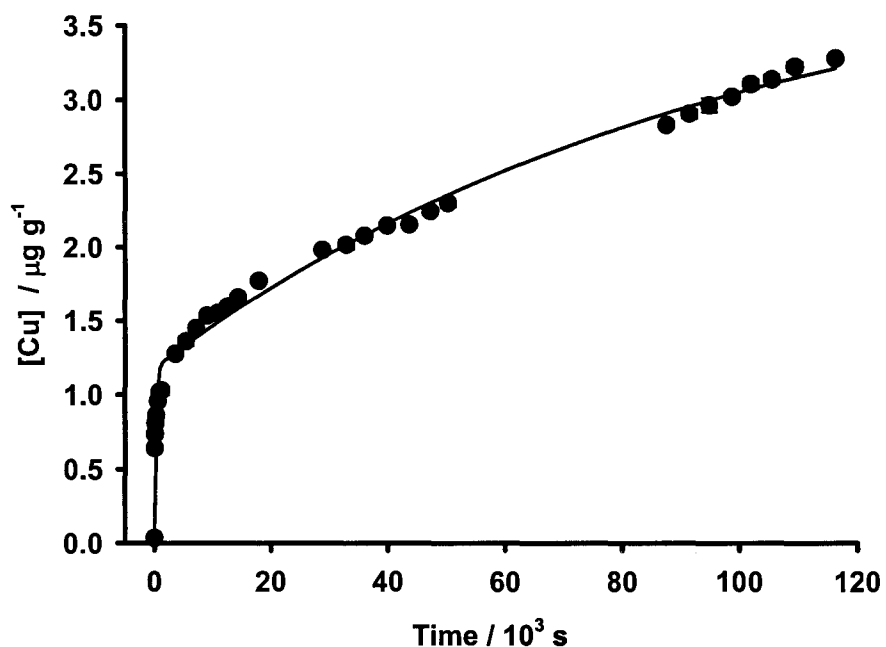


Figure A.17 Cu kinetic curve for sample 63L. Error bars represent one standard deviation of the mean. < 0.063 mm, mass/volume = 0.01, [EDTA] = 0.05 mol/L, pH  $6.00 \pm 0.02$ ,  $23 \pm 2$  °C.

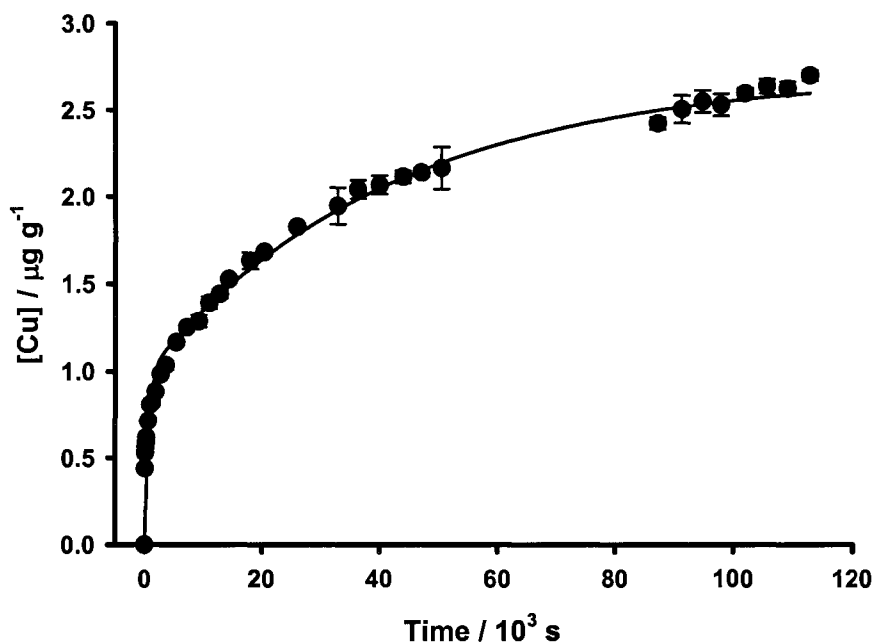


Figure A.18 Cu kinetic curve for sample 63O. Error bars represent one standard deviation of the mean. < 0.063 mm, mass/volume = 0.01, [EDTA] = 0.05 mol/L, pH  $6.00 \pm 0.02$ ,  $23 \pm 2$  °C.

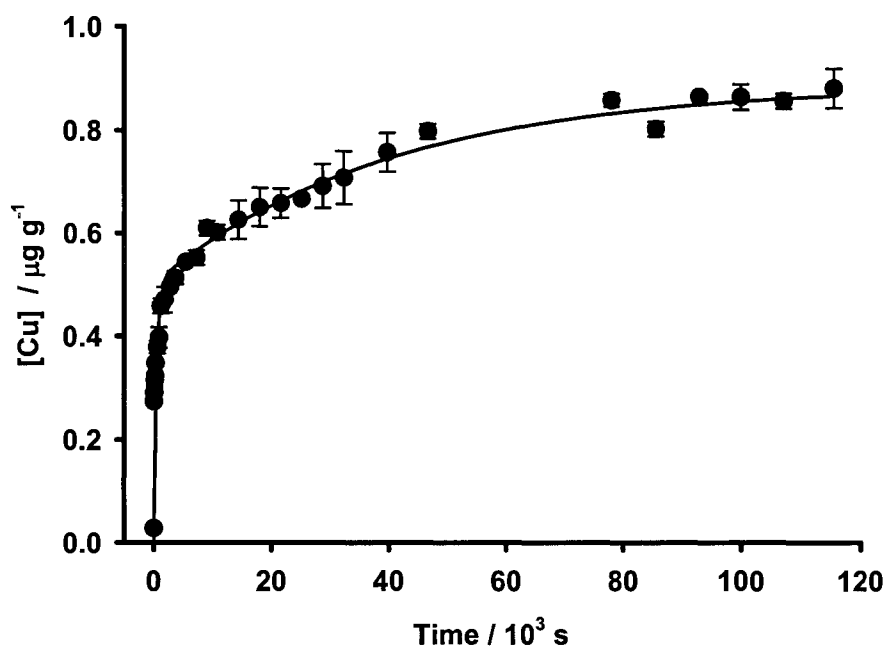


Figure A.19 Cu kinetic curve for sample 64C. Error bars represent one standard deviation of the mean. < 0.063 mm, mass/volume = 0.01, [EDTA] = 0.05 mol/L, pH 6.00 ± 0.02, 23 ± 2 °C.

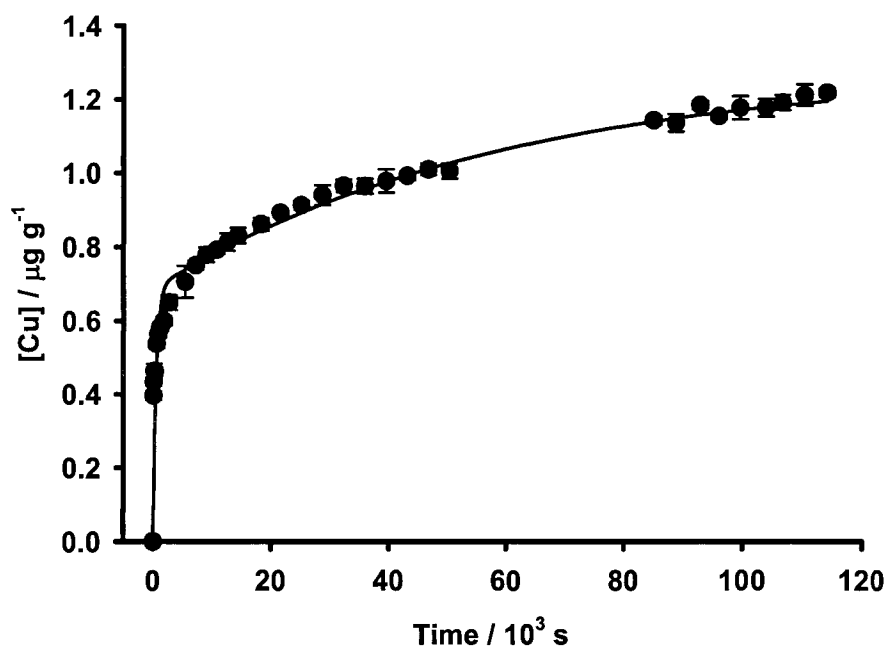


Figure A.20 Cu kinetic curve for sample 64E. Error bars represent one standard deviation of the mean. < 0.063 mm, mass/volume = 0.01, [EDTA] = 0.05 mol/L, pH 6.00 ± 0.02, 23 ± 2 °C.

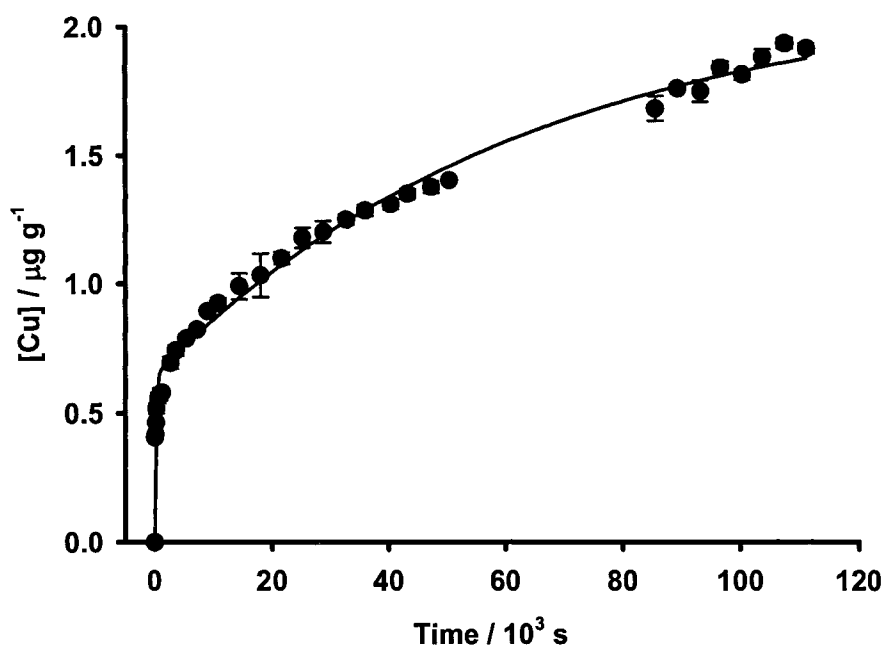


Figure A.21 Cu kinetic curve for sample 64G. Error bars represent one standard deviation of the mean. < 0.063 mm, mass/volume = 0.01, [EDTA] = 0.05 mol/L, pH  $6.00 \pm 0.02$ ,  $23 \pm 2$  °C.

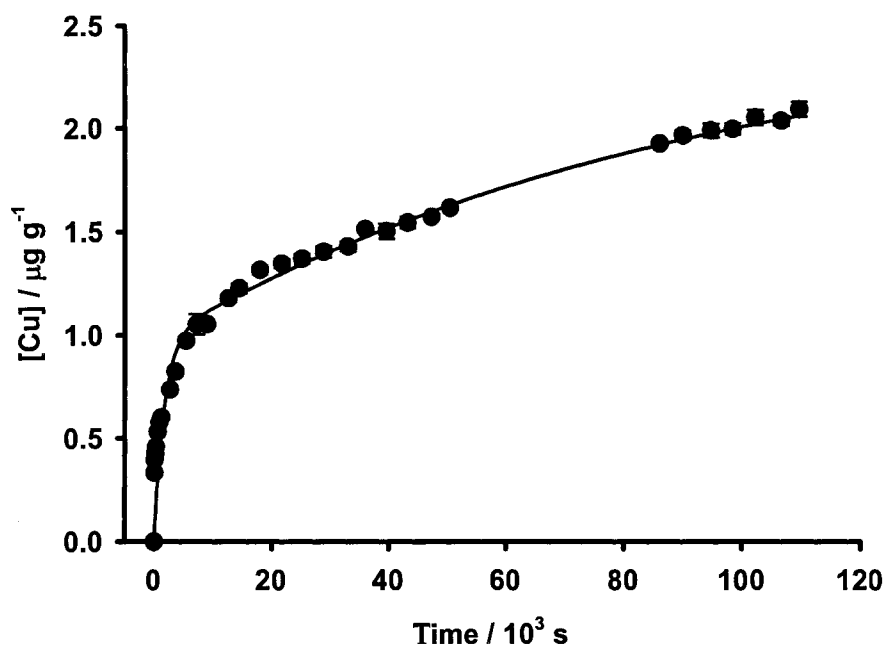


Figure A.22 Cu kinetic curve for sample 64I. Error bars represent one standard deviation of the mean. < 0.063 mm, mass/volume = 0.01, [EDTA] = 0.05 mol/L, pH  $6.00 \pm 0.02$ ,  $23 \pm 2$  °C.

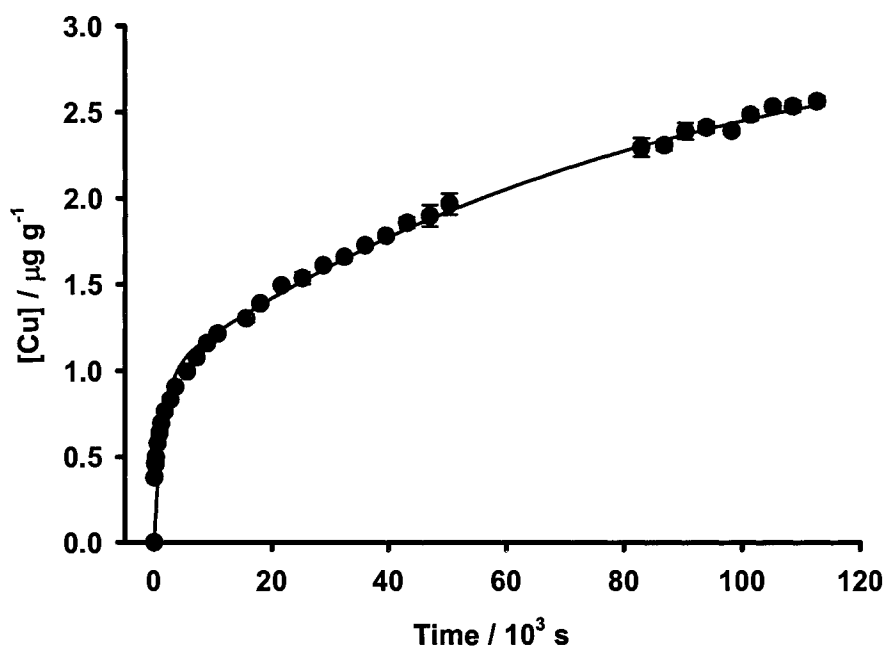


Figure A.23 Cu kinetic curve for sample 64K. Error bars represent one standard deviation of the mean. < 0.063 mm, mass/volume = 0.01, [EDTA] = 0.05 mol/L, pH  $6.00 \pm 0.02$ ,  $23 \pm 2$  °C.

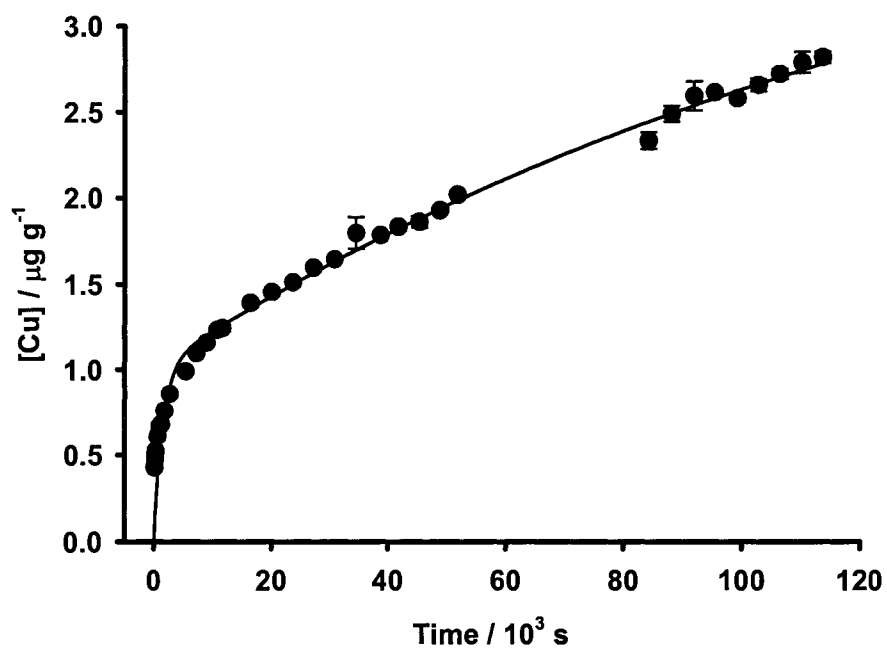


Figure A.24 Cu kinetic curve for sample 64L. Error bars represent one standard deviation of the mean. < 0.063 mm, mass/volume = 0.01, [EDTA] = 0.05 mol/L, pH  $6.00 \pm 0.02$ ,  $23 \pm 2$  °C.